

Assessment of the Out-of-Plane Earthquake Resistance of Reinforced Concrete Frame Structures with Masonry Infill Walls Containing Openings

Anić, Filip

Doctoral thesis / Disertacija

2022

Degree Grantor / Ustanova koja je dodijelila akademski / stručni stupanj: **Josip Juraj Strossmayer University of Osijek, Faculty of Civil Engineering and Architecture Osijek / Sveučilište Josipa Jurja Strossmayera u Osijeku, Građevinski i arhitektonski fakultet Osijek**

Permanent link / Trajna poveznica: <https://urn.nsk.hr/urn:nbn:hr:133:129275>

Rights / Prava: [In copyright](#) / [Zaštićeno autorskim pravom.](#)

Download date / Datum preuzimanja: **2025-02-20**



GRAĐEVINSKI I ARHITEKTONSKI FAKULTET OSJEK
Faculty of Civil Engineering and Architecture Osijek

Repository / Repozitorij:

[Repository GrAFOS - Repository of Faculty of Civil Engineering and Architecture Osijek](#)



Josip Juraj Strossmayer University of Osijek
Faculty of Civil engineering and Architecture Osijek

Postgraduate University Study Programme in Civil Engineering

Assessment of the Out-of-Plane Earthquake Resistance of Reinforced Concrete Frame Structures with Masonry Infill Walls Containing Openings

Filip Anić mag. ing. aedif.

Osijek, April, 2022.

Sveučilište Josipa Jurja Strossmayera u Osijeku
Građevinski i arhitektonski fakultet Osijek

Poslijediplomski sveučilišni studij Građevinarstvo

Procjena potresne otpornosti okomito na svoju ravninu
armirano-betonskih okvirnih konstrukcija s ispunskim
ziđem u kojem se nalaze otvori

Filip Anić, mag. ing. aedif.

U Osijeku, travanj 2022. godine

Prosudbena povjerenstva i bibliografski podaci

Povjerenstvo za prihvaćanje teme doktorske disertacije

Povjerenstvo za prihvaćanje teme doktorske disertacije imenovano na 204. redovitoj sjednici Fakultetskog vijeća Građevinskog i arhitektonskog fakulteta Osijek Sveučilišta Josipa Jurja Strossmayera u Osijeku, održanoj 27. studenog 2018. godine:

1. prof. dr. sc. Ivica Guljaš, dipl. ing. građ. Sveučilište Josipa Jurja Strossmayera u Osijeku, Građevinski i arhitektonski fakultet Osijek (predsjednik Povjerenstva)
2. izv. prof. dr. sc. Davorin Penava, dipl. ing. građ. Sveučilište Josipa Jurja Strossmayera u Osijeku, Građevinski i arhitektonski fakultet Osijek
3. prof. dr. sc. Ivica Kožar, dipl. ing. građ. Sveučilište u Rijeci, Građevinski fakultet

Tema, mentor, prvi i drugi komentor doktorske disertacije prihvaćeni su odlukom Fakultetskog vijeća Građevinskog i arhitektonskog fakulteta Osijek Sveučilišta Josipa Jurja Strossmayera u Osijeku na 205. redovitoj sjednici održanoj 19. prosinca 2022. godine.

Povjerenstvo za ocjenu doktorske disertacije

Povjerenstvo za ocjenu doktorske disertacije imenovano na 6. redovitoj sjednici Fakultetskog vijeća Građevinskog i arhitektonskog fakulteta Osijek Sveučilišta Josipa Jurja Strossmayera u Osijeku, održanoj 9. ožujka 2022. godine:

1. prof. dr. sc. Ivica Guljaš, dipl. ing. građ. Sveučilište Josipa Jurja Strossmayera u Osijeku, Građevinski i arhitektonski fakultet Osijek (predsjednik Povjerenstva)
2. izv. prof. dr. sc. Davorin Penava, dipl. ing. građ. Sveučilište Josipa Jurja Strossmayera u Osijeku, Građevinski i arhitektonski fakultet Osijek
3. prof. dr. sc. Ivica Kožar, dipl. ing. građ. Sveučilište u Rijeci, Građevinski fakultet

Doktorske disertacija prihvaćena je odlukom Fakultetskog vijeća Građevinskog i arhitektonskog fakulteta Osijek Sveučilišta Josipa Jurja Strossmayera u Osijeku na 6. redovitoj sjednici održanoj 9. ožujka 2022. godine.

Povjerenstvo za obranu doktorske disertacije

Povjerenstvo za obranu doktorske disertacije imenovano na 6. redovitoj sjednici Fakultetskog vijeća Građevinskog i arhitektonskog fakulteta Osijek Sveučilišta Josipa Jurja Strossmayera u Osijeku, održanoj 9. Ožujka 2022. godine:

1. prof. dr. sc. Ivica Guljaš, dipl. ing. građ. Sveučilište Josipa Jurja Strossmayera u Osijeku, Građevinski i arhitektonski fakultet Osijek (predsjednik Povjerenstva)

2. izv. prof. dr. sc. Davorin Penava, dipl. ing. građ. Sveučilište Josipa Jurja Strossmayera u Osijeku, Građevinski i arhitektonski fakultet Osijek

3. prof. dr. sc. Ivica Kožar, dipl. ing. građ. Sveučilište u Rijeci, Građevinski fakultet

Doktorske disertacija javno je obranjena 8. travnja 2022. godine na Građevinskom i arhitektonskom fakultetu Osijek Sveučilišta Josipa Jurja Strossmayera u Osijeku.

Doktorska disertacija sadržava 238 stranica, 155 ilustracija, 46 tablica, 8 dodataka i 146 citiranih publikacija.

Mentor doktorske disertacije je izv. prof. dr. sc. Davorin Penava, dipl. ing. građ., Sveučilište Josipa Jurja Strossmayera u Osijeku, Građevinski i arhitektonski fakultet Osijek, Osijek, Republika Hrvatska

Prvi komentor doktorske disertacije je Dr. Vasilis Sarhosis, Associate Professor in Structural Engineering, Sveučilište University of Leeds, sastavnica School of Engineering, Leeds, Engleska, Ujedinjeno Kraljevstvo

Drugi komentor doktorske disertacije je Jun.–Prof. Dr.–Ing. Lars Abrahamczyk, Senior Reseac-rher, Sveučilište Bauhaus-Universität Weimar, sastavnica Institut für Konstruktiven Ingenieurbau, odjel Erdbebenzentrum (EDAC), Weimar, Savezna Republika Njemačka

Istraživanje u okviru doktorske disertacije pripada znanstvenom području tehničkih znanosti, znanstvenom polju građevinarstvo.

Evaluation committees and bibliographical data

Committee for the Recognition of the Doctoral Thesis Topic

The Committee for the Recognition of the Doctoral Thesis Topic was appointed at the 204th regular session of the Faculty Council of the Faculty of Civil Engineering and Architecture Osijek of the Josip Juraj Strossmayer University of Osijek, held on November 27th 2018:

1. prof. dr. sc. Ivica Guljaš, dipl. ing. građ. Josip Juraj Strossmayer University of Osijek, Faculty of Civil Engineering and Architecture Osijek (Committee president)
2. izv. prof. dr. sc. Davorin Penava, dipl. ing. građ. Josip Juraj Strossmayer University of Osijek, Faculty of Civil Engineering and Architecture Osijek
3. prof. dr. sc. Ivica Kožar, dipl. ing. građ. University of Rijeka, Faculty of Civil Engineering.

The topic, mentor, first and second co-mentor of the doctoral thesis have been recognised by the decision of the Faculty Council of the Faculty of Civil Engineering Osijek of the Josip Juraj Strossmayer University of Osijek, at the 205th regular session held on December 19th 2018.

Committee for the Evaluation of the Doctoral Thesis

The Committee for the Evaluation of the Doctoral Thesis was appointed at the 6th regular session of the Faculty Council of the Faculty of Civil Engineering and Architecture Osijek of the Josip Juraj Strossmayer University of Osijek, held on April 8th 2022:

1. prof. dr. sc. Ivica Guljaš, dipl. ing. građ. Josip Juraj Strossmayer University of Osijek, Faculty of Civil Engineering and Architecture Osijek (Committee president)
2. izv. prof. dr. sc. Davorin Penava, dipl. ing. građ. Josip Juraj Strossmayer University of Osijek, Faculty of Civil Engineering and Architecture Osijek
3. prof. dr. sc. Ivica Kožar, dipl. ing. građ. University of Rijeka, Faculty of Civil Engineering.

The doctoral thesis has been recognised by the decision of the Faculty Council of the Faculty of Civil Engineering and Architecture Osijek of the Josip Juraj Strossmayer University of Osijek, at the number regular session held on March 9th 2022.

Committee for the Defence of the Doctoral Thesis

The Committee for the Defence of the Doctoral Thesis was appointed at the 6th regular session of the Faculty Council of the Faculty of Civil Engineering and Architecture Osijek of the Josip Juraj Strossmayer University of Osijek, April 9th 2022:

1. prof. dr. sc. Ivica Guljaš, dipl. ing. građ. Josip Juraj Strossmayer University of Osijek, Faculty of Civil Engineering and Architecture Osijek (Committee president)
2. izv. prof. dr. sc. Davorin Penava, dipl. ing. građ. Josip Juraj Strossmayer University of Osijek, Faculty of Civil Engineering and Architecture Osijek

3. prof. dr. sc. Ivica Kožar, dipl. ing. građ. University of Rijeka, Faculty of Civil Engineering.

The doctoral thesis has been publicly defended on April 8th 2022 at the Faculty of Civil Engineering Osijek of the Josip Juraj Strossmayer University of Osijek

The doctoral thesis contains 238 pages, 155 illustrations, 46 tables, 8 annexes, and 146 cited publications.

The mentor of the doctoral thesis is izv. prof. dr. sc. Davorin Penava, dipl. ing. građ., Josip Juraj Strossmayer Universtiy of Osijek, Faculty of Civil Engineering and Architecture Osijek, Osijek, Republic of Croatia

The first co-mentor of the doctoral thesis is Dr. Vasilis Sarhosis, Associate Professor in Structural Engineering, University of Leeds, School of Engineering, Leeds, England, United Kingdom

The second co-mentor of the doctoral thesis is Jun.-Prof. Dr.-Ing. Lars Abrahamczyk, Senior Reseacrher, Bauhaus-Universität Weimar university, Institut für Konstruktiven Ingenieurbau institute, Erdbebenzentrum (EDAC) department, Weimar, Germany

The research conducted as part of the doctoral thesis is from the scientific area of Technical Sciences, scientific field Civil Engineering.

Izjava o akademskoj čestitosti

Izjavljujem i svojim potpisom potvrđujem kako je doktorska disertacija isključivo rezultat mog vlastitog rada koji se temelji na mojim istraživanjima i oslanja se na objavljenu literaturu, a što pokazuju korištene bilješke i bibliografija. Izjavljujem kako nijedan dio rada nije napisan na nedozvoljen način, odnosno prepisan iz necitiranog rada te kako nijedan dio rada ne krši bilo čija autorska prava. Izjavljujem kako nisam prijavio doktorsku disertaciju s istovjetnom temom na drugom studiju Sveučilišta ili na drugom sveučilištu.

U Osijeku, 8. travnja 2022. godine

Filip Anić, mag. ing. aedif.

Statement on academic integrity

I hereby declare and confirm by my signature that this doctoral thesis is the exclusive result of my own work, which is based on my own research and which relies on published literature, which is demonstrated by the used notes and bibliography. I declare that no parts of this thesis were written in a manner that is not allowed, *i.e.* that they were not copied from an uncited paper, and that no parts of this thesis violate anyone's intellectual property rights. I hereby declare that I have not applied a doctoral thesis with this identical topic at another study programme of this nor other university.

Osijek, April 8th 2022.

Filip Anić, mag. ing. aedif.

Preface

This research was a natural progression from my master's thesis, where many questions were left unanswered. Therefore, in accordance with my master's thesis supervisor, izv. prof. dr. Davorin Penava, we agreed to further our efforts into a PhD program. That led to years of collaboration with him being my PhD supervisor. Our collaboration provided me with an abundance of opportunities and knowledge interchange, for which I'm very grateful.

This thesis is built upon my mentor's dissertation that researched RC frames with and without infill walls and openings, loaded in an in-plane direction. Alongside, the research and this thesis were made possible due to multiple projects, those being: 1) *Influence of Openings on Out-of-Plane Earthquake Resistance of Framed-Masonry Walls* granted by the Josip Juraj Strossmayer University of Osijek, Faculty of Civil Engineering and Architecture Osijek; 2) *Seizmički odziv konstrukcijskog sustava okvir-zide okomito na svoju ravninu temeljem metode katnih pomaka - OoP drift (IZIP-A-GrAFOS-2018)* granted by the Josip Juraj Strossmayer University of Osijek, Faculty of Civil Engineering and Architecture Osijek, and; 3) *Frame-Masonry Composites for Modelling and Standardization - FRAMA (HRZZIP-2013-11-3013)* granted by the Croatian Science Foundation (HrZZ).

The thesis laid here is an accumulated knowledge from experimental and computational investigations done within the scope of the earthquake, otherwise known as the seismic engineering field. It is based on the behaviour of frames with masonry infill walls, loaded in- and out-of-plane direction with the inclusion of openings. A previously untested method of simultaneous in- and out-of-plane drift force loading was used on the specimens mentioned above. Most notably, the thesis contributes to the field by broadening its scarcely researched parts. New mechanisms, behaviours, and findings were established, while the known ones were solidified. Also, a few contradictions were found and pointed out, not only between this and other research but among others themselves.

Also, there were studies that I've done within the scope of the field that was not included in this thesis. For the most part, it is the research done on computational micromodels with an inertial load. Their inclusion would derail the thesis from its straightforward path. Therefore, when needed, the papers with that subject matter were only referenced.

I would also like to express gratitude to my co-mentors dr. Vasilis Sarhosis, Associate Professor, and Jun.-Prof. Dr.-Ing. Lars Abrahamczyk, Senior Reseachrher that have greatly aided me with their knowledge and experience in my PhD journey. Also, they have provided me with a plethora of mobility opportunities and included me in multiple of their research and teaching projects, for which I'm very grateful.

In the aftermath of Croatia's 2020th earthquake, I hope that the research laid here would aid the civil engineering industry in better understanding the complex behaviour of high-rise structures.

In the end, I would like to thank my family. To my mother for being a support and motivator for higher education, my father who influenced my scientific curiosity, and my sister who aided me in my first scientific steps. Also, my wife's and daughter's unselfish support and understating for the time invested here is immeasurable.

Sažetak i ključne riječi

Sažetak: Tijekom trajanja potresa, stambene zgrade su u pravilu opterećene inercijskim i silama među-katnih pomaka. Potresno opterećenje dolazi pod određenim kutom s obzirom na konstrukciju. Ako promatramo ravninu jedne stranice takve konstrukcije, opterećenje se može podijeliti na ono okomito i u smjeru nje. Isto tako se podijelila i literatura koja istražuje potresna opterećenja.

Pregledom literature utvrđeno je kako istraživanja okomito na vlastitu ravninu su većinom provedena s inercijskim, manje s dinamičkim i samo dvije sa silama među-katnog pomaka. U radu su vrednovani analitički modeli za izračun nosivosti okvira s ispunskim zidom na inercijske sile okomite na vlastitu ravninu. Vrednovanje se provelo kroz više različitih eksperimentalnih postavki i rezultata. Iz analize tih modela utvrđene su njihove granice i one s visokom točnošću. Nadalje, uvidom u rezultate eksperimentalnih istraživanja sa sila katnih pomaka i dinamičkog opterećenja, utvrđeno je kako te dvije metode imaju više sličnosti nego isti s metodama inercijskih silama. Uz rijetko istraživano opterećenje sa silama katnih pomaka okomito na vlastitu ravninu, uočeno je kako niti jedno nije napravljeno na uzorcima armirano-betonskih okvira kao niti s utjecajem otvora. Sukladno navedenim, ova disertacija pokušava odgovoriti upravo na te manjkavosti, tj. utvrditi učinak djelovanja sila katnih pomaka u i okomito na smjer ravnine AB okvira sa zidanom ispunom i otvorima.

Istraživanja opisana u ovoj doktorskoj disertaciji su nastavak postojećih istraživanja koja su bila u sklopu druge disertacije. Ta istraživanja odnosila su se na ponašanja AB okvira sa i bez ispunskog zida i otvora, opterećenih u smjeru vlastite ravnine. Otvori su definirani prema tipu (prozor, vrata) i njihovoj poziciji (u-, te izvan središta). Postojeće studije nadograđene su eksperimentalnim ispitivanjima okomito na vlastitu ravninu istih uzoraka, kao i savijanje zida okomito na vlastitu ravninu. Utvrđeno je kako je odgovor okomito na svoju ravninu sustava okvir–ispunsko zide jednostran. To jest, ispuna ne doprinosi značajnije sveukupnom odgovoru, ali okvir prenosi pomake, pa tako i oštećenja na ispunsko zide. Usporedbom s drugim istraživanjima pronađenim u literaturi, utvrđeno je kako su dobiveni rezultati analogni ostalim dinamičkim ispitivanjima kao i onim sa silama katnih pomaka.

Na temelju eksperimentalnih istraživanja u i okomito na vlastitu ravninu, kako okvira sa ispunskim zidom tako i samog zida, razvijeni su i kalibrirani proračunski mikromodeli. Analizom variranih parametra za potrebe kalibracije mikromodela, utvrđeni su ključni parametri odziva istih. Za simulaciju opterećenja u vlastitoj ravnini, to su bili parametri materijalnog modela kontakta i betona. Slično, za simulaciju savijanja zida okomito na vlastitu ravninu, to su bili parametri kontakta i opeke. Sukladno tome, utvrđeno je kako za opterećenje u vlastitoj ravnini okvira s ispunskim zidom sa i bez otvora materijalni model opeke nije igrao značajniju ulogu. S kalibriranim modelima, istraživanje se proširilo na okvire sa i bez ispunskog zida i otvora opterećenih simultano u i okomito na vlastitu ravninu. Takvo opterećenje definiralo se kutom α pod kojim leži njihova rezultanta. Simuliralo se 9 kutova (od 0° do 90°), veličina i razmještaj otvora. Otvori su postavljeni u i izvan središta, a površina im je varirana u omjeru od 0.1, 0.2, te 0.3 u odnosu na površinom ispunskog zida. Sveukupno, ispitano je 180 modela iz kojih su derivirane krivulje međuovisnosti simultanog opterećenja s obzirom na kut djelovanja i otvore. Također, iznašla se jednadžba za procjenu nosivosti istih, a ista je imala dobru podudarnost s istovjetnim simulacijama.

Ključne riječi: armirano-betonski okviri; ispunsko zide; utjecaj otvora; eksperimentalni i proračunski pristup; opterećenje okomito na vlastitu ravninu; simultano opterećenje u i okomito na vlastitu ravninu; interakcijske krivulje simultanog opterećenja; jednadžbe za procjenu nosivosti uslijed simultanog opterećenja.

Abstract and keywords

Abstract: Multi-storey buildings are generally loaded by inter-storey drift and inertial forces during an earthquake event. That seismic event excites the structure in an arbitrary direction. When observing the structure's plane, that load can be divided into in- and out-of-plane forces. The in-plane forces by their nature are inter-storey drift ones, while the out-of-plane ones are both inter-storey drift and inertial.

By examining the literature, it was determined that most of the experiments within the out-of-plane field of research were conducted with inertial, less with dynamical and only two using inter-storey drift force methods. The analytical models for calculating inertial, load-bearing capacity found within the literature were tested against various experiments. From the analysis, their limitations and best fitting equations were derived. Furthermore, from the gathered experimental data, it was observed that the static and quasi-static inter-storey drift force methods have more similarities with dynamical tests than the inertial methods. Aside from the limited out-of-plane inter-storey drift studies, none of which were done with RC frames; the field had a few and conflicting studies with openings. The research laid in this thesis answers just that; the influence of infill walls with and without openings on RC frames subjected to drift driven in- and out-of-plane loads.

This thesis was built upon the existing one covering in-plane cyclic, quasi-static load. The experimental contribution of this thesis included out-of-plane cyclic, quasi-static inter-storey drift load on frames with and without infill walls and openings, along with the out-of-plane bending test of masonry walls. The same materials, techniques, and equipment were used for all three experiments. Openings were varied in their type (window and door) and position (centric and eccentric), while the out-of-plane bending test had load parallel and perpendicular to bedjoints. The out-of-plane drift force tests showed that the infill wall and the frame moved as one and that the infill had an insignificant contribution to the overall behaviour of the frame, *i.e.* the behaviour of the bare frame model was similar to other infilled ones. Yet, the infill wall suffered considerable damage, mostly by separating rows of blocks in bedjoints. This pointed out that the frame to masonry interaction was one-sided, *i.e.* only the frame transfers displacements and damages the infill wall. All the out-of-plane drift force test outcomes are consistent with the literature's dynamical and drift force studies.

After the experiments were conducted, computational models were developed and calibrated against them. The calibration yielded the factors that govern the simulated behaviour of the models. For the in-plane studies, it was the interface (gap) and concrete material model, while for the out-of-plane bend tests for the masonry walls, it was both the interface and masonry material models. Thus, it was concluded that the masonry material model had little influence on the overall behaviour of in-plane simulations. Afterwards, the research was extrapolated to combine in- and out-of-plane loads into a simultaneous action. The combination was described by the angle of the resultant force α . The simulations tested 20 configurations from a bare frame, infill wall with or without openings with their area ratios ranging approximately 0.1, 0.2 and 0.3 in relation to the infill's area. Also, they were positioned centrally or eccentrically, loaded from left or right under nine angle positions (0 to 90°, *i.e.* from in- to out-of-plane). Overall, 180 models were tested, with which interaction curves and equations for estimating load-bearing capacity based on that of the in-plane's bare frame were derived. The estimating equations showed a good fit with the data from the simulations.

Key words: RC frames, masonry infill walls, influence of openings, experimental and computa-

tional approach, out-of-plane drift force load, simultaneous in- and out-of-plane action, simultaneous in- and out-of-plane interaction curves, simultaneous in- and out-of-plane load-bearing equation.

Σύνοψη & Λέξεις κλειδιά

Σύνοψη: Κατά τη διάρκεια ενός σεισμού τα πολυώροφα κτίρια φορτίζονται, κατά κύριο λόγο, από ενδοοροφικές μετατοπίσεις και αδρανειακές δυνάμεις. Το σεισμικό γεγονός διεγείρει τη κατασκευή προς αυθαίρετη κατεύθυνση. Κατά την παρατήρηση του επιπέδου της κατασκευής, το φορτίο μπορεί να χωριστεί σε δυνάμεις εντός και εκτός-επιπέδου. Οι δυνάμεις εντός-επιπέδου είναι από τη φύση τους ενδοοροφικής μετατόπισης, ενώ οι δυνάμεις εκτός-επιπέδου είναι ενδοοροφικών μετατοπίσεων και αδρανειακών δυνάμεων. Εξετάζοντας τη βιβλιογραφία, διαπιστώθηκε ότι τα περισσότερα πειράματα, εντός του ερευνητικού πεδίου, εκτός-επιπέδου διεξήχθησαν με αδρανειακές δυνάμεις, λιγότερα με δυναμικά φορτία, και μόνο δύο με χρήση της μεθόδου μετατόπισης μεταξύ ορόφων. Τα αναλυτικά μοντέλα για τον υπολογισμό της αδρανειακής, φέρουσας ικανότητας που βρέθηκαν στη βιβλιογραφία δοκιμάστηκαν έναντι διαφόρων πειραμάτων. Από την ανάλυση προέκυψαν οι περιορισμοί τους και οι εξισώσεις βέλτιστης προσαρμογής. Επιπλέον, από τα πειραματικά δεδομένα που συγκεντρώθηκαν, παρατηρήθηκε ότι οι μέθοδοι της στατικής και ημιαστικής ενδοοροφικής μετατόπισης έχουν περισσότερες ομοιότητες με τις δυναμικές δοκιμές από τις αδρανειακές μεθόδους. Πέρα από τις περιορισμένες μελέτες ενδοοροφικής μετατόπισης εκτός-επιπέδου (καμία από τις οποίες δεν έγινε με πλαίσιο από οπλισμένο σκυρόδεμα) το ερευνητικό πεδίο είχε λίγες και αντικρουόμενες μελέτες με ανοίγματα. Η έρευνα που διατίθεται σε αυτή τη διατριβή απαντά στο αυτό το πρόβλημα· την επίδραση των τοίχων πλήρωσης με ή χωρίς ανοίγματα σε πλαίσιο οπλισμένου σκυροδέματος που υπόκεινται σε φορτία μετατόπισης εντός και εκτός επιπέδου. Η παρούσα διατριβή βασίστηκε σε υπάρχουσα ερευνά που καλύπτει το εντός-επίπεδου κυκλικό, ημιστατικό φορτίο. Η πειραματική συμβολή αυτής της διατριβής περιλαμβάνει κυκλικό, ημιστατικό ενδοοροφικό φορτίο μετατόπισης σε κουφώματα με ή χωρίς τοίχους και ανοίγματα πλήρωσης, μαζί με τη δοκιμή κάμψης εκτός-επιπέδου τοίχων τοιχοποιίας. Χρησιμοποιήθηκαν τα ίδια υλικά, τεχνικές και εξοπλισμός και για τα τρία πειράματα. Τα ανοίγματα διέφεραν ως προς τον τύπο (παράθυρα και πόρτες) και τη θέση τους (κεντρικά και έκκεντρα), ενώ η δοκιμή κάμψης εκτός-επιπέδου είχε παράλληλο και κάθετο φορτίο στις στρώσεις πλίνθων. Οι δοκιμές δύναμης ενδοοροφικής μετατόπισης εκτός-επιπέδου έδειξαν ότι το τοίχωμα πλήρωσης και το πλαίσιο κινούνταν ως ένα και ότι η πλήρωση είχε μια ασήμαντη συμβολή στη συνολική συμπεριφορά του πλαισίου, δηλαδή η συμπεριφορά του μοντέλου γυμνού πλαισίου ήταν παρόμοια με το μοντέλο με τοίχο πλήρωσης. Ωστόσο, ο τοίχος πλήρωσης υπέστη σημαντική ζημιά, κυρίως με το διαχωρισμό σειρών αρμών στις στρώσεις πλίνθων. Αυτό επισημαίνει ότι η αλληλεπίδραση πλαισίου και τοιχοποιίας ήταν μονόπλευρη, δηλαδή ότι μόνο το πλαίσιο μεταφέρει μετατοπίσεις και φθερίζει τον τοίχο πλήρωσης. Όλα τα αποτελέσματα των δοκιμών δυνάμεων μετατόπισης εκτός-επιπέδου συμφωνούν με τις μελέτες δυναμικών δυνάμεων και δύναμης μετατοπίσεων της βιβλιογραφίας. Μετά τη διεξαγωγή των πειραμάτων, αναπτύχθηκαν υπολογιστικά μοντέλα και βαθμονομήθηκαν σε σχέση με αυτά. Η βαθμονόμηση απέδωσε τους συντελεστές που διέπουν την προσομοιωμένη συμπεριφορά των μοντέλων. Για τις μελέτες εντός-επιπέδου, ήταν η διεπιφάνεια (κενό) και το μοντέλο υλικού σκυροδέματος, ενώ για τις δοκιμές κάμψης εκτός-επιπέδου για τους τοίχους τοιχοποιίας, ήταν τόσο η διεπαφή όσο και το μοντέλο υλικού τοιχοποιίας. Έτσι, συνήχθη το συμπέρασμα ότι το μοντέλο υλικού τοιχοποιίας είχε μικρή επίδραση στη συνολική συμπεριφορά των προσομοιώσεων εντός-επιπέδου. Στη συνέχεια, η έρευνα επεκτάθηκε για να συνδυάσει φορτία εντός και εκτός επιπέδου σε μια ταυτόχρονη δράση. Ο συνδυασμός περιεγράφηκε από τη γωνία της προκύπτων δύναμης α . Οι προσομοιώσεις εξέτασαν 20 διαμορφώσεις από γυμνό πλαίσιο, τοίχο πλήρωσης με ή χωρίς ανοίγματα με τις αναλογίες επιφανειών τους να κυμαίνονται περίπου 0.1, 0.2 και 0.3 σε σχέση με την περιοχή πλήρωσης. Επίσης, τοποθετήθηκαν κεντρικά ή έκκεντρα, φορτωμένα από αριστερά ή δεξιά κάτω από εννέα γωνιακές θέσεις (0 έως 90°, δηλαδή από εντός προς εκτός-επιπέδου). Συνολικά, δοκιμάστηκαν 180 μοντέλα, με τα οποία προέκυψαν καμπύλες αλληλεπίδρασης και εξισώσεις για την εκτίμηση της φέρουσας ικανότητας με βάση αυτή του γυμνού πλαισίου του εντός-επιπέδου. Οι εξισώσεις που παρήχθησαν έδειξαν καλή προσαρμογή με τα δεδομένα από τις προσομοιώσεις.

Λέξεις κλειδιά: πλαίσια οπλισμένου σκυροδέματος, τοίχοι πλήρωσης τοιχοποιίας, επιρροή ανοιγμάτων, πειραματική και υπολογιστική προσέγγιση, φορτίο δύναμης μετατόπισης εκτός-επιπέδου, ταυτόχρονη δράση εντός και εκτός-επιπέδου, ταυτόχρονες καμπύλες αλληλεπίδρασης εντός και εκτός-επιπέδου , ταυτόχρονη φέρουσα εξίσωση εντός και εκτός-επιπέδου.

Zusammenfassung und Schlüsselwort

Zusammenfassung: Während eines Erdbebens werden mehrstöckige Gebäude durch die seismischen Wellen in beliebiger Richtung angeregt und in der Regel durch Stockwerksverschiebungen und Trägheitskräfte belastet. Betrachtet man die Hauptachsen des Bauwerks, so lässt sich diese Belastung in Kräfte parallel (in) und senkrecht zur Ebene aufteilen. Bei den Kräften in der Ebene handelt es sich naturgemäß um Geschossverschiebungen, während die Kräfte senkrecht zur Ebene sowohl aus Geschossverschiebungen als auch aus Trägheitskräften bestehen.

Im Ergebnis der Literaturrecherche konnte herausgearbeitet werden, dass die meisten Experimente senkrecht zur Ebene ein äquivalentes Lastbild zu den Trägheitskräften verwenden, nur wenige mit dynamischen Kräften und nur zwei unter Anwendung von geschossübergreifender Geschossverschiebungen durchgeführt wurden. In der Arbeit wurden die in der Literatur zu findenden analytischen Modelle zur Berechnung der Tragfähigkeit anhand verschiedener Experimente überprüft und die Anwendungsgrenzen sowie die am geeignetsten Gleichungen bestimmt. Darüber hinaus konnte anhand der gesammelten experimentellen Daten festgestellt werden, dass die statischen und quasi-statischen Methoden zur Berechnung der Kräfte infolge Geschossverschiebungen mehr Ähnlichkeiten mit dynamischen Tests aufweisen als die Methoden unter Berücksichtigung der Trägheitskräfte. Abgesehen von den begrenzten Studien zu Geschossverschiebungen senkrecht zur Ebene, von denen keine mit Stahlbetonrahmen durchgeführt wurden, gab es nur wenige und widersprüchliche Studien unter der Berücksichtigung von Öffnungen. Die in dieser Arbeit durchgeführten Untersuchungen befassen sich mit dem Einfluss von Ausfachungswänden mit und ohne Öffnungen auf Stahlbetonrahmen, die Lasten aus Geschossverschiebungen in der und senkrecht zur Ebene ausgesetzt sind.

Die Arbeit baut auf den Ergebnissen bzw. Untersuchungen zur zyklischen, quasi-statischen Belastung von Ausfachungswänden in der Ebene auf. Der experimentelle Beitrag umfasst die zyklische, quasi-statische, geschossübergreifende Driftbelastung senkrecht zur Ebene an Rahmen mit und ohne Ausfachungen und Öffnungen sowie Biegeversuchen senkrecht zur Ebene an Mauerwerksversuchskörpern. Für alle drei Versuche wurden die gleichen Materialien, Techniken und Geräte verwendet. Die Art der Öffnungen (Fenster und Türen) und ihre Position (zentrisch und exzentrisch) wurden variiert. Die Belastung beim Biegeversuch erfolgte senkrecht zur Ebene parallel und senkrecht zu den Lagerfugen. Die Geschossverschiebungstests senkrecht zur Ebene zeigen, dass sich die Ausfachungswand und der Rahmen gemeinsam bewegen und dass die Ausfachung einen unbedeutenden Beitrag zum Gesamtverhalten des Rahmens leistet, d. h. das Verhalten des nackten Rahmenmodells ist ähnlich wie das ausgefüllter Rahmen. Dennoch erlitt die Ausfachungswand erhebliche Schäden, vor allem durch die Trennung von Blockreihen in den Lagerfugen. Dies deutet darauf hin, dass die Interaktion zwischen Rahmen und Mauerwerk einseitig ist, d. h. nur der Rahmen überträgt Verschiebungen und schädigt die Ausfachungswand. Alle Ergebnisse der Geschossverschiebungstests senkrecht zur Ebene stimmen mit den in der Literatur veröffentlichten Studien überein.

Aufbauend auf den Ergebnissen der Experimente werden Berechnungsmodelle entwickelt, anhand dieser kalibriert und die Faktoren ermittelt, die das simulierte Verhalten der Modelle bestimmen. Bei den Untersuchungen in der Ebene sind dies das Modell für die Fuge zwischen Ausfachung und Rahmen sowie das Materialmodell für Beton und bei den Biegeversuchen für die Mauerwerkswände senkrecht zur Ebene auch das Modell für die Fugen / Mörtel und das für Mauerwerk. Daraus wird gefolgert, dass das Materialmodell für Mauerwerk nur einen geringen Einfluss auf das Gesamtverhalten der Simulationen in der Ebene hat. Abschließend werden die Forschungsergebnisse extrapoliert, um Belastungen innerhalb und senkrecht zur Ebene zu einer gleichzeitigen Einwirkung in Form einer resultierenden Kraft zu kombinieren. Die Kombination wird durch den Winkel der

resultierenden Kraft α beschrieben. Hierfür wurden 20 Konfigurationen aus einem Rahmen ohne Ausfachung und mit Ausfachungswänden mit oder ohne Öffnungen mit einem Flächenverhältnis von etwa 0.1, 0.2 und 0.3 im Verhältnis zur Fläche der Ausfachung. Zusätzlich wurden die Öffnungen zentrisch oder exzentrisch positioniert. Alle Modelle wurden von links oder rechts in neun Winkelstellungen (0 bis 90°, d. h. von in- bis senkrecht zur Ebene) belastet. Insgesamt wurden somit 180 Modelle analysiert und daraus Interaktionskurven sowie Gleichungen zur Abschätzung der Tragfähigkeit auf der Grundlage des einfachen Rahmens belastet in der Ebene abgeleitet. Die Abschätzungsgleichungen zeigen eine gute Übereinstimmung mit den Daten aus den Simulationen.

Stichworte: Stahlbetonrahmen, Mauerwerksausfachungen, Einfluss von Öffnungen, experimenteller und rechnerischer Ansatz, Belastung durch Driftkräfte senkrecht zur Ebene, gleichzeitige Einwirkung in und senkrecht zur Ebene, Interaktionskurven.

Contents

I	Introduction	1
1	2019th Albanian earthquake field study	5
1.1	A brief introduction	5
1.2	Reconnaissance mission	6
1.3	Understanding current Albanian seismic regulations	6
1.4	Findings	8
1.5	Conclusions	16
2	Literature overview	19
2.1	General overview	19
2.2	Experimental campaigns	22
2.3	Arching action and boundary conditions	28
2.4	Openings	31
2.5	The effect of slenderness and aspect ratio	33
2.6	Effect of combined in-plane out-of-plane loading	36
2.7	Contrasting outcomes of different load methods and protocols	39
2.7.1	Additional findings	41
2.8	Analytical models	43
2.8.1	Input for the analytical models	50
2.8.2	Analysis model results	50
2.9	Discussion and overview	60
2.9.1	Experimental studies	60
2.9.2	Analytical models	61
2.10	Conclusions	62
2.11	Research hypothesis	64
II	Experimental campaigns	65
3	Prototype structure	69
3.1	Prototype structure design	69
3.2	Specimen design	71
4	Small scale test series	83
4.1	Compression test on masonry units	83
4.2	Masonry triplets tests	83
4.3	Masonry wall compression test	86
4.4	Out-of-plane bending tests of masonry wall	88
4.4.1	Samples preparations	88

4.4.2	Results	88
5	IP-plane test series	93
5.1	Preparation of specimens	93
5.2	Results	93
6	Out-of-plane drift driven test series	105
6.1	Preparation of specimens	105
6.2	Out-of-plane drift driven test set-up	105
6.3	Results	107
6.3.1	Rigid body movement and accidental torsion	107
6.3.2	Hysteresis and load-bearing capacity curves	108
6.3.3	OoP cracks, damage occurrence and frame – infill wall interaction	112
7	Conclusions	123
7.1	In-Plane test series	123
7.2	Out-of-plane test series	123
III	Computational micro-model studies	125
8	Development of a 3D micro-model	129
8.1	Micro-model elements and boundary conditions	129
8.2	Material models	133
8.2.1	Material model for concrete and masonry	134
8.2.2	Interface gap (contact) model	140
8.2.3	Friction spring model	142
8.2.4	Reinforcement model	143
8.3	Elastic plates	143
8.4	Solution of non-linear equations	144
8.4.1	Newton-Raphson method	144
8.4.2	Arc-length method	145
9	Micro-model development, calibration and sensitivity analysis	149
9.1	In-Plane cyclic, quasi-static micro-model evaluation	152
9.2	Out-of-Plane bending tests of masonry walls	166
9.3	Out-of-plane drift driven test on frames with and without masonry infill walls and openings	170
10	Simultaneous IP and OoP load on models with and without infill wall and various openings	179
10.1	Load protocol transition	179
10.2	Opening size and load protocol selection	179
10.3	Results	184
10.3.1	General	184
10.3.2	Influence of gravity load on OoP tests	190
10.3.3	Damage development and resistance mechanisms	191
10.3.4	IP and OoP interaction curves	192
10.3.5	Example of determining load-bearing capacity	196

11 Conclusions and summary of the computational studies	207
11.1 Micro-model development	207
11.2 Micromodel calibration and sensitivity analysis	207
11.3 Simultaneous IP and OoP load on models with and without infill wall and various openings	208
IV Concluding remarks	211
12 Summary and conclusions	213
12.1 Summary	213
12.2 Conclusions	214
13 Recommendations and future work	215
13.1 Recommendations	215
13.2 Future work	216
V Appendix	219

List of Figures

1.1	Map of Albania, showing the location and intensity of shaking	5
1.2	Albania earthquake signal (IGEO, 2021)	6
1.3	ACI Technical Committee 133 team	7
1.4	Evolution of Albanian seismic regulation (Freddi et al, 2021)	7
1.5	Comparison of elastic and design spectra between KTP-N.2-89 and EN1998-1 (Freddi et al, 2021)	8
1.6	Example of commonly used masonry unit	9
1.7	Examples of typical multi-storey buildings	10
1.8	Masonry units sparsely bounded with mortar	11
1.9	Structural damage	12
1.10	Damages to the infill walls	13
1.11	Example of better praxis	17
2.1	Relevant experiments as shared by different fields of study	21
2.2	Occurrences of OoP-specific subjects by year published	21
2.4	Distribution of OoP load methods	24
2.5	Material specifics of experimental tests	25
2.6	Distribution of A_o/A_{in} ratio	26
2.7	Distribution of geometrical characteristics	26
2.3	Opening considered in OoP research	27
2.8	Arching action development phases by different boundary conditions	28
2.9	Types of arching action in relation to boundary conditions	29
2.10	Observed arching action modes with their equivalent models	30
2.11	Force-displacement curves of various boundary conditions	31
2.12	Achieved drift ratios sorted by researchers	32
2.13	Displacement iso areas (colorbar in mm) from Akhoundi et al (2020)	33
2.14	Force <i>vs.</i> displacement graphs of specimens with openings	34
2.15	Failure patterns of OoP specimens with openings	35
2.16	Results of the Mays et al (1998) URM wall test with designated crack occurrence	35
2.17	The Mays et al (1998) prediction of failures (straight and dashed lines) <i>vs.</i> Griffith et al (2007) experimental outcome of load-bearing walls.	35
2.18	Opening to infill area ratio <i>vs.</i> difference in force and displacement from the fully infilled frame, window and door lines were extracted from Mays et al (1998)	36
2.19	Effects of slenderness (<i>*derived from Angel et al (1994)</i>)	36
2.20	OoP force <i>vs.</i> displacement graphs with various previous IP inter-storey drifts	37
2.21	Reduction of OoP capacity by previous IP ISD as found by various researchers	38
2.22	Ricci et al (2018) crack patterns from IP+OoP tests (d_r in %). Blue lines represent the OoP damage, while the red ones represent IP.	39

2.23	IP cyclic envelope of simultaneous IP&OoP loads derived from Flanagan and Bennett (1999b)	40
2.24	Stiffness degradation due to simulations IP and OoP load (Misir et al, 2016)	40
2.25	Examples of dynamical OoP test setups	41
2.26	Structural acceleration results from the shaking table test by Fowler (1994)	42
2.27	Failure modes from Tu et al (2010) experimental campaign	43
2.28	Flanagan and Bennett (1999b) damage state of ISD method	43
2.29	Distribution of mechanical properties from Tab. 2.16	44
2.30	Damage states for R_1 factor (Angel et al (1994))	47
2.31	Variation in differences plotted as quartiles between various analytical models	52
2.32	Absolute differences in various analytical models by specific property, legend same as in Fig. 2.34	53
2.33	Absolute differences in various analytical models by specific specimen, legend same as in Fig. 2.34	54
2.34	Absolute differences in various analytical models by specific specimen	55
2.35	Single variable sensitivity analysis	58
2.36	Multi-variable parameter sensitivity analysis of analytical models	59
2.37	Effects of slenderness (h/t) on ultimate OoP displacement calculations	59
3.1	Compression test on masonry units	69
3.2	Building plan and elevation	72
3.3	Specimen frame reinforcement design	73
3.4	Masonry unit as used in the experiments	74
3.5	Details of FI specimen	77
3.6	Details of CD specimen	78
3.7	Details of CW specimen	79
3.8	Details of ED specimen	80
3.9	Details of EW specimen	81
4.1	Compression test on masonry units (Penava, 2012)	83
4.2	Stress–strain relationship from compression tests of masonry units	84
4.3	Preparation of masonry triplets tests (Penava, 2012)	84
4.4	Tensional failure parallel to bedjoints (Penava, 2012)	85
4.5	Interlocking effect (Penava, 2012)	85
4.6	Determining initial shear strength by Mohr-Coulomb strength theory	86
4.7	Masonry wall specimen testing (Penava, 2012)	87
4.8	Averaged stress – strain behaviour of masonry wall compression tests	88
4.9	URM wall OoP bend test characteristics	89
4.10	URM wall OoP bend test preparation of samples	89
4.11	URM wall samples set for for OoP bend test	89
4.12	URM wall samples characteristic failure modes	90
4.13	OoP bending test strength results	90
5.1	IP test setup	94
5.2	IP load protocol (force control part)	94
5.3	IP test series measuring equipment and boundary condition arrangements	95
5.4	IP hysteresis loops and resistance envelope curves	96
5.5	Positive <i>vs.</i> negative IP cyclic envelopes	99
5.6	In-plane cyclic, quasi-static test crack patterns	103

6.1	Preparation of specimens for OoP drift driven tests	106
6.2	OoP drift driven test load protocol	106
6.3	OoP test set-up	108
6.4	Rigid body movement as recorded by ARAMIS in OoP tests	109
6.5	ARAMIS points used to calculate rotation angle (α)	109
6.6	Rigid body movement as captured by DAQ in OoP tests	110
6.7	Accidental torsion as recorded by ARAMIS through rotation differences from OoP tests	111
6.8	OoP cyclic, quasi static hysteresis - DAQ recordings	114
6.9	OoP cyclic, quasi static hysteresis - ARAMIS recordings	115
6.10	OoP load-capacity curves	116
6.11	OoP mean absolute error between DAQ and ARAMIS sorted by drift ratio and specimens	117
6.12	OoP crack occurrence map	117
6.13	Crack outlines of specimens at the end of OoP testing	118
6.14	Crack photographs of specimens at the end of OoP testing	119
6.15	Differences in rotations between the average rotation of infill wall and frame	120
6.16	OoP displacements and von Mises strains	121
8.1	3D micromodel parts	129
8.2	Micro-model composition of a CW model	130
8.3	Micro-model boundary conditions	132
8.4	Computational model of OoP bending tests	133
8.5	Standardised stress-strain relationship	134
8.6	Standardised biaxial failure function	135
8.7	Stages of crack opening	135
8.8	Softening displacement law in compression	136
8.9	Tension stiffening	136
8.10	Fracture energy	137
8.11	Compressive strength reduction within cracked concrete	138
8.12	Crack model stress and strain state	138
8.13	Plastic predictor-corrector algorithm for plastic flow β	139
8.14	Failure surface for interface elements	140
8.15	Behaviour of interface material model	141
8.16	Cohesion hardening/softening function	142
8.17	Multi-linear spring functions	143
8.18	Reinforcement bilinear law with hardening	144
8.19	Newton-Raphson methods	145
8.20	Example of unstable <i>Newton-Raphson</i> computing due to load controls (Vasios, 2015)	146
8.21	Arc-length method (Vasios, 2015)	147
9.1	Calibration flowchart	150
9.2	Parts of calibration results of BF model	153
9.3	Parts of calibration results from FI model	154
9.4	Calibrated IP cyclic-quasi static micro-model results	158
9.5	Damage state of computational vs. experimental IP model	161
9.6	IP computational positive <i>vs.</i> negative cyclic envelopes	163
9.7	IP infill wall principal stress σ_{\min} (MPa)	164
9.8	Computational model of OoP bending test deformation and crack patterns	167

9.9	Computational model of OoP bending tests maximal principal stress	168
9.10	Behaviour of FI push-over model with newly obtained values	168
9.11	Comprison of modified material model propeties values on FI, IP push-over model .	169
9.12	OoP principal stress of infill walls (no gravity force)	171
9.13	OoP drift driven test computational model simulation results	172
9.14	Computational frames micromodel OoP damage states	174
9.15	OoP displacement maps of frames with infill walls computational models	177
9.16	OoP drift-driven simulation (all models plotted)	178
10.1	Effects of IP load protocols on FI model	180
10.2	Map of recommended and chosen opening sizes	182
10.3	Developed micromodels for further simulations	183
10.4	IP behavior from simultaneous IP and OoP simulations	185
10.5	OoP behavior from simultaneous IP and OoP simulations	186
10.6	Coupled IP and OoP behavior from simultaneous IP and OoP simulations	187
10.7	Resultant resistance force V_R <i>vs.</i> angle (α)	188
10.8	Sorted openings plotted against each other	190
10.9	IP and OoP displacement @ $V_{R,max}$ <i>vs.</i> α	197
10.10	Coupled IP and OoP displacements @ $V_{R,max}$ in relation with angle α	198
10.11	OoP minimal principal stresses @ 1.25 % d_T with gravity load	199
10.12	Resistance mechanism development	200
10.13	Capacity interaction function	201
10.14	Regression results for depending variable α	203
10.15	Constants obtained from optimizing $k(\alpha)$ functions	204
10.16	k_o function <i>vs.</i> data (points) from computational models	205
10.17	Differences between the computational and analytical model	206
10.18	Determination of coefficient for the example	206
1	FI model's minimal principal stress @ $\approx V_{R,max}/2$ on infill wall	221
2	FI model minimal principal stress @ $\approx V_{R,max}$	222
3	FI model minimal principal stress @ $> V_R/2$	223
4	Maximal principal stress of FI model's infill wall	224
5	Minimal normal stress of FI model's frame	225
6	Crack patterns of infill wall @ $\approx V_{R,max}/2$	226
7	Crack patterns of infill wall @ $\approx V_{R,max}$	227
8	Crack patterns of infill wall @ $V_R > V_{R,max}$	228

List of Tables

2.1	Worldwide seismic building codes	22
2.2	OoP experimental loading methods and boundary conditions	24
2.3	OoP loading type	24
2.4	OoP loading method	24
2.5	Additional IP load	24
2.6	OoP experimental tests' material characteristics and subject studied	25
2.7	Masonry type	25
2.8	Laying method	25
2.9	Frame type	25
2.10	OoP experimental tests' geometrical characteristics	26
2.11	subfigure	26
2.12	Distribution of aspect ratio (l/h)	26
2.13	Used vs. suggested terminology for arching action modes	29
2.14	Displacement relations by author	31
2.15	Analytical models developed for the estimation of infilled frame OoP capacity (Anić et al, 2019b)	45
2.16	Various geometrical and mechanical properties of specimens	46
2.17	Analytical solutions for ultimate OoP displacement	47
2.18	Values for previous IP reduction coefficient β in Eq. (2.12) by Morandi et al (2013) .	49
2.19	Modification factor F_r for panels with openings	49
2.20	Values of β for torsional constant J (Ugural and Fenster, 2003)	50
2.21	Range of parameter values which are considered for the parametric analysis	50
2.22	Absolute difference between experimental and calculated capacities per property . .	51
2.23	Difference in % between analytical models and experimental OoP displacement . . .	52
2.24	Differences between calculated and experimental OoP capacities (Eq. 2.23)	56
2.25	Displacement calculation results	57
3.1	Design loads on the prototype structure	70
3.2	Reinforcement details for each cross section	70
3.3	Masonry unit properties	71
3.4	RC frames with masonry infill walls specimens	75
4.1	Results from testing initial shear strength	86
4.2	Results of masonry wall's compression test	88
4.3	OoP bending test strength results	90
5.1	Observed occurrences in IP experiments with relation on inter-storey drift (d_r) . . .	100
6.1	Mapegrout T60 mechanical properties	105

8.1	Boundary condition combinations in relation by simulation type	133
8.2	Initial non-linear cementitious 2 material properties for each constituent	139
8.3	Initial interface material properties	142
8.4	Bilinear steel reinforcement material properties	144
9.1	Tested parameters for both IP and OoP calibration	151
9.2	IP mean average percentage error of calibrated micromodel vs. experimental	157
9.3	Values and differences between computational and experimental outcomes of the wall OoP bending test	166
10.1	Implemented geometrical characteristics of additional openings	181
10.2	Results of nonlinear regression for effect of α	193
10.3	Coefficients for Equation 10.10	194
10.4	Analytical model prediction error	195
13.1	Recommended terminology	217

List of Symbols and Abbreviations

Abbreviations

RC	Reinforced concrete	SS	Structural steel
URM	Unreinforced masonry	OoP	Out-of-plane
IP	In-plane	IP+OoP	OoP behaviour with previous IP damage
OoP+IP	IP behaviour with previous OoP damage	IP & OoP	Simultaneous IP and OoP load
ISD	Inter-storey drift	LVDT	Linear variable differential transformator

Symbols

Latin based

C	Cohesion
E	Modulus of elasticity
E_f	Frame's elasticity modulus
E_m	Masonry's elasticity modulus
G	Shear modulus
G_f	Frame's shear modulus
G_m	Masonry's shear modulus
G_F	Fracture energy
K_{nn}	Normal stiffness
$K_{nn,min}$	Minimal normal stiffness
K_{tt}	Tangential stiffness
$K_{tt,min}$	Minimal tangential stiffness
R	Resistance
S_F	Crack shear stiffness factor
V	Shear force
W	OoP load-bearing capacity (force)
W_d	Critical compressive displacement
d_r	Inter-storey drift
$f_{m,c}$	Masonry's compressive strength
$f_{m,t}$	Masonry's tensile strength
$f_{m,v}$	Masonry's shear strength
$r_{c,lim}$	Reduction of compressive strength due to cracks
s_{max}	Crack spacing
c_{ts}	Tension stiffening
w	OoP load-bearing capacity (pressure)

Greek based

β_p	Direction of plastic flow
ε	Relative displacement
ε_{cp}	Plastic strain at compressive strength
μ	Poisson's ratio
σ	Normal stress
τ	Shear stress
Δ	Difference

Part I

Introduction

Conflicts of interest disclosure Please note that there are many similarities and cross-referencing between this chapter and the Anić et al (2019b) paper. Authors of the referenced paper are the thesis author and his supervisors.

Chapter 1

2019th Albanian earthquake field study

1.1 A brief introduction

An earthquake, 6.4 magnitudes by Richter scale, struck northwestern Albania with an epicentre 16 km west-southwest of Mamurras, at 03:54 CET (UTC+1) on 26 November 2019 (Fig. 1.1).

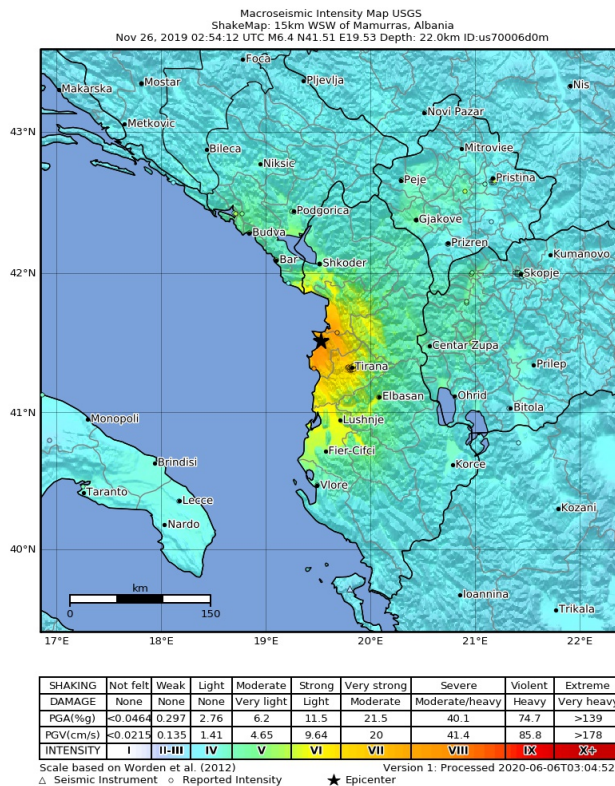


Figure 1.1: Map of Albania, showing location and intensity of shaking. Star marks epicentre. (USGS, 2021)

The earthquake lasted for about 50 seconds (Fig. 1.2) with a total of 51 people killed and about 3000 injured (contributors, 2021).

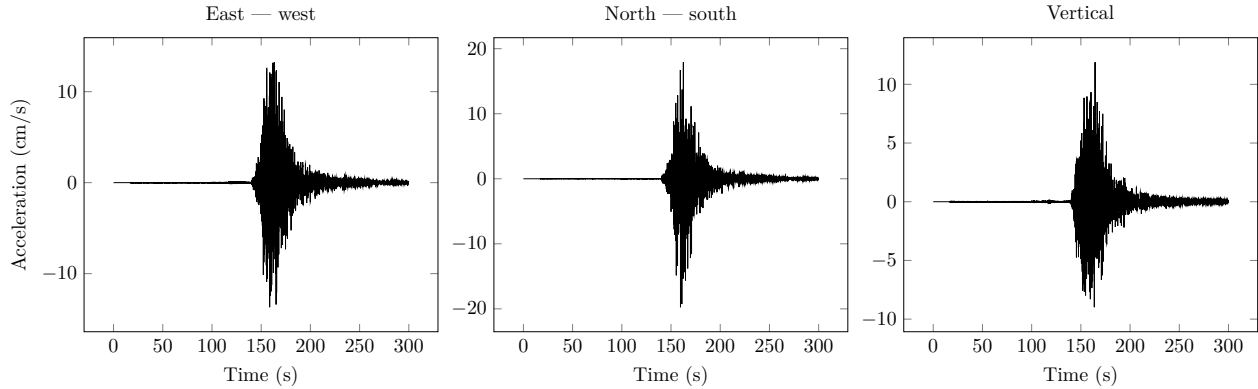


Figure 1.2: Albania earthquake signal (IGEO, 2021)

1.2 Reconnaissance mission

Under the *American Concrete Institute (ACI), Technical Committee 133: Disaster Reconnaissance* mission was formed to surveyed structures from 12th to 19th of January 2020. The mission was organised by dr. Pujol Santiago and led by dr. Schultz Arturo E., dr. Sim Chungwook, dr. Rautenberg Jeff M., dr. Penava Davorin, dr. Abrahamczyk Lars, dr. Mustafaray Eenea, and realised with the help of Anić Filip, Haweyou Melad, Gjoci Andi, Mema Jurgen (Fig. 1.3).

The committee aimed to survey modern, high-rise RC buildings within the city of Durres. A total of 55 buildings were surveyed. The collapsed or heavily damaged ones were not inspected as they were either closed for the public or demolished when the committee was on the field. Also, some damaged parts (*e.g.* infill walls) were removed in order not to jeopardize life and safety.

1.3 Understanding current Albanian seismic regulations

Albania has a long history of seismic regulations, first dating back to 1952. They have progressed through time (Fig. 1.4). The KTP N.2-89 from the year 1989 is the official provision still used

The aforementioned, current official provision of KTP N.2-89 is consistent with other modern provisions, *i.e.* codes such as EN1998 (BSI, 2005), as observable in the following points gathered from Freddi et al (2021):

- The provisions employ a design approach to dissipate energy by providing frames with adequate ductility without compromising their load-bearing capacity;
- The provisions regulate structures uniformity in plan and elevation, along with the guidelines to consider the distribution of mass and stiffness;
- The country is divided into seismic regions, and recognizes 3 basic soil types;
- The code provides guidelines to define the seismic action with consideration of torsional effects, seismic load combination, their factors, and co-factors;
- The structural analysis may be done either by modal response spectrum or by time history analysis;
- Masonry walls are categorized into three strength classes based on units and mortar strength. Masonry walls have a limitation on the maximum distance between the transversal walls,



Figure 1.3: ACI Technical Committee 133 team

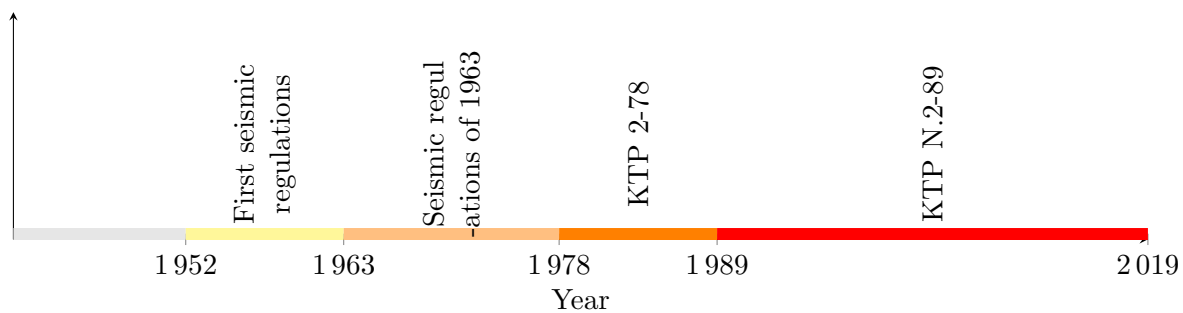


Figure 1.4: Evolution of Albanian seismic regulation (Freddi et al, 2021)

opening size, the distance between the openings, *etc.* It employs and gives directions to design RC tie beams in the masonry infill wall to prevent higher OoP damages by reducing its slenderness;

- The provisions distinguish several lateral resisting RC frames, such as moment-resisting, infilled frames, dual systems, and combinations. The code regulates ductile member detailing, *e.g.* minimum longitudinal reinforcements, maximum stirrups spacing, *etc.* ;
- There are no inter-storey drifts limits, *i.e.* *damage limit state* provided by the code to protect

the infill walls. Conversely, the regulation requires that they maintain their integrity during seismic events without explaining how. It also states that the infill walls should be checked against the out-of-plane failure, which is covered mainly by employing belt beams;

- When elastic and design spectra of KTP-N.2-89 and EN1998-1 (Fig. 1.5) are compared, it is visible that the strength requirements of KTP-N.2-89 are lower.

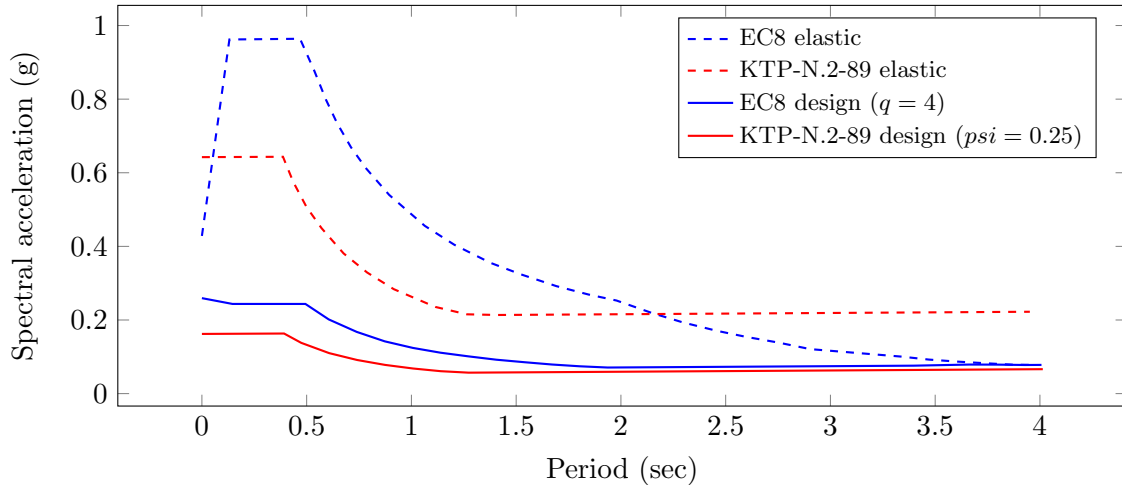


Figure 1.5: Comparison of elastic and design spectra between KTP-N.2-89 and EN1998-1 (Freddi et al, 2021)

1.4 Findings

As previously mentioned, the focus of the Reconnaissance mission was on the modern, high-rise buildings. The inspected ones used RC frames with unreinforced masonry (URM) infill walls. All the buildings used the hollow clay masonry units laid, so the voids were facing horizontal directions (Fig. 1.6). Those units were bounded by regular mortar, although it was used sparingly (Fig. 1.8). Mostly, but not always, there were bedjoints, and no headjoints as visible in Figure 1.8. There were little to no vertical confinements within the infill walls, yet some used the RC belt beam. The belt beams mainly were utilised under the window openings or at the infill wall's midheight. No buildings containing shear walls were found. Yet, there were mostly RC core walls used as elevator shafts. The typical plans of such buildings are presented in Figure 1.7, where the orange-coloured lines are masonry infill walls.

Within the building scoped, most of them had no structural damage. This can be attributed to reasonable structural regulations and workmanship regarding the primary structural system. Contrariwise; among the same inspected buildings, many did suffer anywhere from light to heavy, and unusable damage to the non-structural components, *i.e.* infill walls.

The only structural damage observed was that of the building in Figure 1.9. It was observed that the columns suffered shear damage at their top and bottom. Upon the inspection and during the earthquake, the building was still in construction. The ground floor did not have any infill walls, making them more ductile and suitable for soft-storey effects. Also, this building was the only one that did not have an RC elevator shaft; instead, masonry was used. Therefore, the effect of the seismic core was omitted. All the points above add up to account for the low shear performance of the frames.



Figure 1.6: Example of commonly used masonry unit

The infill walls mostly suffered from the combination of IP and OoP damage. All of the ingrained damages were observed (Fig. 1.10): Diagonal cracks; infill wall detaching from the beams and/or columns; Infill falling out-of-plane; Sequenced failures, their combinations *etc.*

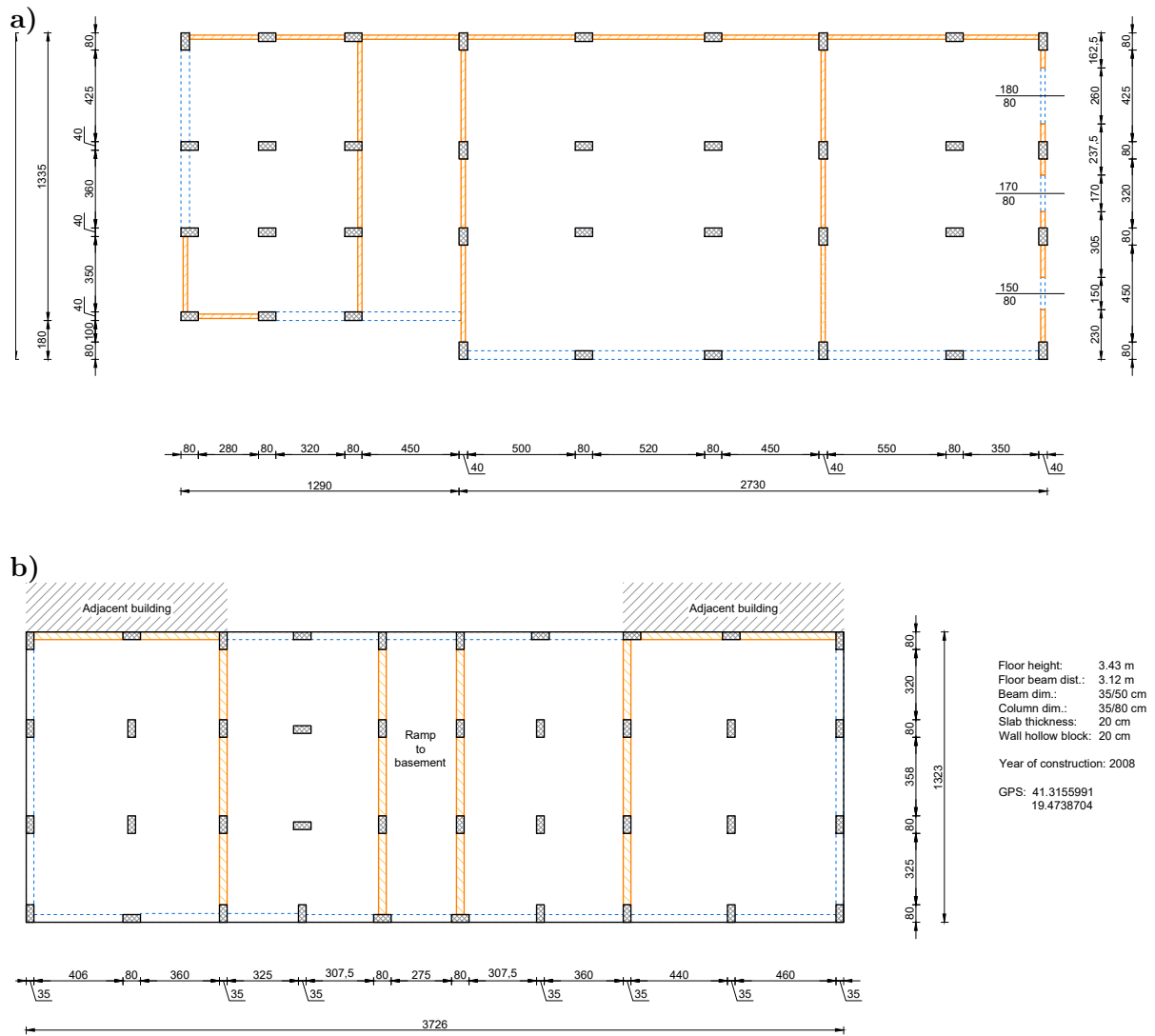


Figure 1.7: Examples of typical multi-storey buildings



Figure 1.8: Masonry units sparsely bounded with mortar



Figure 1.9: Structural damage



Figure 1.10: Damages to the infill walls



Figure 1.10 (cont.): Damages to the infill walls



Figure 1.10 (cont.): Damages to the infill walls

The low performance of the infill walls can be attributed to three main factors, each of them described in the following paragraphs.

Lack of confining elements was the governing factor leading to low-performance of infill walls. The vertical confining elements provide stiffness and boundary conditions necessary for infill walls integrity and stability. The lack of them is evident because the seismic codes themselves do not limit the damage, *i.e.* drift ratios. Yet, the codes regulate the OoP failure by employing the belt beams. They have also underperformed by not attaching them to the vertical confining elements. Therefore, they did not add a significant amount of stability to the system, resulting in parts either under and/or above the belt beam to fall out (*e.g.* Fig. 1.10a).

The non-existing mortar joints can also be blamed. Namely, it is in the Albanian tradition to lay blocks, so the voids are in line with the horizontal direction. However, the mortar is mostly absent in headjoints, and sometimes also in the bedjoints (Fig. 1.8 & 1.6). The lack of mortar in the headjoints bypasses the beneficial *interlocking effect*. The interlocking effect is essentially the slippage of mortar into the voids of the masonry units; thus, joining them into a combined action that can produce, for instance, a 3 fold greater shear resistance when triplets are tested. For more information about the interlocking effect, refer to the Section 4.2. Aside from the lack of mortar on the masonry units, the gap between the upper beam and the masonry wall was, for the most part, partially filled. This can result in reduced OoP performance (see Sec. 2.3).

No particular interventions were done in the case of certain slender walls . In some very slender walls, no measures were used to enhance their compromised OoP stability (Fig. 1.10f). The Albanian codes promote the use of belt beams; whereas, the EN 1998-1 BSI (2005) aside from belt beams, suggests using light wire meshes, wall ties fixed to the columns, and wind posts. As described in the point above, the belt beams did not have the desired effect because there were no vertical confining elements.

In contrast to the points that contributed to low performance of the infill walls, a building that suffered light to no damage was inspected (Fig. 1.11). During both the earthquake and our inspection, the building was under construction. Due to the lack of plaster, cracks were not as apparent as in other cases. Nevertheless, the building had better praxis examples, yet not ideal, contributing to the better performance. This was illuminated in the following two points: 1) The building had vertical and horizontal confinement on the parapet walls. Yet, it lacked the vertical confinement on the intersection of masonry walls and its ends; 2) The masonry units were placed so the voids were facing vertical direction and they were bounded by mortar in both the head- and bedjoints (Fig. 1.11b). Thus, taking advantage of the *interlocking effect*.

1.5 Conclusions

A reconnaissance mission under American Concrete Institute (ACI), Technical Committee 133, was formed to inspect damages to modern high-rise buildings from the 2019th Albanian earthquake. The seismic event caused significant harm to life, safety, and equipment. The damages were caused by insufficient regulations within the national seismic code KTP-N.2-89 and poor workmanship of certain parts. The national codes provided adequate guidelines for the primary systems, observable in little or no damage to the structural systems. Yet, it does not limit the damage, *i.e.* drifts of the secondary structures, *i.e.* masonry infill walls that caused the most harm. The infill walls lacked vertical confinement, and the units were not entirely bound by mortar. Mostly the headjoints



Figure 1.11: Example of better praxis

were lacking which in effect left voids being unfilled with mortar and, by doing so, bypassed the beneficial *interlocking effect*. Even though the national code calls for using belt beams to prevent OoP failures, they were not connected to the confining elements. Thus rendered them obsolete and, with the addition of omitted mortar joints, divided the infill wall into two segments above and under the belt beam that have easily failed in the OoP direction.

Chapter 2

Literature overview

2.1 General overview

The majority of multi-storey buildings in Southern Europe have structural systems composed of RC frames with non-load-bearing unreinforced masonry (URM) walls (Booth and Key, 2006). Most commonly, hollow clay blocks are used as infill units. Most often, blocks are stacked so that the voids are pointing in the vertical direction. However, with the building traditions of countries such as Portugal, Turkey and Albania, blocks are generally laid, so the voids are facing a horizontal direction (de Sousa, 2014; Misir et al, 2016).

Ground motions from earthquakes expose structures to both inertial and inter-storey drift forces. With structural systems composed of infilled frames, the inter-storey drift forces are transmitted to the frame by the displacements of rigid diaphragms *i.e.* slabs. In comparison, inertial forces result from accelerated higher masses, predominately infill walls. Therefore, the failures and damages caused by the inertial forces are usually detectable and expected at higher storeys and with the infill walls with insufficient boundary conditions. On the other hand, more significant inter-storey drift damages are expected at lower storeys, where both shear and gravity forces are greater. Gravity forces from the accumulated masses would aid an additional reduction of the infill's inertial characteristics. Most commonly, the damages from the inter-storey drift forces is observable by the heavy cracking of the frame and the development of plastic hinges. In contrast, the damage from inertial forces are observable in the heavy cracking of the infill and, frequently, the disappearance (falling out) of larger parts of the wall.

During an earthquake event, an inelastic infill wall interacts with a ductile surrounding frame, thus rendering its behaviour and the behaviour of the whole structure. Due to the complexity of the problem itself, this interaction is yet to be implemented in European seismic codes EN1998-1 (BSI, 2005). Therefore, considerable research effort has been made to grasp the complexity mentioned above. Precisely, one of the first written instances of such considerations dates back to the early 1960's (McDowell et al, 1956b; Holmes, 1961). However, aside from the conservative approach, implementing the interaction is still being thoroughly researched and largely unknown at the time of code development. Accordingly, this has resulted in more redundant frames. Such multi-storey structure, made of infilled frames, was tested under FRAMA project (Penava and Sigmund, 2017). The test showed that frames had excellent performance under multiple ground excitations.

Even though the amounting research contributes to the answer of infill wall – frame interaction, its implementation to the codes has two contradicting proponents. The one in favour is from the example of Fardis and Panagiotakos (1997) that argues that due to the unpredictability of peak seismic demands, an engineer should consider every element that would aid the seismic design. This would result in lower economic demands on structures. This view was aided by the empirical view

of strong infills that govern the behaviour or even prevent the collapse of weak RC frame structures. On the other hand, the opposite view can be summarized in the following points: – Masonry walls often contain openings (*e.g.* window, door) or the installations like plumbing, impairing them; – Masonry wall often separates from the infill wall during the earthquake event, and even fall out due to low OoP capacity; – Layouts of masonry walls are changeable through the exploitation life of the building, *etc.*

As mentioned, in favour of understanding the complexity of frame-infill interaction, many studies have been conducted since the early '60s. The field has broadened and divided into four main components, listed by prevalence:

1. In-plane (IP), where the frames are loaded in the direction of their axial plane
2. Out-of-plane (OoP) where the frames are loaded perpendicular to their axial plane
3. Combined IP and OoP load (IP+OoP, OoP+IP and simultaneous)

The IP+OoP describes OoP behaviour due to previous IP damage and vice versa in the case of OoP+IP. Simultaneous action describes a synchronous IP and OoP loading protocol.

The seismic engineering field researches all three loading cases. On the one hand, in terms of OoP loads, only seismic engineering does studies with inter-storey drift forces and dynamical excitations (Fig. 2.1). Dynamical methods are performed on shaking tables, inertial pressurizes the infill, while inter-storey drift methods load the frame. On the other hand, additional branches are involved in studying the effects of inertial force. Namely, blast engineering and others; for instance, the effects of wind (Anderson and Bright, 1976) and soil (Jäger et al, 2008) pressure. The latter two are scarcely researched, while conversely, the blast engineering field is well developed, and they were the pioneers of such testing. The pioneering work was initiated in the early '60s by the Armour Research Foundation, sponsored by the U.S. Air Force, involving authors such as McDowell et al (1956b,a) and Monk (1958). In blast engineering, the OoP load is transmitted by the explosion's blast waves which pressurize the infill. Therefore, the experimental simulation of such an effect was performed by pressuring the infill, most commonly with airbags. So, the blast engineers laid the groundwork for seismic engineering, using identical methods to simulate the OoP inertial forces. Accordingly, many studies from the seismic and blast engineering fields overlap and cross-reference. For instance, Gabrielsen et al (1975) from the blast engineering field cited arching actions observed in the 1967 Caracas (Venezuela) and the 1971 San Fernando (California) earthquakes.

Additionally, various OoP experiments have been conducted on load-bearing brickwork, such as in Drysdale and Essawy (1988); Hallquist (1970); Lam et al (2003); Vaculik (2012). Similar to the blast engineering field, their findings show numerous similarities with seismic research. However, in this thesis, the focus was on the seismic engineering field and infilled frames. Therefore, such papers are sometimes cited but not focused on.

In recent years, OoP loading gained more and more research interest (Fig. 2.2) as previously there was more focus on IP loadings (Asteris et al, 2017). The OoP research encompass experimental surveys (Tab. 2.2–2.10), micro (Reindl et al, 2011; Kuang and Yuen, 2010), macro (Kadysiewski and Mosalam, 2009; Al Hanoun et al, 2019; Furtado et al, 2016b; Di Trapani et al, 2018), and analytical modelling (Tab. 2.15).

The research and the data gathered in the field of earthquake engineering contributed to various cognitions, provisions and codes, termed *anti-seismic regulations for civic and building protection*. Some are regulated nationally, and some internationally. List of such provisions are presented in Table 2.1. From Table 2.1 it is clear that all codes are more or less intertwined, where a majority of codes based upon ACI (2011) provisions from the U.S..

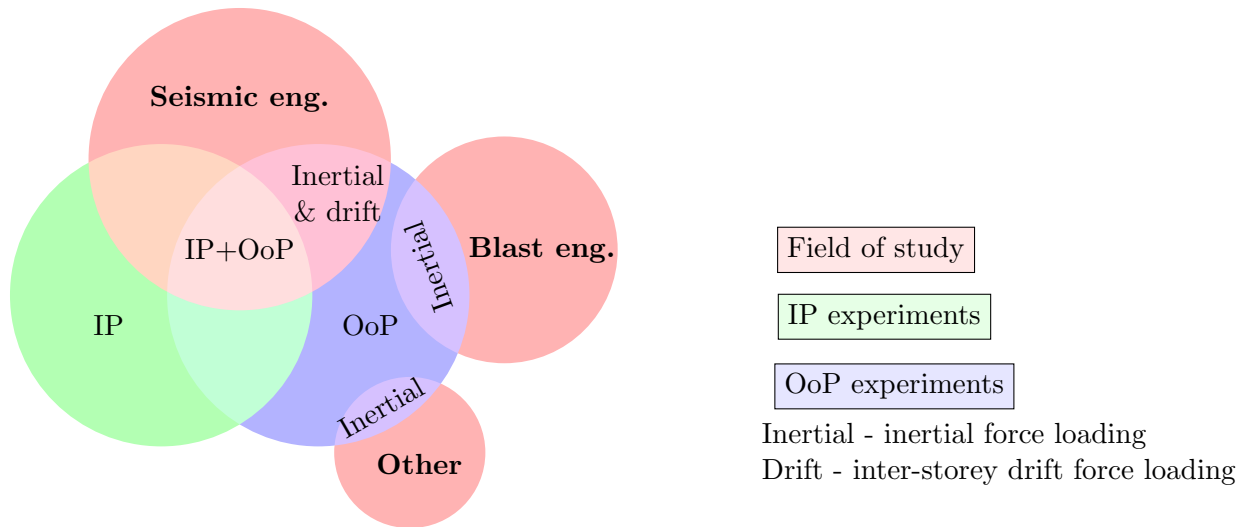


Figure 2.1: Relevant experiments as shared by different fields of study

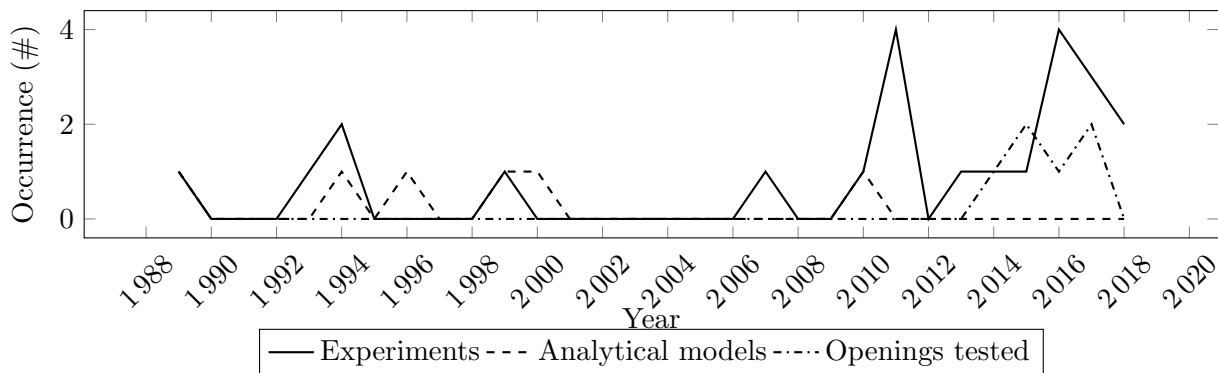


Figure 2.2: Occurrences of OoP-specific subjects by year published

Regarding the perspective of seismic codes on OoP behaviour, European EN1998 provisions (BSI, 2005) only restrict the OoP collapse of slender infills when the height to thickness ratio is $h/t > 15$. In those cases, the code states that special measures should be implemented, such as applying light wire meshes, wall ties fixed to the columns, wind posts, and concrete belts (BSI, 2005). At the same time, the European codes for masonry structures (BSI, 2004b) suggest using Equation (2.8) for calculating OoP, inertial, load-bearing capacity. The use of Dawe and Seah (1989) Equation (2.4, 2.3) for calculating OoP, inertial, load-bearing capacity is proposed by the Masonry Standards Joint Committee and others (1999). Similarly, the Canadian code (Canadian Standards Association and Standards Council of Canada, 1978) does not include a specific method for obtaining the OoP capacity. Instead, they suggest that the arching action (Sec. 2.3) method is to be used. US federal recommendations FEMA 356 (2000); FEMA 273 (1997) and those based upon FEMA, such as the New Zealand codes (NZS-3101, 1995), use the approaches to assess OoP damage types and calculate OoP bearing capacity using Equation (2.10), which is just a simplified version of the one found in Angel et al (1994) (Eq. 2.5).

Eurocode 8 is the general code document followed within the majority of the European continent. They are also broadened with national annexes developed by each country. Furthermore, some countries have developed codes that designers must comply with. They are mostly more detailed than European codes. In terms of the earthquake codes, such examples are the *Italian seismic codes*

Table 2.1: Worldwide seismic building codes

#	Code	Remark
1	European standard <i>Eurocode 8</i> (EN 1998) BSI (2005)	
2	American Concrete Institute ACI-318 ACI (2011)	
3	Applied Technology Council (ATC) - Federal Emergency Management Agency (FEMA 273 & 356) FEMA 273 (1997); FEMA 356 (2000)	
4	Indian Standards on Earthquake Engineering (IS) Standard (2002)	
5	Peruvian Technical Building Standard E.030 NTS (1997)	
6	Chilean Nch433 NCH (1996)	Based upon ACI-05
7	Ecuadorian INEN-5 ECUATORIANO and INEN (1898)	Based upon ACI-318-71
8	Nepal National Building Code NBC-105 MHPP (1995)	Largely following the IS Code
9	Colombian Standards for Seismic Resistant Design and Construction NSR-84 CAEE (1984)	Based upon ACI
10	National Structural Code of the Philippines, Vol. 1, Fourth Edition (NSCP) NSCP (1992)	Based upon ACI
11	New Zealand: Code of Practice for the Design of Concrete Structures, Part 1 (NZS-3101) NZS-3101 (1995)	
12	Israeli Design Provisions for Earthquake Resistance of Structures (SI-413) SI (1995)	
13	Russian Building Code on Construction in Seismic Areas (SNiP-II-7-81) SNiP (1995)	
14	Venezuelan Seismic Code, 1988. Regulations for Earthquake Resistant Buildings CNIC (1988)	
15	Vietnamese Seismic Design Standard TCXDVN 375: 2006 VBS (2006)	Based upon SNiP
16	Canadian Standards Association and Standards Council of Canada	

(NTC, 2008) and *Greece code for Seismic Resistant Structures* (EAK, 2000).

In the case of RC frames with URM walls, EN1992 provisions for concrete (BSI, 2004a) and EN1996 for masonry (BSI, 2004b) are to be followed along with seismic provisions, *i.e.* EN1998 (BSI, 2005). In such structures, EN1998 BSI (2005) primarily covers the ductility class and rebar design specifics, while it ignores infills. More closely, it refers to infill as a secondary element during seismic action. However, it also states that the designer *can* implement the infills effects while not specifying *how*. Such a design approach made frames more redundant, as seen in experiments like FRAMA Penava and Sigmund (2017). This lack of code specifications on the effects of infill wall was the consequence that the code developers most probably took the conservative approach.

2.2 Experimental campaigns

This section covers a review of experimental assessments of infilled frames with regard to OoP and combined loading within the scope of seismic engineering. Data from experimental campaigns are gathered and presented in Tables 2.2 to 2.10. The distribution of various characteristics from Tables 2.2 to 2.10 are plotted in Figs. 2.4 to 2.7.

From the provided Tables 2.2 – 2.10, as well as Figures 2.4 – 2.7 it is visible that frames are made either from RC or structural steel (SS). Some experimented with both in order to contrast strong from weak frames (Klingner et al, 1996; Flanagan and Bennett, 1999a; Wang, 2017). Furthermore,

infill walls were mostly built as single-leafed, clay or concrete blocks. Mostly, they are placed, so the voids are facing vertical direction. However, Portuguese and Turkish research laid blocks horizontally, as are their building traditions, same as is in Albania. This can be a crucial factor, as the blocks–interlocking effects might be reduced. For more about the interlocking effects, please refer to the Section 4.2. Further on, most studies were done by simulating inertial load. Those were done mainly by pressurising/unpressuring an airbag positioned between the infill and the reaction wall. There were exceptions, where the loads were implemented by point or line loads. Then, about one-fourth of the experiments were done by dynamical methods implemented by shake tables. The shake tables excited the specimens by a sine wave or real earthquake signals. Lastly, only two experiments covered the inter-storey drift methods (Flanagan and Bennett, 1999a; Henderson et al, 1993), where the loads were implemented onto the frame rather than on the infill. Half of the studies had cyclic or quasi-cyclic methods; the other half had about the same ratio of monotonic and dynamic methods. Similarly, about half of the experiments covered some IP loading (predominantly previous), while others were purely OoP studies. The predominant method of implementing IP loads was prior to OoP loading. Conjointly, only one study had researched previous OoP loading on IP behaviour (Flanagan, 1994) and only two on simultaneous IP & OoP loads (Flanagan, 1994; Misir et al, 2016). Furthermore, about four-fifths of studies covered clay units, vertically laid with surrounding RC frame.

Additionally, various researchers studied the effects of boundary conditions, gravity loads, openings, etc. The boundary conditions can be a direct result of *workmanship*. This is because it is challenging for a mason to fill, most commonly, the upper gap; that is, the gap between the upper beam and the infill. So, the gap can be fully, partly or even left unfilled. Such a fault can render the overall OoP behaviour and its failure mechanisms. Contrariwise, some researchers as Wilton and Gabrielsen (1973) consider gaps as practical considerations. Such a view is supported by the fact that they act independently from each other by de-bonding the infill from the frame. This was observed in dynamical studies (Tu et al, 2010; Fowler, 1994), when fully bonded, both infill and the frame acted as a single unit. Whereas, if the de-bonding occurred, they behaved more or less independently, resulting in infills falling out (Tu et al, 2010). Apart from the effects of workmanship or its practical considerations, the gaps can directly result from IP or OoP inter-storey drift excitement, as the de-bonding is one of the first events to occur with such a loading type.

The presence of openings in IP studies resulted in lowering its overall bearing capacity and failure mechanism, as demonstrated in numerous studies (Sigmund and Penava, 2014; Surendran and Kaushik, 2012; Tasnimi and Mohebkah, 2011; Kakaletsis and Karayannis, 2009). This was not as obvious in the case of OoP loadings. Figure 2.3 shows openings tested in OoP direction until the year 2020. Presumably, a similar window opening as in Fig. 2.3b was tested by Dawe and Seah (1989); however, figures or detailed descriptions are missing. For the same reason, a presumably similar full-height opening, as in Fig. 2.3e, was tested by Verlato et al (2016). The distribution of infill to opening area ratio (A_{in}/A_o) is plotted in Fig. 2.6. The plot was not displayed as a *box plot*, rather as a *scatter plot* due to the low number of data points (5). The red line in the figure displays the Eurocode 6 (BSI, 2004b) limit for nominal sizes openings. That is, small openings that do not affect the behaviour of walls. In the OoP case, only the opening (Fig. 2.3c) from Preti et al (2012) falls under the negligence size.

Table 2.2: OoP experimental loading methods and boundary conditions

#	Study by	OoP load type	OoP loading method	IP loading method	Gaps considered	
					None @ beam	@ columns
1	Dawe and Seah (1989)	Monotonic	Inertial - AB	No	+	+
2	Henderson et al (1993)	Cyclic	Inter-storey drift	Cyclic	+	-
3	Angel et al (1994)	Monotonic	Inertial - AB	Cyclic	+	-
4	Fowler (1994)	Dynamic	Shaking table	Dynamic	+	-
5	Klingner et al (1996)	Dynamic	Shaking table	Dynamic	+	-
6	Flanagan and Bennett (1999a)	Monotonic & Dynamic	Inertial - AB & inter-storey drift	Cyclic	+	-
7	Hashemi and Mosalam (2007)	Dynamic	Shaking table	No	+	-
8	Tu et al (2010)	Dynamic	Shaking table	No	+	-
9	Komaraneni et al (2011)	Dynamic	Shaking table	Cyclic	+	-
10	Liu et al (2011)	Dynamic	Shaking table	No	+	-
11	Pereira et al (2011)	Cyclic (q-static)	Inertial - double-leaf AB	Cyclic	+	-
12	Rabinovitch and Madah (2011)	Dynamic	Shaking table	No	+	-
13	da Porto et al (2013)	Monotonic	Inertial - L	Cyclic	+	-
14	Hak et al (2014)	Cyclic (q-static)	Inertial - P	Cyclic	+	-
15	Akhoundi et al (2015, 2016)	Cyclic (q-static)	Inertial - AB	No	+	-
16	Furtado et al (2015)	Cyclic (q-static)	Inertial - AB	Cyclic	+	-
17	Petrus et al (2015)	Cyclic (q-static)	Inertial - L	No	+	-
18	Preti et al (2015)	Cyclic (q-static)	Inertial - P load	Cyclic	+	-
19	Misir et al (2016)	Cyclic	Inertial - AB	Cyclic	+	-
20	Mosoarca et al (2016)	Cyclic (q-static)	Inertial - L	No	+	-
21	Verlato et al (2016)	Monotonic	Inertial - P load	Cyclic	+	-
22	Arède et al (2017)	Cyclic (q-stat.) & monotonic	Inertial - AB	Cyclic	+	-
23	Sepasdar (2017)	Monotonic	Inertial - AB	No	+	-
24	Wang (2017)	Monotonic	Inertial - AB	No	+	+
25	Domenico et al (2018)	Cyclic (q-static)	Inertial - P load	No	+	+
26	Rupakhety and Ólafsson (2018)	Cyclic (q-static)	Inertial - AB	Monotonic	+	-

AB - airbag, P - point, L - line

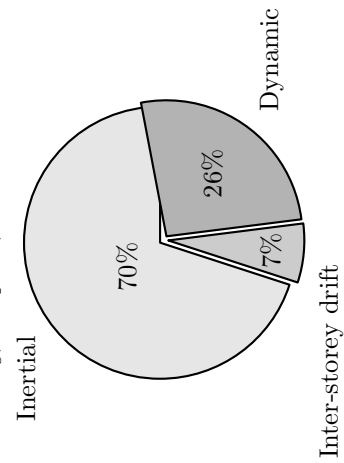


Table 2.3: OoP loading type

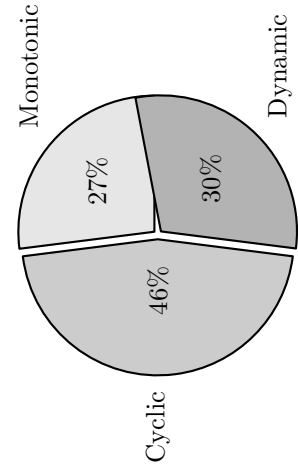


Table 2.4: OoP loading method

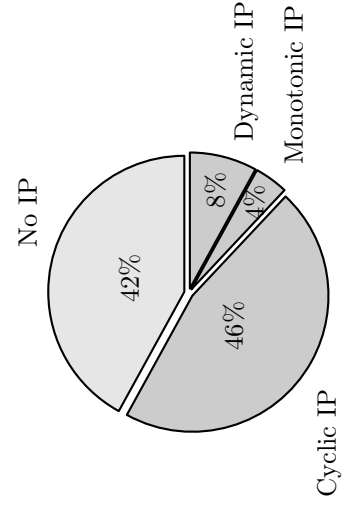


Table 2.5: Additional IP load

Figure 2.4: Distribution of OoP load methods

Table 2.6: OoP experimental tests' material characteristics and subject studied

#	Study by	Frame	Infill	Subject studied
1	Dawe and Seah (1989)	SS	Concrete blocks, dry and normally stacked blocks, boundary conditions	Effects of centric window opening (19%)
2	Henderson et al (1993)	SS	Clay block layed horizontally	OoP+IP loading
3	Angel et al (1994)	RC	Double leaf clay brick & concrete blocks	Infill slenderness variation h/t , variation of mortar type
4	Fowler (1994)	SS	Clay block	Weak and strong frames
5	Klingner et al (1996)	RC	Clay brick	IP+OoP & OoP+IP separate and combined loading
6	Flanagan and Bennett (1999a)	SS	Clay block	Confined and un-confined panels
7	Hashemi and Mosalam (2007)	RC	Hollow clay bricks	Studied weak & strong frame with confined and unconfined infill
8	Tu et al (2010)	RC	Clay brick	Special reinforced beam-infill connections observed
9	Komaraneni et al (2011)	RC	Clay brick	Gap between infill and columns
10	Liu et al (2011)	RC	Concrete blocks	Study included URM & reinforced masonry units
11	Pereira et al (2011)	RC	Hollow clay brick	Full height centric opening (35%) and vertical stripes
12	Rabinovitch and Madah (2011)	RC	Concrete blocks	Centric window opening (20%), Effect of contact surface between airbag & infill
13	da Porto et al (2013)	RC	Clay block	Effects of gravity loading
14	Hak et al (2014)	RC	Clay block	Considered sliding joints to limit infill-frame response (from Preti et al (2012))
15	Akhoundi et al (2016, 2015)	RC	Hollow clay brick	Block: pumice, hollow-fired clay, autoclaved aerated concer. & Brick: insulated & horizontally hollowed
16	Furtado et al (2015)	RC	Single & double leaf hollow clay block layed horizontally	clay brick with 8.5 cm thickness
17	Petrus et al (2015)	SS	Clay block	Innovative infill strenghtening system
18	Preti et al (2015)	SS	Concrete block layed horizontally	Innovative infill system <i>DRES</i> , centric full height opening (30%)
19	Misir et al (2016)	RC	Block: pumice, hollow-fired clay, autoclaved aerated concer. and horizontally hollowed clay brick with 13.5 cm thickness and horizontally hollowed	Innovative test setup
20	Mosoarca et al (2016)	RC	Clay block	Considered centric window opening (17%)
21	Verlato et al (2016)	RC	Clay block	Considered centric door opening (17.6%)
22	Arède et al (2017)	RC	Clay block	Boundary variation study
23	Sepasdar (2017)	RC & SS	Concrete block	Innovative earthquake-safe and eco-friendly infill panel systems
24	Wang (2017)	RC	Concrete block	
25	Domenico et al (2018)	RC	Clay block	
26	Rupakhty and Ólafsson (2018)	RC	Clay block	

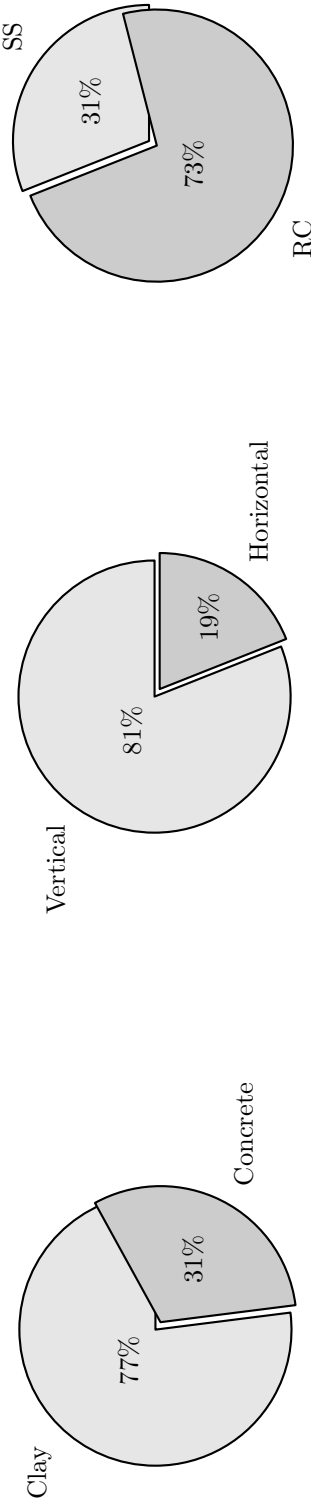


Table 2.7: Masonry type

Table 2.8: Laying method

Table 2.9: Frame type

Figure 2.5: Material specifics of experimental tests

Table 2.10: OoP experimental tests' geometrical characteristics

#	Study by	Infill		Openings		Specimens		
		h/t	l/h	A_o/A_{in} (%)	Type	Scale	# Storeys	Bays
1	Dawe and Seah (1989)	14.74, 20.00, 31.11	1.29	19.05	Window	1:1.0	9	1
2	Henderson et al (1993)	19.20	1.20			1:1.0	2	1
3	Angel et al (1994)	8.73, 39.68, 16.09, 10.73	0.75			1:1.0	8	1
4	Fowler (1994)	10.12	1.64			1:1.0	1	1
5	Klingner et al (1996)	19.52	0.74			1:2.0	2	1
6	Flanagan and Bennett (1999a)	22.40, 11.20, 6.79	1.00			1:1.0	3	1
7	Hashemi and Mosalam (2007)	23.78	1.35			1:1.0	2	1
8	Tu et al (2010)	5.6	0.96			1:1.0	4	1
9	Komaraneni et al (2011)	22.67, 11.33	1.78			1:2.0	3	1
10	Liu et al (2011)	1.90	1.67			1:3.0	2	1
11	Pereira et al (2011)	2.33	2.00			1:1.5	4	1
12	Rabinovitch and Madah (2011)	21.00	0.58			1:1.0	2	1
13	da Porto et al (2013)	22.08	1.57			1:1.0	6	1
14	Hak et al (2014)	12.55	1.43	34.14	Full wall height	1:1.0	5	1
15	Akhoundi et al (2016, 2015)	14.86	1.48	12.45	Window	1:2.0	6	1
16	Furtado et al (2015)	2.33, 1.35	1.29			1:1.0	3	1
17	Petrus et al (2015)	14.00	0.84			1:1.0	1	1
18	Preti et al (2015)	11.50	1.24	7.78	Window	1:1.0	2	1
19	Misir et al (2016)	8, 8.51, 10.53, 14.85, 23.53	1.80			1:1.0	6	1
20	Mosoarca et al (2016)	1.40	0.76			1:1.0	3	1
21	Verlato et al (2016)	9.17	1.40	33.25	Full wall height	1:1.0	4	1
22	Arède et al (2017)	1.53	1.83			1:1.0	5	1
23	Sepasdar (2017)	10.89	1.37	17.38	Window	1:2.0	4	1
24	Wang (2017)	10.89	1.37	17.38	Door	1:2.0	4	1
25	Domenico et al (2018)	29.38	1.28			2:3.0	3	1
26	Rupakhety and Ólafsson (2018)	7.60	1.84			1:1.0	7	1

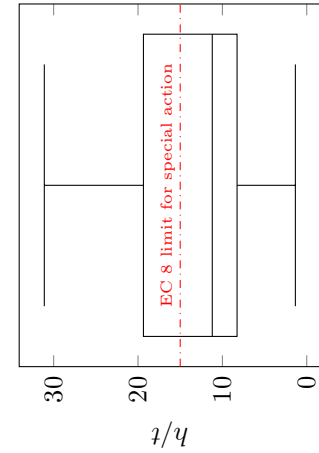
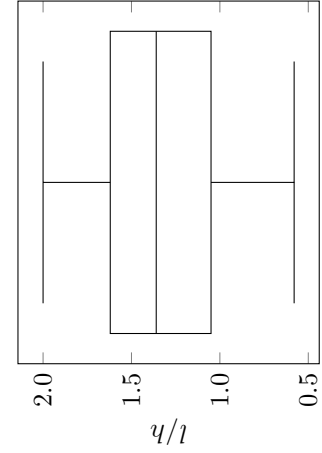
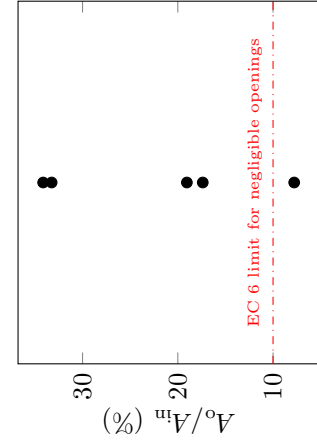
Table 2.11: subfigure
Distribution of slenderness (h/t)Table 2.12: Distribution of aspect ratio
(l/h)Figure 2.6: Distribution of A_o/A_{in} ratio

Figure 2.7: Distribution of geometrical characteristics

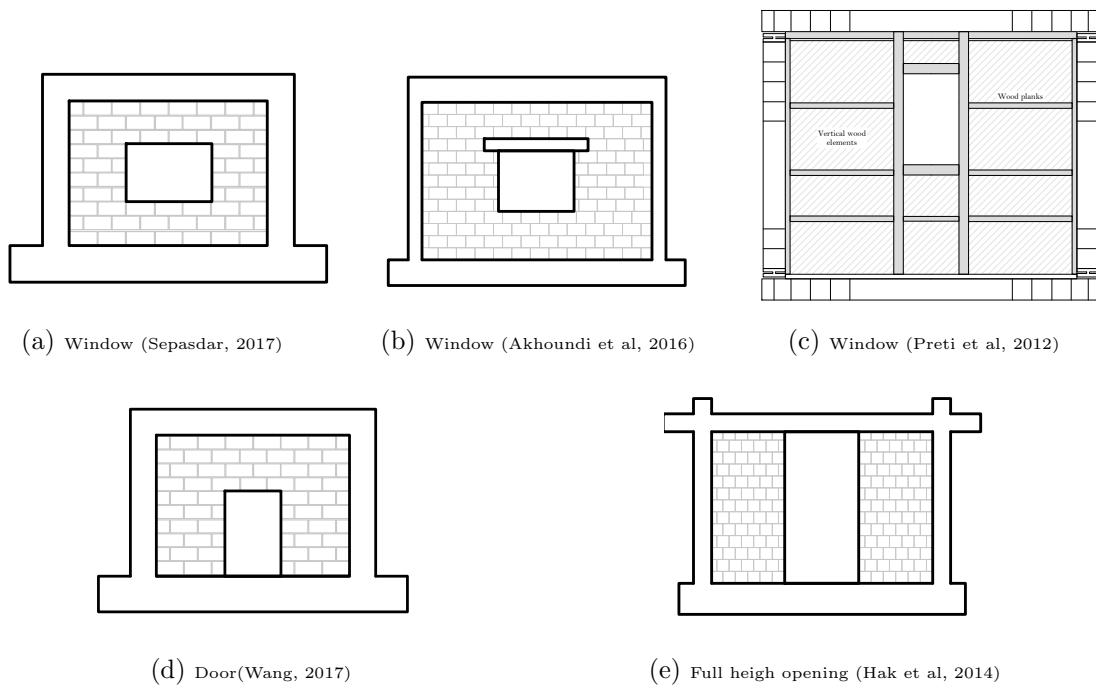


Figure 2.3: Opening considered in OoP research

2.3 Arching action and boundary conditions

The most important finding in the field of OoP behaviour is certainly the *arching action*. It was firstly founded by Armour Research Foundation in 1951 when they tested the blast resistance of load-bearing walls. McDowell et al (1956b) in 1956, under the aid of U.S. Air Force, presented a discussion on arching action hypothesis, and the same year published it as a theory (McDowell et al, 1956a). It was expected that the wall would bend due to the uniform pressure of the blast wave, causing flexural failure. So, a simply supported beam with a uniform continuous load was the appropriate mechanical system. However, the tests showed a six-fold greater load-bearing capacity than that predicted by flexural theory. It was later found that a different mechanism occurs. Namely, infill cracks and thus separates into two rigid bodies that clamp on their ends. Those clamping points compress, rendering the whole system into a three-hinged arch, hence the name *three-hinged arching action*. So, due to clamping, arching action, additional normal forces in the wall resist the transversal one. In fact, the resistance mechanism is the same as in the three-hinged arch. In addition to finding the arching action theory, McDowell et al (1956a) were also the first to formulate the OoP bearing equation (Eq. 2.2).

Further on, Gabrielsen et al (1975) also from the field of blast engineering, detailed the formation of arching action (Fig. 2.8). If the wall is fully bounded by frame (Fig. 2.8a), the wall bends as a simply supported beam would. After reaching a critical point, the wall cracks. The wall separates into two rigid bodies that open up on one and clamp on the other corner when cracked. Thus, forming the arching action that has three hinges in vertical, and four in horizontal direction (Figs. 2.10a, 2.10e). This kind of arching action is sometimes termed as *two-way* or *rigid arching action*. The forming of a *gapped-arching* action (Fig. 2.10b), sometimes referred to as *one-way arching action* is differed; as due to the gap, the wall bends as a cantilever would. The wall, at some point, clamps on the upper beam and bends until it reaches the critical point. When it cracks, it forms a three-hinged arch both in vertical and horizontal direction (Figs. 2.10b, 2.10f). However, the vertical arch is not a true arch, as it has the upper linear part and lower non-linear (Fig. 2.10b). Hence, it has a lower bearing capacity.

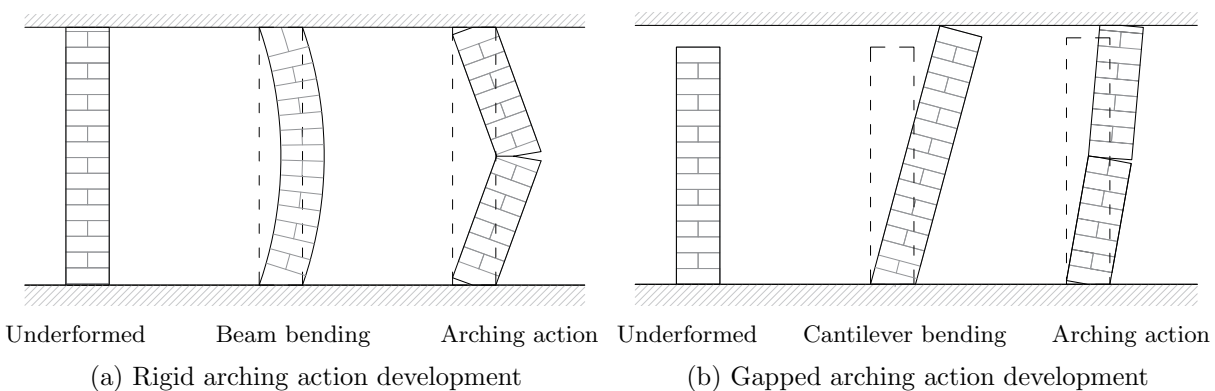


Figure 2.8: Arching action development phases by different boundary conditions

Most commonly, the fully bounded and infill-beam gap boundary conditions were tested (Tab. 2.2). However, few had tested the columns-infill gaps. With such boundary conditions, the three-hinged arch forms only on the vertical strip, *i.e.* there is no arch support in the horizontal direction (Fig. 2.9c). Hence, this type of arching action is truly one-directional (one-way arching). Contrari-

Table 2.13: Used vs. suggested terminology for arching action modes

Boundary conditions	Hinges (#)		Terms from literature	Suggested terms
	Vertical	Horizontal		
Fully bounded (Fig. 2.9a)	3	4	Two-way action, Rigid arching action	Rigid arching action, Fully bounded arching action
Beam-infill gap (Fig. 2.9b)	3	3	One-way action Gapped arching action	Gapped arching action Single gap arching action
Columns-infill gap (Fig. 2.9c)	3	0	/	Double gap arching action One-way arching action

wise, many authors use one-way action for a single gap arching action, even though it has both horizontal and vertical arching. However, the horizontal arching has one less hinge when compared to the fully bounded arching action. Nevertheless, it also thrusts on the columns. So, this kind of term can be misleading; the proposed terminology was assembled in Table 2.13. Additionally, some authors refer to red lines in figure 2.9 as *yield lines*. However, this is not accurate, as the blocks do not yield. They rotate about those lines; so, a more appropriate term would be *hinge lines* as proposed by Hobbs et al (1994).

Additional arching action modes were found, namely, four and two hinged arching actions. The four hinged arching action (Fig. 2.10d) was found by Varela-Rivera et al (2012) on the testing of *confined masonry*. Nonetheless, this kind of arching action can be excepted with tall infills as is in the case of horizontal four hinged arching action (Fig. 2.10a). Such arching actions consists of non-linear parts on the end and linear parts on the middle part (Fig. 2.10d). Further, the two-hinged arching action (Fig. 2.10c) is not an arch at all; rather, a compression strut. However, for the sake of uniformity, it will be termed as such. It was found by Tu et al (2010), and it is the only instance of mentioning or detailing an arching action in dynamical experiments. The two-hinged arching action forms when infill cracks on the tension sides of the panel (top and base), thus forming a strut (not arch) between the opposite compression sides. Therefore causing the panel segment to rock between the crushed ends rigidly. Furthermore, Tu et al (2010) concluded that such behaviour is analogous to a slender rocking pier.

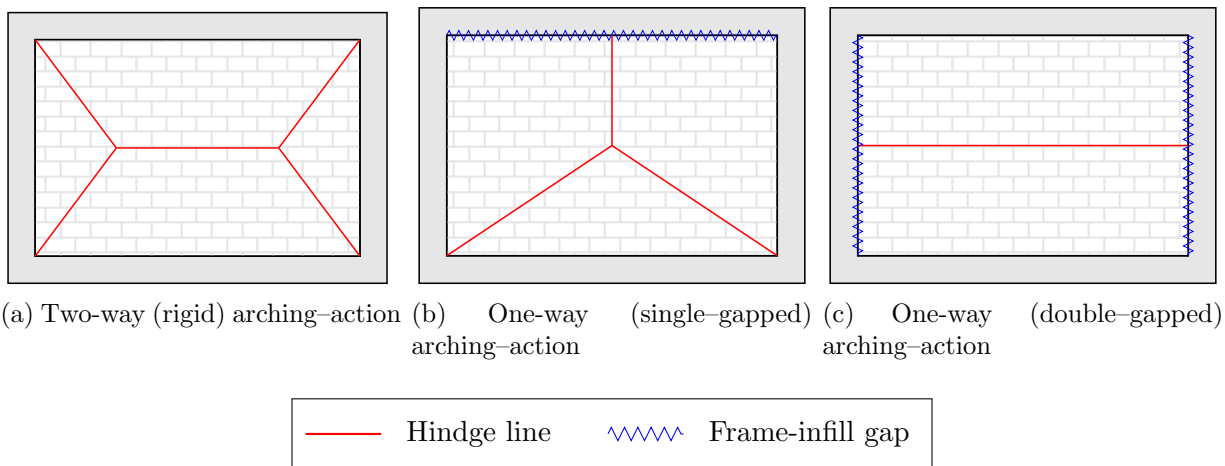


Figure 2.9: Types of arching action in relation to boundary conditions

As observable, the less the boundary, the fewer hinges were formed. This inevitably causes

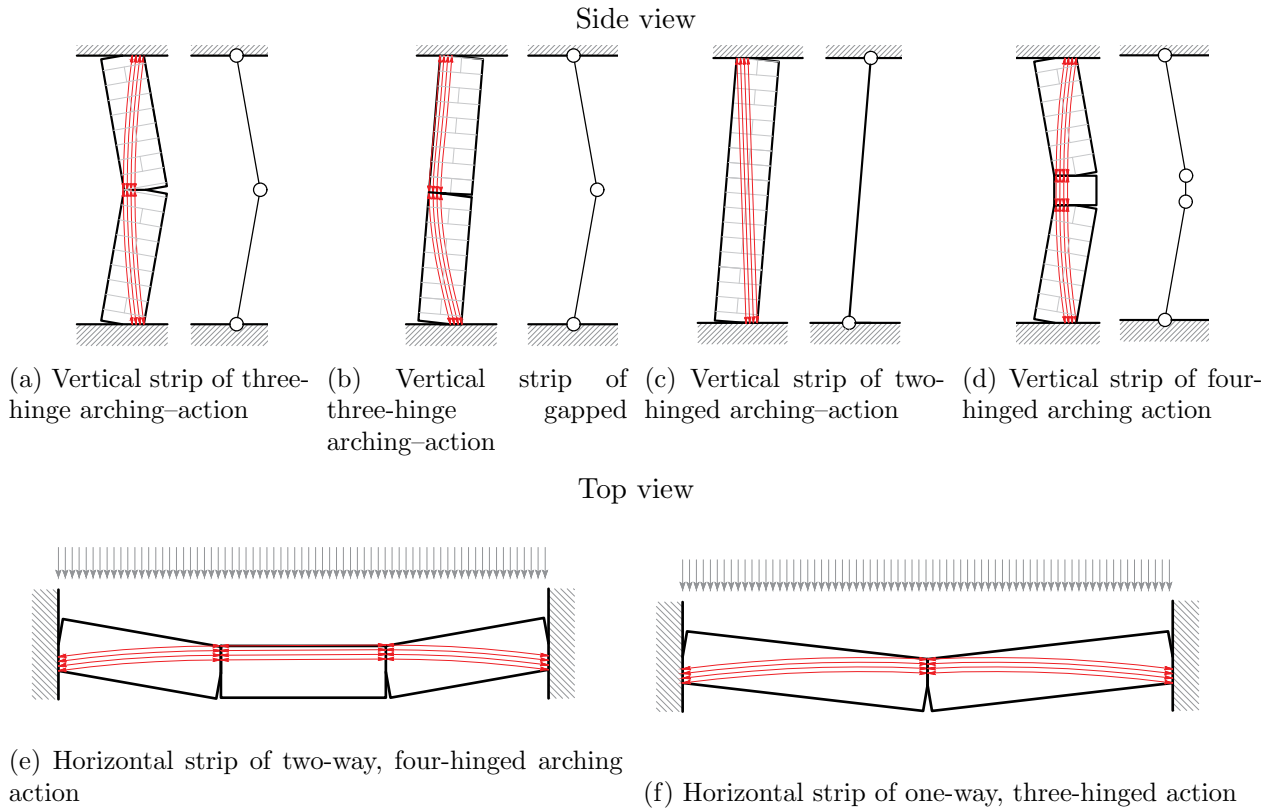


Figure 2.10: Observed arching action modes with their equivalent models

the loss to the load-bearing capacities (Fig. 2.11) and in some cases deformation capabilities (Fig. 2.11b). The fact that there is difference in reduction to no reduction in deformation capabilities between the same boundary conditions of Dawe and Seah (1989) versus Domenico et al (2018) (Fig. 2.11a vs. 2.11b) experiments can; perhaps, be a result of difference in slenderness. Whereas Dawe and Seah (1989) panels were much thicker when compared to Domenico et al (2018)'s. For the same reason, there is a significant difference in initial stiffness between the specimens of Dawe and Seah (1989) experiment, unlike those of Domenico et al (2018).

Since the arching action showed beneficial effects on the OoP behaviour the displacements were put in relation with infill walls height (drift ratio) and to its thickness d/t in Figure 2.12 and Table 2.14. Therefore, the OoP experiments showed great stability enduring drifts at about 3.52 % average. Yet, some did go near 9 % drift ratio (Ricci et al, 2018). Most research stopped the testing not due to collapse; rather, they were limited by equipment or targeting displacement. The relation with the thickness was pointed out as, to answer the question, will the deformations exceed the thickness of the infill wall $d/t > 1$. As showed, most did. Nevertheless, some reached the threshold at about the maximum force, while others were near the end of the loading procedure. Furthermore, the drift ratios were plotted in relation to the EN1998-1BSI (2005) limits where 0.50 % d_r is the limit for non-ductile and 0.75 % d_r is the limit for ductile, non-structural elements connected to the structure. The 1.00 % is for non-structural components that are not connected to the structure.

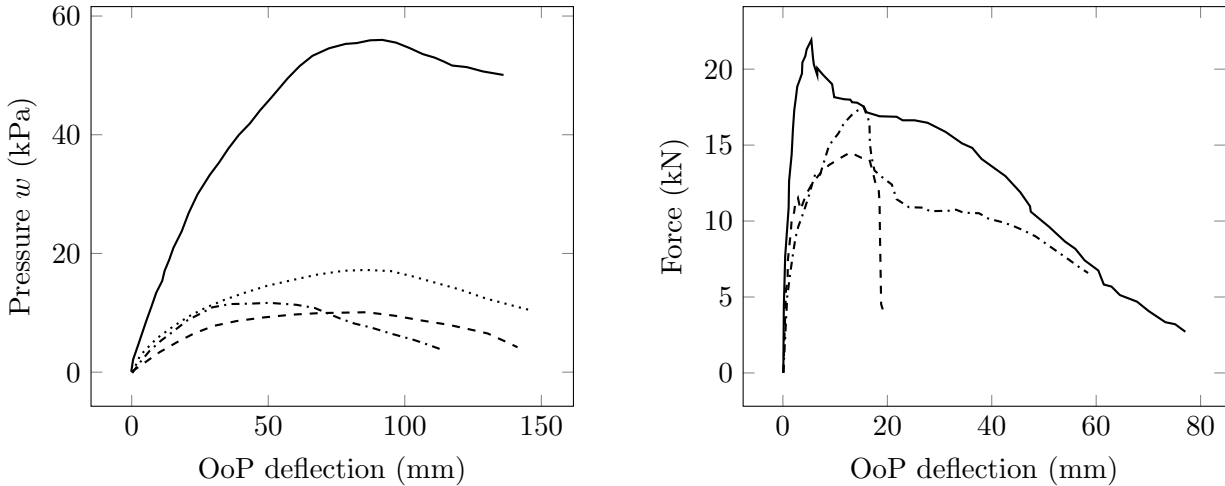
(a) Pressure *vs.* deflection (Dawe and Seah, 1989)(b) Force *vs.* deflection (Domenico et al, 2018)

Figure 2.11: Force-displacement curves of various boundary conditions

Table 2.14: Displacement relations by author

Research	d (mm)		d/t (%)		d_r (%)		Wall collapsed
	Max	End	Max	End	Max	End	
Dawe and Seah (1989)	91	136	101.1	151.1	3.3	4.9	?
Domenico et al (2018)	5	77	6.8	96.3	0.3	4.2	No
Akhoundi et al (2020)	24	80	21.8	72.7	1.5	4.9	?
Wang (2017)	12	12	13.3	13.3	1.2	1.2	No
Hak et al (2014)	53	75	15.1	21.4	1.8	2.5	No
Angel et al (1994)	33	63	68.4	131.4	2.0	3.9	No
Furtado et al (2015)	22	70	14.7	46.7	1.0	3.0	No
Average			34.47	76.13	1.57	3.52	

? - not specified

2.4 Openings

As mentioned, the presence of openings in IP studies resulted in lowering its overall bearing capacity and failure mechanism (Sigmund and Penava, 2014; Surendran and Kaushik, 2012; Tasnimi and Mohebkah, 2011; Kakaletsis and Karayannis, 2009). However, this is not so clear in the OoP studies. However, it must be stated that:

1. There were no systematic studies of openings (only single studies);
2. There were no inter-storey drift or dynamical load studies with openings, *i.e.* all had inertial load;
3. There were no eccentric openings tested.

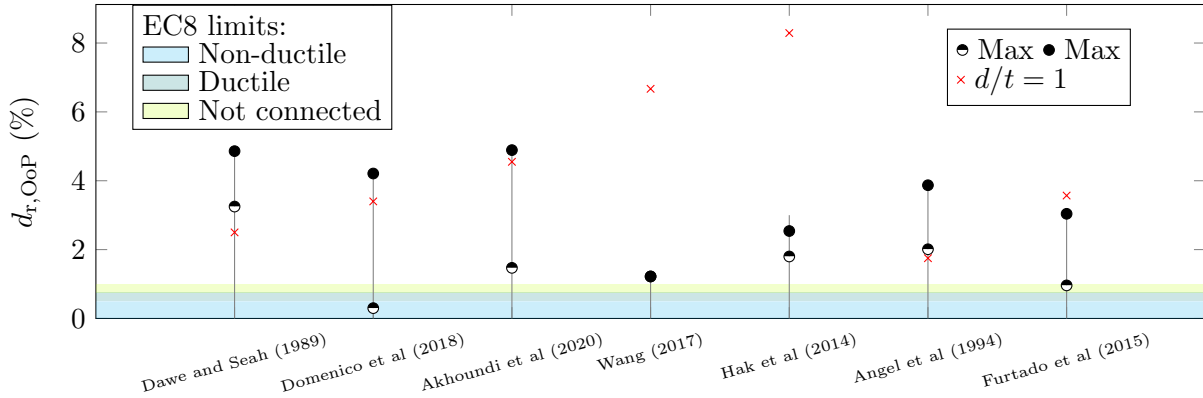


Figure 2.12: Achieved drift ratios sorted by researchers

All openings that were tested until the time of writing this thesis are displayed in Figure 2.3. Presumably, a similar window opening as in Fig. 2.3b was tested by Dawe and Seah (1989); however, figures or detailed descriptions are missing. For the same reason, a presumably similar full-height opening, as in Figure 2.3e, was tested by Verlato et al (2016).

Experimental campaigns showed that openings do result in the reduction of deformation capabilities, but not all agree if there is a reduction in load-bearing capacities (Fig. 2.14). For instance, Akhoundi et al (2016); Dawe and Seah (1989) showed that there is no reduction, while Wang (2017); Sepasdar (2017) the opposite (Fig. 2.14a *vs.* 2.14b). Note that Dawe and Seah (1989) research paper does not include a load-displacement graph. Rather, it is written that there is no significant difference; however, when comparing ultimate force between the two, the difference adds up to about 9 % (Dawe and Seah (1989), Tab. 5). In the case of full wall height opening, Hak et al (2014) paper nor anything published to the date of writing of this thesis does not provide any input in the behaviour of their specimen. On the other hand, the specimen from Verlato et al (2016) (Fig. 2.14c) shows a decrease in both load-bearing and deformation capabilities when compared to its counterpart; fully infilled frame, but with greater previous IP damage (2.4 % d_r). Therefore, the control specimen is not favourable, so extrapolated, one would expect the difference to be greater if there were no IP damage. Note that the vertical axis in Figure 2.14a was originally set as a pressure (q). However, for the sake of uniformity Figure 2.14, it was recalculated to a force (F) using Equation 2.1.

$$F = q(A_{\text{infill}} - A_{\text{opening}}) \quad (2.1)$$

Furthermore, all research agrees that the arching action was achieved; however, it was limited due to the presence of openings. The arching action effect is clearly visible when comparing displacement iso-area plot of fully infilled frame and that with a window opening (Fig. 2.13a *vs.* 2.13b). They are, in essence, very similar; however, with limited and off-centred displacements. This is also visible in the crack patterns of frames with openings in their infills. Furthermore, the existence of arching action is also visible in the cracking patterns between those with (Fig. 2.15) and without (Fig. 2.8) openings. Infill with door opening crack patterns from Figure 2.15a may not resemble any clear arching action mode. From one point of view, door opening creates a boundary condition where both sides of the wall cannot thrust on one side. Also, there is a separation between beam and infill. Therefore, boundary conditions may resemble double gapped action (Fig. 2.9c), where hinge and/or crack lines are nearly straight. Similarly, if one looks at the crack development stages from Mays et al (1998) research of load-bearing RC walls, it conveys an impression that the 1st crack

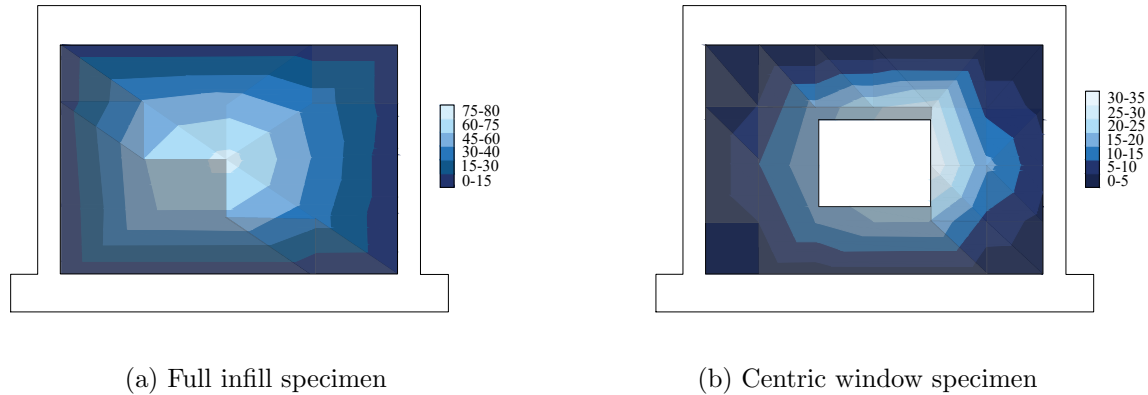


Figure 2.13: Displacement iso areas (colorbar in mm) from Akhoundi et al (2020)

divides the wall into two parts and forms seemingly different boundary conditions. Those newly formed boundary conditions resemble a double gapped (Fig. 2.9c) in the case of eccentric door (Fig. 2.16b). While in the case of both door and window opening (Fig. 2.16a), the double gapped arching action was developed between the two, as the rest of the cracks were diagonal.

Furthermore, Mays et al (1998) predicted the standard arching action crack/hinge patterns (Fig. 2.9) with full and gapped boundary conditions of wall with and without window opening (Fig. 2.17). This was tested and confirmed by the Griffith et al (2007) research as shown in Figure 2.17.

The reason behind different load-bearing capacities is debatable, as it can be in the scope of slenderness, aspect ratio, mechanical characteristics, lintel or others. Therefore, for the sake of clarification, this research did include some of the findings from load-bearing masonry (no frame). Firstly, Mays et al (1998) had load-bearing RC walls tested with inertial load to mimic the pressure from explosions. With both his physical and numerical findings Mays et al (1998) a linear change in ultimate load in relation to opening type was found (Tab. 2.19). Moreover, they found that there is also an increase in ultimate force with the increase of door size. Contrariwise, with the window opening, there is a certain decrease. It is to be noted that Akhoundi et al (2016) found that ultimate force increased by about 2 % in favour of infilled frame with window opening. The aforementioned relation from Mays et al (1998) was plotted along with the findings of infilled frames in Figure 2.18. It is visible that any logical outline cannot be derived.

2.5 The effect of slenderness and aspect ratio

Due to arching action phenomena, it is to be expected that aspect ratio would play a role. Furthermore, authors such as Moghaddam and Goudarzi (2010); Dawe and Seah (1989); Furtado et al (2018); Shapiro et al (1994) stated that slenderness might limit or bypass arching action. Along with the analogy of plate theory, slender plates have membrane dominant stresses, while thick ones are flexural.

There was no large scale test on the effects of slenderness; however, some findings can and were extracted from the literature and plotted in Figure 2.19. It is to be noted that the findings from Angel et al (1994), were grouped by matching masonry's compressive strength (f_m), identical mortar type (N - normal, L - lime) and previous IP drift. Furthermore, the shaded area marks a *special action* requirement as stated by BSI (2005). It states that any slenderness bigger than 15 should use some kind of infill strengthening, *e.g.* the application of: light wire meshes, wall ties fixed to the columns, wind posts and concrete belts (BSI, 2005). Conclusively, with an increase in

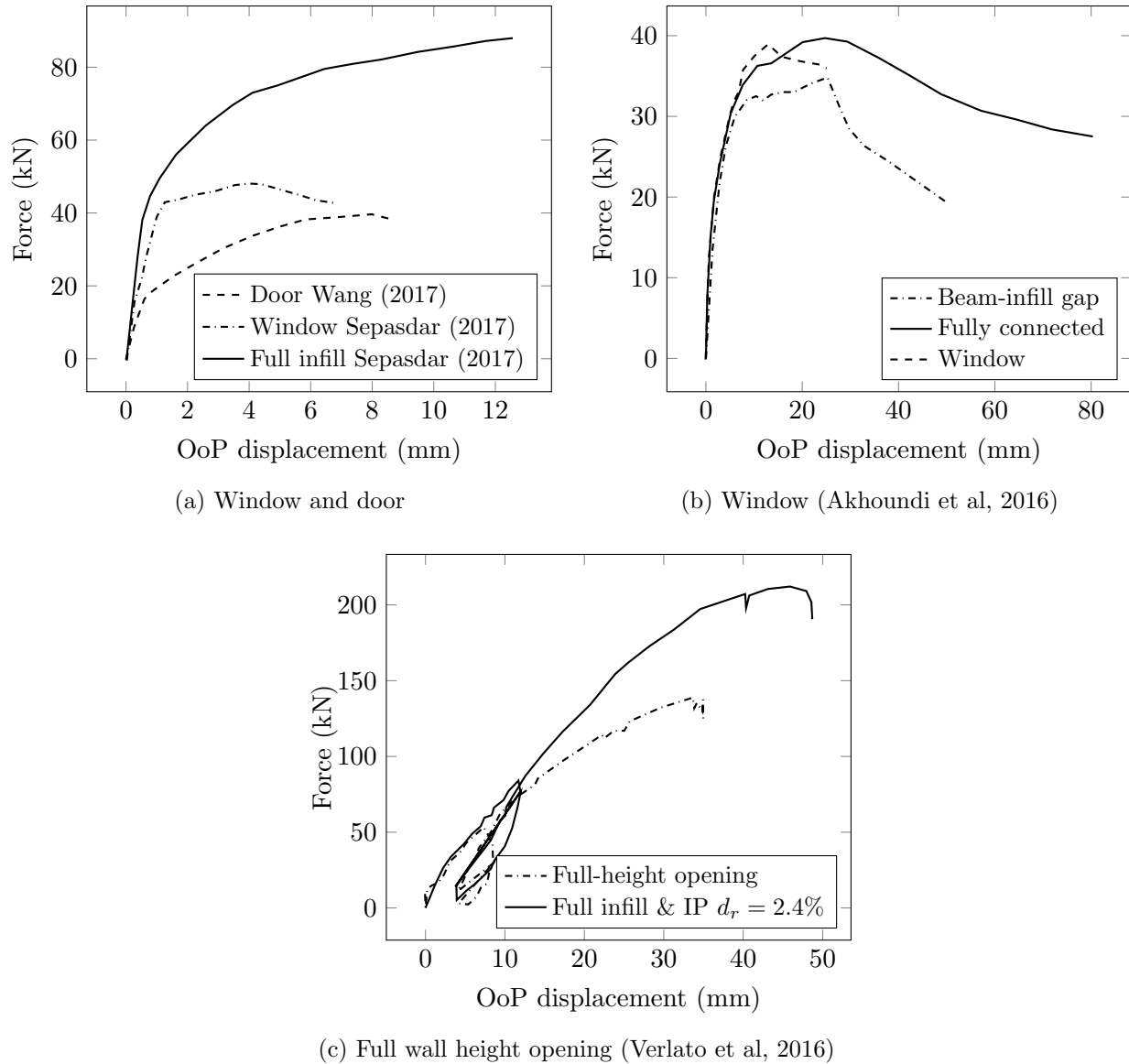


Figure 2.14: Force *vs.* displacement graphs of specimens with openings

slenderness, there is a decrease in ultimate load. This was implemented in the analytical formulas, where slenderness is one major factor in calculating load-bearing capacity (Sec. 2.8).

For instance Flanagan and Bennett (1999b) found that an increase of wall thickness from 100 to 200 mm (*i.e.* $h/t = 22 \rightarrow 11$) resulted in a three times greater ultimate force. In other words, the doubling of infill thickness tripled its OoP load-bearing capacity. Furthermore, Komaraneni et al (2011) had a combination of dynamical and inertial load tests that had frame fixed from OoP translations and added mass to the infill. They found that specimens with a higher degree of slenderness experienced higher acceleration amplification (inertial forces) with the maximum observed at the mid-height. Yet, less slender specimens acquired an almost linear profile of acceleration response along with the height. Albeit with the maximum value near the top.

Furthermore, there were no studies that directly studied the aspect ratio. However, few points were gathered or extrapolated from the literature. With an aspect ratio near to 1, it is expected that the “X” pattern would form (Fig. 2.17, bottom-right picture). So, the horizontal cracking between

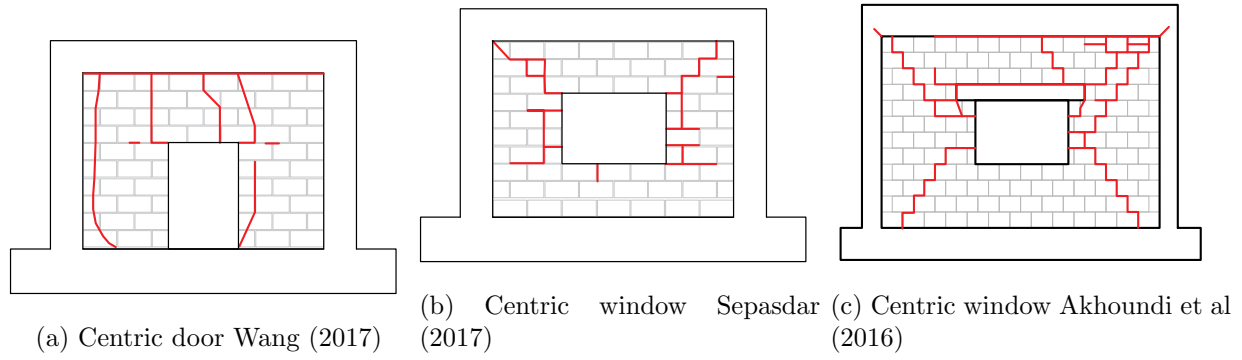


Figure 2.15: Failure patterns of OoP specimens with openings

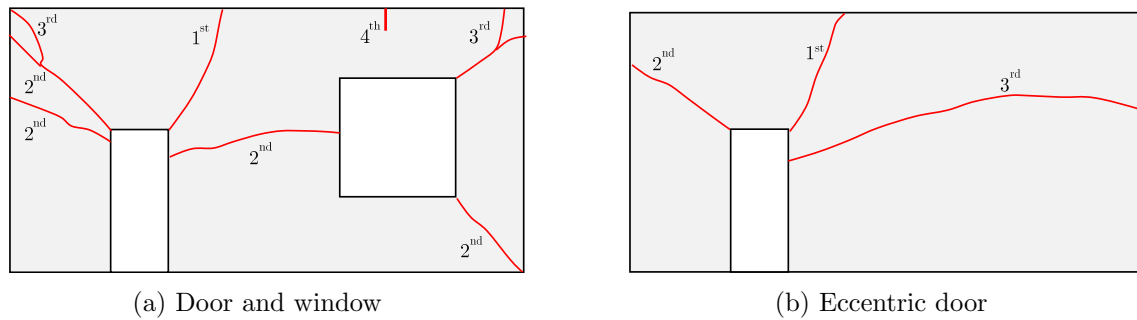


Figure 2.16: Results of the Mays et al (1998) URM wall test with designated crack occurrence

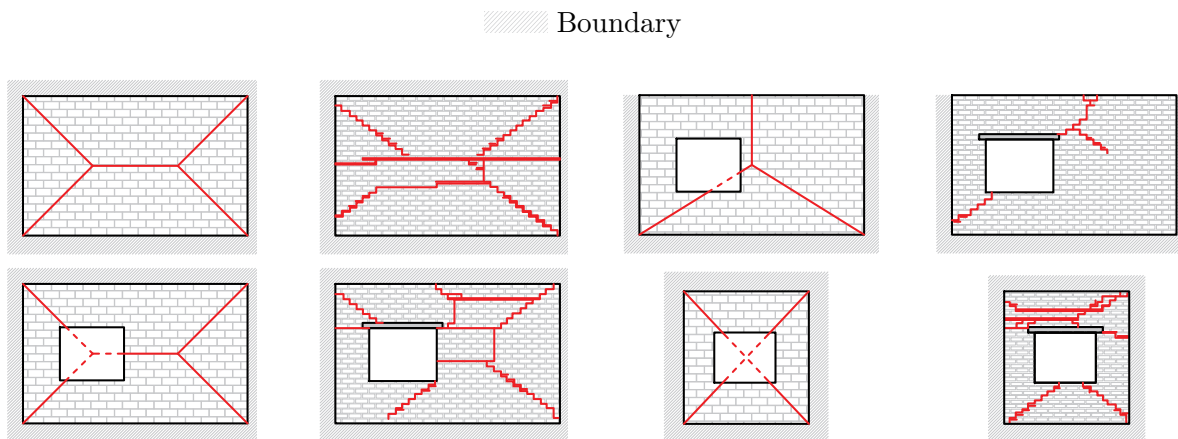


Figure 2.17: The Mays et al (1998) prediction of failures (straight and dashed lines) vs. Griffith et al (2007) experimental outcome of load-bearing walls.

the diagonal ones (Fig. 2.9a) does not develop. Also, by having a higher wall, a four-hinged arching action can be expected (Fig. 2.10d).

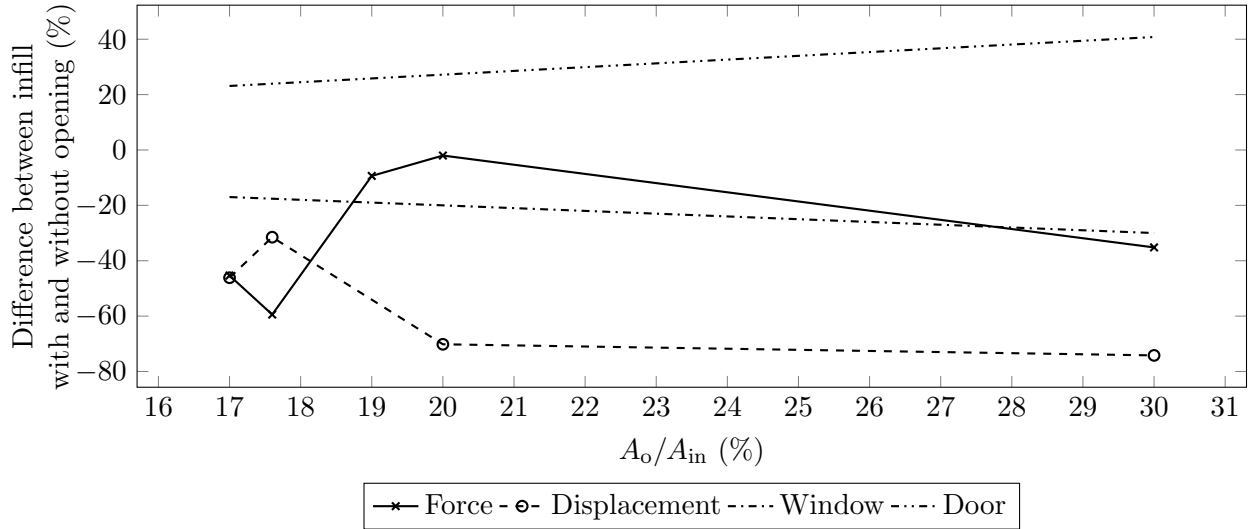


Figure 2.18: Opening to infill area ratio vs. difference in force and displacement from the fully infilled frame, window and door lines were extracted from Mays et al (1998)

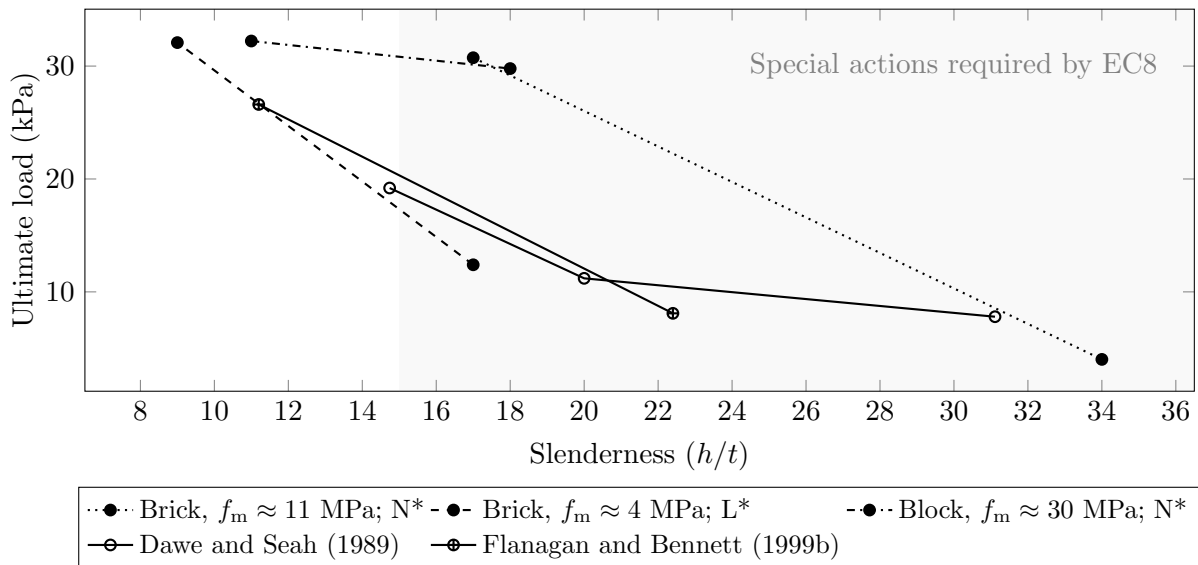


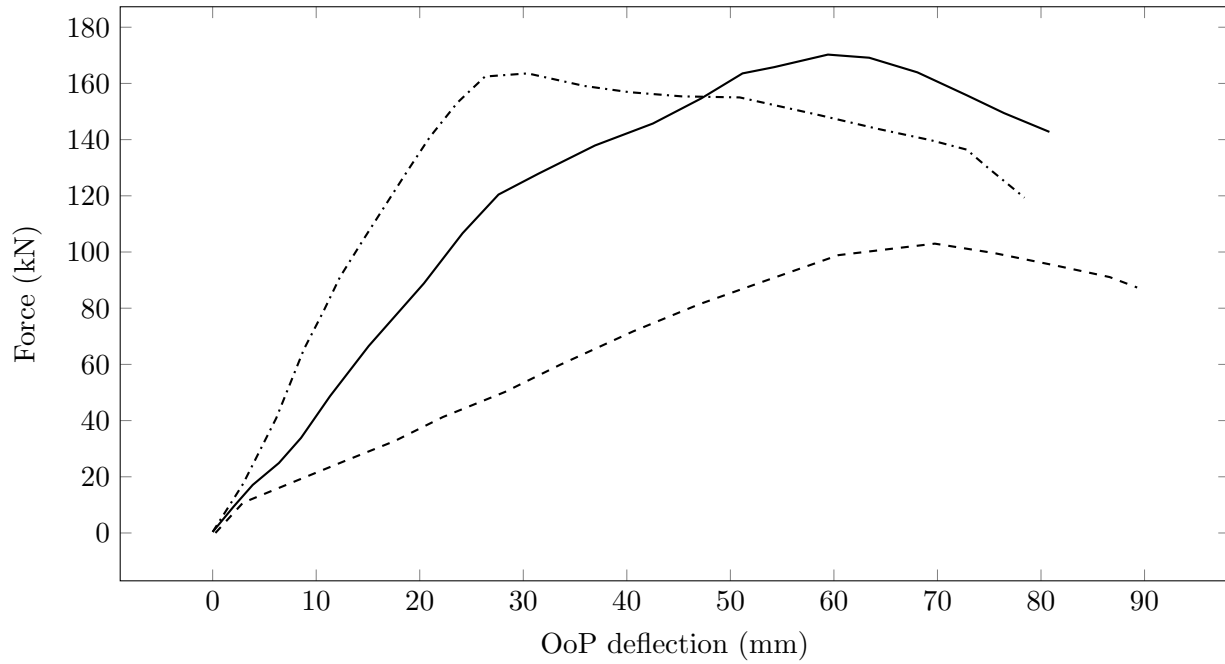
Figure 2.19: Effects of slenderness (*derived from Angel et al (1994))

2.6 Effect of combined in-plane out-of-plane loading

Roughly, half of experiments tested the effects of IP load (Fig. 2.4). Only Henderson et al (1993) and Flanagan and Bennett (1999b) tested previous OoP damage, while Misir et al (2016) and again Flanagan and Bennett (1999b) had simultaneous IP & OoP load.

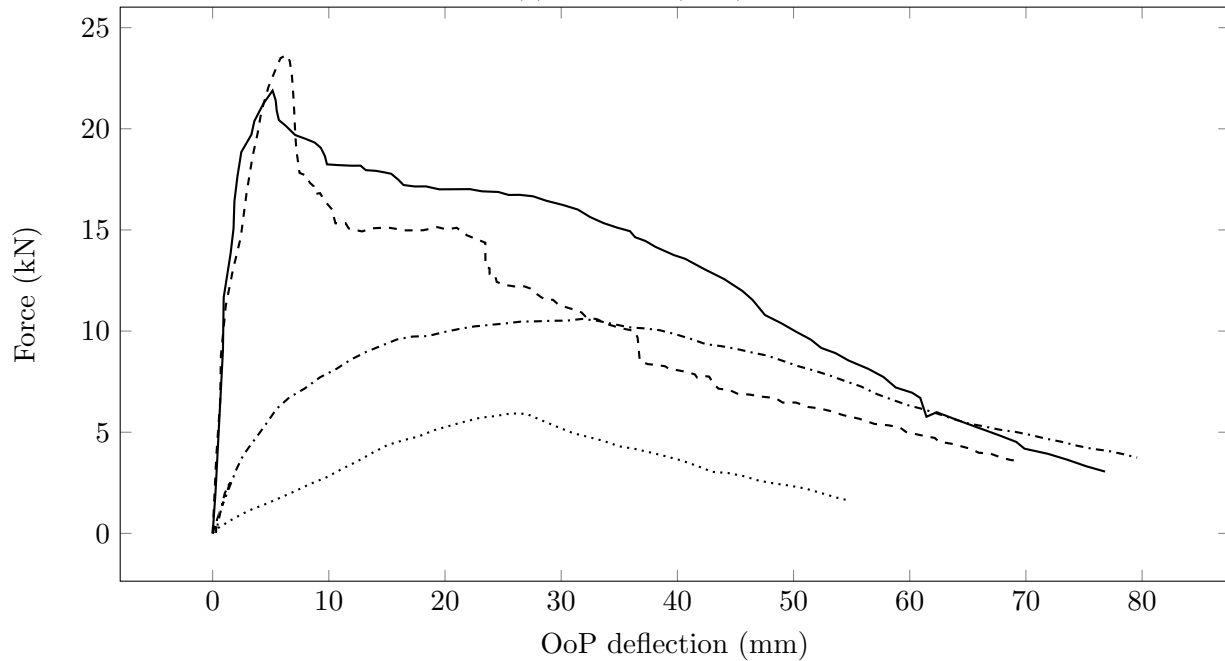
In the case of previous IP inter-storey drift damage, the frame is firstly loaded in IP direction until targeted inter-storey drift is achieved, then it is de-loaded and finally loaded in OoP direction. Various researchers found a reduction in both load-bearing capacity and initial stiffness as visible in Figure 2.20. Intuitively, due to cracking, the infill becomes softer. Therefore, with more considerable IP inter-storey drift there is, the more degradation of initial stiffness there will be *i.e.* a softer response. In terms of OoP capacity reduction, findings from various research were gathered,

recalculated in order to gain the reduction value; it was finally plotted in Figure 2.21.



$d_{r,IP}$ (%) | — 1.50 --- 2.50 1.00

(a) Hak et al (2014)



$d_{r,IP}$ (%) | — 0.00 --- 0.16 0.37 0.58

(b) Ricci et al (2018)

Figure 2.20: OoP force vs. displacement graphs with various previous IP inter-storey drifts

From the Figure 2.21 it is visible that reductions can add up to as much as 90 % for relatively small IP $d_r = 0.5$ % Ricci et al (2018), while on the other hand there was about 60 % reduction for a lower inter-storey drift of $d_r = 1.6$ % (Wang, 2017; Sepasdar, 2017). From the graph it is clear that there is no obvious pattern, and that the complexity of frames themselves dictate the reduction. Note that the question mark (?) in Hak et al (2014) curve is not a measured value; rather, their prediction.

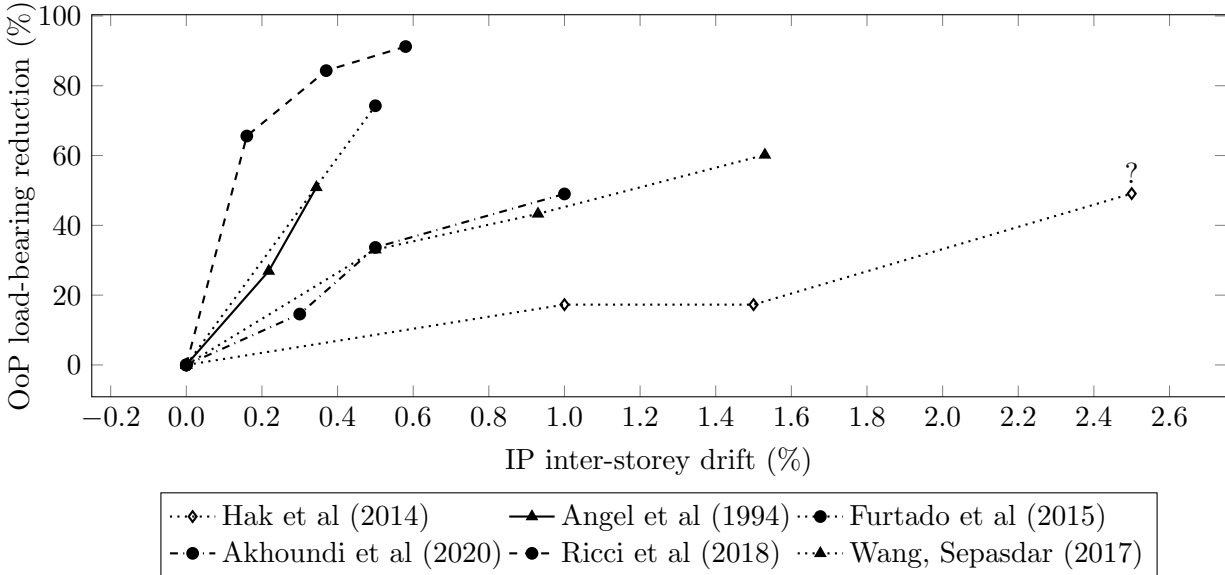


Figure 2.21: Reduction of OoP capacity by previous IP ISD as found by various researchers

By examining Figure 2.22 it is visible that the ingrained rigid arching action hinge line (Fig. 2.10e) pattern emerges from the cracks for IP inter-storey drift's of 0.16 and 0.37 %. Contrariwise, for the drift of 0.58 % unknown pattern is formed. The same is visible with other researches. Even though there is no clear pattern on the latter, the arching action is achieved, although limited, as visible in Figure 2.20b.

The research of OoP+IP by Flanagan and Bennett (1999b) was carried out in reversed order. That is, firstly the OoP inertial load was applied by pressurising the airbag, after reaching the targeted value it was de-pressurised. After that, the IP inter-storey drift cyclic, quasi-static load was applied. The study found that there are significant alterations to IP behaviour due to previous OoP load. Analogously to IP+OoP, due to cracking the compression strut is softer; thus resulting in limited IP response.

The simultaneous IP&OoP loading protocol was performed by Flanagan and Bennett (1999b); Misir et al (2016). Both concluded that even though heavy damage was observed, the specimens showed outstanding stability. This is certainly visible from the IP cyclic envelope derived from Flanagan and Bennett (1999b) in Figure 2.23. The exceptional stability can undoubtedly be attributed to the fact that arching action was formed due to inertial OoP load. Thus, it created additional compressive stress to the existing IP's compressive strut's stress, rendering the frame and infill both stable and stiff. The question arises as to would the behaviour be similar if the inertial force was cyclic rather than constant? Probably not, as the de-loaded infill would behave as OoP+IP protocol.

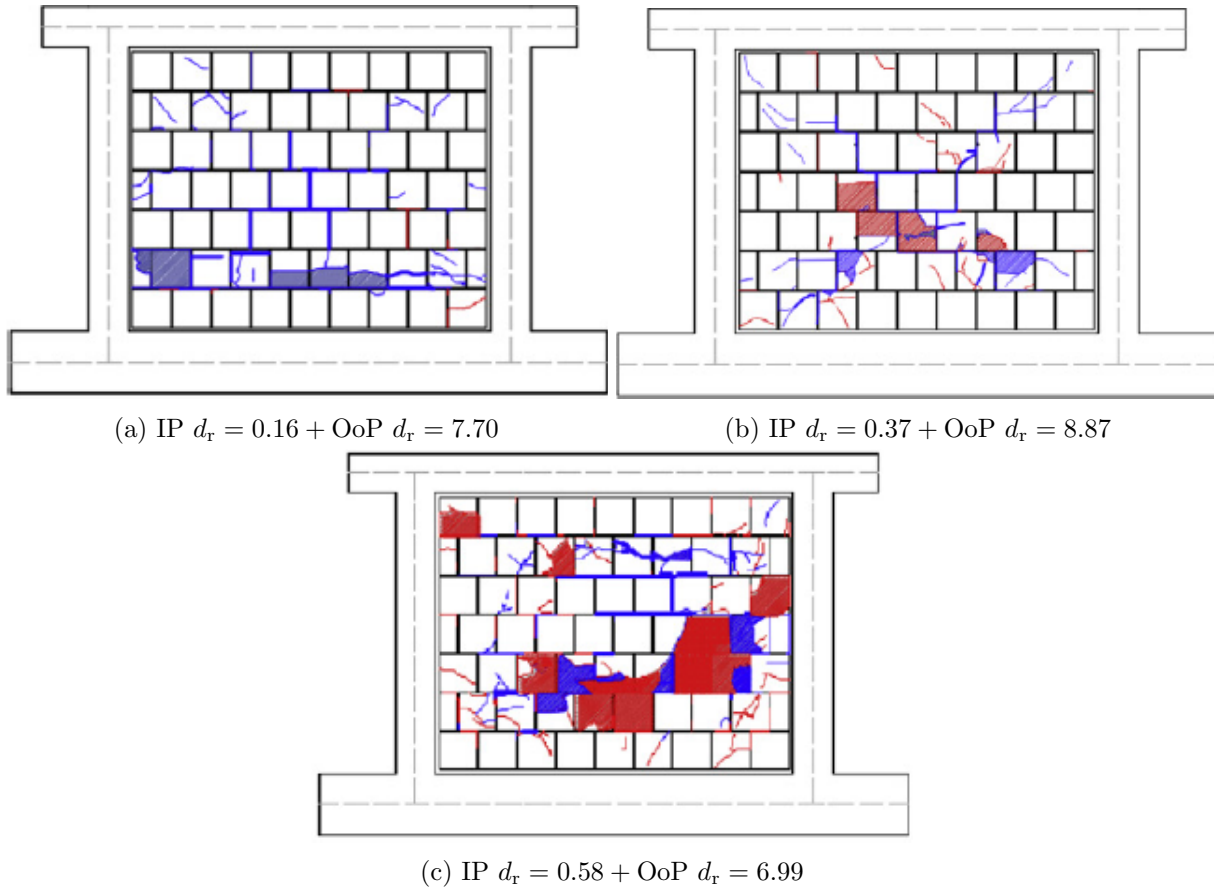


Figure 2.22: Ricci et al (2018) crack patterns from IP+OoP tests (d_r in %). Blue lines represent the OoP damage, while the red ones represent IP.

2.7 Contrasting outcomes of different load methods and protocols

Benedetti and Benzoni (1984) stated that during an earthquake event, there are two types of forces acting upon a building. Those are inertial and inter-storey drift forces, with the latter being more severe. The inertial forces occur by excited masses within a building. In the scope of infilled frames, such forces are dominant in the infill wall during the inter-storey drift on the frame. The inter-storey drift forces are transmitted into the structure through the movement of the slab (rigid diaphragm). So, it is clear that those two forces would provide contrasting results; moreover, another question arises as to how they compare to dynamical methods. The latter can be considered the closest simulation to the earthquake motions.

One can refer to the dynamical methods by Fowler (1994); Tu et al (2010) as they have the most detailed reports. Fowler (1994), had a two bay structural system with SS frames connected via slab and a truss at the ends (Fig. 2.25a). Similarly, Tu et al (2010) had a two bay structural system of RC frames, however, only connected by a thick RC slab (Fig.2.25b). Furthermore, Tu et al (2010) had 4 specimens with following properties: **PF** no panel; **B1** Single wythe confined masonry; **B2** double wythe confined masonry; **A1** single wythe infill.

Both Fowler (1994) and Tu et al (2010) found that the infill had similar or greater accelerations than the surrounding frame (Fig. 2.26b). Also, Fowler (1994) found that the highest acceleration occurs at the top and over two-thirds of infills height (Fig. 2.26a). This is a bit of surprise, as the

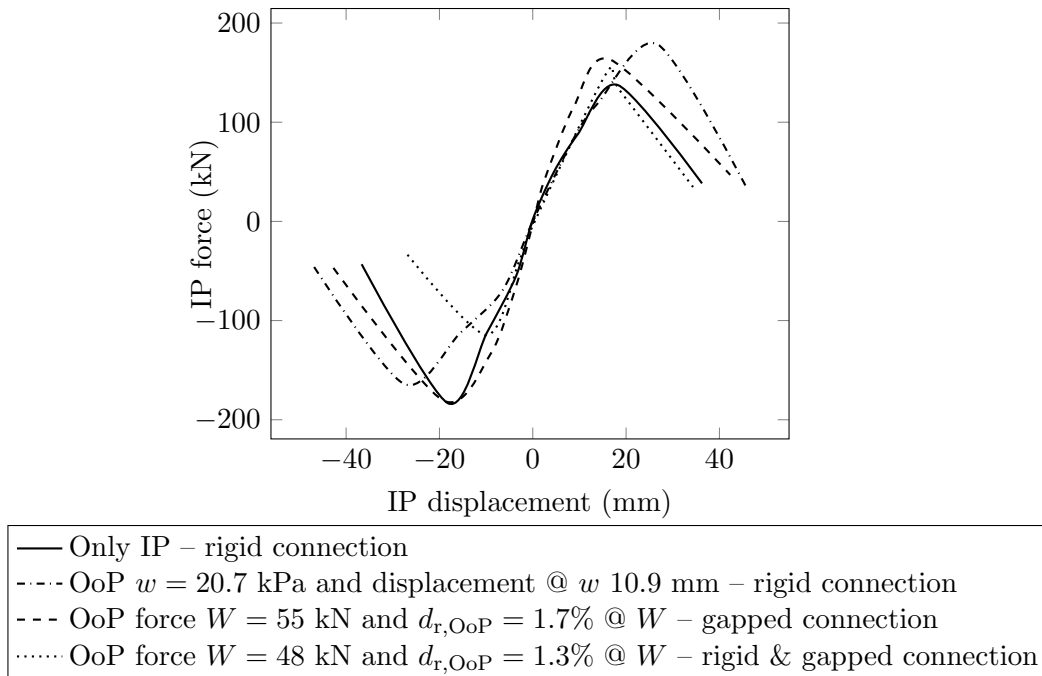


Figure 2.23: IP cyclic envelope of simultaneous IP&OoP loads derived from Flanagan and Bennett (1999b)

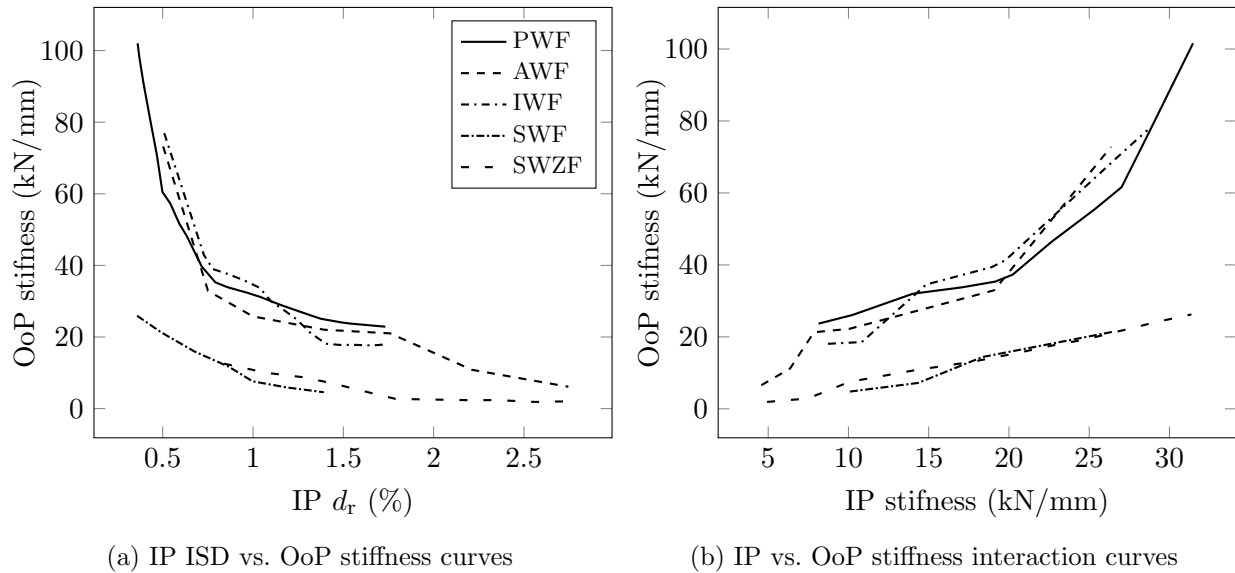


Figure 2.24: Stiffness degradation due to simulations IP and OoP load (Misir et al, 2016)

centre of the infills mass would be at its midpoint. This could most probably be addressed to the boundary conditions. Furthermore, these findings show a difference in inertial characteristics of frame and infill, which goes hand in hand with inertial force experiments. However, both the frame and infill moved together as a single unit. This is not concise with inertial force methods, as the frame is fixed from translation.

By examining the crack patterns caused by inertial force methods (Figs. 2.8, 2.15) and those of dynamical methods (Fig. 2.27b), it is clear that they are significantly different. Namely, the most

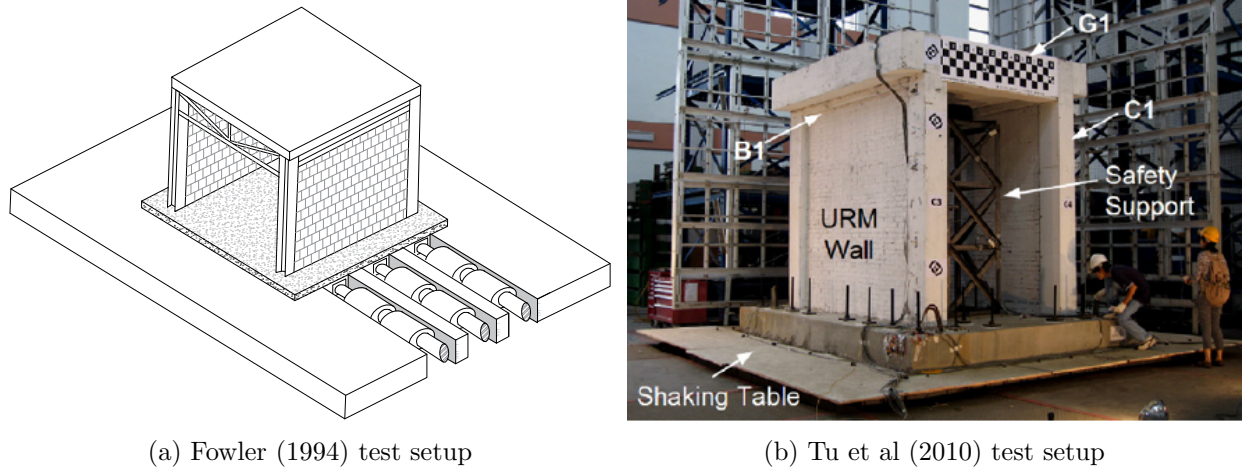


Figure 2.25: Examples of dynamical OoP test setups

obvious difference is that in the case of the dynamical method, the frame is more damaged in comparison to the inertial load methods, with the latter being more or less undamaged. Furthermore, the damage to the infill itself was different. In the case of the dynamical method, the crack or hinge lines developed on the bottom and in the upper third, consisting of mostly horizontal ones. While in the case of inertial loading, the infill was damaged with an “X” like pattern. Both points are beside the different loading methods, also the result is that in the case of inertial load, the frame is restrained from translation; hence, it cannot accumulate any significant amount of damage.

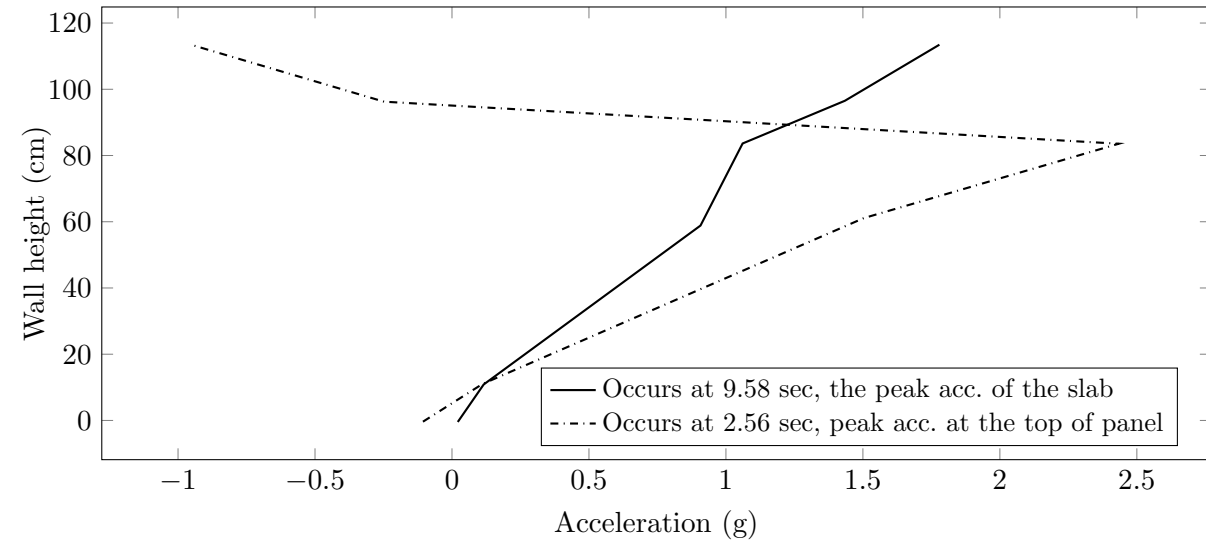
However, when dynamical is compared to the damage state of inter-storey drift method as displayed in Figure 2.28, it is evident that they are more similar. The damage was observed on the frame rather than the infill wall in both cases. Moreover, the crack patterns of the infill resemble each other.

In summation, one can conclude that inter-storey drift is more similar to the dynamical method and, therefore, with a real earthquake itself. However, the dynamical test was performed on single storey specimens. In those cases, inter-storey drift forces are more dominant, while inertial ones are on upper floors. Also, if there is a loss in connection with the surrounding frame, e.g. from IP loads, poor workmanship, an inertial force failure can occur even though the inter-storey drift ones were dominant. This was observed in Tu et al (2010) experiment (Fig. 2.27a). Hence, the behaviour is very complex.

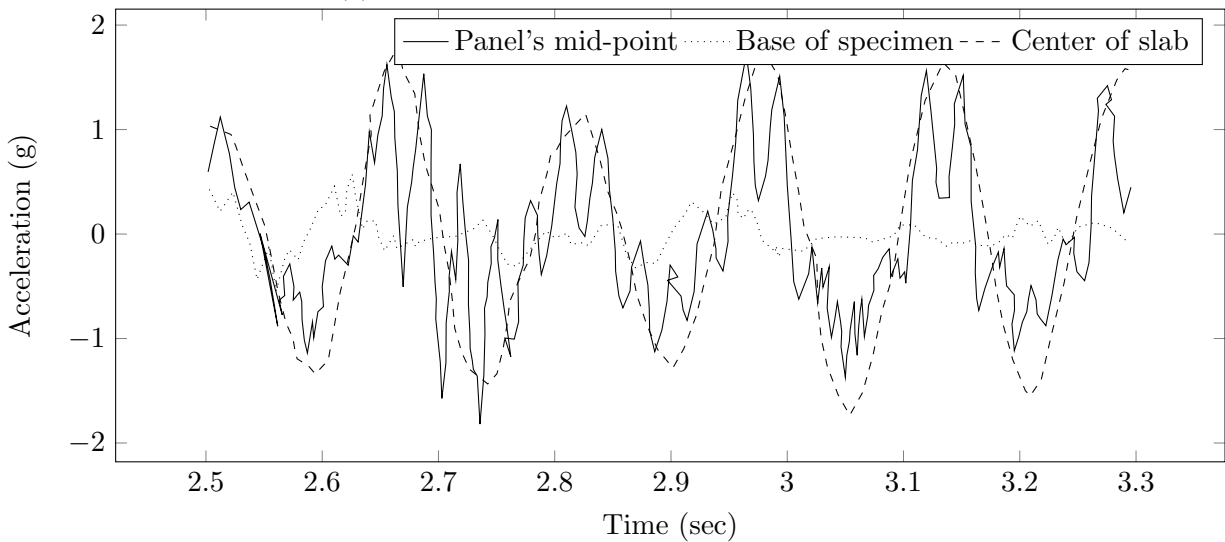
2.7.1 Additional findings

There are numerous findings in the field not covered in this literature review. Some of them that are relevant are listed below as they were not related to the previous sections:

1. Mortar type influences the OoP bearing capacity with inertial force methods (Shapiro et al, 1994). Moreover, Shapiro et al (1994) noted that the *lateral* is directly proportional to the *compressive strength* of mortar itself;
2. Tu et al (2010) concluded that there are no significant differences between OoP behaviour of confined and unconfined masonry infills;
3. Shapiro et al (1994) found that gravity load affected OoP stiffness up to the point where OoP forces overcame it. After which, there were no observable differences between the specimens



(a) Instantaneous accelerations vs. wall height



(b) Instantaneous accelerations vs. wall height

Figure 2.26: Structural acceleration results from the shaking table test by Fowler (1994)

with and without gravity load. Following, Furtado et al (2018) found that gravity load affected the crack patterns in its shapes and development. Note that both research teams applied gravity load to columns;

4. Wang (2017) compared the effects of the surrounding RC frame with that of structural steel (SS) tested by Sepasdar (2017). Both had identical infills and loading methods. He found that in the case of SS frame, there was about 40% less cracking and ultimate load dropped by 48%. Furthermore, it was found that the SS frame also had 83% lower ultimate and cracking stiffness and only 57% in the RC frame. Wang (2017) stated that such differences might be attributed to the fact that the flange acted as a flexural steel plate that increased twisting. Also, the RC beam was clamped to the floor, and the steel frame was clamped on two steel beams that might have allowed additional deflections and rotations. Nevertheless, it

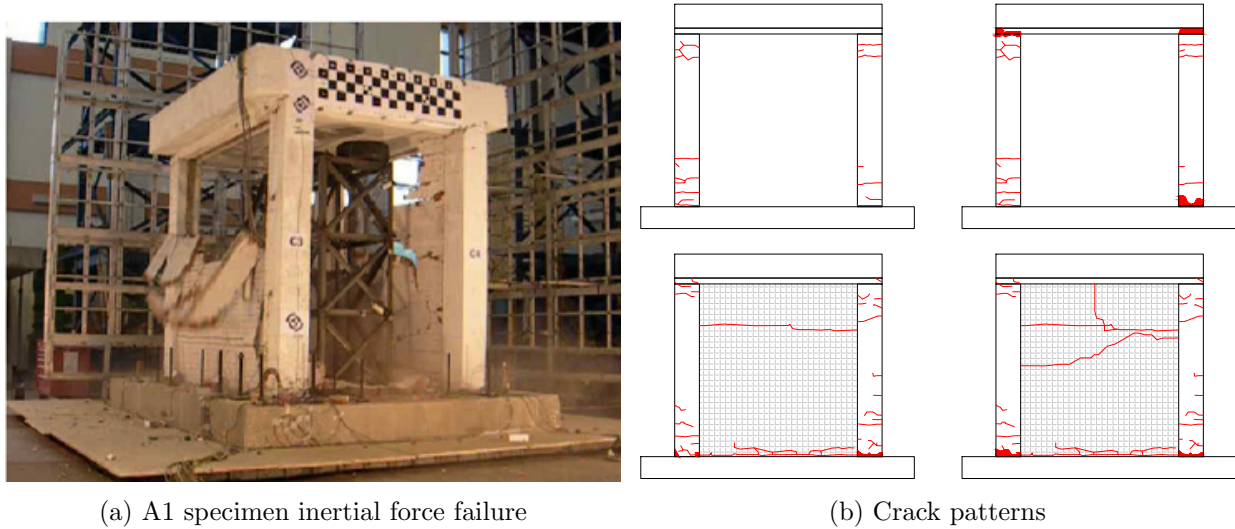


Figure 2.27: Failure modes from Tu et al (2010) experimental campaign

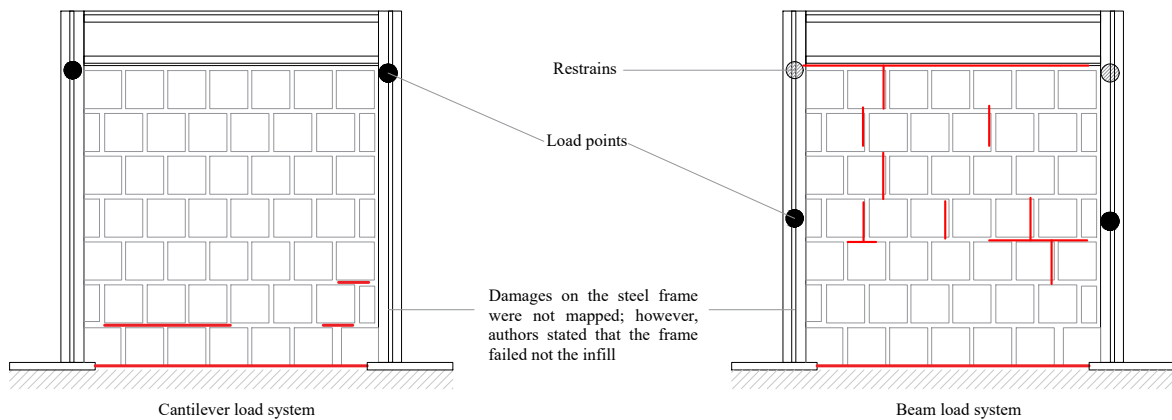


Figure 2.28: Flanagan and Bennett (1999b) damage state of ISD method

demonstrated that boundary conditions contribute mainly to the behaviour of superstructure.

2.8 Analytical models

This section covers all relevant analytical models as published by the year 2020. *Relevant models* refer to those that were done based on infilled frame experiments, while those of load-bearing masonry were excluded with few exceptions. In addition, *flexural based models* as those from Drysdale and Essawy (1988); Haseltine (1976); Hendry (1973) were also discarded, as the arching action rather than flexural is the prevalent effect occurring with the inertial loads. For more information on flexural models, refer to the paper by Asteris et al (2017). Notably, there is also a series of equations of walls load bearing on impact force on walls proposed by Hobbs et al (1994), and an equation for retrofitted infills to blast load by Hrynyk and Myers (2008). Both of them were excluded from this research.

Furthermore, the researcher covered the parametric sensitivity analysis to gain insight into the

reliability, governing factors, stability and equations limits.

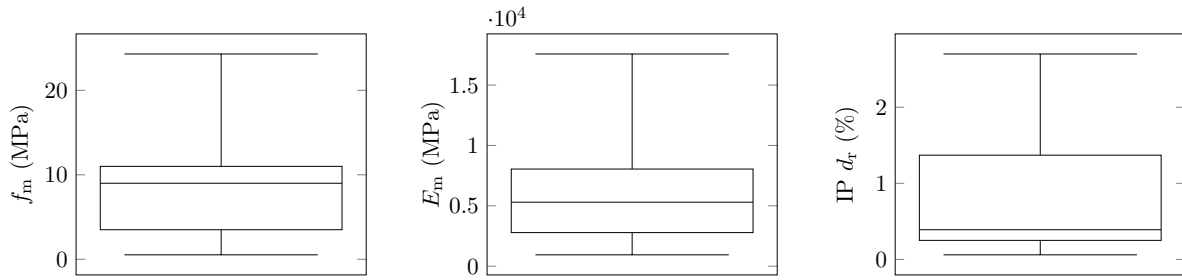
The blast engineering field firstly developed the analytical models by the same research group that discovered arching action theory (McDowell et al, 1956b,a). Firstly, the flexural theory was used; however, it provided six-fold reduced capacities. After the arching action effect was found, the Equation 2.2 based on the vertical three-hinged arch was formulated. From there, similar methods and equations were developed both in the blast and seismic engineering field.

$$w = \gamma \frac{f_m}{2(h/t)^2} \quad (2.2)$$

where γ depends on the h/t ratio.

It is to be noted that there were no equations developed in attribution with the inter-storey drift nor dynamical methods. Also, all equations encompass only vertical, three-hinged arch.

All relevant models are displayed in Table 2.15, while parameters needed for the parametric analysis are displayed in Table 2.16. The range of some parameters are displayed as a box plot in Figure 2.29. The equations developed for the calculation of maximum OoP displacement are displayed in Table 2.17.



(a) Distribution of masonry's compressive strength (b) Distribution of masonry's elastic modulus (c) Distribution of previous IP inter-storey drift

Figure 2.29: Distribution of mechanical properties from Tab. 2.16

Dawe and Seah (1989) were the first researchers to develop an equation for calculating the load-bearing capacity of infilled frames. They developed two sets of equations, one for rigid (Eq. 2.4) and second for gapped arching action (Eq. 2.3). They have incorporated the effects of the frame, namely through columns (α) and beams (β) axial and torsional stiffness. Conversely, in gapped arching action, the effects of the beam were left out. Note that they are the only authors to also include the torsional capabilities of the surrounding frame.

Angel et al (1994) were the first to incorporate effects of previous IP damage through R_1 factors in the Equation (2.5). These factors can be determined visual as suggested in Figure 2.30 or by the use of the Equation (2.17). However, the use of the latter is somewhat complicated as a designer should know the required displacements. The R_2 factor takes the surrounding frame and boundary conditions into account.

Table 2.15: Analytical models developed for the estimation of infilled frame OoP capacity (Anić et al, 2019b)

#	Author	Load-bearing capacity equation	Action	Remark																																
1	Dawe and Seah (1989)	$w_1 = 0.8 \frac{f_m^{0.75} t^2 \alpha}{l^{2.5}}$ $w_2 = 0.8 f_m^{0.75} t^2 \left(\frac{\alpha}{l^{2.5}} + \frac{\beta}{h^{2.5}} \right)$	<p>(1.3) Gapped (w_1); $\alpha \leq 75$</p> <p>(1.4) Rigid (w_2); $\alpha \leq 50$</p>	$\alpha = \frac{1}{h} (E_{fc} h^2 + G_{fc} t h)^{0.25}$ $\beta = \frac{1}{l} (E_{fb} l^2 + G_{fb} t l)^{0.25}$																																
2	Angel et al. (1994)	$w = R_1 R_2 \frac{2 f_m \lambda}{h/t}$	<p>(1.5) Rigid or Gapped (depends on R_2)</p>	<p>R_1, by damage state (Fig. 25)</p> <table border="1"> <thead> <tr> <th>h/l</th> <th>λ</th> <th>Moderate</th> <th>Severe</th> </tr> </thead> <tbody> <tr> <td>5</td> <td>0.129</td> <td>0.997</td> <td>0.994</td> </tr> <tr> <td>10</td> <td>0.060</td> <td>0.946</td> <td>0.894</td> </tr> <tr> <td>15</td> <td>0.034</td> <td>0.888</td> <td>0.789</td> </tr> <tr> <td>20</td> <td>0.021</td> <td>0.829</td> <td>0.688</td> </tr> <tr> <td>25</td> <td>0.013</td> <td>0.776</td> <td>0.602</td> </tr> <tr> <td>30</td> <td>0.008</td> <td>0.735</td> <td>0.540</td> </tr> <tr> <td>35</td> <td>0.005</td> <td>0.716</td> <td>0.512</td> </tr> </tbody> </table> <p>Alternatively, R_1 can be calculated using Eq. 17 In case of a gap: $R_2 = 0.357 + 2.488e-5 E_f l$ (use kN/m²) If $R_2 > 1 \Rightarrow R_2 = 1$ In case of no gap (fully bounded wall) $R_2 = 1$</p>	h/l	λ	Moderate	Severe	5	0.129	0.997	0.994	10	0.060	0.946	0.894	15	0.034	0.888	0.789	20	0.021	0.829	0.688	25	0.013	0.776	0.602	30	0.008	0.735	0.540	35	0.005	0.716	0.512
h/l	λ	Moderate	Severe																																	
5	0.129	0.997	0.994																																	
10	0.060	0.946	0.894																																	
15	0.034	0.888	0.789																																	
20	0.021	0.829	0.688																																	
25	0.013	0.776	0.602																																	
30	0.008	0.735	0.540																																	
35	0.005	0.716	0.512																																	
3	Klinger et al. (1996)	$W = 8 \frac{M_{yv}}{h} (l-h) + 8 \frac{M_{yh}}{h} \ln(2) \left(\frac{x_{yv}}{x_{yh}} \right) \ln \left(\frac{l}{l-h/2} \right)$	Rigid	$x_{yv} = \frac{t f_m}{1000 E_m \left(1 - \frac{h}{2\sqrt{(h/2)^2 + l^2}} \right)}$ $M_{yv} = (0.85 f_m / 4) / (t - x_{yv})^2$																																
4	Flanagan and Bennett (1999a)	$w_2 = 0.73 f_m^{0.75} t^2 \left(\frac{\alpha}{l^{2.5}} + \frac{\beta}{h^{2.5}} \right)$	Rigid	$\alpha = \frac{1}{h} (E_{fc} h^2)^{0.25}$ $\beta = \frac{1}{l} (E_{fb} l^2)^{0.25}$ <p>If $h/t < 8 \rightarrow t = h/8$</p>																																
5	EC 6 BSI (2005)	$w = f_m (t/a)^2$	Rigid	Use if $t/a < 20$; a is l or h																																
6	Drysdale and Hamid (2005)	$w = \min \left\{ \frac{0.61 f(t/h)^2}{0.61 f(t/l)^2} \right\}$	Rigid	$f_j = \min\{f_m, f_{c, mortar}\}$																																
7	FEMA 356 (2000)	$w = 0.7 \frac{f_m^{1.2}}{h/t}$	Rigid	h/t 5 10 15 25																																
8	Moghaddam and Goudarzi (2010)	$w = \min \left\{ \begin{aligned} w_{cr} &= \frac{0.85 f_m}{(h/t)^2} - \left(\frac{0.12 + \frac{0.45 f_m}{\alpha}}{E_m} \right) \frac{f_m}{E_m} \\ w_{max} &= \frac{0.18 E_m}{(0.12 + 0.045/\alpha)(h/4)^4} \end{aligned} \right.$	<p>w_{cr} crushing failure</p> <p>Rigid</p> <p>w_{max} transverse instability failure</p>	$\alpha = \frac{384 E_{fb} h}{E_m t l^4}$																																
9	Morandi et al. (2013)	$w = \left(0.72 \left(\frac{t}{h} \right)^2 f_m + 7.2 \frac{t}{l h^2} A_s f_y \right) \beta$	Rigid	$\beta = \begin{cases} r & d_w \leq d_m \\ 0 & d_m < d_w < d_u \\ 1 & d_w > d_u \end{cases}$ <p>For values of r, d_m and d_u see Tab. 9</p> <p>A_s: area of vertical reinforcement in tension, f_y: yield strength</p>																																
0	Ricci et al. (2018)	$w = 1.95 \frac{t^{1.59}}{f_m^{0.3}} \frac{5}{h^{2.96}}$	Rigid	(1.13)																																

Note: Use MPa and mm. The output of equations is in MPa. * For calculation of x_{yh} , replace h with l in x_{yv} equation. For calculation of M_{yh} , replace x_{yv} with x_{yh} ; d_w : expected IP drift

Table 2.16: Various geometrical and mechanical properties of specimens

Author	Specimen	t (mm)	l (mm)	h (mm)	Frame type	Column size (mm×mm)	Beam size (mm×mm)	f_m (MPa)	E_m (MPa)	E_F (MPa)	Capacity w (kPa)	Displacement (mm)	Remark
Dawe and Seah (1989)	WE1	190									22.30	n/a	Trust type joint reinforcement
	WE2	190									19.20	n/a	Plain masonry panel
	WE3	190									7.80	n/a	dry-stack panel
	WE4	140									11.20	n/a	Plain masonry panel
	WE5	90	3600	2800	SS	W250 × 58	W200 × 46	24.3	17575	210000*	7.80	n/a	Plain masonry panel
	WE6	190									10.60	n/a	Plain masonry panel
	WE7	190									14.70	n/a	Truss type joint reinforcement
	WE8	140									13.40	n/a	Restraints against slipping
	WE9	190									17.40	n/a	Window opening
Angel et al (1994)	1	48						11.50	8046		8.19	n/a	Pure OoP, S mortar
	2	48						10.81	8046		4.02	n/a	IP (0.34% d_t) + OoP, N mortar
	3	48						10.14	5212		5.99	n/a	IP (0.22% d_t) + OoP, Lime mortar
	4	92						22.90	12438		29.78	n/a	IP (0.09% d_t) + OoP, N mortar
	5	143	2740	1630	RC	305×305	203×254	21.46	11624	24821	32.22	n/a	IP (0.06% d_t) + OoP, N mortar
	6	98						4.59	2137		12.40	n/a	IP (0.25% d_t) + OoP, Lime mortar
	7	98						11.00	2923		30.74	n/a	IP (0.25% d_t) + OoP, N mortar
	8	187						3.50	2358		32.08	n/a	IP (0.39% d_t) + OoP, Lime mortar
Flanagan and Bennett (1999b)	25	100				W250 × 45	W310 × 52				8.10	25.30	Plain masonry panel
	18	200				W250 × 45	W310 × 52	5.60	5300		26.60	11.50	Plain masonry panel
	19	200	2240	2240	SS	W250 × 45	W310 × 52			199948	21.70	19.30	IP (0.8% d_t) + OoP
	22	330				W410 × 60	W460 × 113	2.29	5040		39.50	49.50	Plain masonry panel
Hak et al (2014)	TA1										13.25	n/a	IP (1.50% d_t) + OoP
	TA2	235	4220	2950	RC	350×350	350×350	4.64	5299	32000*	8.11	n/a	IP (2.00% d_t) + OoP
	TA3										13.01	n/a	IP (1.00% d_t) + OoP
Alkhoundi et al (2015)	SIF-A										8.86	25.00	Beam - infill gap
	SIF-B	110	2415	1635	RC	160×160	270×160	1.00	1000*	32000*	10.13	12.00	Plain masonry panel
	PIF-A										9.88	25.00	Window opening
Furtado et al (2015)	inf.01										7.76	22.00	OoP monotonic + gravity load
	inf.02	150	4200	2300	RC	300×300	300×500	0.53	941.9	24300	7.25	12.00	OoP cyclic
	inf.03	150+110									1.76	1.50	OoP cyclic + IP (0.5% d_t), 2 leafed
Sepasdar (2017)	IF-W										43.70	4.30	Window opening
	IF-ND										66.30	12.50	Plain masonry panel
	IF-D1	90	1350	980	RC	180×180	180×180	9.00	7650	16911	44.40	6.60	IP (0.66% d_t) + OoP
	IF-D2										26.40	9.90	IP (2.70% d_t) + OoP
Wang (2017)	IF-RC-DO										36.20	7.90	Door opening
	IF-RC-TG										18.50	3.90	Beam - infill gap
	IF-RC-SG				RC	180×180	180×180	9.00	7650	16911	36.50	7.40	Columns - infill gaps
	IF-RC-ID	90	1350	980							37.60	7.70	IP (1.37% d_t) + OoP
Domenico et al (2018)	IF-S				SS	W150 × 30	W150 × 30			201172	34.30	15.10	Steel frame
	OOP_4E										4.09	5.40	All bounded
	OOP_3E	80	2350	1830	RC	200×270	200×270	1.80	1517	32000*	3.39	14.60	Beam - infill gap
	OOP_2E										8.42	17.00	Columns - infill gaps

* Estimated

Table 2.17: Analytical solutions for ultimate OoP displacement

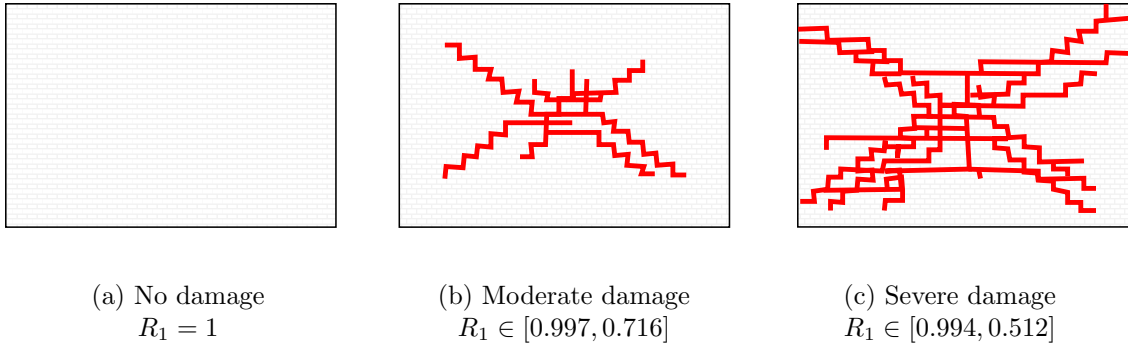
#	Author	Ultimate displacement	Remark
1	Klingner et al (1996)	$x_y = \frac{t f_m l}{1000E \left(1 - \frac{h}{2\sqrt{(h/2)^2 + t^2}} \right)}$ (2.14)	
2	FEMA 273 (1997)	$d = \frac{0.002h^2/t}{1 + \sqrt{1 - 0.002(h/t)^2}}$ (2.15)	For $h/t \leq 22.3$
3	Flanagan and Bennett (1999b)	$d = \frac{0.002h^2/t}{1 + \sqrt{1 - 0.001(h/t)^2}}$ (2.16)	For $h/t \leq 31.6$

$$R_1 = 1 \text{ if } \frac{\delta}{2\delta_{cr}} < 0.5 \text{ i.e. undamaged state}$$

else

$$R_1 = \left[1.08 - 0.015 \frac{h}{t} - 0.00049 \left(\frac{h}{t} \right)^2 - 0.000013 \left(\frac{h}{t} \right)^3 \right] \frac{\delta}{2\delta_{cr}} \quad (2.17)$$

where δ is the maximum IP displacement and δ_{cr} is the displacement at the cracking load

Figure 2.30: Damage states for R_1 factor (Angel et al (1994))

Klingner et al (1996) developed an Equation (2.6) based on Bashandy (1995) model for load-bearing wall. Klingner et al (1996) refined the equation on the observations of infill frame experiments. However, the effects of the frame were not incorporated. From Equation (2.6), another can be derived for the calculation of peak OoP displacement (Eq. 2.14). Furthermore, the equation was based on both horizontal and vertical arching action. Therefore, if one arching direction is removed, the remainder equations (Eq. 2.18 & 2.19) could be the first in an attempt to comprehend double-gapped arching action.

$$W_{yv} = \frac{M_{yv}}{h}(l - h) \quad (2.18)$$

$$W_{yh} = 8 \frac{M_{yh}}{h} \ln(2) \left(\frac{x_{yv}}{x_{yh}} \right) \ln \left(\frac{l}{l - h/2} \right) l \quad (2.19)$$

where W_{yv} can be used for infill with both columns disconnected, and W_{yh} for infill with both beams disconnected.

Flanagan (1994) developed the Equation (2.7) that is the modified version of rigid arching action equation formulated by Dawe and Seah (1989) (Eq. 2.3). The modifications were to the first constant, value of 4.5 was hanged to 4.1; followed by the removal of torsional effects from both column and beam stiffness. Additionally, Flanagan and Bennett (1999b) modified the FEMA 273 (1997) equation of peak deflection by changing the constant of 0.002 to 0.001 under the square root (Eq. 2.15).

BSI (2004b) gives straightforward Equation 2.8 for brickwork, that is only depended on its slenderness and compressive strength.

Drysdale and Hamid (2005) provide a plain Equation (2.9) for load-bearing brickwork similar to aforementioned BSI (2004b) Equation (2.8). The equation itself is unique, because it calls upon the use of compressive strength either from mortar or brick. Furthermore, the authors also included calculating the bearing capacity of gapped arching action and axial shortening of the infill. However, the method is complex as it requires the data of hardly obtainable parameters, *e.g.* mid-span deflection, the height of an arch, length of the compressive force, *etc.* Hence, it was not included in this overview.

FEMA 356 (2000); FEMA 273 (1997) Equation 2.10 used a simplified version of Angel et al (1994) equation (Eq. 2.5), as published by the same authors in Abrams et al (1996). The simplification was set by the removal of previous IP damage ($R_1 = 1$) and the presumption of infill fully bounded by the frame ($R_2 = 1$). Furthermore, FEMA 273 (1997) developed an Equation (2.15) in order to determine peak OoP displacement.

Moghaddam and Goudarzi (2010) proposed an Equation (2.11) with two modes of failure that are dependent on the infills slenderness. In essence, thick infills will most likely fail by crushing at the boundaries (w_{cr}) while slender ones due to large transverse deflection (w_{max}). Therefore, the w_{max} does not include the masonry's compressive strength. Also, the effects of the frame were included through stiffness parameter α .

Morandi et al (2013) were the first to proposed an equation for infilled frames that implements the panels strengthening via rebars in the bedjoint or the mesh in the plaster (Eq. (2.12)). Additionally, researchers added a parameter β that reduces the OoP load-bearing capacity due to previous IP load. The aforementioned parameter is determined by the relation of (d_w), ultimate (δ_u) and damage limitation (d_m) IP drift together with OoP reduction factor r_a (Tab. 2.18). When the strengthening segment of the equation is excluded, the equation resembles that of BSI (2004b); Drysdale and Hamid (2005) (Eqs. 2.8 & 2.9)

Table 2.18: Values for previous IP reduction coefficient β in Eq. (2.12) by Morandi et al (2013)

Estimated inter-storey drifts in correspondence to limit state	Limit state	Unreinforced	Lightly reinforced	
			Rebars in the bedjoint	Mesh in the plaster
	Damage limitation d_m	0.30 %	0.35 %	0.50 %
	Ultimate d_u	1.00 %	1.00 %	2.20 %
Assumed fraction of OoP resistance r_a corresponding to peak infill resistance		0.20	0.30	0.40

Ricci et al (2018) developed Equation 2.13 by applying a semi-empirical approach to five of their mechanical and geometrical parameters. The equation gained by the approach with the highest p value was set and proposed in the paper. From the equation itself, one can see that researchers neglected the effects of the frame. The authors also developed an equation to calculate the load that causes cracking.

No specific equations were developed for infilled frames that would include the effects of openings. However, **Mays et al (1998)** developed one for blast loaded brickwork (Eq. 2.20). The equation is devised in such a way that one should firstly calculate resistance w using an arbitrary equation *e.g.* using a suitable one from Table 2.15. The resistance is thus modified using F_r factor and opening to wall ratio A_o/A_i . The modification factor is obtained based on opening type (Tab. 2.19); and since it is from the blast engineering field, there is a reference to blast-resistant openings.

$$w_o = w + wF_r \left(\frac{A_o}{A_i} \right) \quad (2.20)$$

Table 2.19: Modification factor F_r for panels with openings (Mays et al, 1998)

Panel type	Blast-resistant openings	Opening location	F_r
One window	No	Central and offset	-1.00
One door	No	Central	+1.36
One door	No	Offset	-0.13
Two windows	No	Evenly distributed	-0.05
One window + one door	No	Evenly distributed	-0.41
One window	Yes	Central and offset	-3.07
One door	Yes	Central and offset	-2.73
Two windows	Yes	Evenly distributed	-2.62
One window + one door	Yes	Evenly distributed	-2.59

Notes on analytical models. A few discrepancies were observed during the research. Namely, a few differences were found between certain articles. Most of the time, constants were changes from converting units (US and SI). For example, Dawe and Seah (1989) had constant 800, however, when Flanagan and Bennett (1999b); Wang (2017); Pasca et al (2017) referred to the same equation, the constant was 0.8. Therefore, for the sake of uniformity, every equation was modified to SI units, using MPa, mm*etc.* For the same reason, FEMA 356 (2000) constant of 144 (Eq. 2.10) was changed to $0.99 \approx 1.00$.

Peculiarly, De Risi et al (2019) wrote and referenced equation by Ricci et al (2018). However, they were different; the constant in De Risi et al (2019) paper was raised to an exponent, while in the original paper, it was set as a multiplication. In this thesis, the equation was corrected; however, the original paper (Ricci et al, 2018) was cited as they were their developers.

2.8.1 Input for the analytical models

The model analysis was performed on the mechanical and geometrical characteristics as displayed in Table 2.16. Furthermore, the parametric analysis was carried out on IF-ND specimen tested by Sepasdar (2017) as it had the best matching with analytical models.

Equation (2.4, 2.3) call for the value of torsional constants J . In the case of rectangular sections Equation (2.21) was used in relation with Table 2.20. In the case of non-rectangular section, such as those of SS, the constant was obtained thought the table from Tools for Engineer website (2019).

$$J = \beta ab^3 \quad (2.21)$$

where β is obtained through linear interpolation by using Table 2.20

Table 2.20: Values of β for torsional constant J

a/b	1.000	1.500	2.000	2.500	3.000	4.000	5.000	6.000	10.000	∞
β	0.141	0.196	0.229	0.249	0.263	0.281	0.291	0.299	0.312	0.333

Furthermore, parametric, *i.e.* sensitivity analysis range of values was established as presented in Table 2.21. In the case parameters such as $h/t \in [5, 35]$ could not be incorporated as a single variable, the thickness was set to the original value of $t = 90$ mm, while the value for height was obtained as a range with $h = t \cdot h/t$. Analogously for the aspect ratio h/l , h was set as a constant, such that slenderness was not influenced. In the case of modifying masonry's compressive strength, elastic modulus (E_m) was altered with the use of Equation 2.22.

Table 2.21: Range of parameter values which are considered for the parametric analysis

Parameter	Range
Slenderness	$h/t \in [5, 35]$
Aspect ratio	$l/h \in [0.5, 3.0]$
Frame element section size	$b_b \in [50, 500]$ mm
Masonry's compressive strength f_m	$f_m \in [1, 35]$ MPa

$$E_m = f_{m,k} \cdot K_E \quad (2.22)$$

where K_E is 1000 in accordance with the Annex of the EN1996-1-1 provision (BSI, 2004b).

2.8.2 Analysis model results

The results of analytical model analysis as well as the parametric analysis are presented in Tables 2.22–2.25 and plotted in Figures 2.31–2.36. In Table 2.22 the overall, absolute difference between the analytical model and experiments was plotted. Analogously, Table 2.23 showed the same as latter, but for the displacements. The term *plain masonry* relates to URM infill walls without any special features, e.g. no gaps, openings, etc.

The results of the calculated data are presented in Tables 2.23 and 2.25.

Table 2.22 presents the overall absolute difference sorted by various properties and equations. Table 2.23 on the other hand, presents a difference between experientially and analytically obtained load-bearing capacities. Likewise, Table 2.23 displays the differences in displacements. The term plain masonry panel in Tables under this sub-section mean that the panel has no special features like gaps, previous IP damage, openings *etc.*

Figure 2.32 displays the differences in each specimen by equations and their property. The absolute difference was limited to 350 %. The difference by each specimen and equation are plotted in Figure 2.33 with difference limit set to ± 600 %. The closed up version of the same graph with the limits of ± 100 % are plotted in Figure 2.34. Hence, some models outside the range were omitted from the plot. Likewise, Figure 2.31 graphs the error variabilities; showing the extremes, quartiles and medians.

The findings of the single-variable parametric analysis are shown in Figure 2.35 with the left side showing the results of two-way actions and the right side those of gapped actions. The multi-variable parametric analysis is plotted in Figure 2.36. All differences were calculated with the use of an Equation (2.23)

$$\Delta w = \frac{w_{\text{analytical}} - w_{\text{experiment}}}{w_{\text{experiment}}} \quad (2.23)$$

Table 2.22: Absolute difference between experimental and calculated capacities per property

Property	Difference by Eq. # (%)									
	(2.4,2.3)	(2.5)	(2.6,2.18)	2.7	(2.8)	(2.9)	(2.10)	(2.11)	(2.12)	(2.13)
Total	99	236	98	75	78	276	203	46	822	30
RC frame	159	327	131	122	89	607	402	55	1358	33
SS frame	43	66	71	38	70	46	66	40	94	27
Plain masonry panel	73	78	80	80	67	273	235	47	82	28
Beam-infill gap	303	67	n/a	n/a	n/a	n/a	n/a	n/a	n/a	n/a
Columns-infill gap	n/a	n/a	277	n/a	n/a	n/a	n/a	n/a	n/a	n/a
Openings	56	66	65	62	63	180	129	43	68	47
Concrete units	40	330	58	44	58	80	89	44	1125	32
Clay units	187	79	165	133	99	618	403	618	216	26
Previous IP load	n/a	526	n/a	n/a	n/a	n/a	n/a	n/a	2466	n/a

*n/a - not applicable

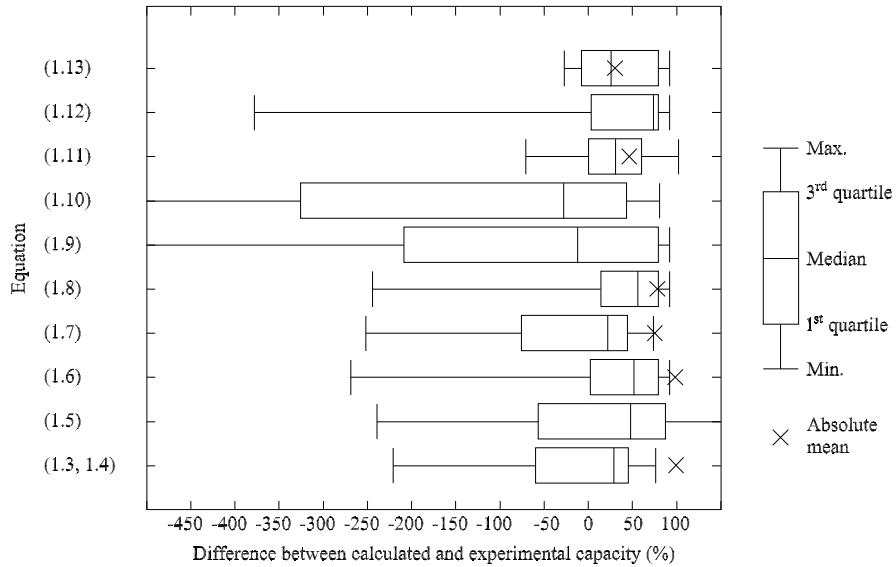


Figure 2.31: Variation in differences plotted as quartiles between various analytical models

Table 2.23: Difference in % between analytical models and experimental OoP displacement

Author	Specimen	Eq. (2.16)	Eq. (2.14)	Eq. (2.15)	Remark
Flanagan and Bennett (1999a)	25	153.67	$\in \mathbb{C}$	158.81	Plain masonry panel
	18	170.79	140.86	131.66	Plain masonry panel
	22	-57.32	-19.31	-20.29	Plain masonry panel
Akhoundi et al (2016)	SIF-B	147.86	131.83	115.14	Plain masonry panel
Furtado et al (2016c)	inf_01	91.84	85.55	71.03	OoP monotonic load
	inf_02	251.70	240.18	213.55	OoP cyclic
Wang (2017)	IF-S	-42.46	-24.56	-27.10	Steel frame
Sepasdar (2017)	IF-ND	-42.46	-8.86	-27.10	Plain masonry panel
Domenico et al (2018)	OOP_4E	986.99	$\in \mathbb{C}$	817.16	Plain masonry

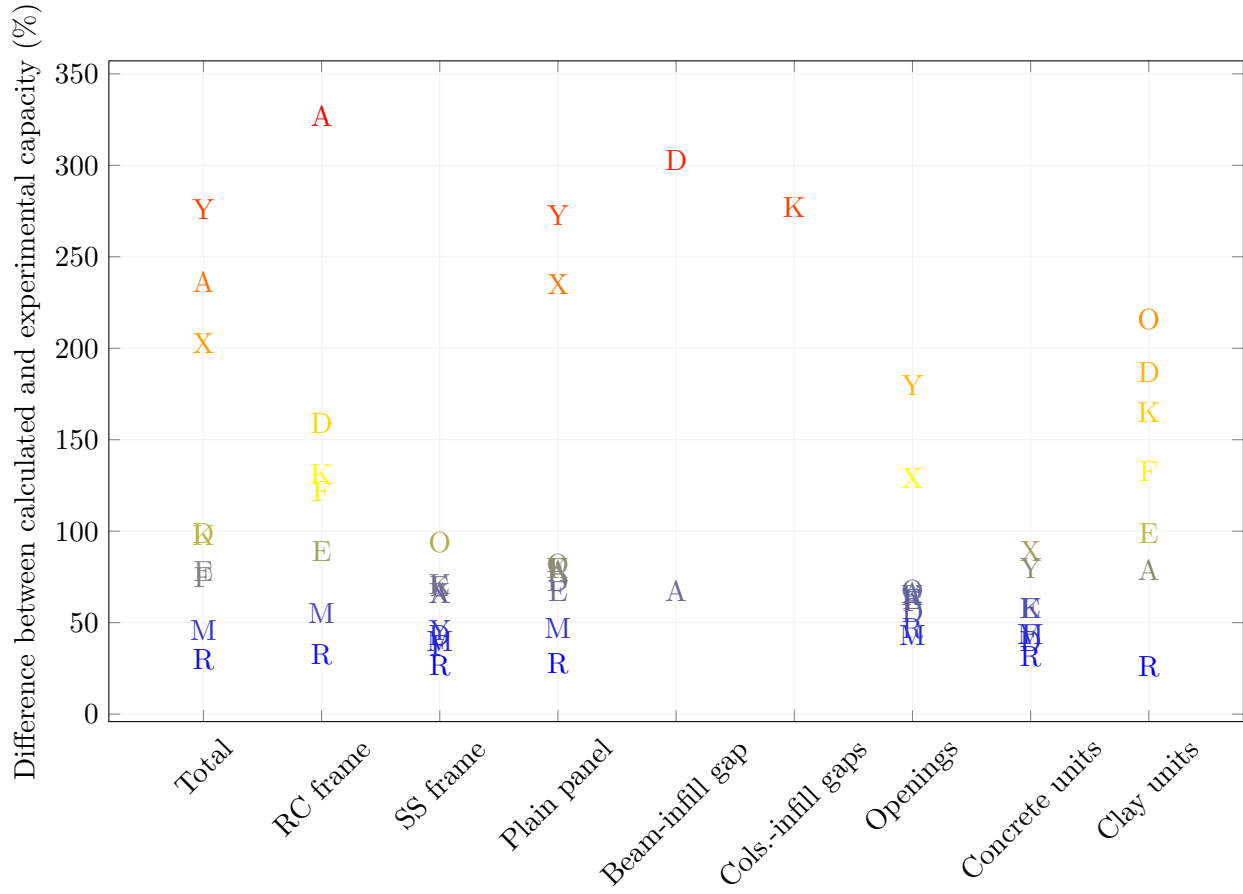


Figure 2.32: Absolute differences in various analytical models by specific property, legend same as in Fig. 2.34

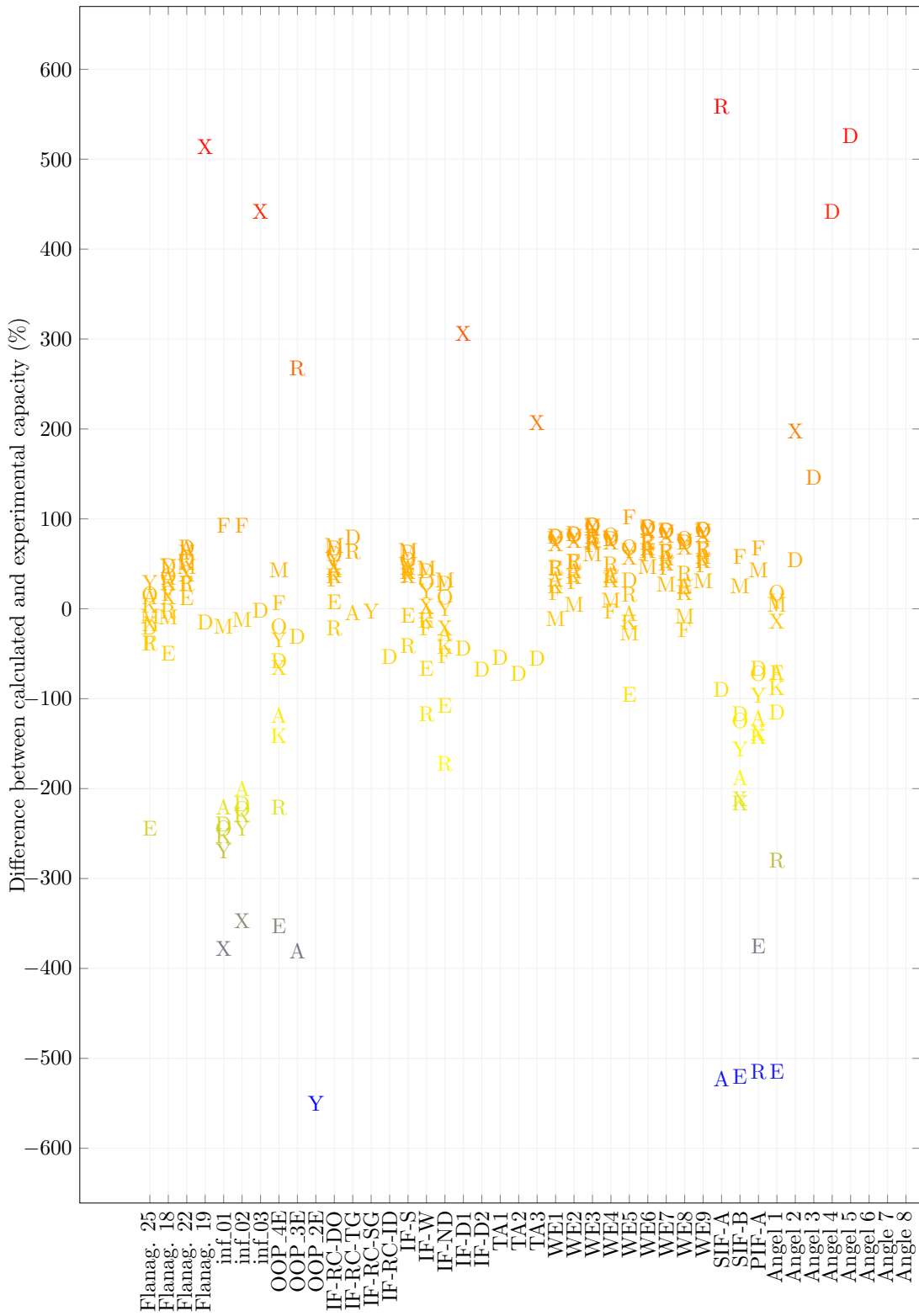
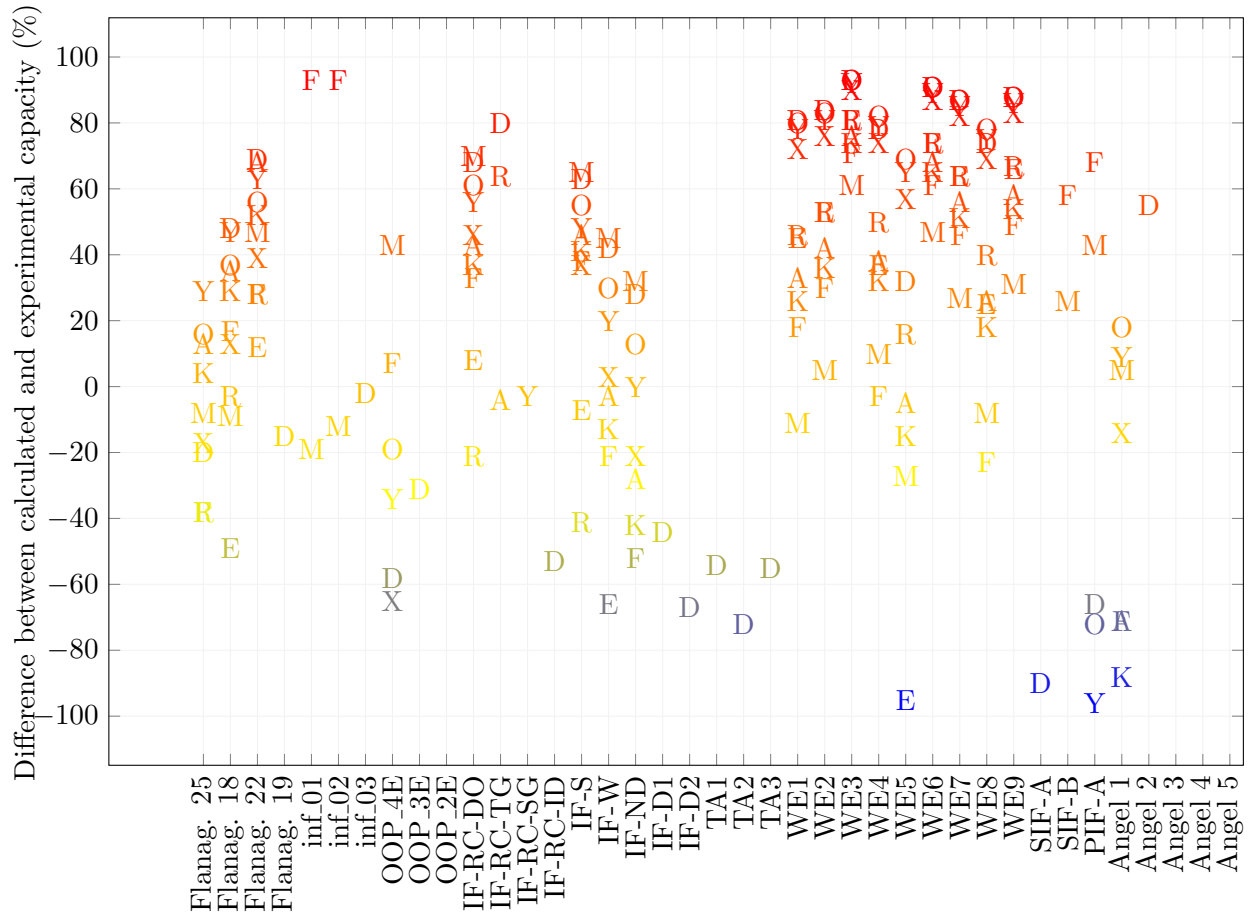


Figure 2.33: Absolute differences in various analytical models by specific specimen, legend same as in Fig. 2.34



D	Dawe and Seah (1989)	(2.3,2.3)	A	Angel et al (1994)	(2.5)
K	Klingner et al (1996)	(2.6,2.18)	F	Flanagan and Bennett (1999a)	(2.7)
E	BSI (2004b)	(2.8)	Y	Drysdale and Essawy (1988)	(2.9)
X	FEMA 356 (2000)	(2.10)	M	Moghaddam and Goudarzi (2010)	(2.11)
O	Morandi et al (2013)	(2.12)	R	Ricci et al (2018)	(2.13)

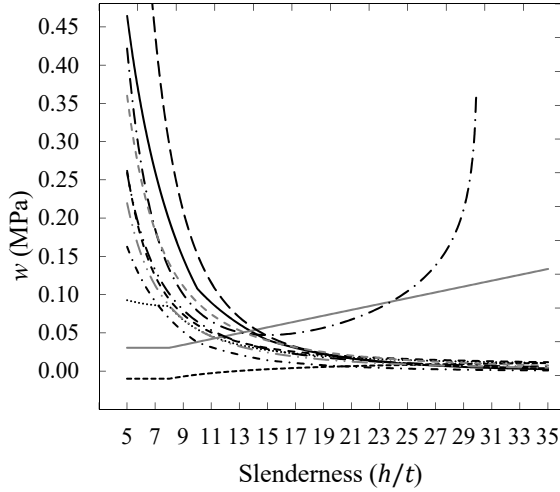
Figure 2.34: Absolute differences in various analytical models by specific specimen

Table 2.24: Differences between calculated and experimental OoP capacities (Eq. 2.23)

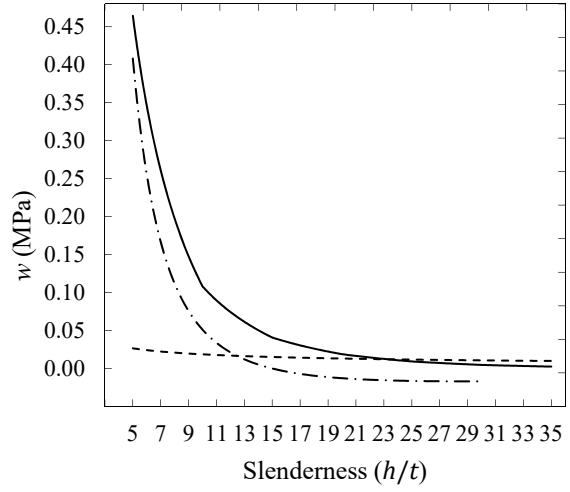
Author	Specimen	Δ by Eq. # (%)										Remark
		3&4	5	6&19	7	8	9	10	11	12	13	
Dawe and Seah (1989)	WE1	81	33	26	18	45	78	72	-11	80	46	Trust type joint reinf.
	WE2	84	42	36	30	53	81	76	5	83	53	Plain masonry panel
	WE3	93	76	74	71	81	92	90	61	93	81	Dry-stack panel
	WE4	78	38	32	-3	37	79	74	10	82	50	Plain masonry panel
	WE5	32	-5	-15	102	-95	65	57	-27	69	16	Plain masonry panel
	WE6	91	68	65	61	74	89	87	47	91	74	Plain masonry panel
	WE7	87	56	51	46	64	85	82	27	87	64	Trust type joint reinf.
	WE8	74	26	18	-23	25	75	69	-8	78	40	Restraints against slipping
	WE9	88	58	54	49	66	86	83	31	88	67	Window opening
Angel et al (1994)	1	-115	-71	-88	-71	-514	9	-14	5	18	-280	Pure OoP, S mortar
	2	55						198				IP d_r 0.34% + OoP
	3	146						599				IP d_r 0.22% + OoP
	4	442						3661				IP d_r 0.09% + OoP
	5	526						6413				IP d_r 0.06% + OoP
	6	1026						2712				IP d_r 0.25% + OoP
	7	1065						2809				IP d_r 0.25% + OoP
	8	3721						7240				IP d_r 0.39% + OoP
Flanagan and Bennett (1999a)	25	-20	13	4	-38	-244	29	-17	-8	16	-38	Plain masonry panel
	18	48	35	29	17	-49	47	13	-9	37	-3	Plain masonry panel
	22	69	68	52	28	12	63	39	47	56	28	Plain masonry panel
	19	-21						514				IP d_r 0.8% + OoP
Hak et al (2014)	TA1		-58									IP d_r 1.50%
	TA2		-74									IP d_r 2.00% + OoP
	TA3		-59									IP d_r 1.00% + OoP
Akhoundi et al (2016)	SIF-A	-90	-523									Beam - infill gap
	SIF-B	-117	-188	-216	58	-520	-156	-211	26	-124	-700	Plain masonry panel
	PIF-A	-66	-121	-142	68	-375	-96	-138	43	-72	-514	Window opening
Furtado et al (2016b)	inf.01	-239	-221	-252	93	-868	-269	-378	-19	-244	-1782	OoP mono. + gravity load
	inf.02	-217	-200	-229	93	-804	-244	-347	-12	-222	-1658	OoP cyclic
	inf.03	-13						442				OoP cyc. + IP d_r 0.5%, 2 leaf.
Sepasdar (2017)	IF-W	42	-3	-13	-21	-66	20	3	45	30	-117	Window opening
	IF-ND	28	-28	-42	-52	-107	0	-21	32	13	-172	Plain masonry panel
	IF-D1	-48						306				IP d_r 0.66% + OoP
	IF-D2	-69										IP d_r 2.70% + OoP
Wang (2017)	IF-RC-DO	68	43	37	33	8	56	46	70	61	-21	Door opening
	IF-RC-TG	80	-4	64								Beam - infill gap
	IF-RC-SG						-3					Columns - infill gaps
	IF-RC-ID	-56										IP d_r 1.37% + OoP
	IF-S	63	46	41	38	-7	48	37	65	55	-41	Steel frame
Domenico et al (2018)	OOP_4E	-58	-119	-141	7	-353	-34	-65	43	-19	-221	All bounded
	OOP_3E	-31	-381									Beam - infill gap
	OOP_2E						-550					Columns - infill gaps

Table 2.25: Displacement calculation results

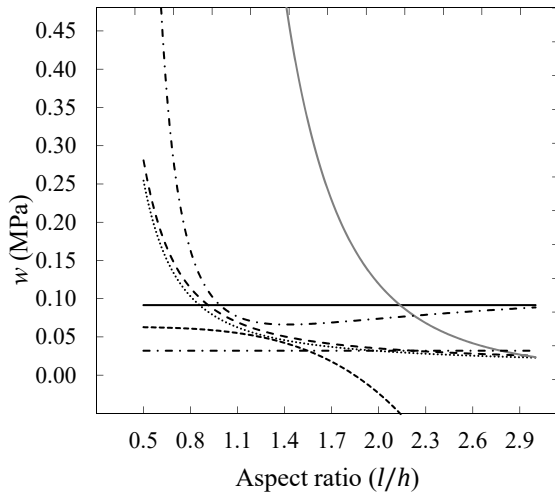
Author	Specimen	Equation			Remark
		(2.14)	(2.15)	(2.16)	
Flanagan	25	153.67	$\in \mathbb{C}$	158.81	Plain masonry panel
and	18	170.79	140.86	131.66	Plain masonry panel
Bennett	22	-57.32	-19.31	-20.29	Plain masonry panel
(1999a) Akhoundi et al (2016)	SIF-B	147.86	131.83	115.14	Plain masonry panel
Furtado	inf_01	91.84	85.55	71.03	OoP monotonic + gravity load
et al	inf_02	251.70	240.18	213.55	OoP cyclic
(2016b) Wang (2017)	IF-S	-42.46	-24.56	-27.10	Steel frame
Sepasdar (2017)	IF-ND	-42.46	-8.86	-27.10	Plain masonry panel
Domenico et al (2018)	OOP_4E	986.99	$\in \mathbb{C}$	817.16	All bounded



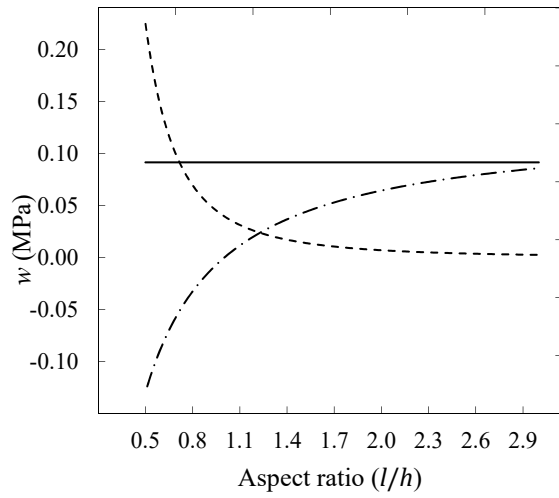
(a) Effects of slenderness on two-way action



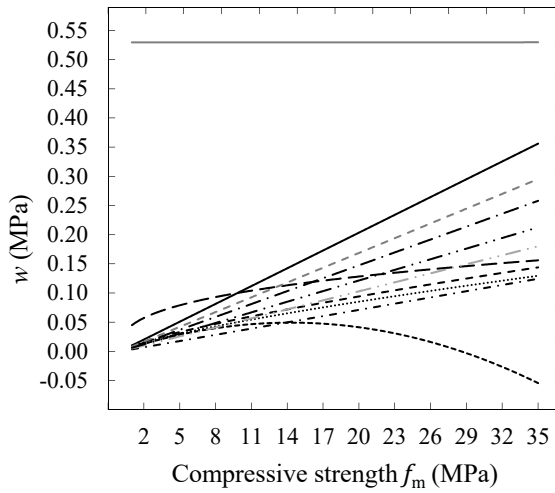
(b) Effects of slenderness on one-way action



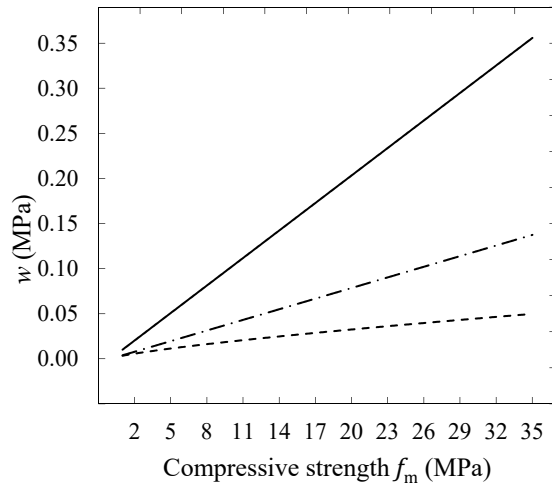
(c) Effects of aspect ratio on two-way action



(d) Effects of aspect ratio on one-way action



(e) Effects of compressive strength on two-way action



(f) Effects of compressive strength on one-way action

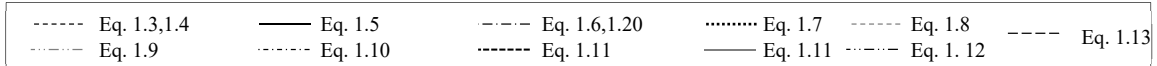
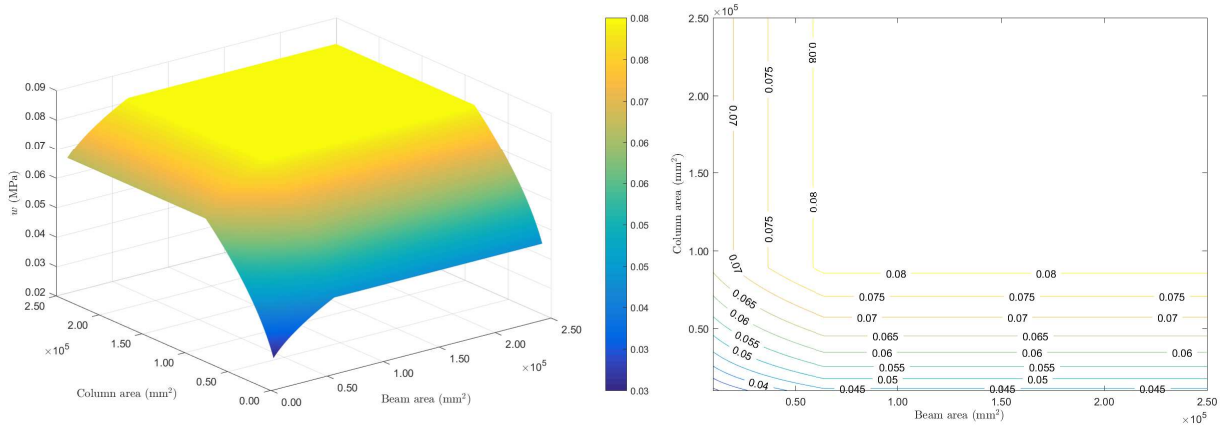
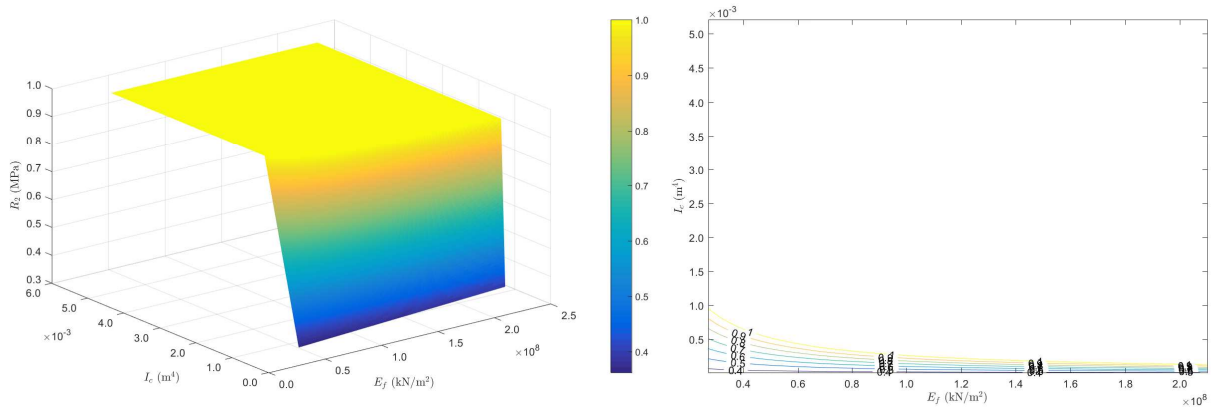


Figure 2.35: Single variable sensitivity analysis



(a) Effects of frames' section size on Equation (2.3)



(b) Effects of frame trough columns' moment of inertia I_c and elastic modulus E_f on R_2 coefficient from m Eq. 2.5

Figure 2.36: Multi-variable parameter sensitivity analysis of analytical models

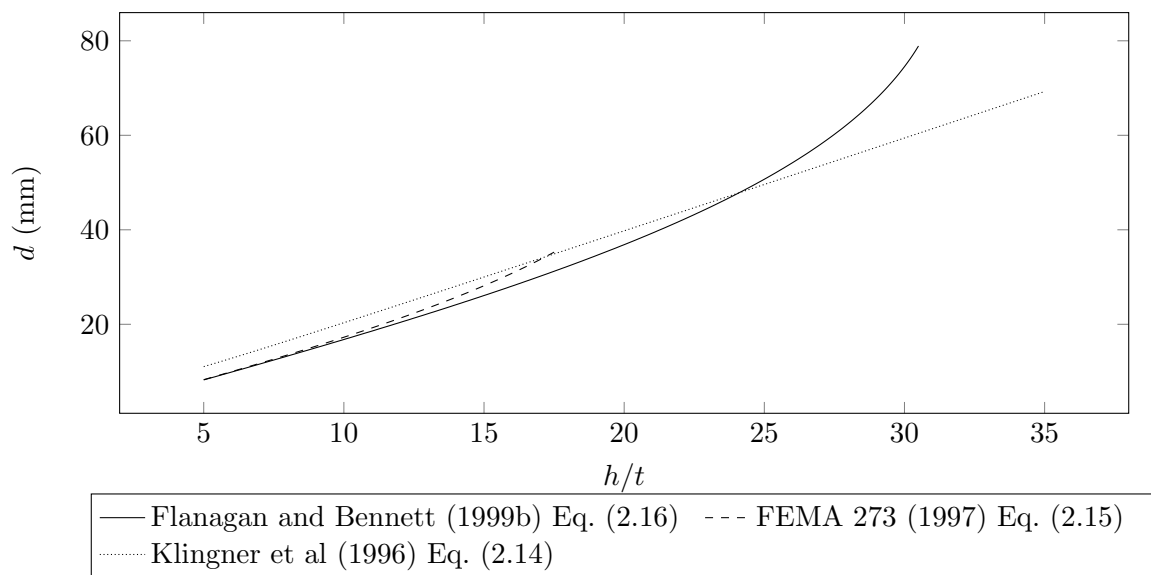


Figure 2.37: Effects of slenderness (h/t) on ultimate OoP displacement calculations

2.9 Discussion and overview

2.9.1 Experimental studies

Three principal experimental methodologies from OoP and combined IP and OoP were found by their loading methods: 1) inertial forces; 2) inter-storey drift; and 3) dynamical excitation. Dynamical methodologies are undoubtedly the best option for understanding the complete behaviour of frames with masonry infill walls under seismic load. However, they are more expensive, harder to control and require more sophisticated equipment. Thus, more straightforward methods are used, namely, inertial and inter-storey drift force methods with static and quasi-static (cyclic) load protocols. Both isolate the specific forces that act upon a structure during seismic excitation.

From Tables 2.2 to 2.10 and Figs. 2.4 to 2.7, it can be observed that most experiments were carried out using the inertial-cyclic load method, with approximately half of them had previous cyclic IP load. Most frames were made from RC, while infill walls were made using unreinforced clay masonry, laid out in a manner that, the voids were facing the vertical direction. The slenderness of the infill walls was in the range of $h/t \in [1.35, 39.68]$ with the majority positioned below the Eurocode 8 (BSI, 2005) limit for special measures (11.20 median). The aspect ratios were in the range of $l/h \in [0.58, 2.00]$, with a median of 1.36. One researcher tested the opening under the area of negligence by Eurocode 6 (BSI, 2004b), while the rest were above. From Tab. 2.7, it can be observed that masonry's compressive strength was in the range of $f_m \in [0.53, 24.30]$ MPa with a median of 9 MPa. Low instances of f_m were mainly used in studies from Portugal, where traditionally, blocks have lower strength as they are laid out horizontally. Likewise, masonry's elastic modulus was in the range of $E_m \in [942, 17575]$ MPa with a median of 5300 MPa. The previous IP inter-storey drifts were applied in the range of $d_r \in [0.06, 2.70]$ % with a median of 0.39 %.

While investigating different kinds of loadings, it was found that there were considerable differences between the inertial and storey-drift force methods. The most obvious difference was that the inertial force method damaged the infill while leaving the frame practically undamaged. The opposite was demonstrated in the case of the inter-storey drift force method. Additionally, it was found that the dynamical have more similarities with inter-storey drift force methods *e.g.* infill wall and frame move together as a single unit, the frame had more damage than the infill, *etc.* On the other hand, it was found that the infill wall had the same or greater acceleration than the frame. Therefore, it was more prone to inertial forces. Considering that both the infill wall and the frame move as one and that the infill wall is more susceptible to inertial forces, it is to be expected that the infill wall could fall out in a real earthquake scenario. The indicated is more plausible when boundary conditions were not valid, due to, for example, poor workmanship, previous IP damage due to which the frame and the infill wall are disjointed; hence the joined movement is compromised. This scenario was suspected in the case of A1 specimen from Tu et al (2010) dynamical research (Fig. 2.27a).

The blast engineers firstly developed the inertial force method to simulate the effects of blast wave pressurising the infill. They had expected a *bending action*, yet they found a six-fold greater *arching-action*. The arching-action mentioned above is also the main outcome of the inertial force method. In detail, when the infill wall is loaded and after reaching the critical point, it cracks in the middle and between the beams. Those points form clamping locations through which the infill wall develops a *three-hinged-arch* (Fig.2.7). The infill wall uses the same mechanics as a three-hinged arch to resist transversal force, *i.e.* through additional normal ones. A similar analogy was found within the plate and shell theory, where the membrane forces resist transversal ones. Furthermore, they both have similar yield lines concerning boundary conditions (Fig. 2.9). Note that, as mentioned

by Hobbs et al (1994) the term *yield line* can be misleading. The infill walls do not yield; rather, they rotate about those lines, so a more appropriate term would be *hinge-line*. Certain factors can bypass or limit the arching action, such as: boundary conditions; slenderness; aspect ratio; gravity loads; infill type; mortar type; previous actions; and openings. Note that the only instance of arching action observed in dynamical methods was a two-hinged arch (truss) by Tu et al (2010) (Fig. 2.10c). The beneficial effect of arching-action is also observable in the large drift ratios, that can exceed the infill wall's thickness (Fig. 2.12, Tab. 2.14)

Boundary conditions were sometimes referenced either as a result of workmanship, practical consideration or previous damage that have shown notable effects on OoP behaviour. It affects the arching action development and failure modes, load-bearing and deformation capabilities. An example of poor workmanship would be that it is tough to fill the bedjoint between the upper beam and the infill wall; hence, it can be absent in many cases. Furthermore, a practical consideration contemplation was proposed by Wilton and Gabrielsen (1973), where they argue that in order to isolate the movement of the infill wall from the frame, one should remove certain boundary conditions. And finally, the first event of IP drift is the debonding of the frame and infill wall; thus, boundary conditions are changeable through time.

Seven independent studies were carried out to observe the effects of openings. Those included: 1 door, 4 windows and 2 full-wall height openings, all placed centrally. Note that no studies published their results on full-wall height openings to the day of writing of this thesis. All studies observed a drastic decreases in deformation capabilities. The same cannot be stated for load-bearing capacities. Namely, two specimens with window openings did not observe any lowering, while one window and door opening did. The reason is yet to be found; however, a limited arching-action can inevitably develop despite the presence of openings.

Both the infill's slenderness and the aspect ratio have affected OoP behaviour. As the arching action is a function of compressive forces, it is intuitive that slenderness and the aspect ratio could lower or elevate the infill's bearing and deformation capacities. It has also been found that, depending on slenderness, the infill may fail due to transverse instability or by crushing at the boundary. In other words, with thick infills, the arching action could be bypassed.

2.9.2 Analytical models

There were ten analytical models developed (Tab. 2.15) specifically for the determination of load-bearing capacities for frames with masonry infill walls (*flexural-based* excluded). All were developed on the observations from inertial force driven experiments. Among those ten, two of them are modified versions of pre-existing ones. Namely, Equation (2.7) from Flanagan and Bennett (1999a) was a modified version of Dawe and Seah (1989) equation (2.3), while equation (2.10) was a simplified version of equation (2.5) from Shapiro et al (1994). Certain equations target various effects as: boundary conditions, effects of the surrounding frame, previous IP damage. The effects of the surrounding frame were implemented in six models, mainly through the torsional capabilities of frames parts. The equations developed to account for boundary conditions considered full and single-gapped conditions, while also the author of this thesis derived a double gapped arching action equation (2.19) from Klingner et al (1996).

Furthermore, three analytical models were developed for the calculation of OoP deflection at peak load (Tab. 2.17). Likewise, all of those equations were developed on the basis of inertial force experiments. Also, equation (2.16) from Flanagan and Bennett (1999a) research is a modified version of a pre-existing equation (2.15) and equation (2.14) was derived from the load-bearing equations (2.6).

It was observed that both the deflection and load-bearing analytical models differ greatly among

each other and in comparison with experimental outputs. It was found that the best correlations were with concrete units and plain masonry infill walls (Tab. 2.22, Fig. 2.32). Overall, equation (2.13) by Ricci et al (2018) had the best correlation with experimental data. It had the smallest variations of errors (Fig. 2.31) and was stable with regards to all parameters (Fig. 2.35). The equation mentioned above was developed using the semi-empirical approach with data from various experiments, while others developed their equations mostly based on their experimental data. Additionally, equation (2.11) by Moghaddam and Goudarzi (2010) had a good correlation with the experimental data. The equation mentioned above had two failure mode types based on infill walls slenderness; namely, the *transverse instability* and *crushing at the boundaries* failure modes, with transverse instability mode being the prevalent one. Author of this thesis along with its mentors derived equations (2.18, 2.19) for double gapped arching-action from the equation (2.6) by Klingner et al (1996). It was used to check the loading-bearing capacity of infill wall and columns gap systems. It had a substantiation difference with the experimental data of $\approx 277\%$. However, when compared with the IF-RC-SG specimen from Wang (2017), it had an error of 3.27% . Therefore, the equation has the potential for further development.

The previous IP damage factor R_1 (Eq. 2.5) has had poor performance with experimental data outside their own. As seen in Figures 2.20 and 2.21 the reduction varies largely between the authors; for example, 1.0% d_r resulted in a reduction at about 20% (Hak et al, 2014), while 0.6% d_r about 90% . Therefore, it is to be expected that such differences would be hard to grasp with single factor that was based on infill walls slenderness and observable damage state (Fig. 2.30). Likewise was the case of β factor from Morandi et al (2013) equation (2.12). However, the equation was limited to IP 1.0% $d_r(\delta_u)$, therefore in some cases there were no OoP load-bearing capacities.

The only equation (2.20) for addressing the openings from Mays et al (1998) research was found to be inconsistent with the researches from the field (Fig. 2.14). Whereas, Mays et al (1998) even suggest that with the door opening, there should be an increase in load-bearing capacity (Tab. 2.19) to that of the fully infilled frame. This can be attributed to the fact that Mays et al (1998) did the research based on load-bearing RC walls.

The parametric, *i.e.* sensitivity analysis revealed a few stability issues. Namely, due to negative numbers in Equation (2.6)'s natural logarithm and equations (2.16, 2.15) square root produced complex numbers (C). Therefore, the newly found limits were previously incorporated in the equation remarks as visible in Tables 2.15 and 2.17. Also, with the parametric analysis, it was found that the infill wall slenderness along with its compressive strength were the equations governing factors (Fig. 2.35). Slenderness was observed to have had more differences in load-bearing capacity of thick infill walls than the slender ones.

The effects of the frame were minimal (Fig. 2.36a), which justifies the omission of torsional effects from Dawe and Seah (1989) equation (2.4, 2.3) by Flanagan and Bennett (1999b) equation (2.7). Likewise observed in Angel et al (1994) experimental outcomes; where in the case of one-way the effects are minimal and non-existing in two-way arching-action. Therefore, the lack of frame's effects in equations (2.6, 2.13) is justifiable and they are mutually interchangeable with the load-bearing masonry equations.

2.10 Conclusions

Multi-storey buildings are often composed of a ductile load-bearing frame and inelastic non-bearing infill walls. During a seismic event, both the frame and infill wall interact and render the behaviour of the whole structure. Also, the structure is then loaded by both inter-storey drift and inertial forces in both in-plane and out-of-plane directions. Therefore, to comprehend and better understand the behaviour of the two, the field of infilled frames' research spread into three main components:

in-plane, out-of-plane and combined loadings. With the latter being: out-of-plane behaviour with previous in-plane damage, vice-versa and simultaneous in- and out-of-plane loadings.

The out-of-plane test methods can be divided into three segments: 1) the dynamical excitation; 2) inertial and 3) inter-storey drift force method. The inertial force method was the most practised test type, usually done with airbags. In contrast, the inter-storey drift force method was employed only twice. The primary outcome from the inertial force tests was the *arching-action*. The infill wall bends and cracks, developing clamping points that form a *three-hinged* arching action. With it, the infill wall resists transversal through additional normal forces and renders the load-bearing capacity about 6 fold greater than expected with flexural-action. No arching-action-like mechanism was found with storey-drift, while only two-hinged action was mentioned with the dynamical methods. It was found that various conditions can limit or bypass the arching action, such as: boundary conditions; infill walls slenderness; openings; combined loadings; gravity loads; mortar and infill unit type; aspect ratio; and *etc.*

Comparing the out-of-plane methods, the inertial and storey drift forces differ significantly. Namely, the latter damaged the frame, while the infill wall was only slightly damaged. Vice versa was in the case of the inertial force method. In comparison with dynamical methods, it was found that both methods share similarities with it. Yet, the storey drift force method had arguably more. This can be added to the facts that all inspected specimens had one storey where the inertial forces are low. However, the mixture of both inertial and storey drift fails was also possible as observed in one of the dynamical experiments. Namely, in the previous experiment, one of the specimens lost its boundary condition. This resulted in disjointed movement between the frame and the infill wall, and ultimately due to infill wall's proneness to inertial excitation, the infill wall fell out.

It was found that analytical models produced widely dispersed outputs among each other and with experimental data. Two best correlations between the analytical models outputs and experimental data were found in two equations, that of Ricci et al (2018) (Eq. 2.13) followed by Moghaddam and Goudarzi (2010) model (Eq. 2.11). Furthermore, the slenderness and compressive strength of the infill wall units were found to have the greatest effects on the analytical model's outputs. The effects of the frame on the analytical model's outcome were minimal. Therefore, the equations from frames with infill walls and load-bearing brickwork are mutually interchangeable for the inertial force load-bearing capacity. The factors developed to reduce the out-of-plane load-bearing capacity due to previous IP loads were insufficient for specimens outside of those on which they were developed. The same can be stated in modifying factors for the effects of openings and boundary conditions. During the sensitivity analysis, few unstable parameters were found mainly by producing complex numbers. The limitations for the unstable parameters were thus included in the Table 2.15 with listed analytical models.

Overall, from the literature review, it is visible that the field lacks the following points:

1. More research on simultaneous in-plane and out-of-plane loading and combined out-of-plane followed by in-plane loading;
2. A systematic study on the effects of openings, with various geometries, positions, combinations and confinements. This is especially true for storey-drift and dynamical methods;
3. Arching action development in dynamical and storey-drift out-of-plane experimental methods, possibly with multi-storey structures;
4. Equations that would not only comprehend the out-of-plane load-bearing capacity of plain masonry but also: in-plane damage, openings, boundary conditions, storey-drift capacity, etc.;
5. Experimental set-up consisting of both storey-drift and inertial forces;

6. More studies on storey-drift out-of-plane methods, especially with reinforced concrete frame and clay masonry infill walls;

This thesis will cover some of the above points with storey drift driven experiments and numerical simulations.

2.11 Research hypothesis

Within the given dissertation, the seismic resistance of RC frames with and without infill walls and openings will be researched in the in- and out-of-plane direction, both experimentally and computationally. The openings will be varied in their position and size. The 3D computational micromodels will be validated against experiments. Also, a simplified model will be either developed or modified based on the data from simultaneous IP and OoP loads, as currently, they do not exist. In that sense, interaction curves will be derived along with the simplified model. Their governing factors will be obtained from the computational models, and from varying opening size simulations, the recommendations for the industry will be outlined.

The end goal is to determine the limits when the infill wall either contributes or counteracts the specimens' overall behaviour. Considering the varying opening sizes, types and positions within the infill walls of the RC frames, loaded in- and out-of-the-plane, the following hypotheses were drawn:

1. Calibrated computational micromodels can simulate IP and OoP behaviour based on the experimental ones;
2. Calibrated computational micromodels can predict different types of damages based on the IP and OoP interaction;
3. Openings of different types, sizes, and positions along with the infill walls without them contribute to the overall seismic resistance and failure mode based on the direction of seismic loading;
4. With the aid of experimental and computational limit-state data, a simplified model is constructible.

Part II

Experimental campaigns

Conflicts of interest disclosure Please note that there are many similarities and cross-referencing between this chapter and the Anić et al (2019) and Anić et al (2021a) paper. Authors of the referenced paper are the thesis author and his supervisors. Furthermore, the part of dissertation about IP behaviour and certain precedented testings were a part of dr. Penava's dissertation (Penava, 2012) and subsequent papers as Sigmund and Penava (2014), while the structure prototype and specimens were designed by dr. Zovkic (Zovkić, 2013).

Chapter 3

Prototype structure

3.1 Prototype structure design

As mentioned in the previous section (Sec. 2.10), this dissertation covers the behaviour of RC frames with and without unreinforced masonry infill walls and openings. The specimens were designed as a part of a seven-storey building and were made in 1:2.5 scale. This section briefly describes the selection process and the characteristics of specimens used in the experimental studies. The selection process, scaling, and other matters were not a part of this dissertation and, therefore, not covered here. For more information, refer to Zovkić (2013) or Penava (2012) thesis (in Croatian) from where this section was realised.

The selected building represents a typical seven-storey structure consisting of RC frames, two-way bearing slabs, and unreinforced masonry infill walls (Fig. 3.1). The building's plan and elevation are presented in Figure 3.2.

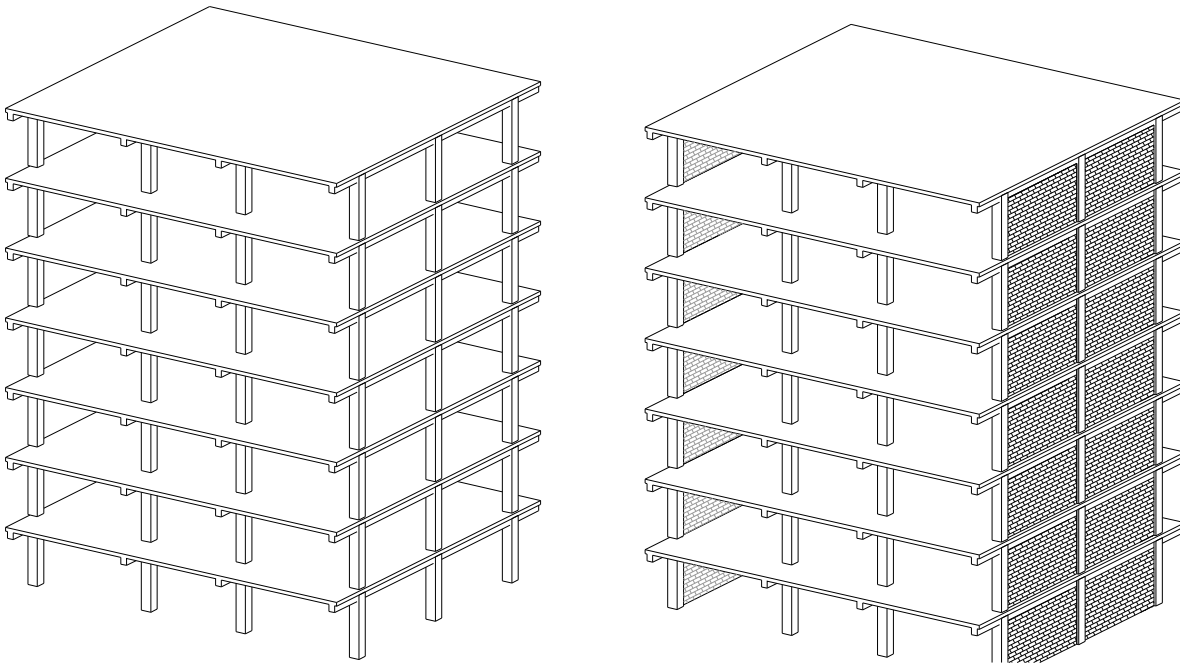


Figure 3.1: Compression test on masonry units

The design load that was imposed on the prototype structure was calculated using Table 3.1.

The self-weight of the structure itself was calculated within the software's internal calculator. The RC design was done using statical and spectral analysis of the 3D structure using Tower 5, v.24 (Radimpex Software d.o.o., 2012).

Table 3.1: Design loads on the prototype structure (Zovkić, 2013)

Floor	Self-weight		Imposed load		Designed seismic load	
	kN/m ²	kN/m*	kN/m ⁺	kN/m	kN/m	(2. importance factor, $\gamma_I=1$)
Roof	2.00			1.25		Soil type B
6 th	1.75	12.00	1.00	3.00	1.00	a_g/g 0.20
5 th - 1 st	1.75	12.00	1.00	3.00	1.00	q 3.90

* self-weight from infill wall

+ self-weight from façade

With the design load, the RC frames were designed using BSI (2005) provisions as a medium ductility class (DCM). The reinforcement design is plotted in the Figure 3.3. The B500B type was the reinforcement of choice, while a C25/30 was used for the concrete (EN1992-1, BSI (2004a)).

Reinforcement design, used for all specimens in Table 3.4 is plotted in the Figure 3.3 while the details of reinforcement for every section designed in the same Figure is displayed in Table 3.2.

Table 3.2: Reinforcement details for each cross section from Figure 3.3

Cross section		Longitudinal reinforcement		Shear reinforcement	
Notation	Dim. (cm)	Bars & spacing	Reinf. ratio ρ_l (%)	Bars & spacing	Reinf. ratio ρ_w (%)
A-A	30/42.5	14 ϕ 16 mm	0.16	ϕ 8 mm / 15.0 cm	0.22
B-B	30/42.5	12 ϕ 16 mm	0.14	ϕ 8 mm / 15.0 cm	0.22
C-C	20/20.0	12 ϕ 10 mm	2.36	ϕ 6 mm / 7.5 cm	0.38
D-D	12/20.0	10 ϕ 10 mm	3.27	ϕ 6 mm / 7.5 cm	0.63
E-E	12/20.0	4 ϕ 10 mm	1.31	ϕ 6 mm / 10.0 cm	0.47

The central frame from the ground floor of the prototype structure (Fig. 3.2) was selected as a referenced frame, *i.e.* specimen for the later experimental campaigns. The specimen was scaled to a 1.0:2.5 ratio, which translates to the actual aspect ratio of 4.5 : 3.25 m \Rightarrow 1.8 : 1.34 m. Likewise, the infill thickness was scaled from 30 to 12 cm; RC beam section from 30 \times 50 cm to 12 \times 20 cm and columns 50 \times 50 to 20 \times 20 cm. The scaling was calculated using Harris and Sabnis (1999). Whereas the prototype and specimens had similar properties, for example, 1) The masonry wall units that had the same void volume; hence, within the same group in accordance with BSI (2004b); 2) Mortar had the same mixture and thickness in both cases; 3) The masonry units were sliced at mid-height; therefore, the same number of bedjoints was achieved.

From the statical calculations, the designed gravity load was calculated on the prototype structures (N_P) and adopted for each specimen N_S by preserving the value of compressional stress (Eq. 3.1). Thus, it is equivalent to 365 kN on each column.

$$N_s = \frac{N_P}{A_P} A_S \quad (3.1)$$

Where index P stand for prototype and S for specimen.

The hollowed clay masonry block units were obtained from a local distributor, "Cigлана IGM d.o.o." from Sladojevci, Croatia. They were classified as Group II by the BSI (2004b) provisions.

Likewise, the masonry units were previously cut at mid-height to satisfy the 1:2.5 scale and preserve the same number of bedjoints. Finally, the dimensions of masonry units as used in experiments are shown in Figure 3.4. The physical and mechanical properties of the masonry blocks are presented in Table 3.3. In order to bond the masonry units, a general-purpose M5 (EN1996-1, BSI (2004b)) mortar type was used. Accordingly, the mortar had a 5 MPa compressive strength after 28 days with the volumetric cement to lime and sand ratio of 1:1:5.

Table 3.3: Masonry unit properties (Penava, 2012)

Physical properties			Mechanical properties				
			Gross		Nett		
Length	250.00	mm	$E_{mu,h}$	12496.25	MPa	4002.00	Mpa
Width	120.00	mm	$E_{mu,b}$	4428.08	MPa	949.00	Mpa
Height	65.00	mm	$f_{mu,c,h}$	46.21	MPa	14.79	Mpa
t_{web}	6.00	mm	$f_{mu,c,b}$	16.10	MPa	3.49	Mpa
t_{shell}	10.00	mm	$\varepsilon_{mu,h}$	3.70	%	3.70	%
V_{unit}	1950.00	cm ³	$\varepsilon_{mu,b}$	3.64	%	3.64	%
V_{holes}	1073.30	cm ³	ρ_{mu}	2390.00	kg/m ³	760.00	
V_{holes}/V_{unit}	55.04	%					

3.2 Specimen design

From the structure prototype, a central frame was selected for further research (Fig. 3.2) that includes the effects of openings and infill walls. The openings were selected and designed in Penava (2012) thesis (in Croatian). They were selected based on architectural guidelines for residential- and work-spaces following Neufert et al (1980).

In detail, the rectangular window and door openings were normalised based on half-width blocks (125 mm) to reduce the number of cuttings. Openings were positioned both centrally and eccentrically, whereas the eccentric ones were shifted for their half-width. Which nevertheless satisfies the BSI (2004b) condition where the column had to be shifted for 1/5 wall height ($> 0.26m$). All the specimens and their geometrical properties are presented in Table 3.4. All the openings by the size of their areas were conditioned as significant by BSI (2004b).

All the openings had an RC lintel above them; their height was the same as blocks, *i.e.* 10 cm. The $\phi 6$ mm rebars were used as both longitudinal and shear reinforcement. The shear reinforcement was spaced on 5.5 cm near the supports, while 9.3 cm or 8.7 at the middle of the door or window opening.

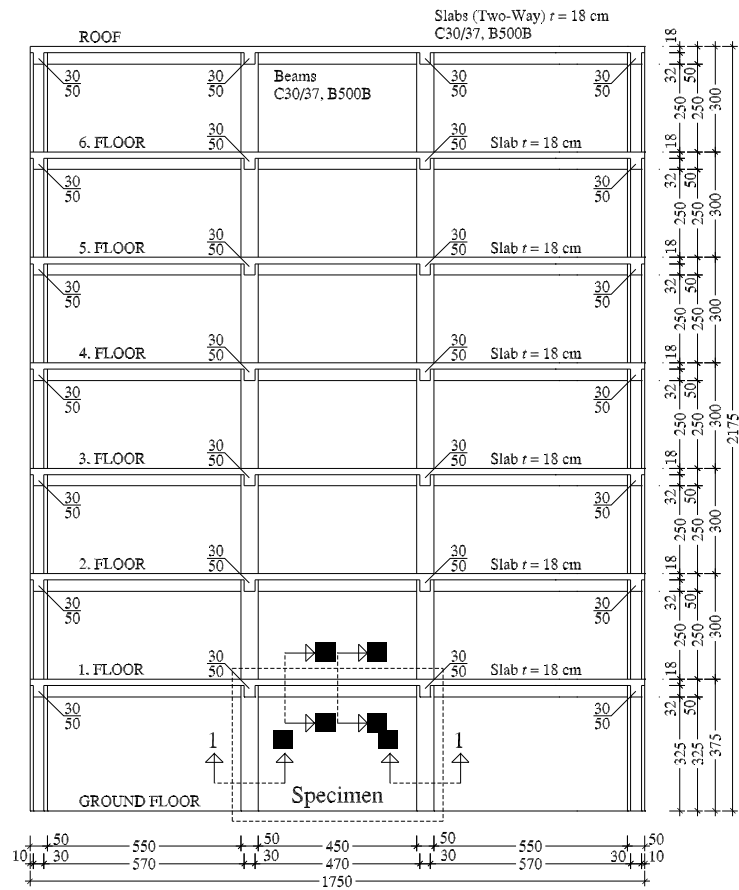
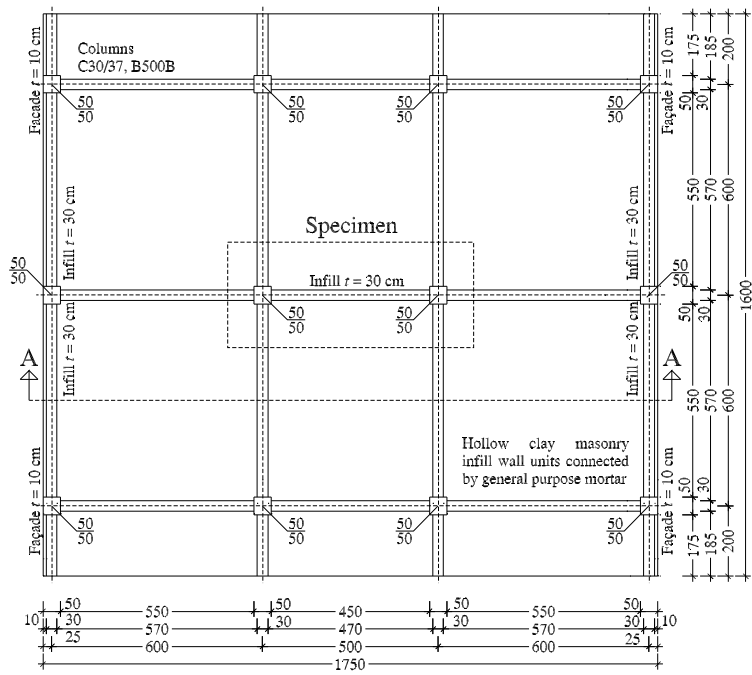


Figure 3.2: Building plan and elevation

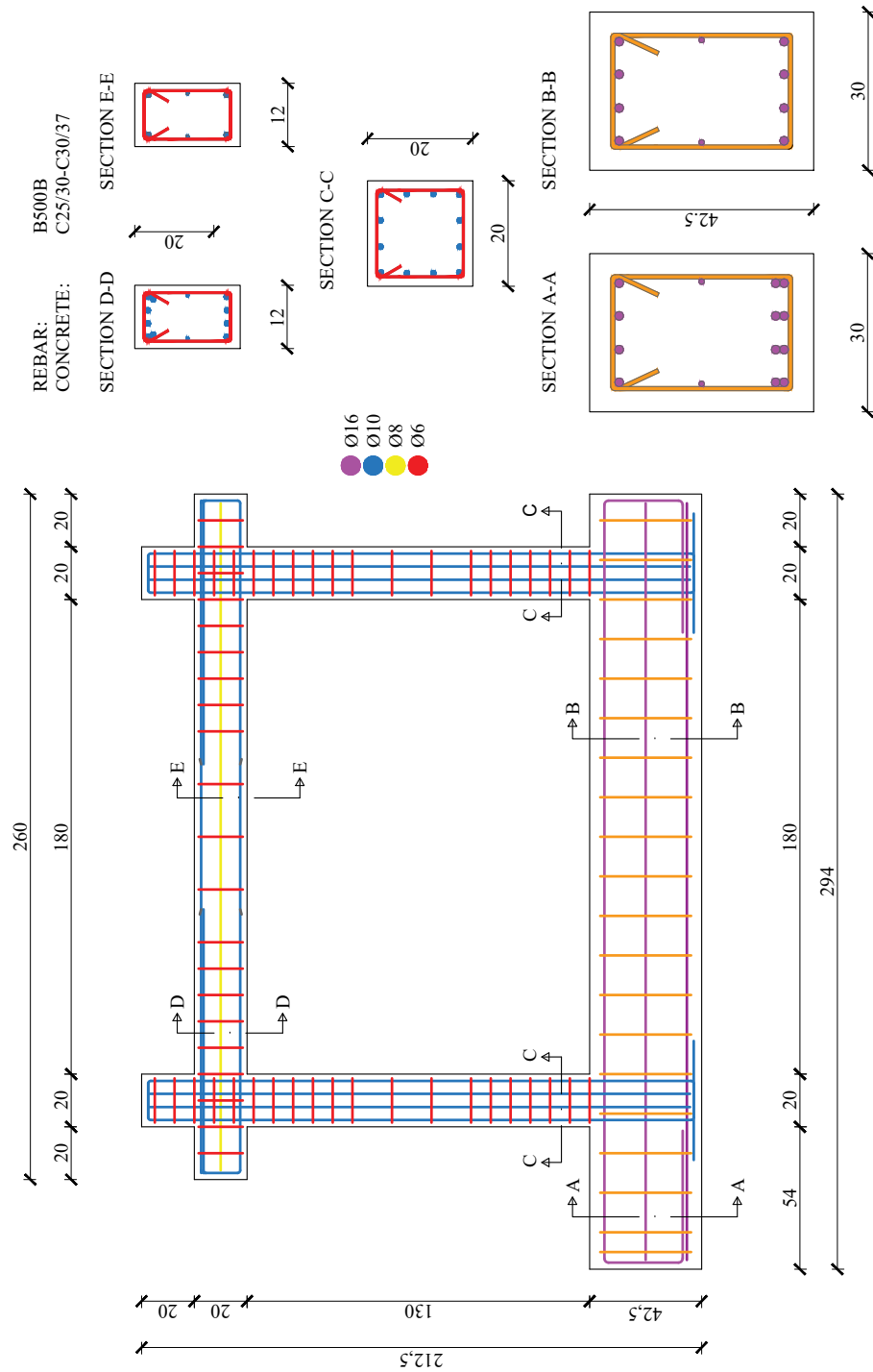


Figure 3.3: Specimen frame reinforcement design (Zovkić, 2013)

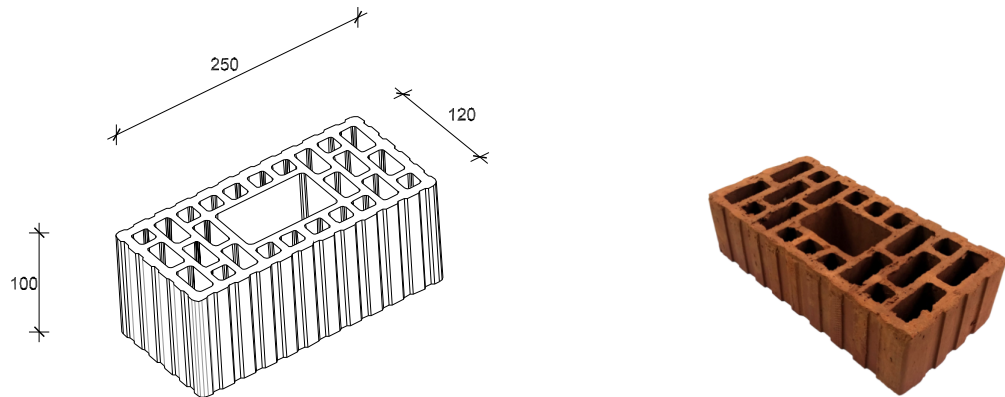
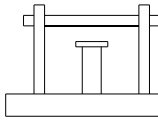
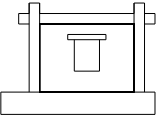
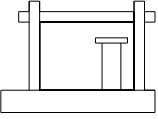
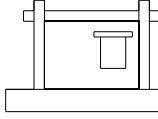
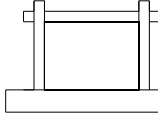
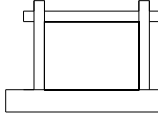


Figure 3.4: Masonry unit as used in the experiments

Table 3.4: RC frames with masonry infill walls specimens

Model mark	Appearance	Opening	
		Type and area	Position
CD		Door $l_o/h_o = 0.35/0.90$ m $A_o = 0.32$ m ² $A_o/A_i = 0.14$	Centric $e_o = l_i/2 = 0.90$ m
CW		Window $l_o/h_o = 50.0/60.0$ cm $A_o = 0.30$ m ² $A_o/A_i = 0.13$	Centric $e_o = l_i/2 = 0.90$ m $P = 0.40$ m
ED		Door $l_o/h_o = 0.35/0.90$ m $A_o = 0.32$ m ² $A_o/A_i = 0.14$	Eccentric $e_o = h_i/5 + l_o/2 = 0.44$ m
EW		Window $l_o/h_o = 50.0/60.0$ cm $A_o = 0.30$ m ² $A_o/A_i = 0.13$	Eccentric $e_o = h_i/5 + l_o/2 = 0.44$ m $P = 0.40$ m
BF			Bare frame
FI			Full infill

The Bareframe (BF) specimen had no infill wall, *i.e.* only the RC frame was tested.

The fully infilled frame (FI) specimen (Fig. 3.5) had infill wall and no openings. The infill wall measured $L_i \times H_i \times T_i = 1.80 \times 1.30 \times 0.12$ m.

The centric door (CD) specimen (Fig. 3.6) had infill wall and door opening that was positioned at the centre. Therefore, the opening was positioned $O_o = 0.90$ m from the edge of the infill wall to the centre line of the opening. The infill wall measured same as the FI specimen, while the opening measured $L_o \times H_o = 0.35 \times 0.90$ m, which gives an area of $A_o = 0.32$ m². Above the opening, RC lintel spanning $L_L = 0.60$ m was positioned. RC lintel had the height of $H_L = 0.10$ m, *i.e.* same as the height of the masonry unit.

The centric door (CW) specimen (Fig. 3.7) had an infill wall and window opening that was positioned at the centre. Therefore, the opening was positioned at $O_o = 0.90$ m, measuring from the edge of the infill wall to the centre line of the opening. The infill wall measured same as FI

specimen, while the opening measured $L_o \times H_o = 0.50 \times 0.60$ m, which gives an area of $A_o = 0.30$ m². Above the opening, RC lintel spanning $L_L = 0.75$ m was positioned. RC lintel had the height of $H_L = 0.10$ m, *i.e.* same as the height of the masonry unit. Below the opening, there was a parapet wall with the height of $H_N = 0.40$ m.

The eccentric door (ED) specimen (Fig. 3.8) had infill wall and door opening that was positioned at the centre. Therefore, the opening was positioned $O_o = 0.44$ m from the edge of the infill wall to the centre line of the opening. The infill wall measured same as FI specimen, while the opening measured $L_o \times H_o = 0.35 \times 0.90$ m, which gives an area of $A_o = 0.32$ m². Above the opening, RC lintel spanning $L_L = 0.60$ m was positioned. RC lintel had the height of $H_L = 0.10$ m, *i.e.* the same as the height of the masonry unit.

The eccentric door (EW) specimen (Fig. 3.9) had an infill wall and window opening that was positioned at the centre. Therefore, the opening was positioned $O_o = 0.51$ m, measuring from the edge of the infill wall to the centre line of the opening. The infill wall measured same as FI specimen, while the opening measured $L_o \times H_o = 0.50 \times 0.60$ m, which gives an area of $A_o = 0.30$ m². Above the opening, RC lintel spanning $L_L = 0.75$ m was positioned. RC lintel had the height of $H_L = 0.10$ m, *i.e.* the same as the height of the masonry unit. Below the opening, there was a parapet wall with the height of $H_N = 0.40$ m.

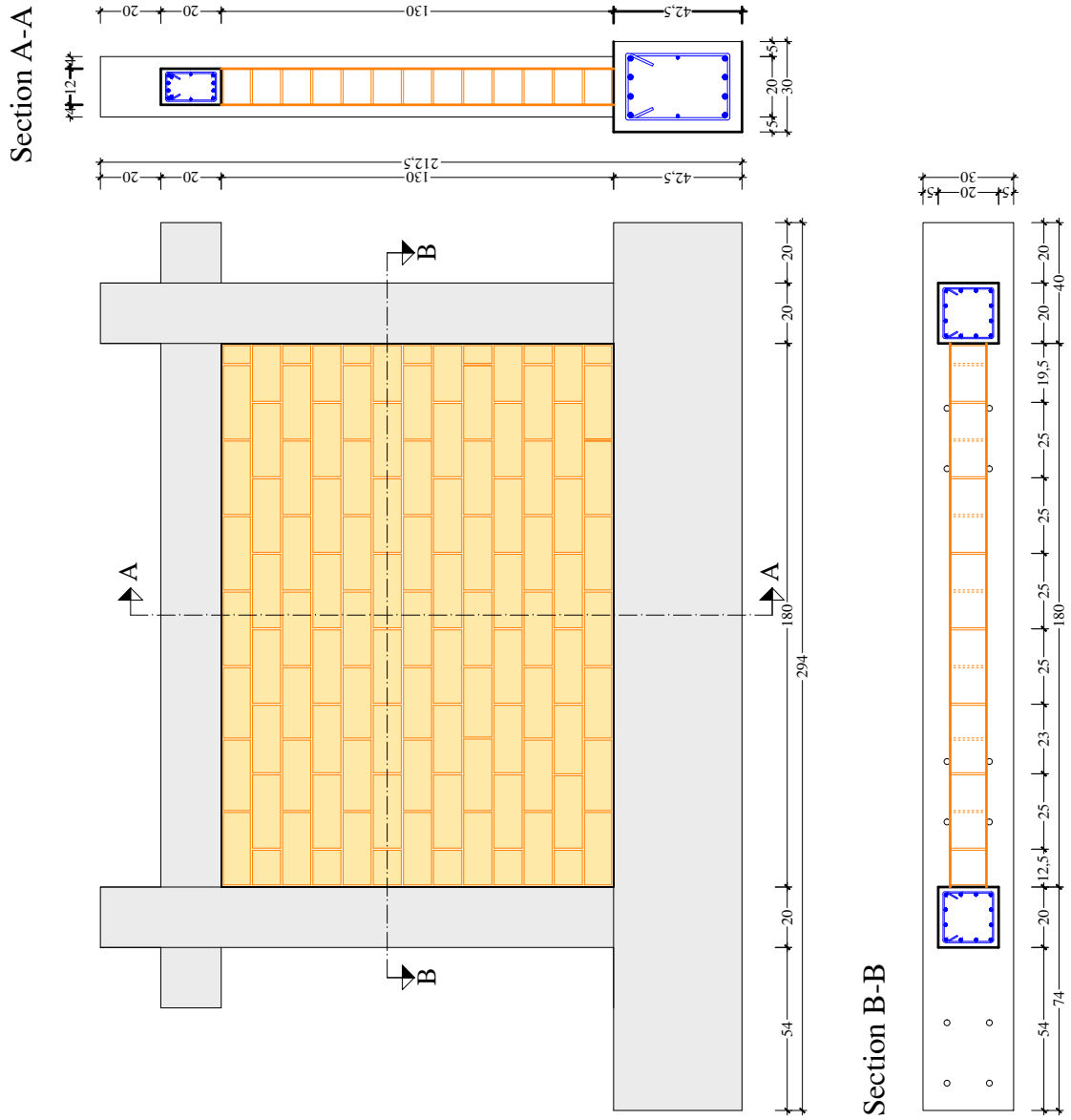


Figure 3.5: Details of FI specimen

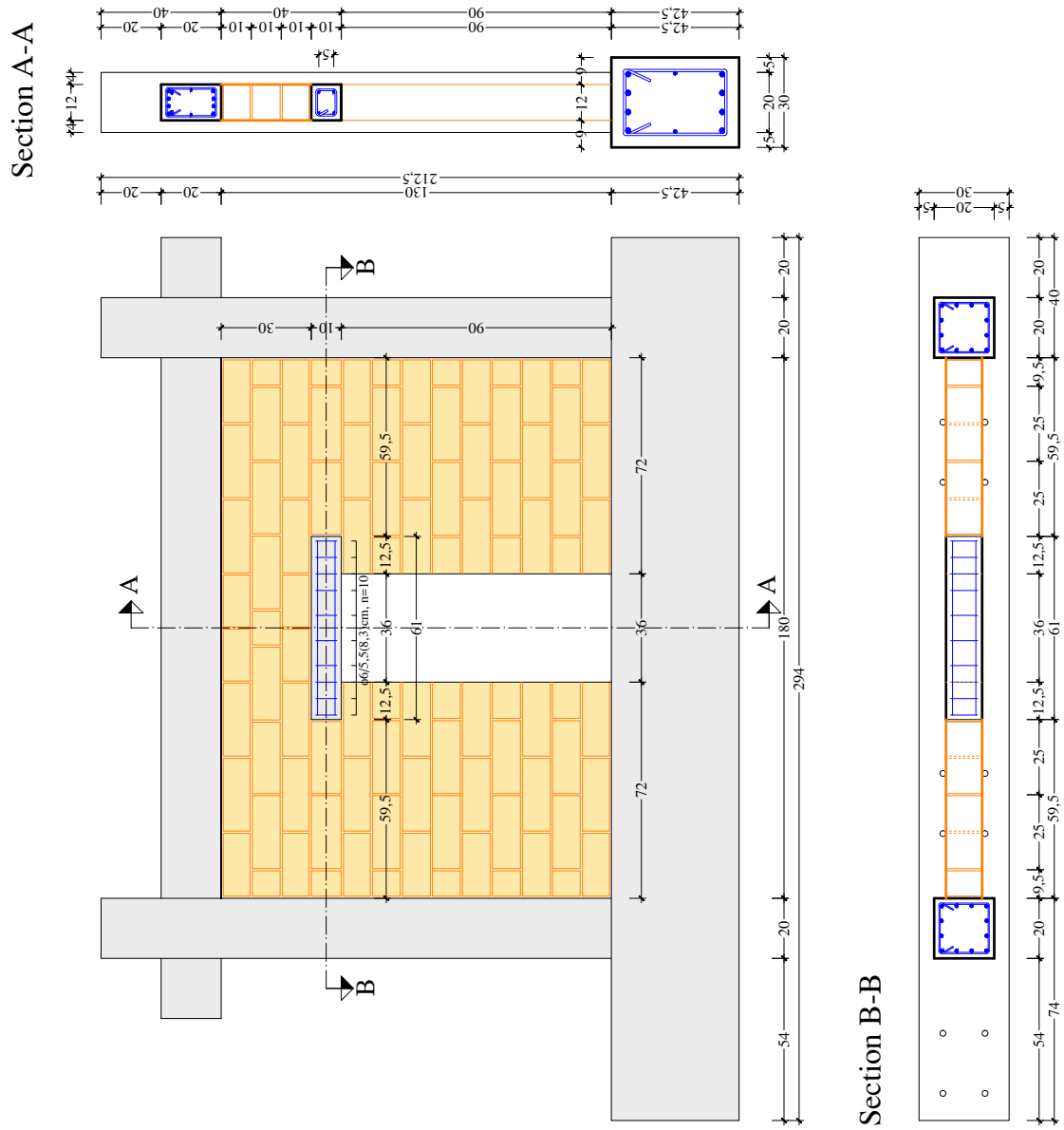


Figure 3.6: Details of CD specimen

Chapter 4

Small scale test series

4.1 Compression test on masonry units

Compression tests on masonry units were executed in accordance with BSI (2015) provisions (Fig. 4.1). The obtained mechanical properties are presented in Table 3.3. From the provided Table 3.3, it is clear that the properties parallel to voids are ≈ 3 times greater than perpendicular to them. The stress to strain relationships of the units on compression test in both parallel and perpendicular direction to the voids was practically linear, as it is visible in Figure 4.2a.



(a) Perpendicular to the direction of voids



(b) In direction of voids

Figure 4.1: Compression test on masonry units (Penava, 2012)

4.2 Masonry triplets tests

The masonry triplets (Fig. 4.3) were tested with and without pretension in accordance with BSI (2002) provisions.

The typical failure mode was not the expected *sliding failure* type of the central unit and its joints. Instead, it was the breakage of the block unit, *i.e.* breaching its tensional strength. Such failure modes were not covered within the EN 1052-3:2002 (BSI, 2002) provisions. This failure mode was a product of unit-to-unit interlock by mortar, *i.e.* *interlocking effect*. That is, due to units voids, the mortar slipped into the voids thus interlocking the units (Fig. 4.5) in joint action.

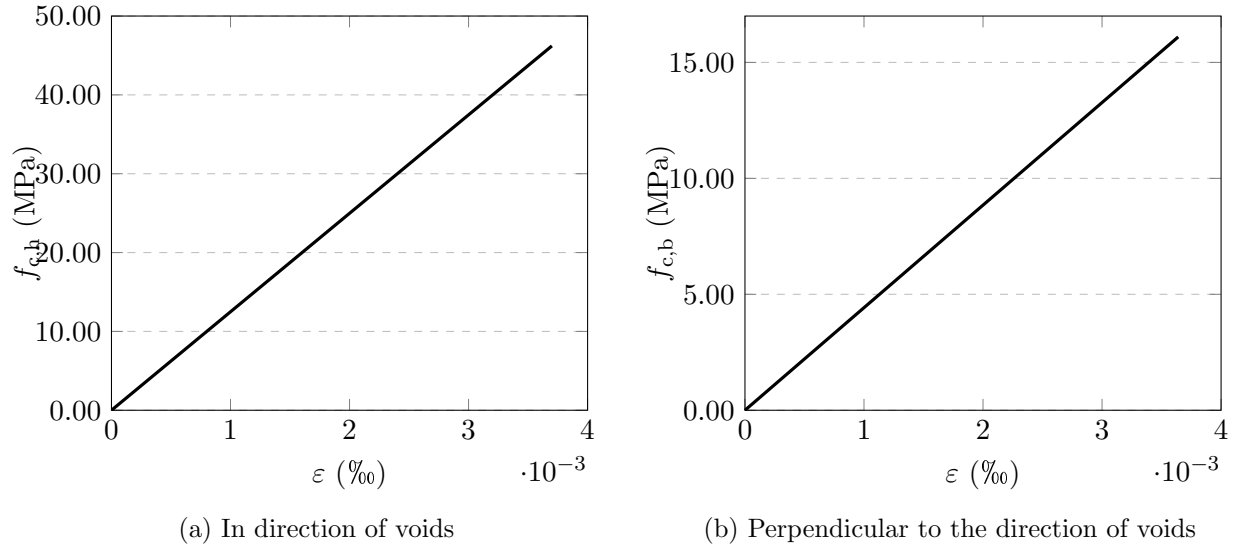


Figure 4.2: Stress–strain relationship from compression tests of masonry units (Penava, 2012)

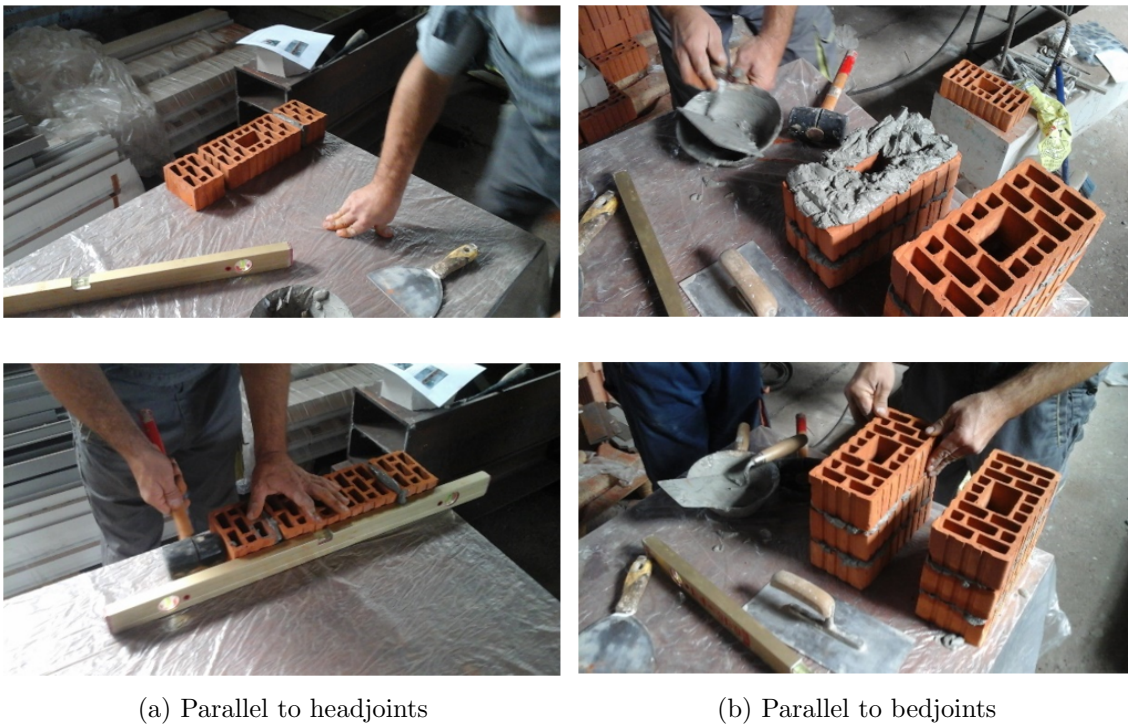


Figure 4.3: Preparation of masonry triplets tests (Penava, 2012)

Consequently, when the mortar was stopped from slipping into the voids by filling the voids with paper, the shear strength had halved (Fig. 4.6, Tab. 4.1) and the *sliding failure* occurred.

The results from triplet tests are presented in Figure 4.6 and Table 4.1. The tests included specimens where the mortar was and was not permitted to slip into the blocks voids. The tests where the mortar slippage was allowed included 12 samples, whereas, when the slippage was permitted, only 3 specimens were tested. As stated in previous paragraph, the shear strength is nearly double (f_{v0} 0.35 vs. 0.72 MPa) while friction angle ($\tan \alpha$ 0.24 vs. 0.77 MPa) nearly tripled the value when



Figure 4.4: Tensional failure parallel to bedjoints (Penava, 2012)

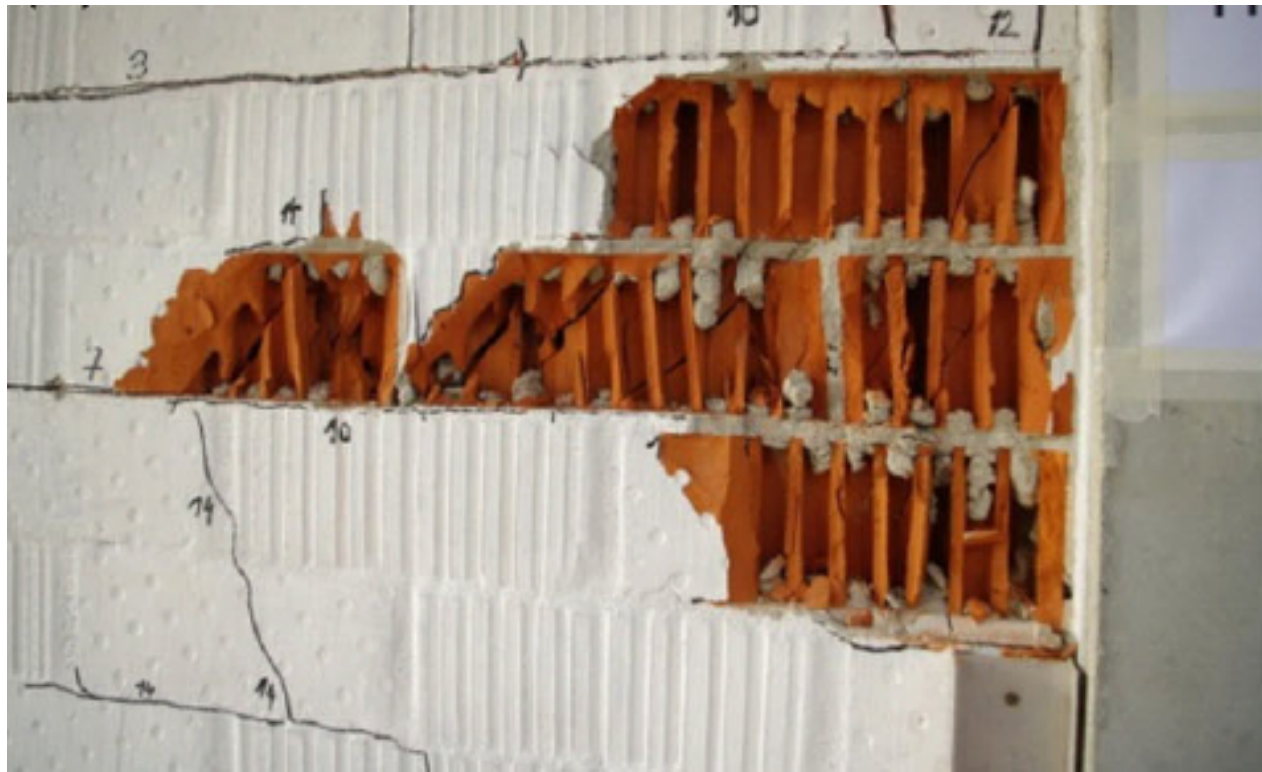


Figure 4.5: Interlocking effect (Penava, 2012)

the mortar was allowed to slip into the voids.

Table 4.1: Results from testing initial shear strength Penava (2012)

Specimen	Normal stress $f_{p,n}$ (MPa)	Shear strength $f_{v,0}$ (MPa)	
		No mortar slippage	Mortar slippage
1	0.20	0.28	0.83
2	0.20	0.49	
3	0.20	0.43	
Mean	0.20	0.4	
1	0.60	0.5	1.14
2	0.60	0.61	
3	0.60	0.34	
Mean	0.60	0.46	
1	1.00	0.65	1.45
2	1.00	0.62	
3	1.00	0.5	
Mean	1.00	0.59	
Mean value of initial shear strength f_{v0} (MPa)		0.35	0.72
Characteristic initial shear strength f_{vk0}		0.25	
Inner friction angle $\tan \alpha$		0.24	0.77
Characteristic inner friction angle $\tan \alpha_k$		0.19	

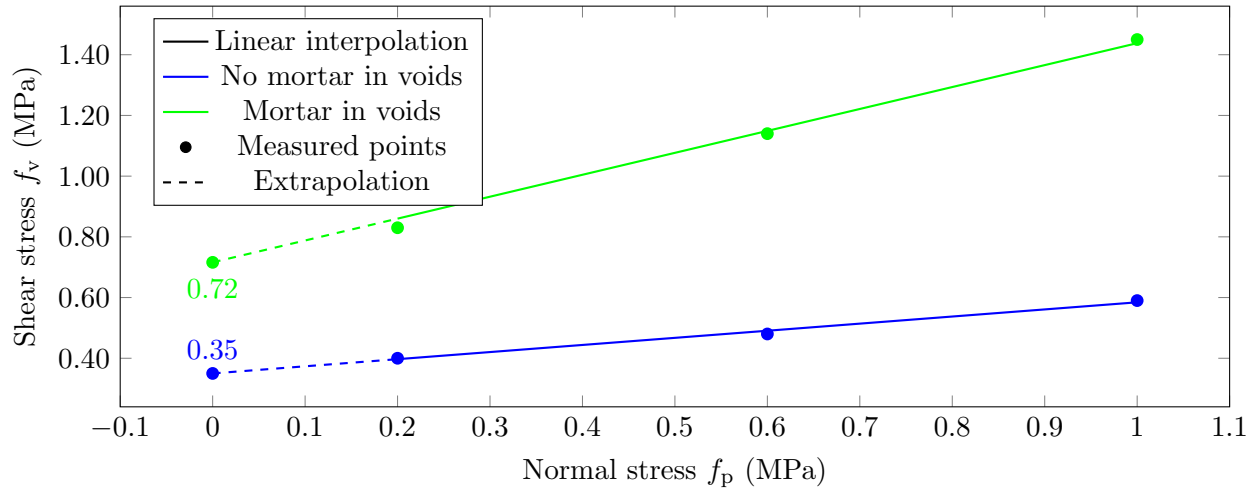


Figure 4.6: Determining initial shear strength by Mohr-Coulomb strength theory

4.3 Masonry wall compression test

The masonry wall specimens were assembled using the units and mortar mentioned above. They were tested following the CEN (2004) provisions. The tests consisted of 3 specimens, loaded by a hydraulic cell and measured by force transducers. The deformations were recorded by 4 LVDT's (Fig. 4.7c). A steel beam was used in order to diminish the localization of stress.

Force F_w and displacement d_w at failure are presented in Table 4.2. In Figure 4.8, an averaged stress to strain behaviour of the previous tests are plotted. The specimens' behaviour was in line with those expected by the standard.



(a) Specimens



(b) Testing



(c) LVDT placement

Figure 4.7: Masonry wall specimen testing (Penava, 2012)

Table 4.2: Results of masonry wall's compression test

Number of samples n	Max. force F_w (N)	Max. stress f_w (MPa)	Max. displacement d (mm)	Max. strain ε (‰)
1	52337	0.86	0.39	2.17
2	127176	2.08	0.90	5.00
3	52284	0.85	0.39	2.17
Average	77266	1.26	0.56	3.11

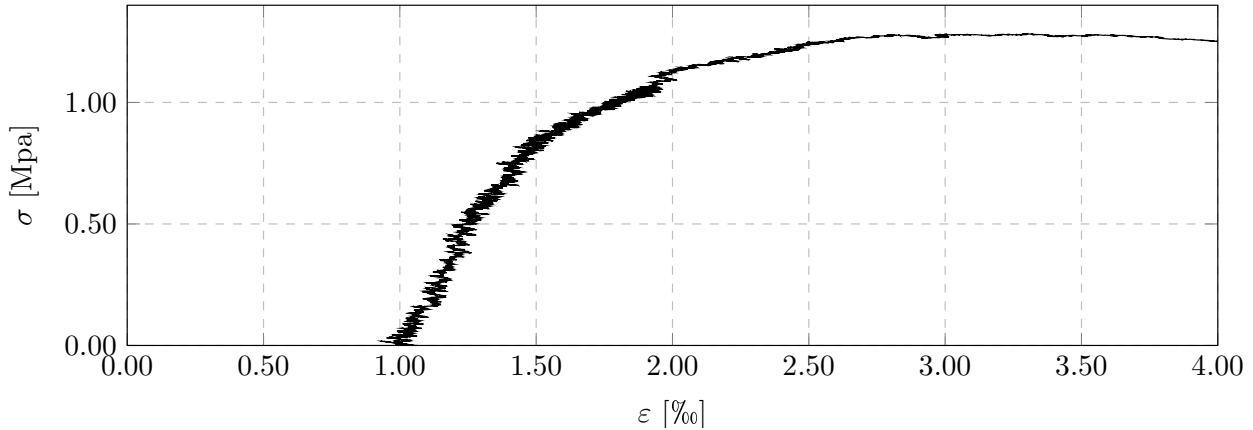


Figure 4.8: Averaged stress – strain behaviour of masonry wall compression tests

4.4 Out-of-plane bending tests of masonry wall

4.4.1 Samples preparations

These tests were done by the student of this thesis, therefore, they are described in more detail.

This dissertation's focus is on OoP behaviour; therefore, OoP bending tests of URM walls were carried out following EN 1052-2:2002 (CEN, 2002) provisions. The provision calls for two test set-ups, one with the load parallel and the other perpendicular to the bedjoints. Also, the provision states that the minimum number of wall samples should be 3 per test type. On the other hand, Sorić (2016) recommends using 10. The latter was accepted. The preparations were done following the provisions as well (Fig. 4.10)

The specimens were designed following the CEN (2002) provisions and are shown in Figure 4.9.

The specimens were tested with *Controls 50-C1201/BFR by 50-C1200/8* apparatus (Fig. 4.11), with its internal hardware set to correspond the boundary conditions as described in Figure 4.9.

4.4.2 Results

Specimens failed as predicted (Fig. 4.12); namely, when the load was parallel to the bedjoints, the failure occurred when the tensional strength of mortar-unit connection in the bedjoints was reached. The wall specimens thus separated into two parts (Fig. 4.12a). On the other hand, those with perpendicular load had a failure that occurred through headjoint mortar and the blocks themselves. Thus, by breaching the tensional strength of blocks (Fig. 4.12b).

The flexural strength (f_x) was calculated using Equation (4.1).

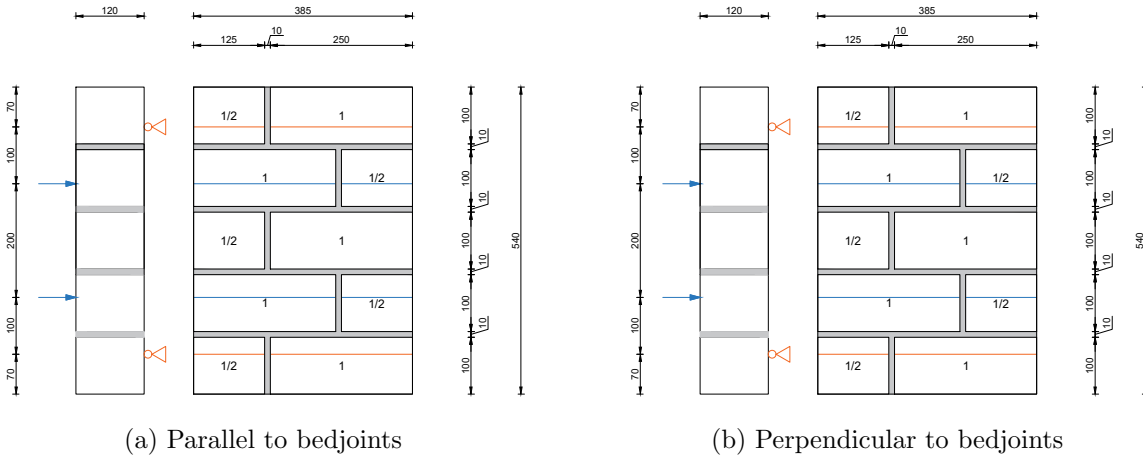


Figure 4.9: URM wall OoP bend test characteristics



Figure 4.10: URM wall OoP bend test preparation of samples

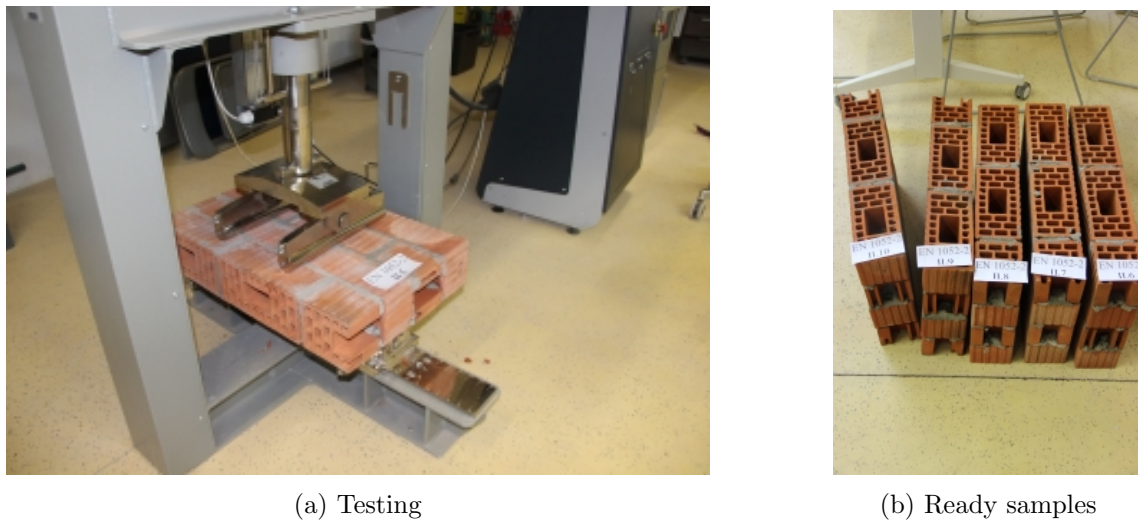


Figure 4.11: URM wall samples set for for OoP bend test

$$f_x = \frac{3F_{\max}(l_1 - l_2)}{2bt} \quad (4.1)$$

Where F_{\max} is maximum force, l_1 distance between supports, l_2 distance between loads, b specimen

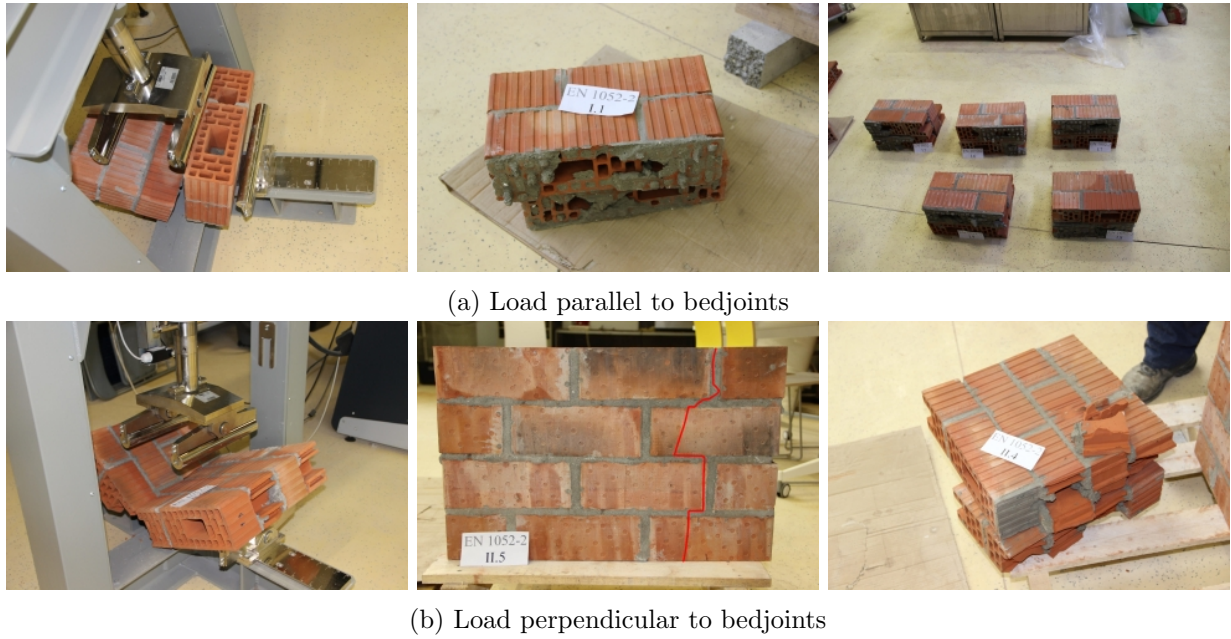


Figure 4.12: URM wall samples characteristic failure modes

length and t specimen thickness.

The results are presented in Table 4.3 and Figure 4.13. The strength of wall units subjected to OoP bending when the load was parallel to bedjoints was similar to mortar –masonry unit connection strength (adhesion). Likewise, when the load was perpendicular, the strength was the tensional strength of masonry perpendicular to its voids. OoP flexural strength when the load was parallel to bedjoints was about 45 % smaller when compared to strength perpendicular to bedjoints. Also, the strength variation was greater when the load was parallel to bedjoints.

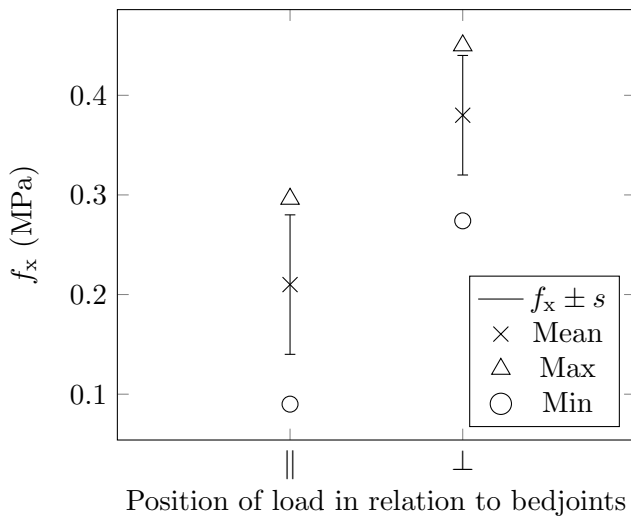


Table 4.3: OoP bending test strength results

Properties	Load pos. bedjoints		Unit
		⊥	
F_{max}	4.07	6.69	kN
f_x	0.21	0.38	MPa
s	0.07	0.06	MPa
c_v	0.28	0.18	/

F_{max}	Maximum OoP force
f_x	OoP flexural stress
s	Standard deviation
c_v	Variation coefficient

Figure 4.13: OoP bending test strength results

Chapter 5

IP-plane test series

5.1 Preparation of specimens

All six specimens that were described in Section 3 were subdued to IP cyclic, quasi-static loading within the setup as described in Figure 5.1 in the works by Penava (2012). Hence, the details about the experiments were omitted as it was not an integral part of this thesis. Only the necessary information that aid the further work were presented.

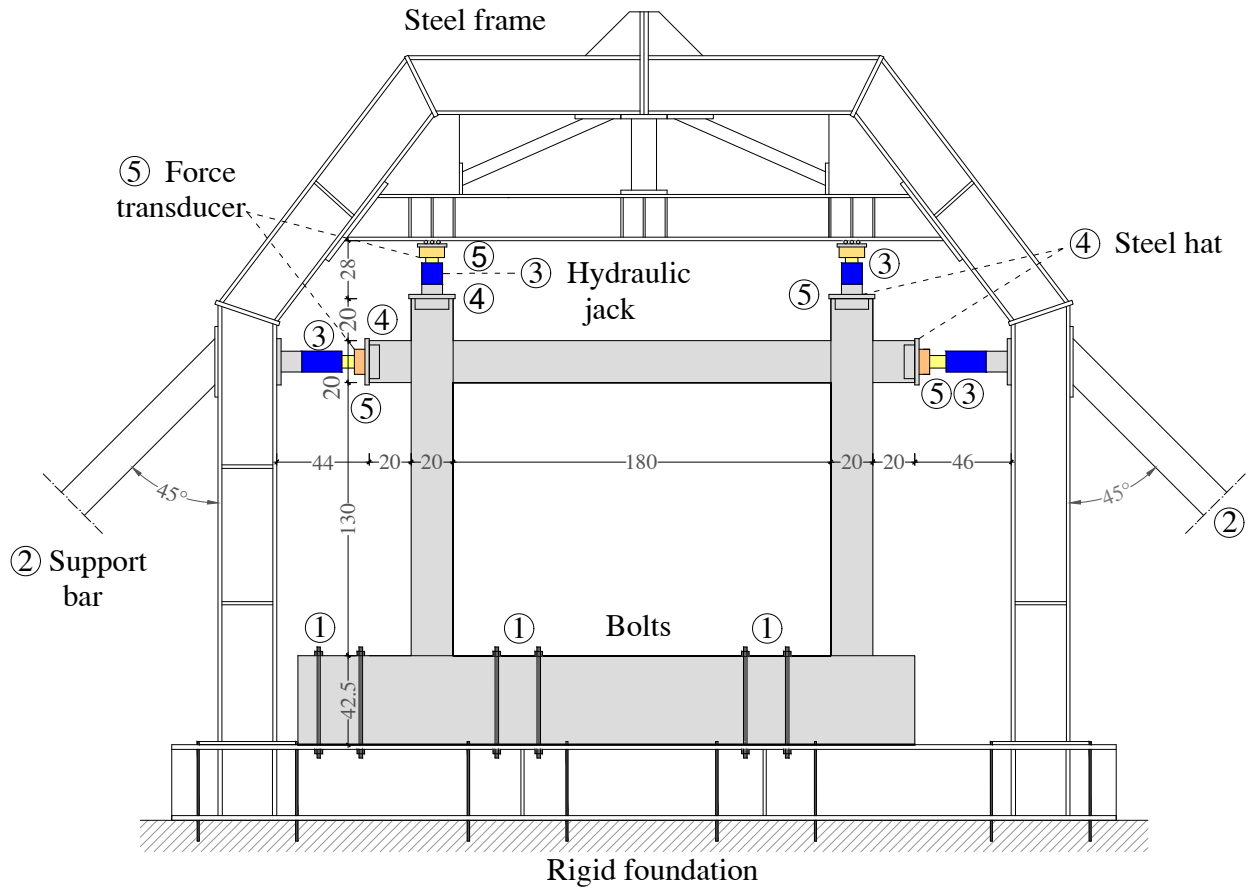
In this paragraph the elements as enumerated in Figure 5.1 are referenced in brackets (#). The specimens were placed inside the robust steel frame (1), fixed to a strong floor. The fixations were held at both the foundation beam and at the foot of backing columns (5) by anchoring bolts. The specimens themselves had vertical holes drilled in the lower beam, where the fully threaded steel studs (4) were placed; thus, they connected the foundation beam to the steel frame (1). Both gravity and IP loads were transmitted using hydraulic presses (2). The loads were recorded by force transducers (3). Hydraulic presses were controlled manually via a hydraulic pump.

The IP *i.e.* horizontal cyclic, quasi-static load was introduced to the specimens via protocol as designated in Figure 5.2. The force control was used with ± 10 kN steps, repeating each end-step twice. The protocol was executed until the force stagnated, after which displacement control was used (pushover). The experiment kept the vertical forces at 365 kN on each column with ± 10 % variance.

In Figure 5.3 the boundary conditions and the arrangement of displacement measuring devices are presented on a CD specimen. In this paragraph, parts of measuring equipment as designated in Figure 5.3 are referenced through brackets (#), whereas, a is referred for front and b for backside. Same placement patterns were used on others, except for BF and FI specimens. The BF specimen had no infill wall; thus, there was no equipment outside the frame. On the other hand, the FI specimen did not have diagonal wire measuring devices around the openings (11a, 11b, 12a, 12b) as others did. Additionally, diagonal displacements were measured on the infill wall (10a, 10b) and the frame (9a, 9b) to measure the compression struts' displacements. Deformers were placed at the RC columns foot (3, 4) and on the upper beam near the columns (1, 2). Deformers were placed to measure local deformations where the plastic hinges were likely to occur. Linear variable differential transducers (LVDT) were placed on the ends of upper beams (5, 6) and columns (7, 8) to measure horizontal and vertical displacements.

5.2 Results

The hysteretic loop from the second load cycles and their envelopes are presented in Figure 5.4. The second cycle was chosen to connect with the pushover part and for a more reliable representation



- | | | | | | |
|---|----------------------------|---|-----------------|---|-------------------|
| 1 | Steel frame | 2 | Hydraulic press | 3 | Force transducers |
| 4 | Fully threaded steel studs | 5 | Backing column | | |

Figure 5.1: IP test setup

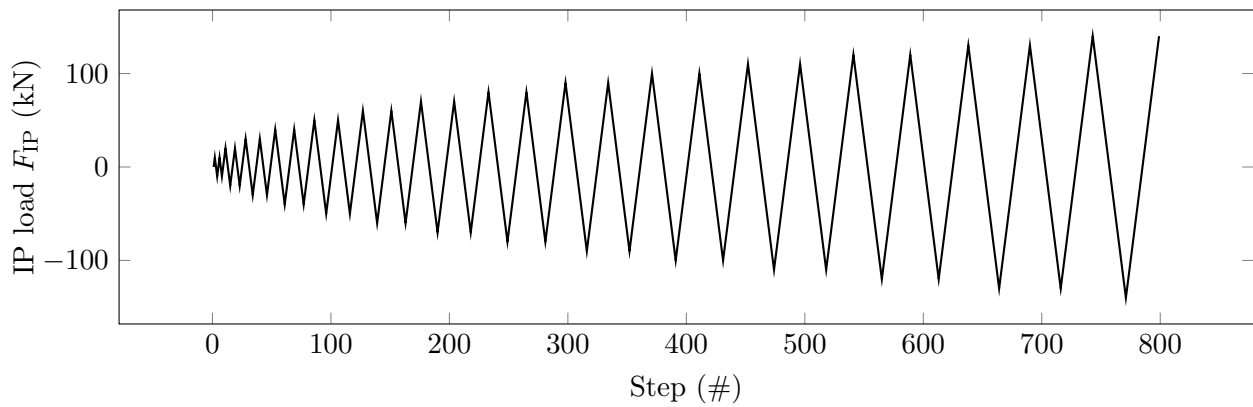


Figure 5.2: IP load protocol (force control part)

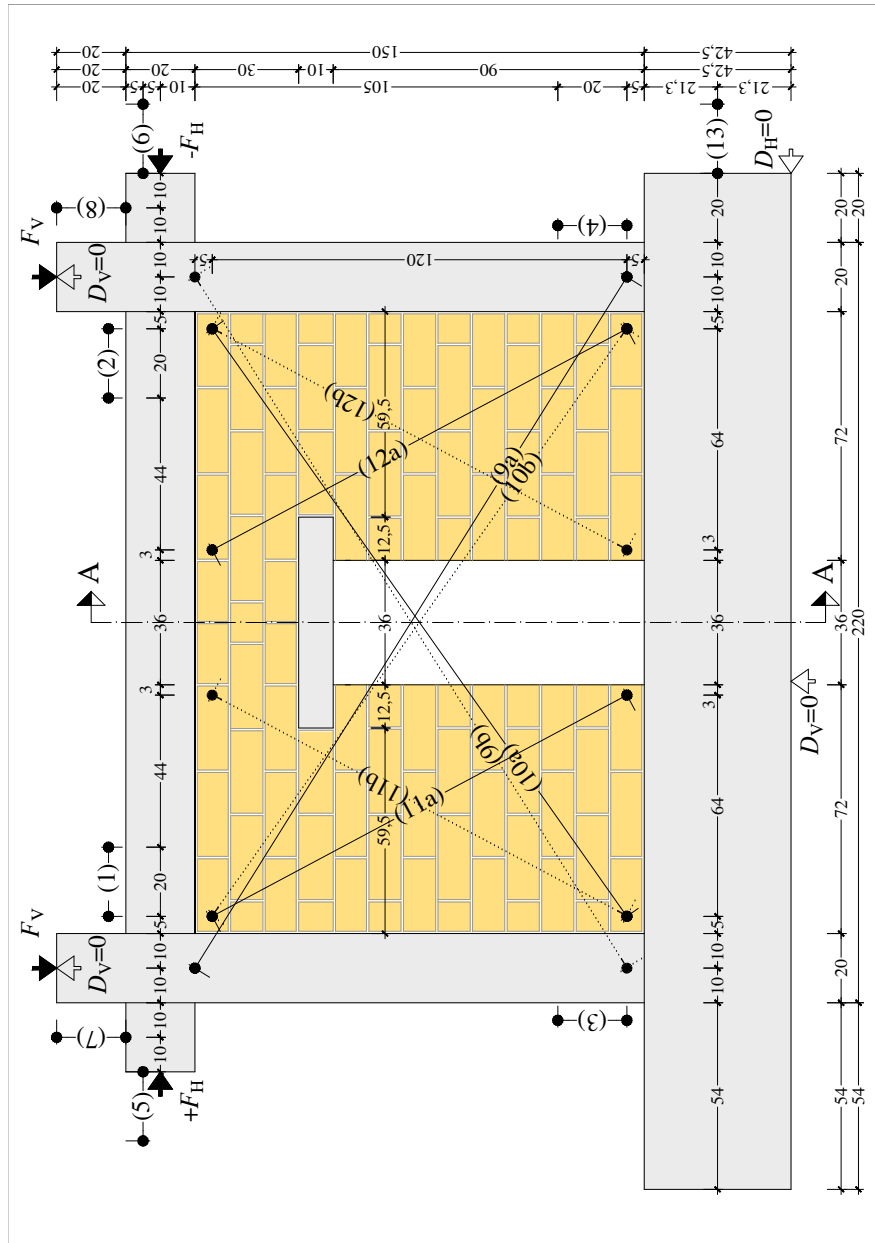


Figure 5.3: IP test series measuring equipment and boundary condition arrangements

of the infill wall's current damage state.

It was observed that the specimens had linear-elastic behaviour up to the *slight-damage* level at 0.05 – 0.10 % d_r . Afterwards, the stiffness decreased with stimulations lateral load resistance increased. At 0.20 – 0.30 % d_r lateral load resistance peaked and was either maintained or slightly increased up to 0.50 % d_r . Afterwards, the degradation started and reached BF's load-capacity at about 1.00 % d_r .

The infill wall and the frame behaved as a single unit up to the drift of 0.50 %. The infill wall's influence on the overall behaviour observed considerable loss at about 0.75 – 1.00 % d_r . However, the load-bearing capability did not degrade to the BF's; instead, it was about 1.25 times higher.

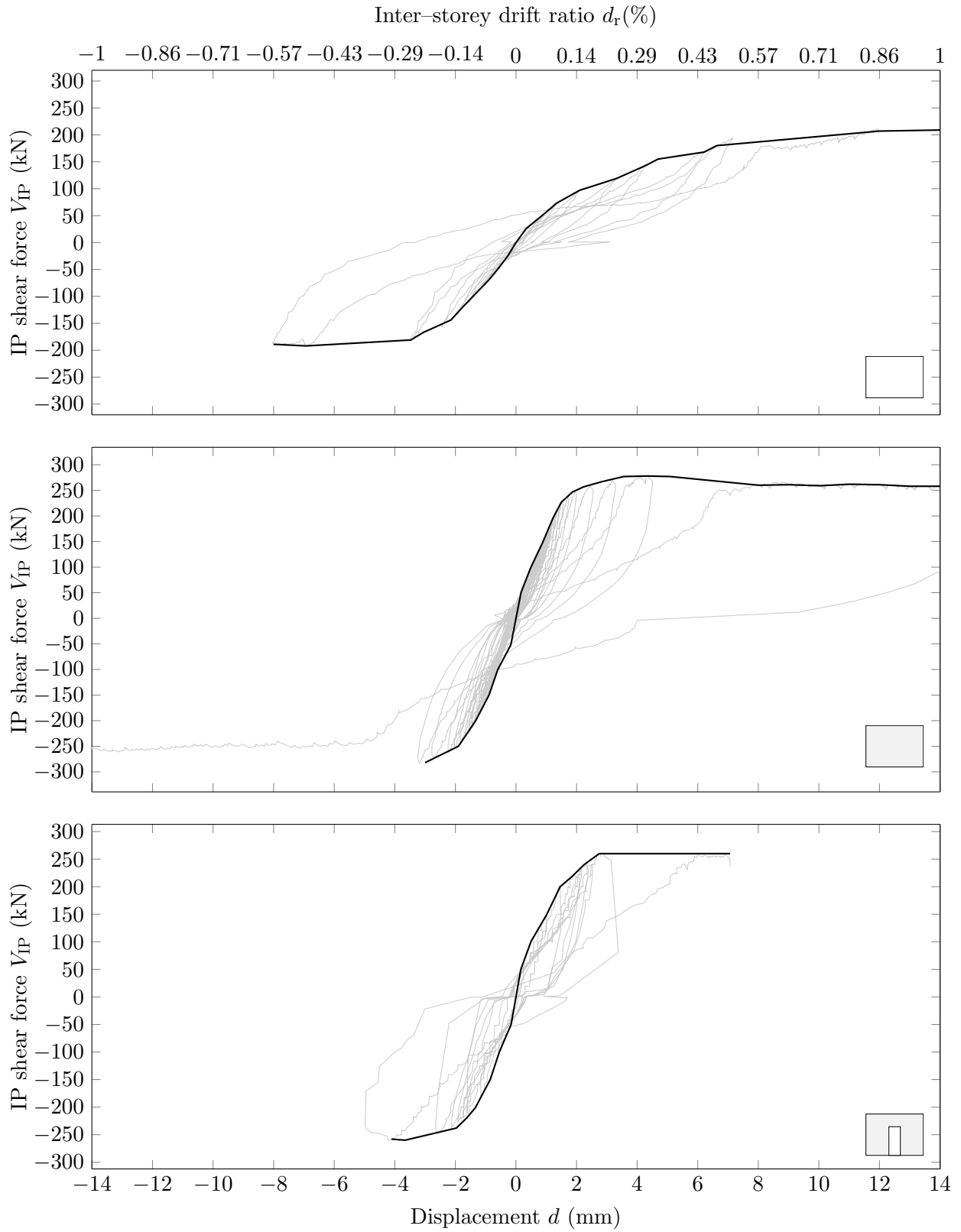


Figure 5.4: IP hysteresis loops and resistance envelope curves

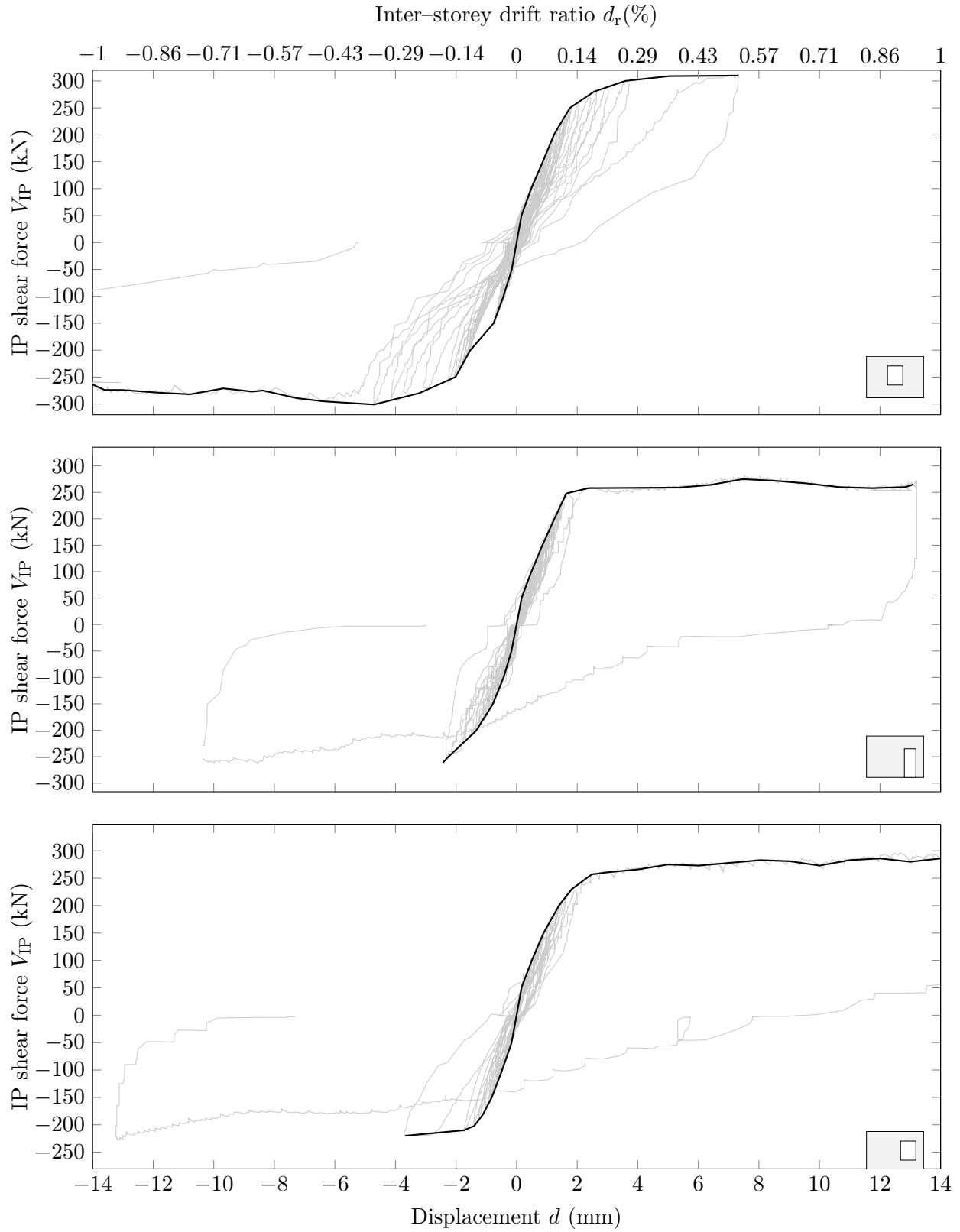


Figure 5.4 (cont.): IP hysteresis loops and resistance envelope curves

The positive *vs.* negative IP cyclic envelopes were compared in Figure 5.5. There were measurable differences in all specimens. In the case of BF and FI ones, the slight drop in load-bearing capacity can be attributed to *Bauschinger effect* in the reinforcement along with previously damaged concrete.

The *Bauschinger effect* describes the lowering of the stress response on the inverse part of the cycling curve of the reinforcing steel after the yielding point was reached. For example, if the yielding point $f_{y,t}$ in tension is reached and it cycles to the same point in compression $f_{y,c}$, the latter would be lower $f_{y,t} > f_{y,c}$. The cause of the effect is attributed to microscopic stress distribution of the material.

Nevertheless, in the case of specimens with openings, there is a shift in initial stiffness as well as a drop in load-bearing capacity that could not be attributed to the *Bauschinger's effect* entirely. The differences were attributed to stiffness degradation, the direction of loading and experimental specific matter.

The stiffness degradation would mean that the infill wall was already cracked *i.e.* softened when loaded in the opposite direction. At the same time, the load direction is critical with eccentric openings if loaded in the direction of longer infill wall segment; unlike the shorter side, there is more area to develop compressive strut. Therefore, the performance would be greater in that direction until the infill wall is crushed, where they would line up.

The observed occurrences of cracks and damages are presented in Table 5.1, where they are described by the specimen at various drift ratios. The crack patterns *i.e.* damage states at the end of loading are presented in Figure 5.6. From the data, the infill failure mechanism could be described in three basic modes: 1) Bending; 2) Shear (diagonal); 3) Bedjoint sliding shear failure.

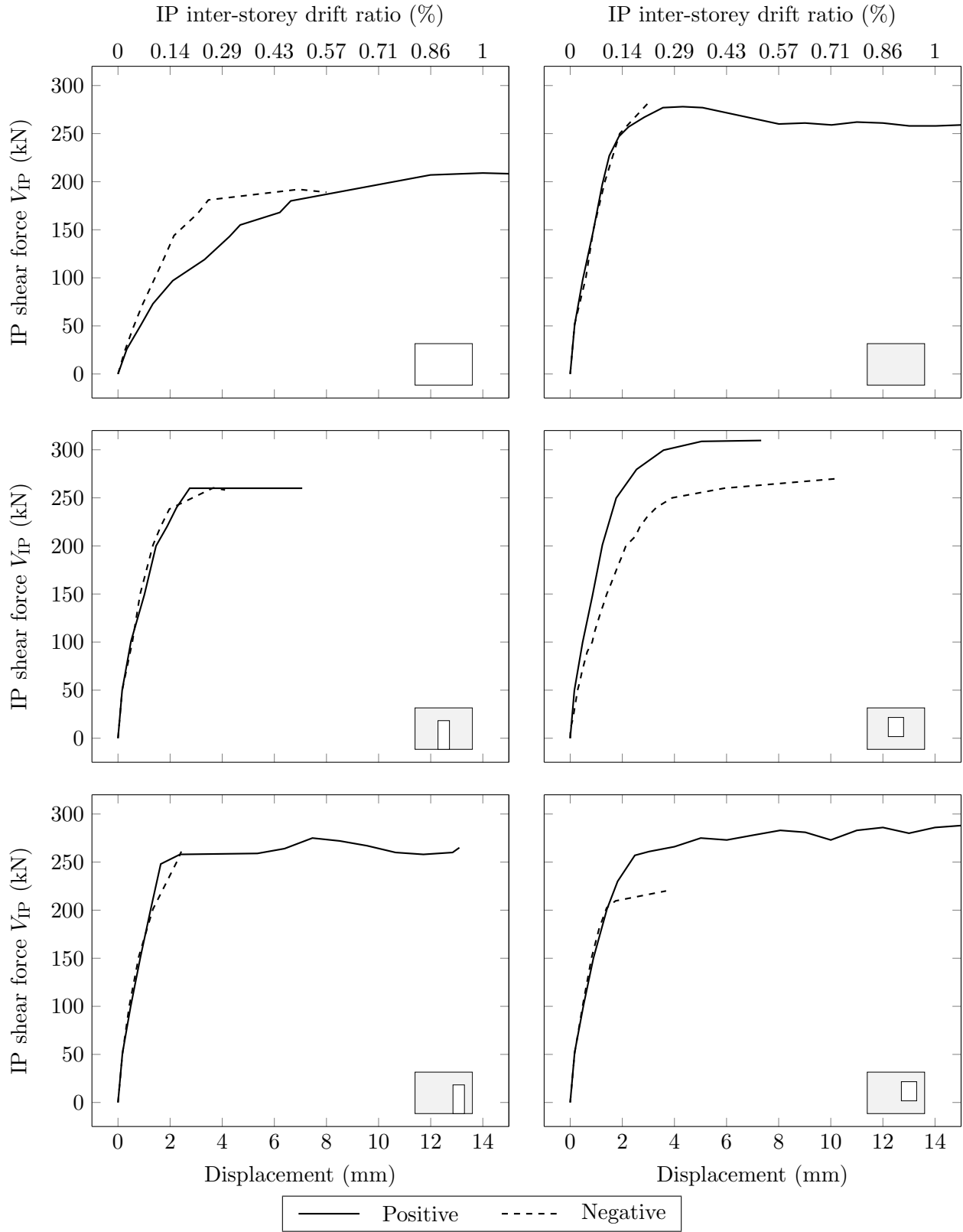


Figure 5.5: Positive *vs.* negative IP cyclic envelopes

Table 5.1: Observed occurrences in IP experiments with relation on inter-storey drift (d_r)

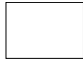

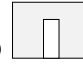
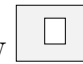
Specimen	d_r (%)	Occurrence
BF 	0.41	Tensile cracks occurred at the bottom of the columns.
	0.76	Tensional cracks observed on upper beam.
	0.86	Paring of cover concrete in the columns.
FI 	0.05	Upper beam - infill wall bedjoint failure. Upper corners developed hairline cracks.
	0.06	Second bedjoint failure in the upper third part of the infill wall.
	0.16	Thin, step cracks formed from corners to bedjoint failure line under 45°. Horizontal failure in the lower third of the infill wall.
	0.42	The existing cracks widen, while the crushing occurred between the columns and infill wall.
	0.49	Tensile and crushing cracks observed on the upper beam and columns. Bedjoint failure in the thirds, infill wall crushing in the contact with the
	1.09	columns and diagonal cracks that stretch from infill walls corners to the middle caused infill wall failure.
	CD 	0.10
0.14		Debonding of infill wall and lintel, diagonal cracks between RC columns formed.
0.19		Failure of bedjoint that stretches from top of the lintel to end of the infill wall.
0.35		Significant widening of existing cracks.
0.42		Hairline cracks observed on top and bottom of columns.
0.50		Infill wall detaches from columns. Infill wall had diagonal failure and corner crushing, which left the infill wall unstable.
CW 	0.11	Diagonal cracking trough blocks and mortar between upper beam and lintel.
	0.12	Horizontal tensional cracks in the openings corner, about blocks width in length.
	0.16	Diagonal tensional cracking between the columns and openings, infill wall completely debonds from upper beam, and vertical cracks start forming above the opening.
	0.18	New diagonal cracks occur, while existing are enlarging. Above and below the opening, bedjoint fails, causing the infill wall to separate in parts left and right of the opening.
	0.28	Greatest load-bearing shear force measured, openings corners begin to crush.
	0.49	Diagonal cracks widen significantly, and spread left and right of the opening.
	0.49	Deboding of columns and infill wall was observed in the lower half of the specimen.
0.49	Multiple hairline cracks on the bottom and top of the columns.	

Table 5.1 (cont.): Observed occurrences in IP experiments with relation on inter-storey drift (d_r)



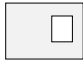
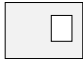
Specimen	d_r (%)	Occurrence
CW 	0.57	Widening of tensional cracks and parings of cover concrete due to crushing.
	0.79	Tensional hairline cracks appear on the upper beam.
	0.86	Complete crushing failure of openings corner.
	1.29	Damages to the parts of the infill wall left and right of the opening, caused by multiple tensional diagonal cracks under 65° slope. Degrading in load-bearing capacity.
	1.29	Cracks extend through whole height of the section, while cover concrete debonds.
ED 	0.09	Slippage on upper beam-infill wall contact near the upper corners. Afterwards, diagonal cracks forms that advances to lintel. Diagonal hairline cracks occur on the larger part of the infill that stretches from column to the opening.
	0.11	Tensional stress causes separation of mortar joints and masonry infill units, while cracks occur on separate corners of the infill wall due to crushing.
	0.11	Crossed cracks occur due to tension, sloped under 45°. Failure of bedjoint that stretches from lintel to the end of infill wall caused separation of the infill wall into to parts: beside and atop the opening.
	0.43	Short hairline cracks occurred on the concrete columns.
	0.57	Widening of tensional diagonal cracks. In the openings and infill walls corners, the outer shells of the clay block fall off. Max. Force of 276 kN was achieved
	0.72	Tensile cracks extend tough whole height of the column.
	0.78	Short hairline cracks occurred on the upper beam.
	0.92	The cover concrete at the bottom of columns falls off.
0.93	The shorter side of masonry infill wall had cracked significantly, while the corners were completely crushed. Multiple diagonal cracks formed, while the existing ones have widened. Infill walls had a diagonal tensile failure between the frame and the opening. Failure of openings corners due to crushing.	
EW 	0.10	Slippage on upper beam-infill wall contact near the upper corners. Afterwards, diagonal cracks forms that advances to lintel.
	0.12	Diagonal hairline cracks occur on the larger part of the infill that stretches from column to the opening. Crushing of corners caused crack formation in that area.
	0.14	Failure of bedjoint that stretches from top of the lintel to end of infill wall. Infill wall debonds from the columns, causing openings corners to crush.

Table 5.1 (cont.): Observed occurrences in IP experiments with relation on inter-storey drift (d_r)

Specimen	d_r (%)	Occurrence
EW 	0.22	Diagonal cracks extend through the masonry units and mortar.
	0.29	Multiple tensional diagonal cracks formed. Vertical hairline cracks occurred above the openings corners.
	0.41	Hairline cracks observed on tensional parts of columns.
	0.58	Tensional diagonal cracks caused clay blocks outer shell to fall out at the infill walls corners. Failure of bedjoint at top of lintel.
	0.64	Tensional cracks widen while the crushing parts caused paring of cover concrete.
	0.71	Tensional cracks observed on upper beam.
	1.30	Openings top corner separates from the rest of the infill wall. Infill wall failed at 291 kN due to bedjoint failement and tensional diagonal cracking.

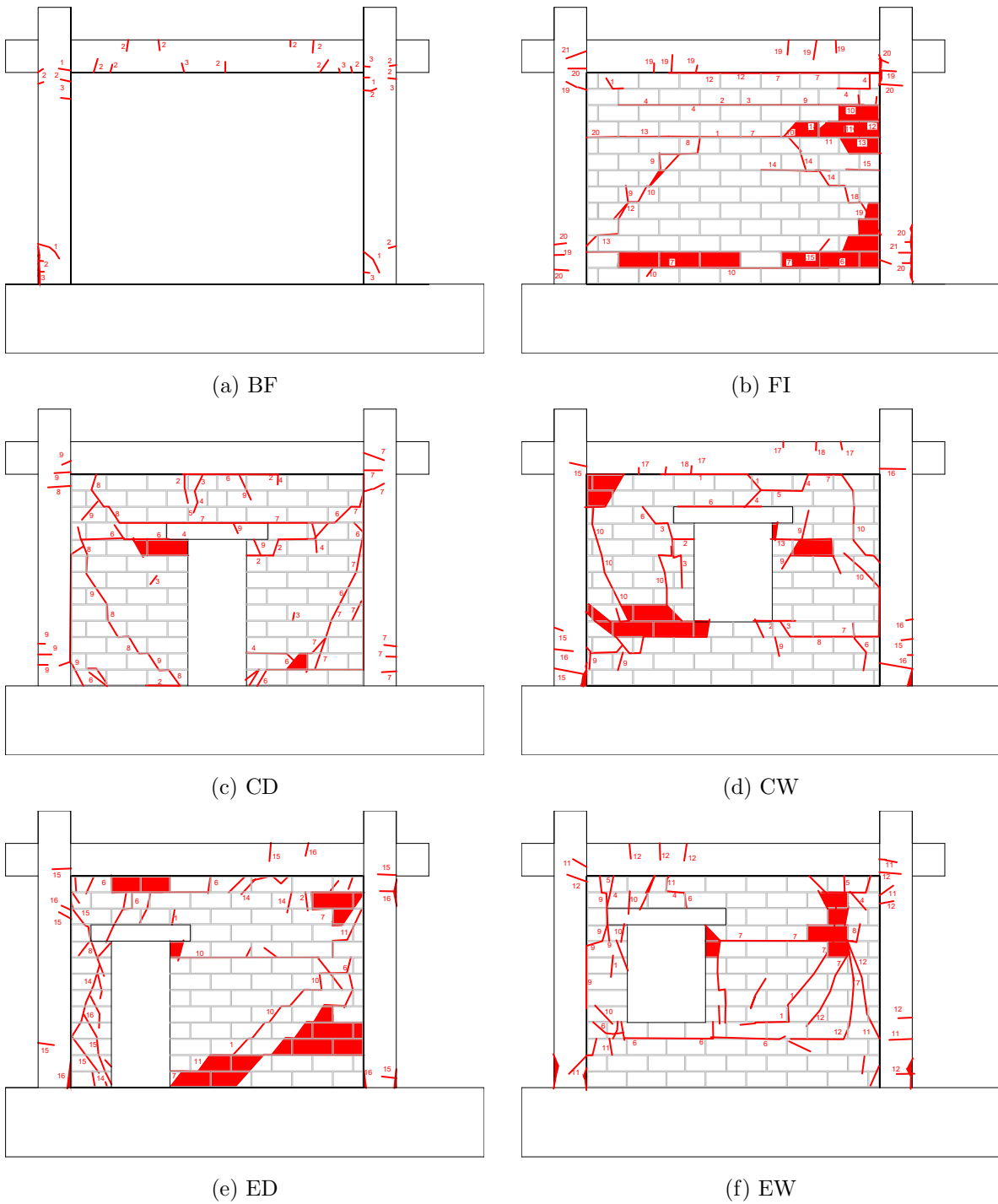


Figure 5.6: In-plane cyclic, quasi-static test crack patterns

Chapter 6

Out-of-plane drift driven test series

6.1 Preparation of specimens

In this chapter, an experimental series that consisted of OoP *drift driven tests* is presented. The term *drift driven tests* was used with such a small number of experiments, the label *method* would be overestimated. The specimens used for this series are the same as those used in IP test series (Sec. 5) detailed in Section 3. Since the same specimens were previously used for the IP test series, they were properly prepared for OoP tests.

The preparation of specimens consisted of removing the infill wall, repairing the frame and reconstructing the infill wall with/without their respected openings (Fig. 6.1). The damages to the concrete were classified as *light* following FEMA 306 (ATC, 1998) provisions, only encompassing the damages to the cover concrete. The damaged, loose parts were removed, and the cavities' surfaces were roughened. Next, a fibre-reinforced, sulphate-resistant thixotropic mortar, Mapegrout T60, was applied to the cavities (Fig. 6.1a) as it provided the best matching mechanical properties (Tab. 6.1) to the surrounding concrete. Afterwards, infill walls and lintels, where applicable were reconstructed (Fig. 6.1b). Finally, the specimens were painted white, and the front side was dotted in black to form a stochastic pattern (Fig. 6.1c) for the *digital image correlation* (DIC).

Table 6.1: Mapegrout T60 mechanical properties

Property	Value	Unit
Compressive strength	60.00	MPa
Flexural strength	8.00	MPa
Elastic modulus	27.00	GPa
Adhesion to concrete	> 2.00	MPa

6.2 Out-of-plane drift driven test set-up

The OoP drift driven test consisted of cyclic, quasi-static load with force control until yielding was reached. After which, a push-over displacement control was used with +5 mm increments. The force control used ± 5 kN steps in one direction and was repeated twice. Unlike the IP, the OoP test series did not include gravity loads. The protocol is presented in the Figure 6.2.

The experimental set-up is presented in the Figure 6.3 and trough this paragraph parts of the set-up will be referenced in brackets (#) as designated on Figure 6.3a. The specimens were fixed by 2 pairs of steel braces (3). The braces were fastened to rails (5) with a special mechanism (detail

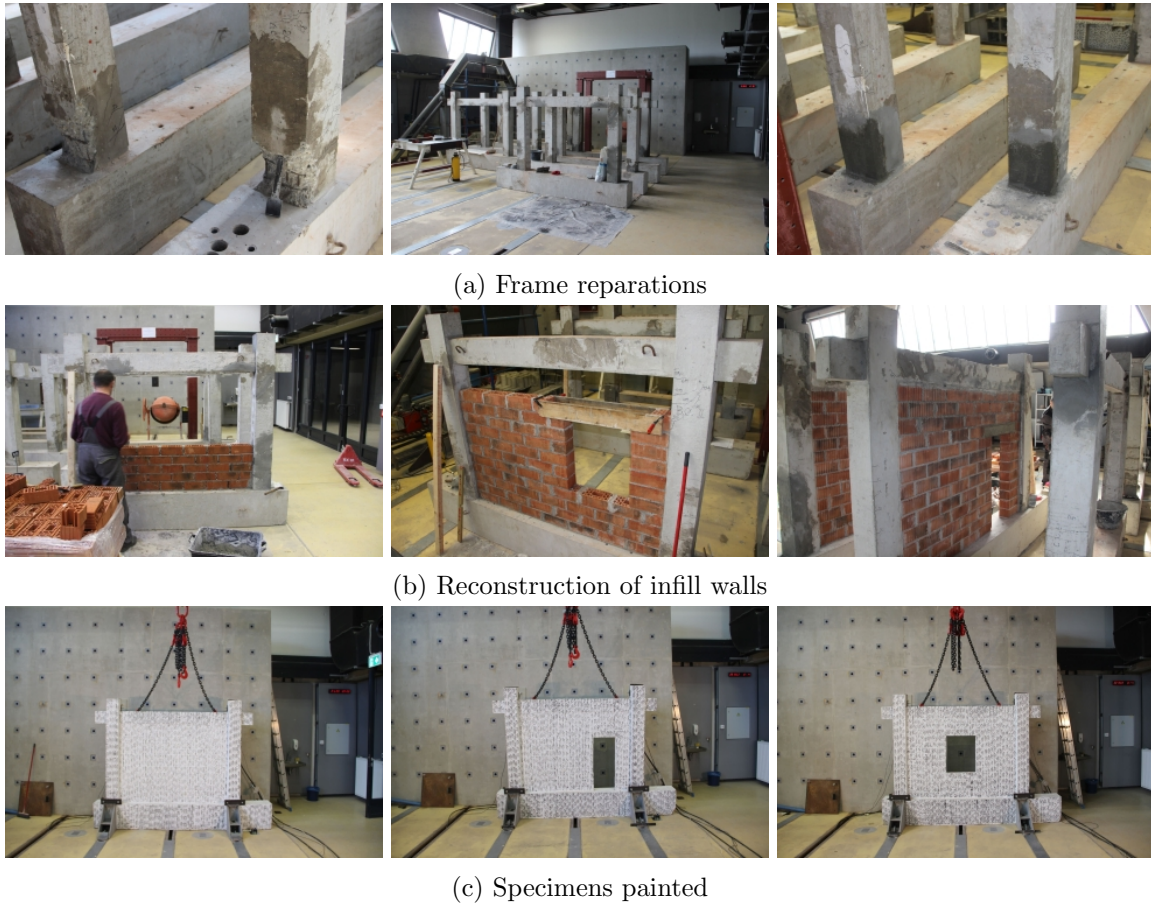


Figure 6.1: Preparation of specimens for OoP drift driven tests

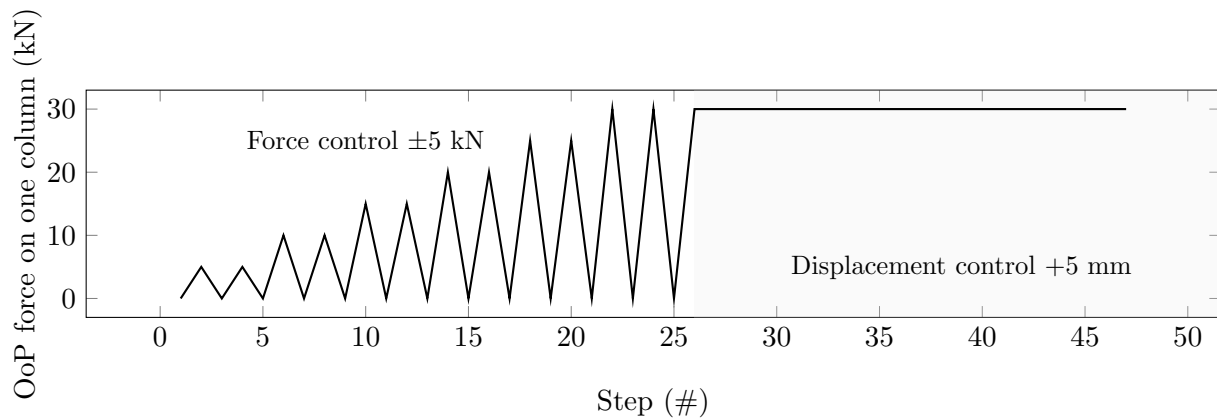


Figure 6.2: OoP drift driven test load protocol

on the left side). Additionally, the two opposite braces (3) were connected by two fully treated M20 studs. Furthermore, a special steel cap (2) was made that was used to place the force transducers (9) at the beam-column mid-line intersection (detail on the right side). The force transducers (9) were loaded by hydraulic presses (7). Also, steel cap (2) was used to place *linear variable differential transformers* (LVDT) (8) beside the presses. Additionally, 5 LVDTs were located on the lower beam, two horizontal pairs on the opposite side and one vertical on the top of the beam. Those were used

to measure accounts of rotation and/or slippage. Due to property and well-being concerns, a safety chain (1) connected the upper beam to a crane. Two separate acquisition tools were used: 1) Dewesoft SIRIUS-HD-16xSTGS data acquisition system (DAQ) utilized the hardware, *i.e.* force transducers (9) and LVDTs (8); 2) GOM ARAMIS (6) optical measuring system. The DAQ was set as a primary acquisition tool, ARAMIS was used to capture components that the hardware could not (e.g. infill wall-frame interaction, relative rotations, *etc.*). ARAMIS used 5 MP cameras set in front of the specimens to measure depth and plane deformations. However, force transducers were not connected to the ARAMIS; so, the averaged forces from the DAQ were calculated inputted.

6.3 Results

6.3.1 Rigid body movement and accidental torsion

Both DAQ and ARAMIS recorded evidence of *rigid body movement* (RBM). The RBM was found by the bottom beam's LVDTs, and by ARAMIS's internal software. The RBM was evident by the displacements at the lower beam, as recorded by the DAQ (Fig. 6.6). Figure 6.6 shows left and right LVDT recordings, where it is clear that there was a rotation that was magnified with the increase of load. Also, from the same graphs, it was visible that there was torsion. However, the torsion will be discussed later in this subsection.

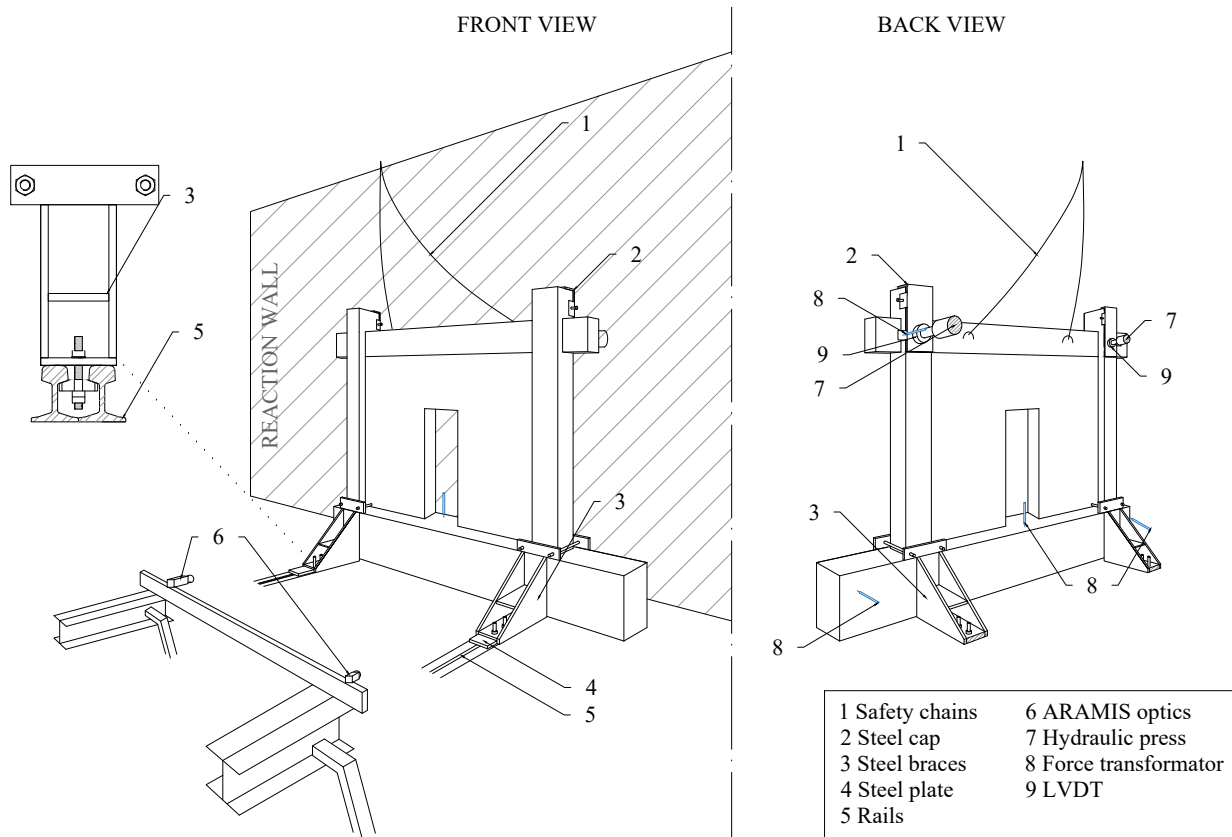
The RBM from the DAQ was corrected by deducting the projected RBM displacements from the recordings of the upper LVDTs by the use of Equation (6.1). It was calculated that the deformation from the top of the lower beam magnifies 4.29 times when it is projected at the upper beam's mid-height.

$$d_{\text{RBMcorr}} = d_{\text{raw}} - 4.29d_{\text{bottomLVDT}} \quad (6.1)$$

Note that in the case of BF specimen (Fig. 6.6a), there is only one graph, as in the case of that specimen, a *digital dial indicator* was used to record the displacements of the lower beam. Because it does not record continuously, the values were read manually for every endpoint of the loading protocol. Hence, a function was formed to generate data beyond the domain of the recordings. The function was essentially set to trace forces loaded, held, unloaded. So, in the time interval of achieving, holding, and unloading the forces, an appropriate displacement was fed to the interval. Thus, generated peaks and valleys. In between, linearly spaced values were added to connect the two. LVDTs were used with other specimens in order to avoid the aforementioned problems.

ARAMIS's internal software also recorded the RBM and it was corrected by adjusting displacements relative to those of the lower beam (Fig. 6.4), by using points as described in Figure 6.5.

Accidental torsion was also captured by both DAQ and ARAMIS. Due to a number of facts, the torsion was an inevitable occurrence, mainly being that each hydraulic press was operated manually with a single hydraulic pump and that the force control was used up to the yielding. However, the differences between the rotations of the two columns and strips of the infill wall (Fig. 6.7) were perceived as minuscule; therefore, no actions had taken place in order to integrate its effects.



(a) Test scheme



(b) Specimens set-up for testing

Figure 6.3: OoP test set-up

6.3.2 Hysteresis and load-bearing capacity curves

The hysteresis of each specimen corrected for RBM as recorded by DAQ is plotted in the Figure 6.8. The recording frequency was set to 5 Hz, and signals were filtered, using a *1-D Savitzky-Golay finite-*

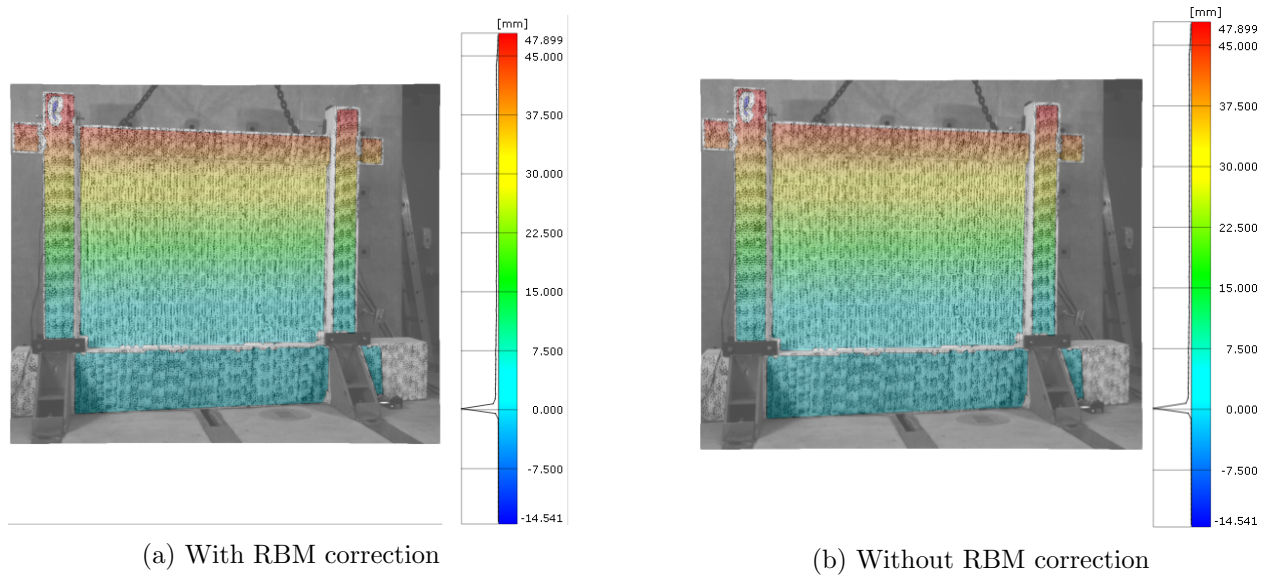


Figure 6.4: Rigid body movement as recorded by ARAMIS in OoP tests

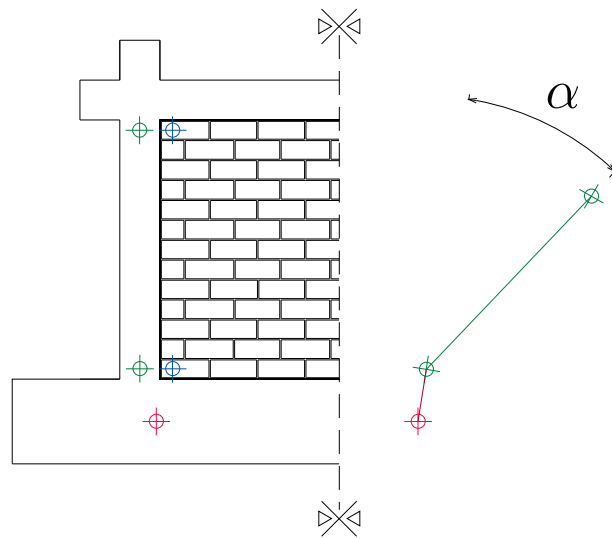


Figure 6.5: ARAMIS points used to calculate rotation angle (α)

impulse response (FIR) filter. The filter smooths the data without distorting the signal tendency. This is achieved by a process known as convolution, *i.e.* by fitting successive subsets of adjacent data points with a low-degree polynomial, using the method of linear least squares (Savitzky and Golay, 1964). The following coefficients were used: length of the filter window = 51; polynomial order = 2; order of the derivative = 0; interpolation mode.

The hysteresis recorded by ARAMIS is plotted in the Figure 6.9. The ARAMIS had recorded set in sequences on the peak values, *i.e.* during force control on every peak and total unload value and every +5 mm during the displacement control protocol (Fig. 6.2). Therefore, the hysteresis has linear loops. Furthermore, since force transducers were not connected to the ARAMIS, the forces were read from the DAQ; they were averaged and fed to the ARAMIS software. Afterwards, the

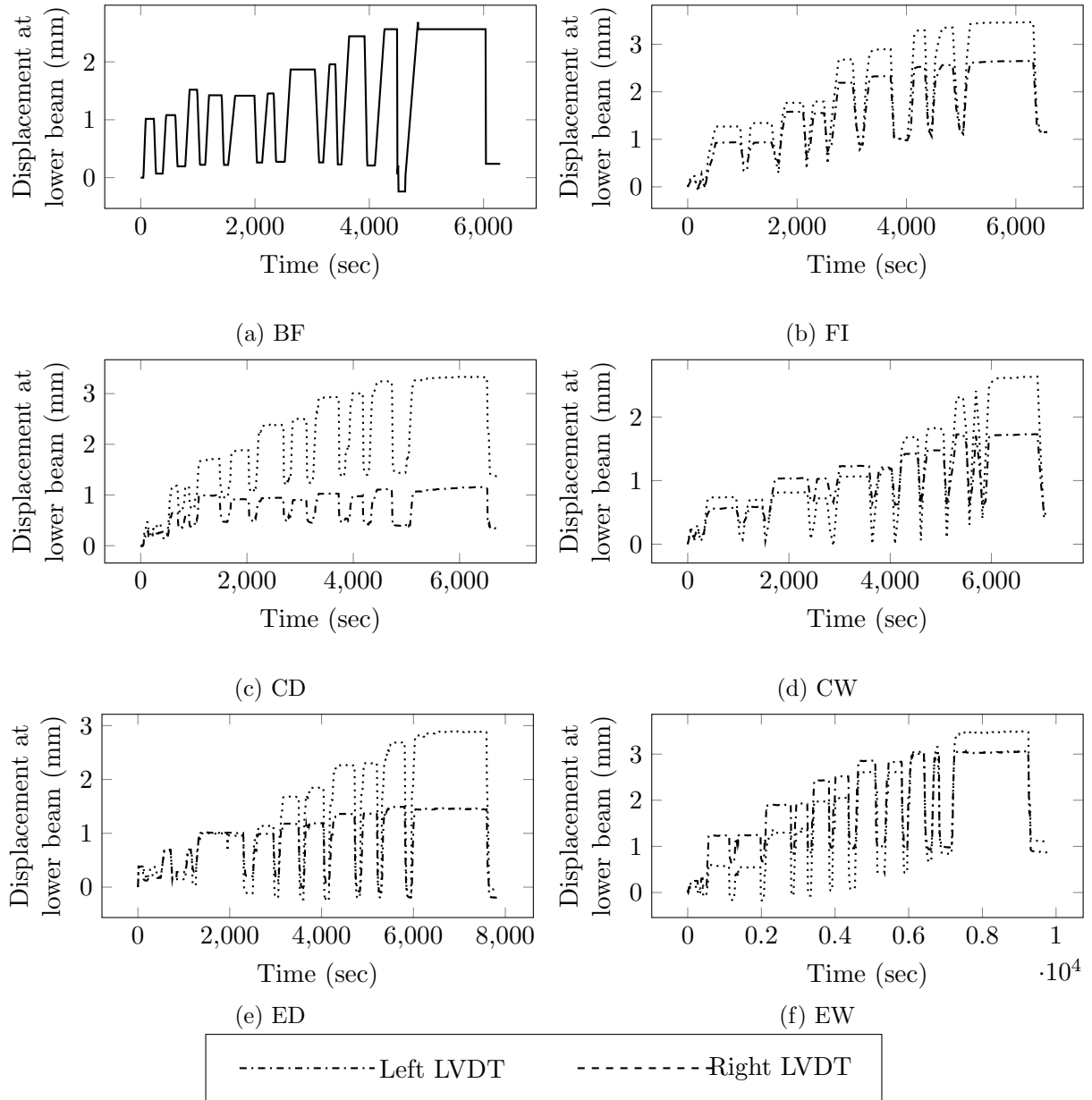
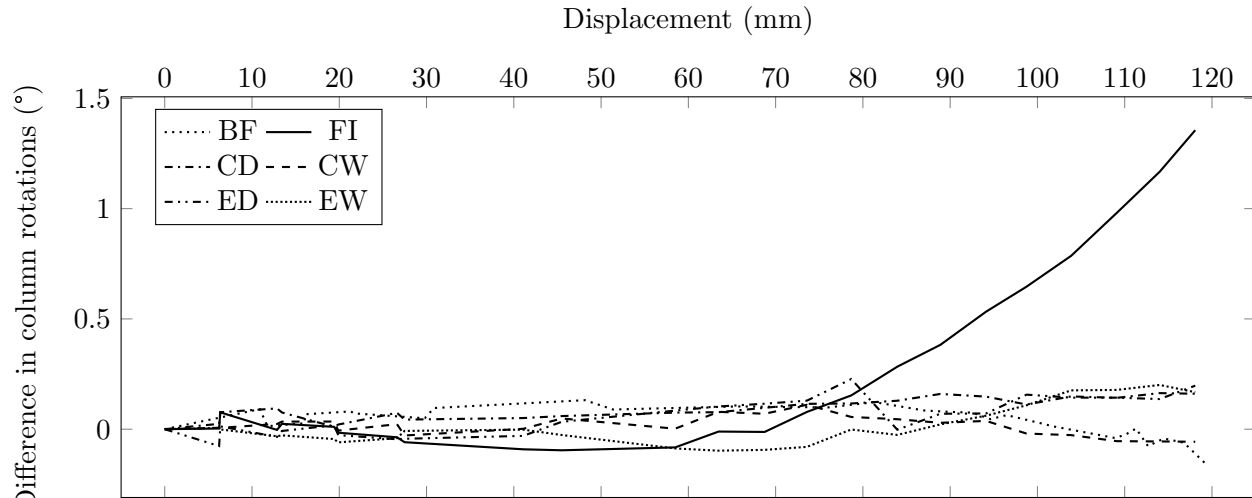


Figure 6.6: Rigid body movement as captured by DAQ in OoP tests

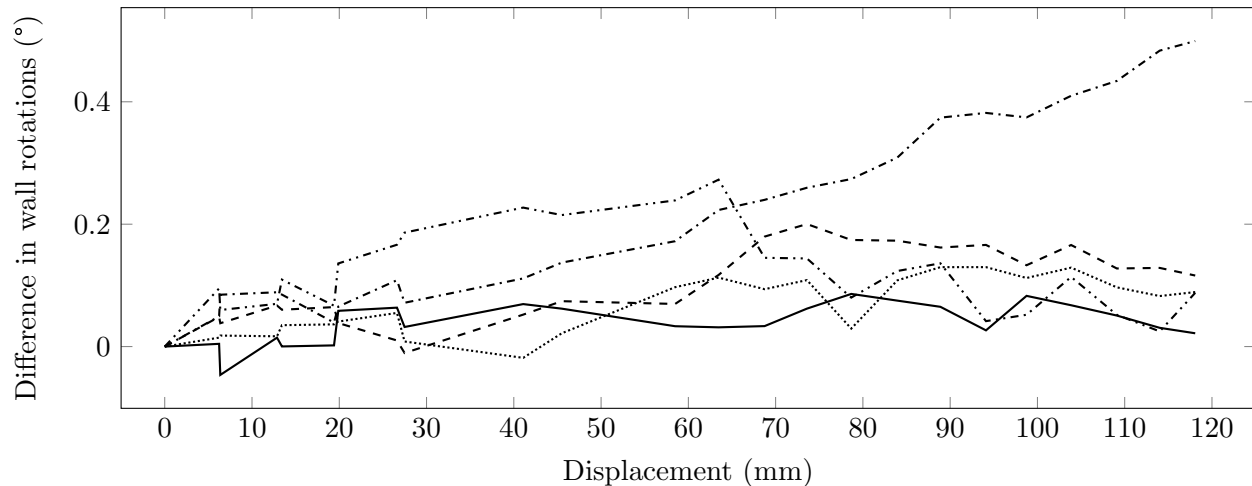
forces were doubled (2 columns) and used for the creation of graphs in Figure 6.9.

Note that the BF model has, compared to the other specimens, smaller displacement reach (Fig. 6.10a). This was because this was the first specimen tested, and it had an LVDT with only 10 cm reach. Nevertheless, the hydraulic press was pushed to its full stroke, which was captured by ARAMIS (Fig. 6.9a). Later on, the longer 15 cm reach LVDTs were used.

From the hysteresis, it is visible that the loops were relatively linear, especially when compared to the IP hysteresis loops (Fig. 5.4), pointing to the fact that the dissipation of energy was minimal. Therefore, the infill wall and, with it, the openings did not have a significant role in overall behaviour. This is also visible because stiffness and load-bearing capacities between the specimens were similar.



(a) Difference in opposite wall's end rotations



(b) Difference in rotations of opposite columns

Figure 6.7: Accidental torsion as recorded by ARAMIS through rotation differences from OoP tests

The same was observed by Fowler (1994) in his dynamic experiments.

In Figure 6.10, the OoP cyclic, quasi-static envelopes are displayed. It is visible that the FI model had the lowest load-bearing value. This conflicting case was likely due to a number of facts, the main being the randomness of the degree in previous IP damages and their repairs.

The differences between the two measuring systems were addressed through comparison of cyclic envelopes of the DAQ and ARAMIS recordings (Fig. 6.10) as presented in Figure 6.11. Figure 11 is divided into two parts, difference by each and for all specimens at every +0.5 % drift ratio. The *mean absolute error* (MAE) was calculated by using Equation (6.2). Linear interpolation was used to calculate forces at the intended drift ratios. Overall, the differences were minor, while the greatest was at lower drift ratios. The differences between the two systems of measurements can also be largely attributed to the fact that the recordings from the DAQ constituted the sum of the left and right force, while ARAMIS had an averaged left and right force from the DAQ and multiplied by 2.

$$\text{MAE} = \frac{1}{n} \sum_{j=1}^n |W_j - \hat{W}_j| \quad (6.2)$$

Where: W is the OoP force with the index referring to the data logger; n is the number of elements.

6.3.3 OoP cracks, damage occurrence and frame – infill wall interaction

The cracks were recorded and drawn upon the specimens during the pauses when the peak force was reached, and the press held at place. However, after the specimens yielded ($\approx 5.5\% d_r$), the crack recordings stopped due to safety reasons, and cracks were recorded after unloading. The state of crack coverage at the end of experiments are presented in Figures 6.13 and 6.14. From the figures, it is visible that all the specimens had similar crack patterns. There was damage to the lower parts of the columns and the infill wall on the tension side. Most of the infill wall's cracks were the uncoupling of block rows, *i.e.* cracks on the bedjoints, while on the compression side, there was crushing at the columns foot (Fig. 6.14g). Only the specimens with window openings (CW, EW) had cracks on the compression side.

The infill wall crack occurrences and their specifics plotted against OoP force, displacement and drift ratios are displayed in Figure 6.12. The figure shows that the infill wall had cracks starting at around 1.25 – 2.00 % drift ratio. Like IP's, the first events were de-bonding infill from the surrounding frame. The outlier of the crack occurrences was the EW model with cracks at 0.75 % drift ratio. From those points, the cracks developed upwards; again, predominantly in the bedjoints similar to the pure wall bend tests (Sec. 4.4). Outside the infill wall and columns headjoint contact cracks, only specimens with window openings (CW, EW) had a few of them in the infill wall itself. Also, no cracks were observed on blocks. Unlike specimens with eccentric openings (ED, EW), FI model and those with centrally positioned openings (CD, CW) had approximately symmetrical crack patterns. Whereas, with eccentric openings, more bedjoint cracks appeared on the shorter side of the wall beside the openings. The bedjoint cracks were found besides openings, rendering the system of the aforementioned non-existing boundary with detached infill wall loose. Hence, the specimens with openings had a comparatively greater damage state than the FI specimen.

The observed crack patterns are consisted with both drift-driven subjected to 1.7 % drift ratio by Flanagan (1994) (Fig. 2.28) and dynamical tests by Tu et al (2010) (Fig. 2.27b). In the research by Flanagan and Bennett (1999b), his cantilever specimen had nearly identical crack/damage occurrence. However, his beam and Tu et al (2010) specimens did also have cracks in the upper parts of the infill. This is due to the nature of beam-bend like loading of the Flanagan (1994) specimen and the Tu et al (2010) gravity load and upper beam boundary condition imposed by the RC slab.

To investigate the interaction between the infill wall and the frame, ARAMIS was used to measure the average displacement of the two. From there, the difference in the rotation was calculated and plotted against OoP displacement and drift ratio in Figure 6.15. The abrupt turnabout in the direction of curves was from the specimens unloading. Furthermore, from the figure, there was some degree of segregated behaviour. Initially (0 – 1.4% d_r), there was some cluttered behaviour, probably due to frame and infill wall arranging. Afterwards, behaviour is more stable and differences gradually increase. It is visible that the eccentric opening specimens (ED, EW) had the most significant difference through all test sequences, while the fully infilled (FI) specimen had a sudden increase at about 5 % d_r . The specimens with centric openings (CD, CW) had the lowest difference in rotations.

The OoP displacement and von Mises strain maps captured by ARAMIS optics are presented in Figure 6.16. The colour bars of displacements maps are in millimetres (mm) and strain in percentages (%). The maps are extracted from the yielding point of each specimen. Note that

von Mises strain values cannot be taken into account exactly, as the hollow clay blocks have heavy anisotropic mechanical properties (Tab. 3.3). Instead, the accumulation of strains can be used to interpret the behaviour of the specimens. From the strain maps, it is visible that specimens with eccentric openings (ED, EW) had strain concentrations between the column and infill wall (Figs. 6.16j & 6.16k). However, this can also be a noise from ARAMIS measurements that usually occurs if geometry abruptly changes, like depth. Otherwise, there is an accumulation of strains visible in all specimens heavily at the column's foot. The displacement maps are more or less similar amongst specimens, with constant change in displacements. Again, this confirms the jointed frame and infill wall movements, as it was observed with dynamical experiments (Fowler, 1994; Tu et al, 2010).

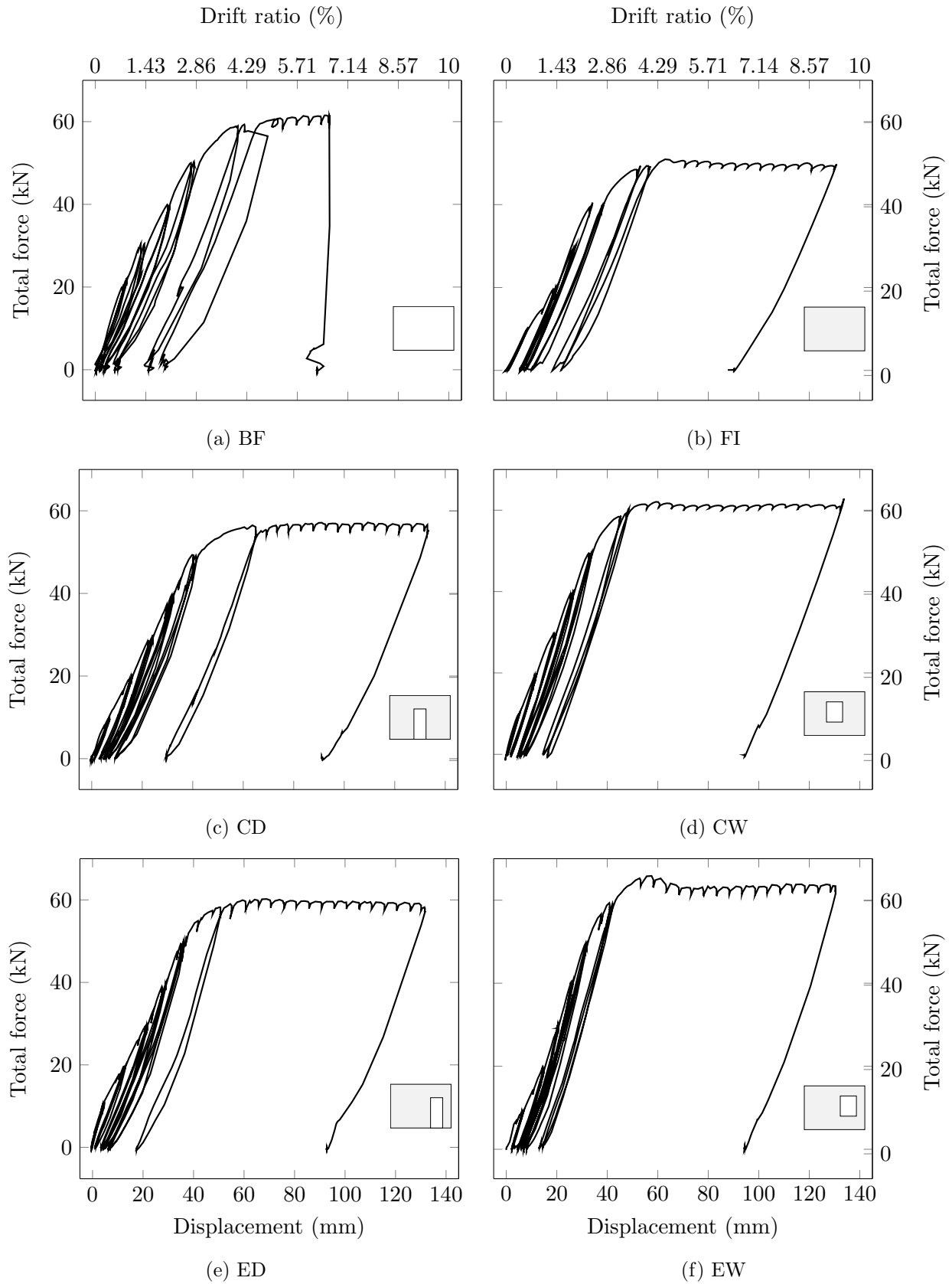


Figure 6.8: OoP cyclic, quasi static hysteresis (RBM corrected) - DAQ

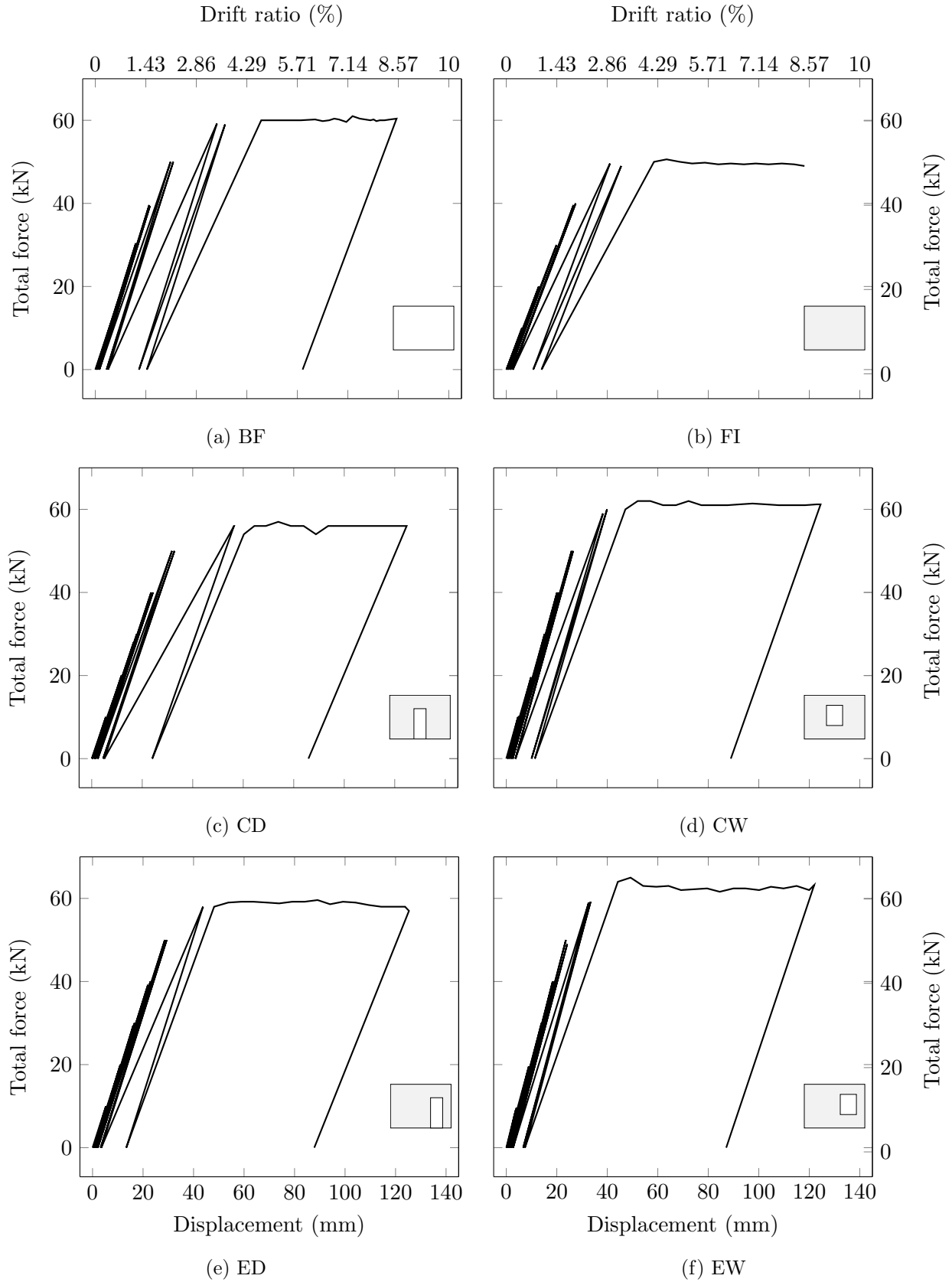
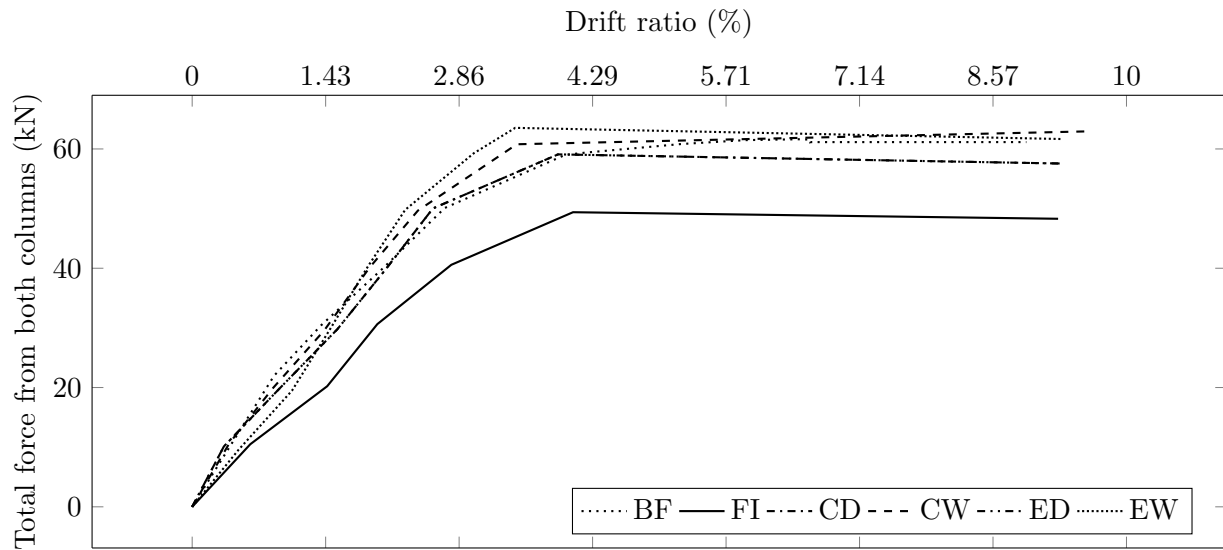
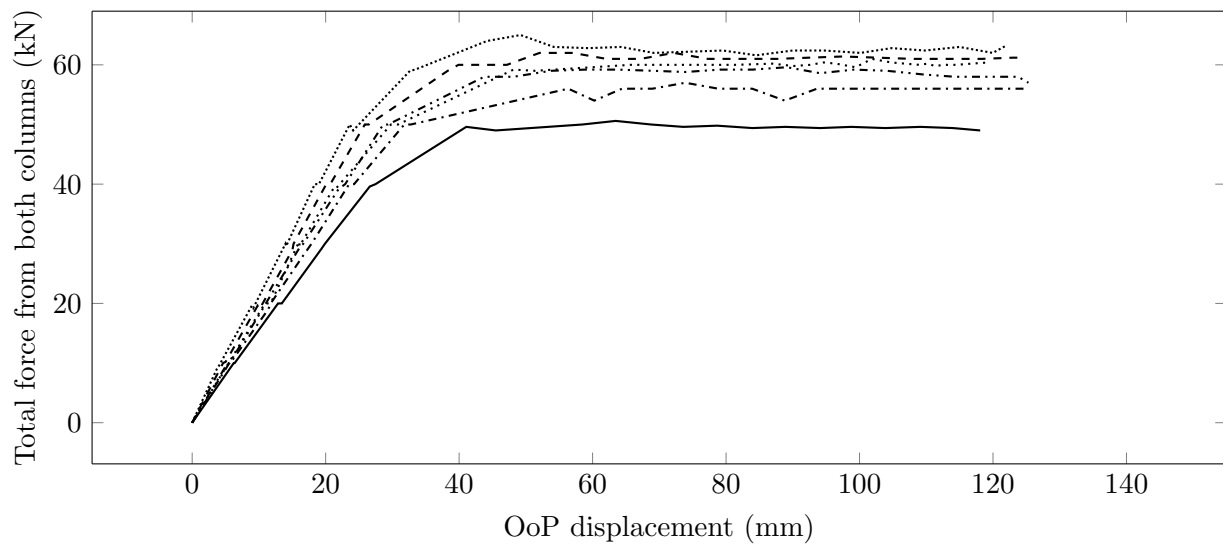


Figure 6.9: OoP cyclic, quasi static hysteresis (RBM corrected) - ARAMIS



(a) Envelopes extracted from DAQ signals



(b) Envelopes extracted from ARAMIS & DAQ signals

Figure 6.10: OoP load-capacity curves

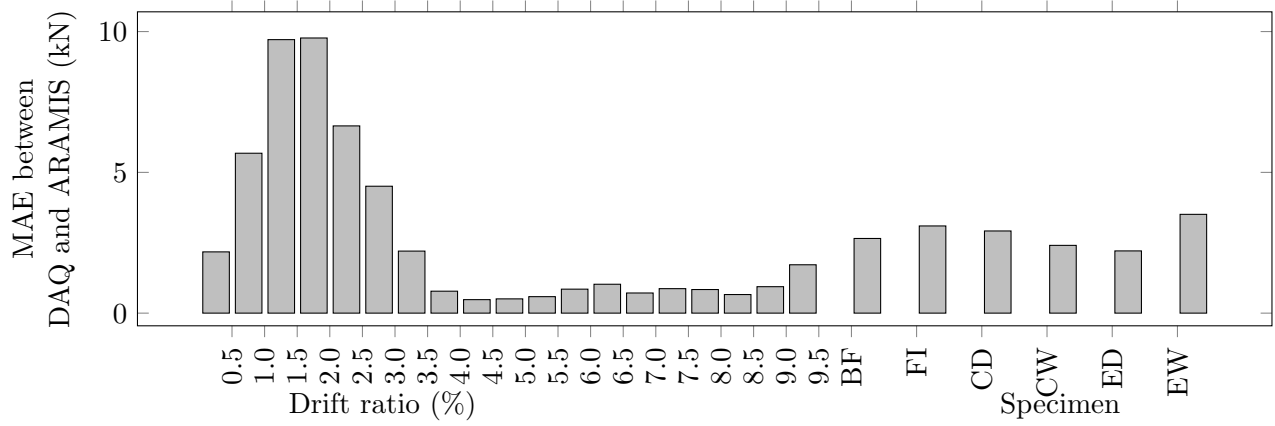


Figure 6.11: OoP mean absolute error between DAQ and ARAMIS sorted by drift ratio and specimens

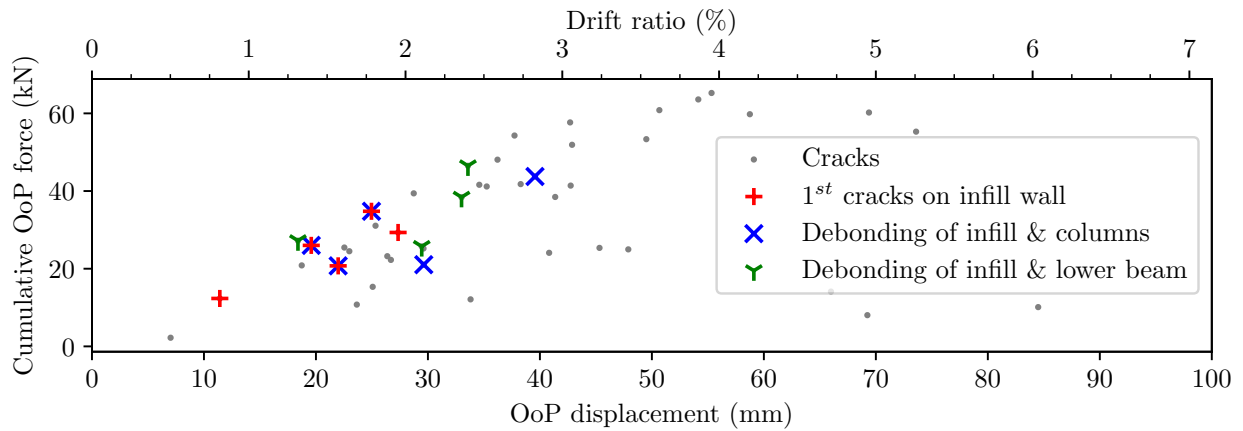


Figure 6.12: OoP crack occurrence map

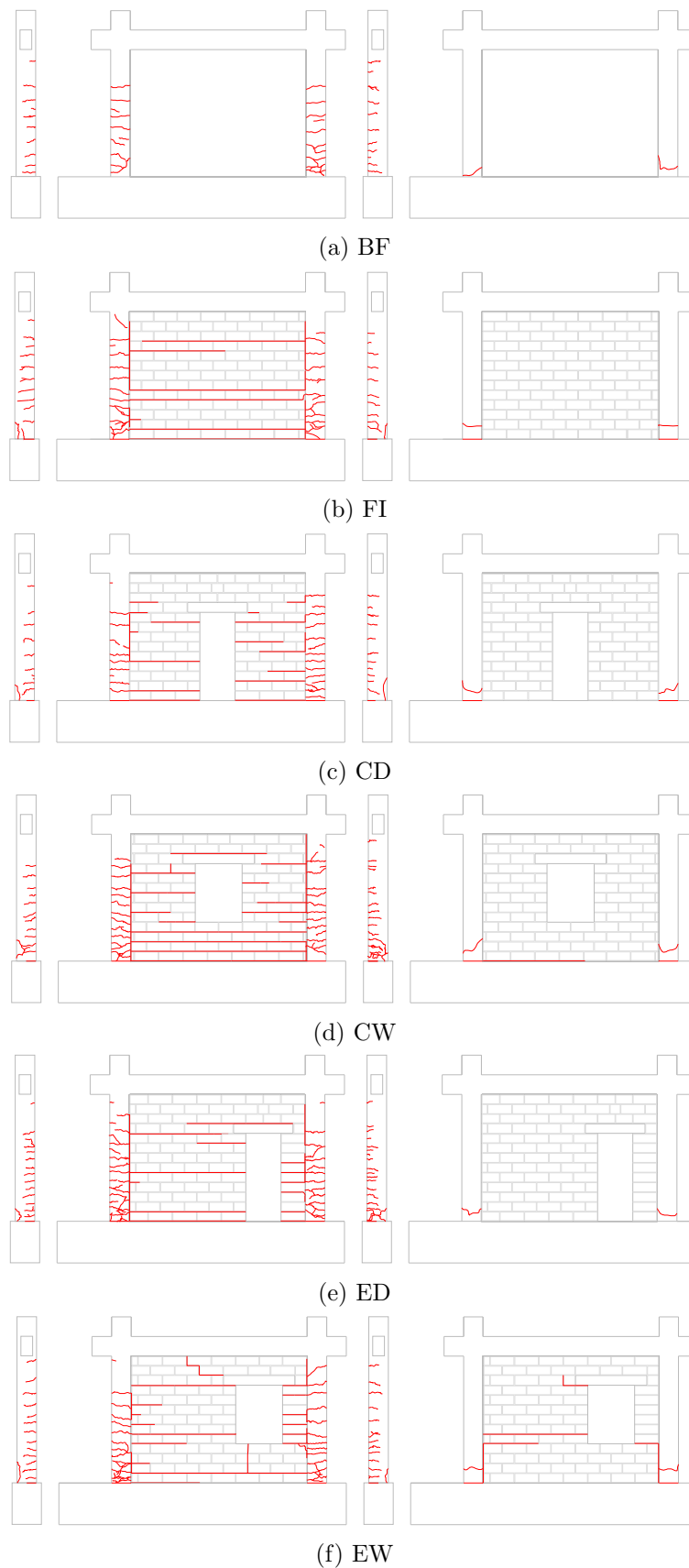
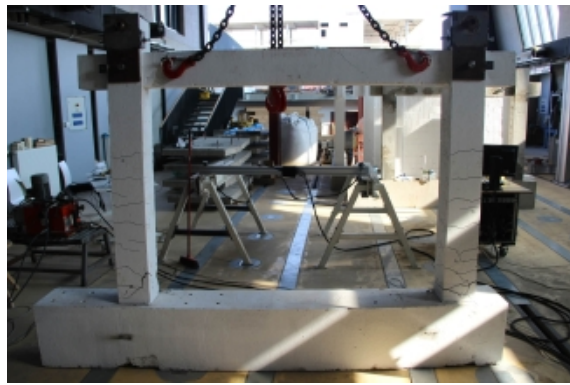


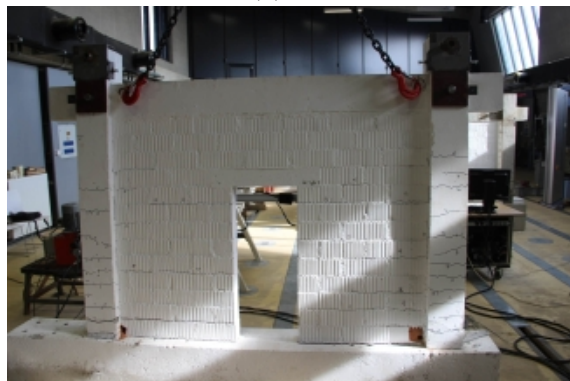
Figure 6.13: Crack outlines of specimens at the end of OoP testing



(a) BF



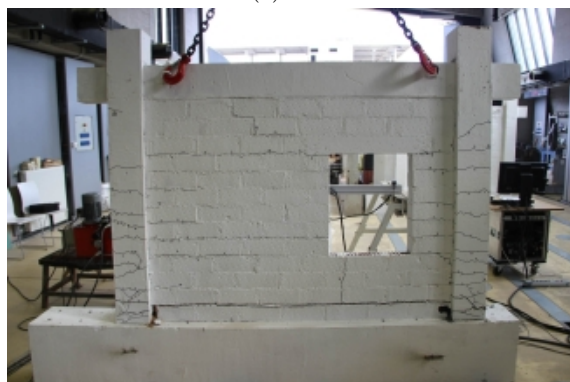
(b) FI



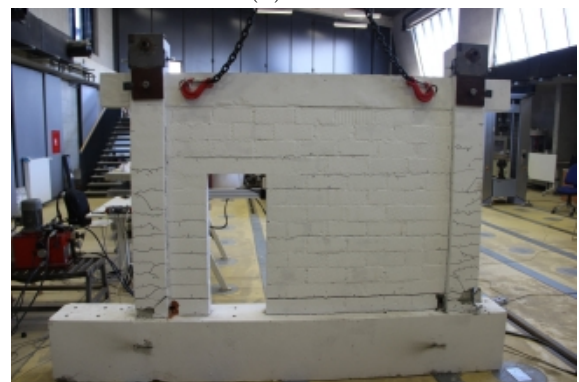
(c) CD



(d) CW



(e) ED



(f) EW



(g) Details

Figure 6.14: Crack photographs of specimens at the end of OoP testing

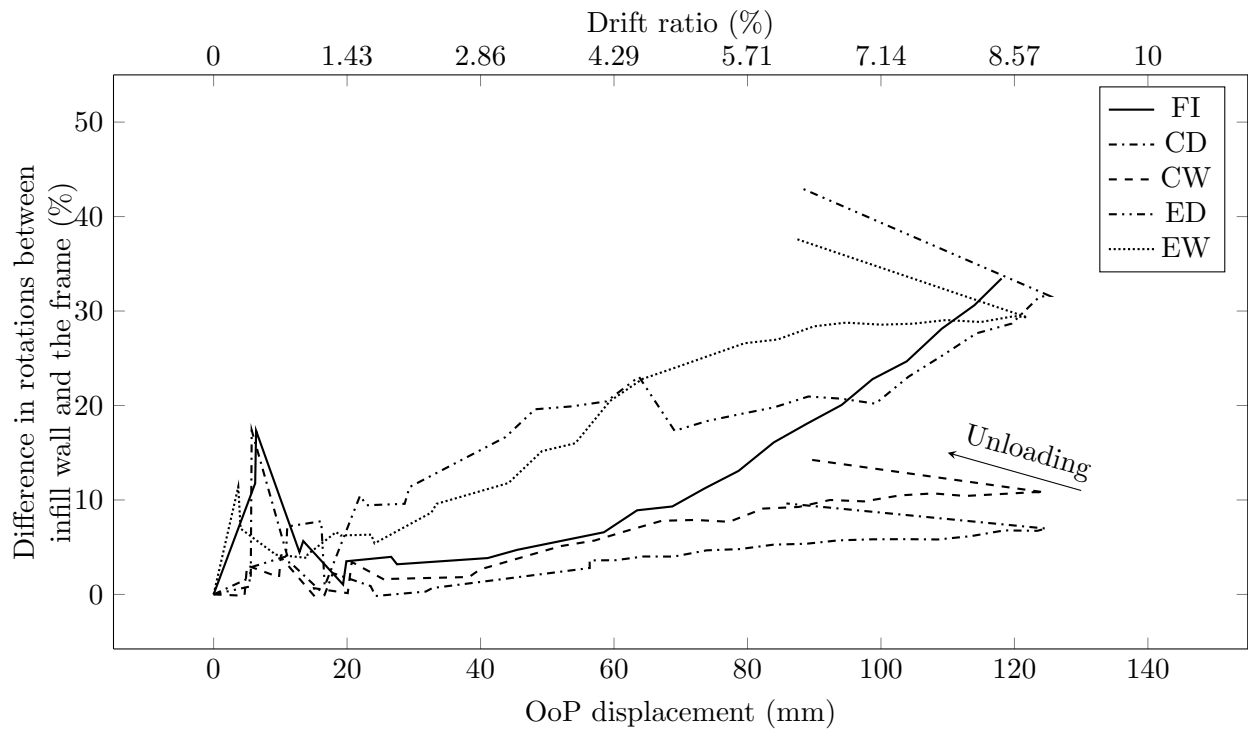


Figure 6.15: Differences in rotations between the average rotation of infill wall and frame (corrected for RBM)

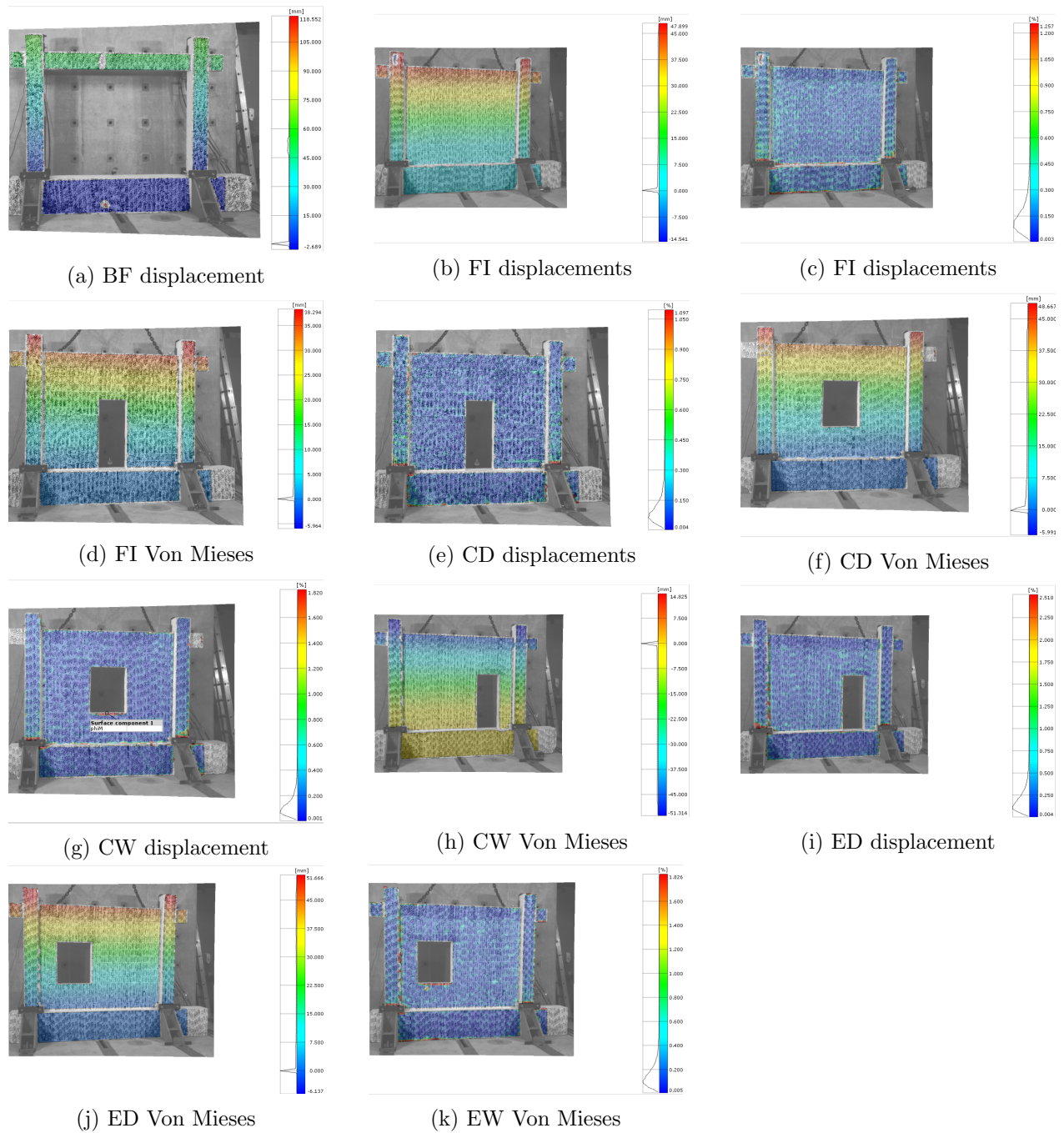


Figure 6.16: OoP displacements and von Mises strains (RBM corrected) at the point of yielding

Chapter 7

Conclusions

Small scale test series were done to determine the mechanical and physical properties of materials used in other experiments and computational studies.

7.1 In-Plane test series

The IP test series were carried out in the Penava (2012) PhD thesis. Therefore, only the necessary information that would aid the understanding of further studies are presented.

The specimens included a ground floor frame of a 7 storey building. The frame was designed as a medium ductility class (DCM) by EN 1998-1 provision (BSI, 2005). The specimens were scaled to a 1:2.5 ratio with 365 kN of gravity load from upper stories in each column. The specimens included a: bare RC frame (BF); fully infilled RC frame (FI); RC frame with centric door opening in the infill wall (CD); RC frame with centric window opening infill wall (CW); RC frame with eccentric door opening in the infill wall (ED); RC frame with an eccentric window opening in the infill wall (EW). The infill wall hollow clay masonry units classified as group 2 by EN 1996-1 provision (BSI, 2004b) were collected from a local distributor. By the same provision, a general-purpose mortar M5 was used to bind them. RC lintels were used above the openings. The specimens were subjected to cyclic, quasi-static force-controlled load protocol.

The infill wall largely contributed to the specimen's behaviour in terms of initial stiffness and load-bearing capacity. The effects of openings were apparent and measurable. The openings obstructed the development of diagonal struts, rendering the infill wall's influence less effective. The eccentrically positioned openings had the lowest performance, especially when loaded in the direction closer to the shorter infill wall side.

The specimens failed in 3 primary ways, 1) bending (BF); 2) bedjoint sliding (FI); 3) Diagonal failure (CD, CW, ED, EW).

7.2 Out-of-plane test series

The OoP tests included the same set of specimens as those used in IP series *i.e.* BF; FI; CD; CW; ED; EW. Since the aforementioned specimens were used previously, the infill walls were removed and reconstructed, and the concrete was repaired.

The OoP test series included OoP drift load applied to the column – upper beam mid-line, and unlike the IP series, the gravity load was not used. The test set-up is visible in Figure 6.3a. Two acquisition systems were used; the primary system used LVDTs and force transducers connected to the Dewesoft SIRIUS-HD-16xSTGS data acquisition system (DAQ), while the secondary was using stereophotogrammetry via GOM ARAMIS. ARAMIS was used only to capture the compression

side of the tests. Furthermore, as the force transducers were not connected to the ARAMIS, the two-column averaged force was calculated and fed to the software. The difference between the two systems was negligible (Fig. 6.11). The load was applied cyclically, quasi-statically (Fig. 6.2) in one direction with force control of ± 5 kN step with double repetition until yielding was reached ($d_r > 4\%$). Afterwards, displacement control was used with $+5$ mm increments until hydraulic presses pistons reached their full stroke ($\approx 10\%$ d_r).

As assumed, evidences of both accidental torsion (Fig. 6.7) and rigid body movement (RBM) (Figs. 6.4 & 6.6) were observed. The accidental torsion resulted from operating each hydraulic press manually using a single pump. Nevertheless, the torsional effects were minimal and were not addressed. On the other hand, the effects of RBM was evident and not easily dismissed, as even the small rotations of the lower beam trough leverage increased the displacements of the upper beam nearly more than 4 times. Therefore, the recordings from the DAQ had their values subtracted to accommodate the rotation, while ARAMIS had an internal protocol that corrected the displacements in relation to the lower beam.

Generally, the specimens exhibited stable behaviour, enduring drift ratios of up to 10 %. That was certainly achievable by the absence of gravity load. Both infill wall and the frame developed heavy crackings and damages (Figs. 6.13 & 6.14). The cracks on the frame developed on both compression and tension sides. Whereas, infill wall is mostly on the tension side, most notably, on the bedjoints. For the most part, the cracks started from the low end of the infill walls and columns and gradually progressed upwards. The first feats of cracks on the infill walls were the detachments from the columns at around 1.25 % – 2.25 % drift. Similarly, detachments from the lower beam occurred at around 1.25 % – 2.50 % drift. Therefore, it was established that the infill walls had: a) light damage of up to $< 1.25\%$ d_r ; b) heavy damage, but usable infill wall between 1.25 – 2.00% d_r ; c) heavy damage, and unusable infill wall above $d_r > 2.00\%$. The specimens with eccentric openings accumulated more and uneven damages. Even though it was found that the frame and infill wall behaved like one, a certain degree of rotational differences between the two was captured by ARAMIS (Fig. 6.15).

Overall, neither the infill wall nor the openings had a significant impact on the behaviour of the specimen, the stated was observed in the following points: 1. The OoP had more a linear response when compared to IP hysteresis (Fig. 6.8 *vs.* 5.4); therefore, the energy dissipation from the infill walls was not present; 2. Load-bearing capacities, deformation capabilities, initial stiffnesses nor the yielding points were affected; 3. Displacements and von Mises strain maps did not show a significant difference between the frames and the infill walls (Fig. 6.16).

The findings mentioned above are consistent with both findings from the dynamical studies by Tu et al (2010), Fowler (1994) and drift driven tests on steel frames by Flanagan (1994).

Even though the infill wall did not affect the overall behaviour, it was found that the infill wall and frame interaction was unidirectional; that is, only the frames drove the infills behaviour. Frame transmitted movements to the infill wall that caused heavy damage that could lead to life, safety and property risk.

This experimental series lacked gravity loads that would reduce the deformation capabilities of the specimens and render its damage pattern. Also, by the same token, it lacked bi-directional loadings that would also render its behaviour. To address these lacking, numerical studies were carried out.

Part III

Computational micro-model studies

Conflicts of interest disclosure Please note that there are many similarities and cross-referencing between this chapter and the Anić et al (2021b, 2019a) papers. Authors of the referenced paper are the thesis author and his supervisors.

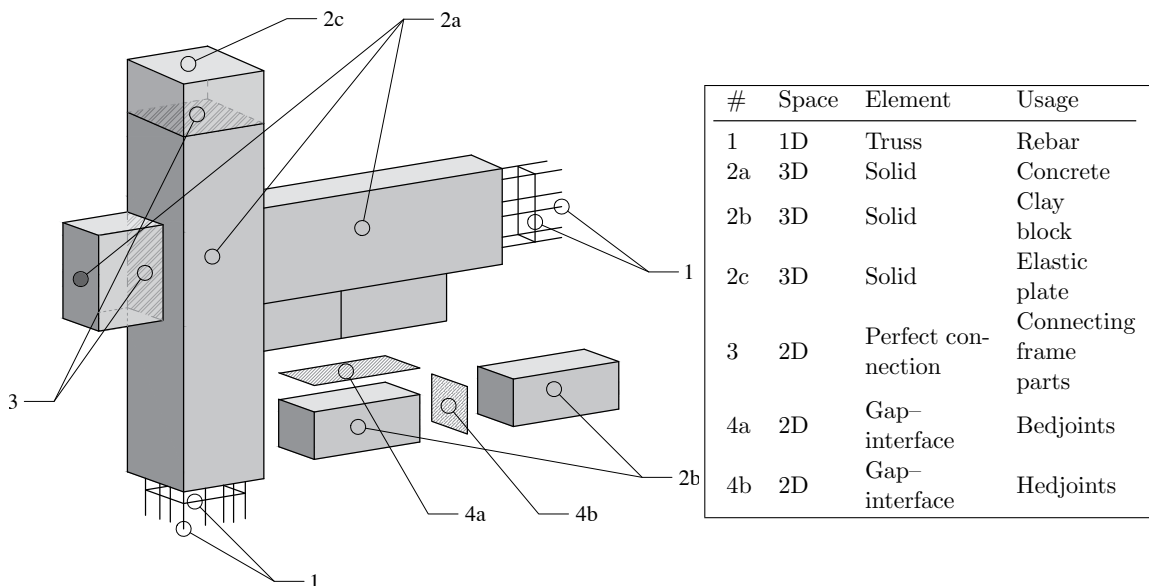
Chapter 8

Development of a 3D micro-model

In this chapter, the development in terms of elements, material models, boundary conditions and their initial values are described.

8.1 Micro-model elements and boundary conditions

The micro-models were assembled from 3, 2, and 1D elements (Fig.8.1) . The 3D solid elements were used to model elastic plates, concrete, and clay block elements. The elastic plates were used to transmit point loads. The 1D truss elements were used to model reinforcement that perfectly connected to the surrounding concrete. In the case of rebar overlapping, their areas were added to a single bar. The connecting 3D solid parts of the frame had *perfect connection* between them. In contrast, the connections between the frame and infill wall and among block units, gap-interface 2D elements were introduced. Those elements had zero thickness, and they do not model pure mortar behaviour; rather, the block-mortar relationship. All the elements within a micro-model are presented in Figure 8.2. The finite element (Fig. 8.2d) size was set to 4 cm wide cube elements, the same as used with 2D micro models. Smaller elements would increase the already high computational time of 5.04 days for IP cyclic, quasi-static FI model.



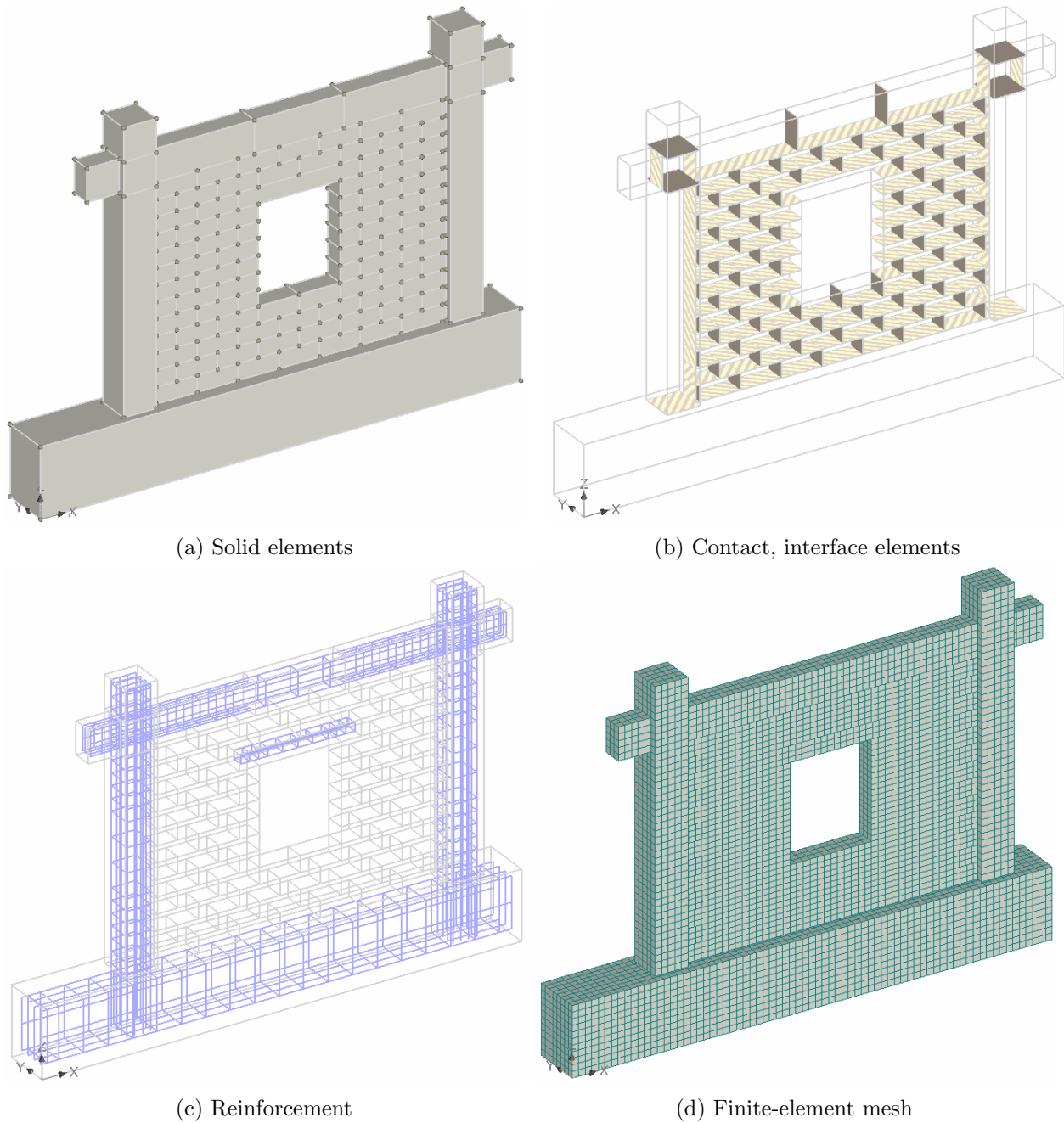
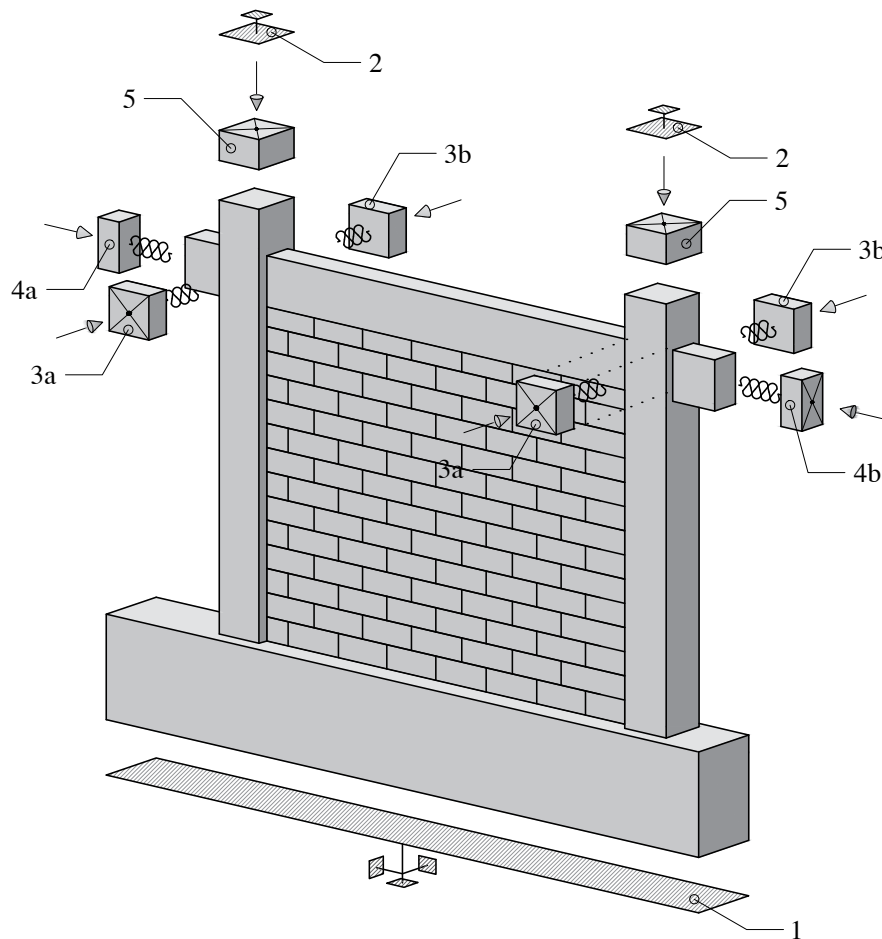


Figure 8.2: Micro-model composition of a CW model

Note that mortar joints were not modelled separately as they would prolong the computational time while not significantly capturing the properties that interface material by itself does not cover. Moreover, even if the mortar joints were modelled, the interface material model would have to be implemented between the mortar and masonry. There would be a need to simulate both bond strength and interlocking effects.

All the boundary conditions used in some combinations are presented in Figure 8.3. Through this paragraph, those elements are referred to through brackets (#). The combinations used in regard to specific simulations are presented in Table 8.1. Whenever the vertical, i.e. gravity load,

was used, it was transferred via column plates (5) with 73 kN point force for each 5 steps. Afterwards, the column supports (2) in z direction were activated on the top of the column plates (5). Due to the large vertical, *i.e.* gravity load of 365 kN that was introduced in the experiments in the column ends, resultant friction could not be undermined even though the rolling supports were used. Hence, the spring elements were introduced to simulate the friction. When the IP experiments were simulated, gravity load and foundation supports (1) were used for the first 5 steps. Afterwards, the IP (x direction) forces were activated interchangeably on 4a and 4b plates along with column and foundation supports. The forces followed the same load protocol as in the experiments (Fig. 5.2) with ± 5 kN load step. The IP (x direction) springs were activated only on the plates where the force was active in the direction against it. When the OoP experiments were simulated, the foundation supports (1), and OoP plates (3a) were used with forces. Forces followed the same one-directional load protocol as in the experiments (Fig. 6.2) with ± 5 kN load steps. Note that no OoP spring (y directions) was not applied on the plates (3a) because there was no gravity load. The IP pushover simulation had gravity load and foundation supports (1) active for the first 5 steps. Afterwards, the IP (x direction) prescribed deformation with 0.5 mm/step was applied to the IP plate (4a). In the case of eccentric openings, ED and EW models were loaded in $+x$ and $-x$ direction separately via (4a) or (4b) plates. For the OoP pushover simulations, the gravity load was also introduced through 5 steps. Afterwards, the OoP (y direction) prescribed deformation with 0.5 mm/step was applied to the OoP plate (3a). In the case of combined IP&OoP simulations, the same protocols and boundary conditions were used as described in this paragraph's IP and OoP pushover simulations. Whereas the IP and OoP prescribed deformations were active simultaneously.



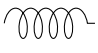
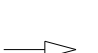

#	Element	Space	Direction
1	Foundation support	Surface	x, y, z
2	Column support	Surface	z
3a-d	OoP plates	3D solid	/
4a,b	IP plates	3D solid	/
5	Column plates	3D solid	/
	Spring	Surface	$\pm y$ for el. 3a-d $\pm y$ for el. 4a,b
	Force		$-z$
	Force/Prescribed def.	Point	$\pm x$ for el. 4a,b $\pm y$ for el. 3a,b

Figure 8.3: Micro-model boundary conditions

Also, a computational model was developed to simulate OoP wall bending tests as described in section 4.4. In short, two test series were conducted with line load perpendicular (\perp) and parallel (\parallel) to the bedjoints. Each test series tested 10 specimens, and both were made and tested following EN 1052-2:2002 provisions (CEN, 2002). When the load was parallel to the bedjoints, the failure of the specimens occurred by reaching the bond strength of bedjoints. The wall specimens were thus broken into two parts (Fig. 4.12a). Contrariwise, the perpendicular load had caused failure through

Table 8.1: Boundary condition combinations in relation by simulation type

#	Simulation type	Elements used from Fig. 8.3	Load type	
			IP	OoP
1	IP cyclic, quasi static	1, 2, 4a, 4b, 5	F	
2	OoP cyclic, quasi static (1 direction)	1, 3a without spring	F	
3	IP pushover	1, 2, 4a or 4b	d_p	
4	OoP pushover	1, 2, 3a or 3b		d_p
5	Combined IP&OoP pushover	1, 2, 3a, 3b, 4a, 4b, 5	d_p	d_p

* F - force; d_p - prescribed deformation.

headjoint mortar as well as in the blocks themselves. Thus, by breaching the tensional strength of blocks (Fig. 4.12b). The results are provided in Figure 4.13 and Table 4.3.

The aforementioned developed OoP bend test models and their boundary conditions are presented in Figure 8.4. As visible, the models were simplified by not including parts of block elements that extend beyond the supports. Both supports and loads were line-type. Supports on both ends had translations fixed in z and y direction while x was on one end fixed and on the other free. Therefore, the mechanics are that of a simply supported beam. When the line loads in both computational models are multiplied by their length, the resultant force adds up to 0.5 kN/step. The model had parts of its solid, i.e. block elements connected by *perfect connection* as those elements had to be separated to apply line load directly on the solids. Other connecting parts of the models are head- or bedjoint connections.

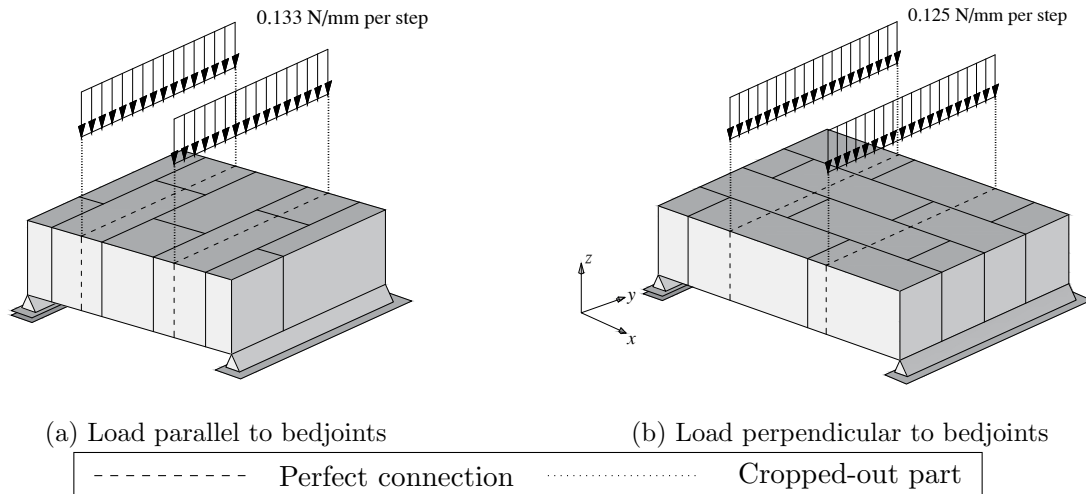


Figure 8.4: Computational model of OoP bending tests

8.2 Material models

This section describes material models used for modelling the behaviour of physical specimens. The section also presents the recommended values and limits of specific parameters that were later used for calibration and sensitivity analysis (Sec. 9).

8.2.1 Material model for concrete and masonry

For both concrete and clay block macromodels, a fracture-plastic model *CC3DNonLinCementitious2* material model was used. The model combines constitutive models for tensile (fracturing) and compressive (plastic) behaviour. In addition to *SBETA* material, both material models were recommended by the software developers to simulate brick or concrete (Červenka et al, 2012).

The fracture model is based on the orthotropic *smearred crack* formulation and *crack band* model. It uses *Rankine failure criterion* or *maximum stress theory*, exponential softening, and it can be used as either rotated or fixed crack model. The hardening/softening plasticity model is based on *Menétrey-Willam failure surface*. It can be used to simulate concrete cracking, crushing under high confinement, and crack closure due to crushing in other material directions (Červenka et al, 2012).

The biaxial, non-linear material behaviour is described with equivalent stress σ_c^{ef} (mostly principal stress) and with it, equivalent strain ε^{eq} (Fig.8.5). In simple terms, the equivalent strain is the product of uniaxial stress $\sigma_{c,i}$ and elasticity modulus $E_{c,i}$ in i direction. Given the assumptions, the material damage is caused by $\sigma_{c,i}$. Furthermore, in Figure 8.5 an example of unloading is presented at point U . From it, it is visible that σ_c^{ef} vs. ε^{eq} relation is not unique; rather, it is depended by previous steps. The point of change from unloading begins with a change in the sign of the increment of the effective stress. If the loading starts after unloading is completed, the unloading direction is formed to the last point of loading U .

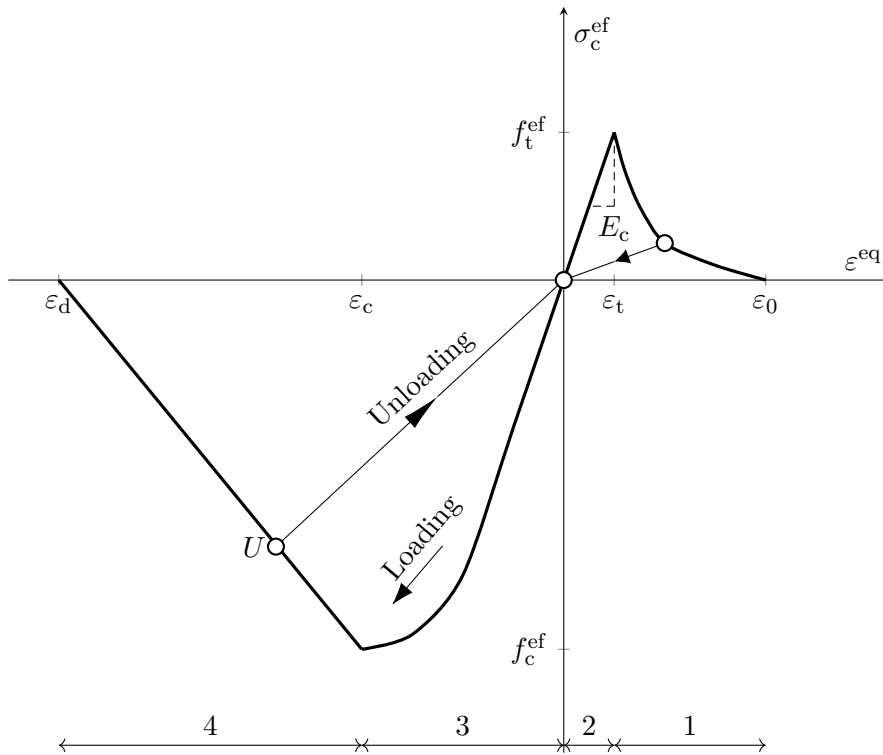


Figure 8.5: Standardised stress–strain relationship

The biaxial failure criterion was adopted from the work by Kupfer et al (1969) and it is visualized in Figure 8.6. Within the figure, σ_1 and σ_2 denote the principal stresses and f_c compressive strength of a concrete cylinder. The strength of the concrete is predicted under the assumption of a proportional stress path under the biaxial state. In the tension-compression state, the failure function continues linearly from the point $\sigma_{c1} = 0$ and $\sigma_{c2} = f_c$ into the tension-compression region

with the linearly decreasing strength (Červenka et al, 2012).

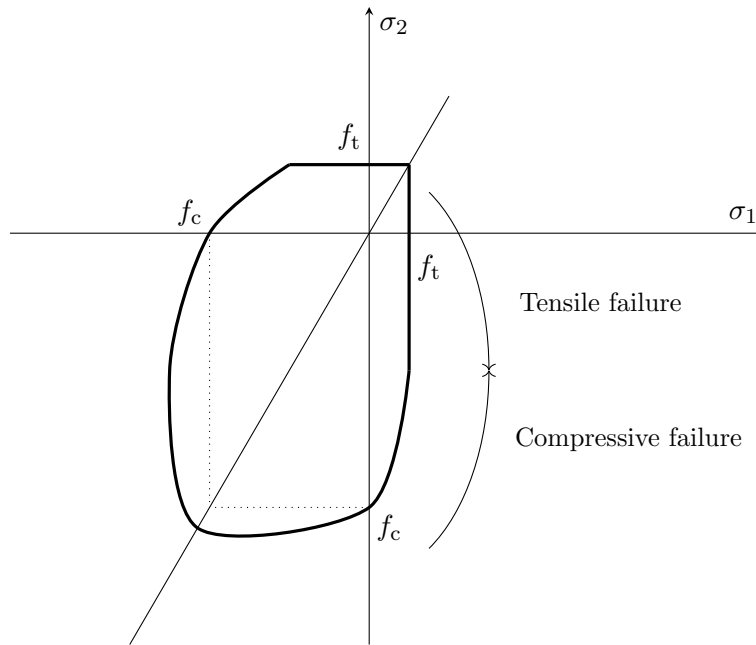


Figure 8.6: Standardised biaxial failure function

The computational crack formation process can be divided into 3 stages, as shown in Figure 8.7. The untracked stage occurs in the domain prior to reaching tensile strength. Afterwards, potential cracks form with decreasing tensile stress on the crack face due to a *bridging effect*. After the stress drops to zero, cracks continue to expand without stress.

It is assumed that under *the fictitious compression plane model* compressive failure is localized in a plane normal to the direction of negative, *i.e.* compressive principal stress. The residual deformation after reaching compressive strength is compressive softening. The compression softening is linear and is defined by the endpoint termed *plastic deformation* w_d (Fig. 8.8). In the research done by van Mier (1986), the plastic deformation was estimated to $w_d = 0.5$ mm in the case of normal concrete.

Due to reinforcement, concrete cracks cannot fully develop and concrete contributes to steel

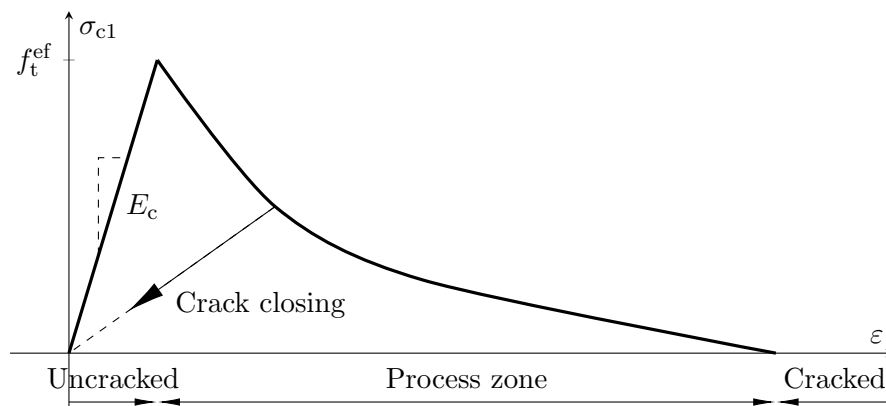


Figure 8.7: Stages of crack opening

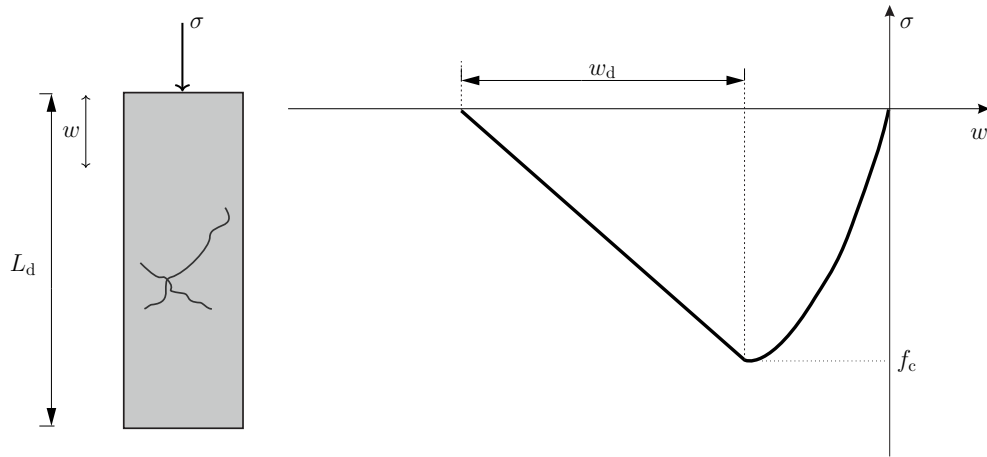


Figure 8.8: Softening displacement law in compression

stiffness. This effect is called *tension stiffening* c_{ts} . This factor represents the relative limiting value of tensile strength in the tension softening diagram. The tensile stress cannot drop below the value given by the product of $c_{ts}f_t$ (Fig. 8.9). The recommended default value for c_{ts} is 0.4. In this thesis, all models except one used the default value. The mentioned exception had the value of 0.3.

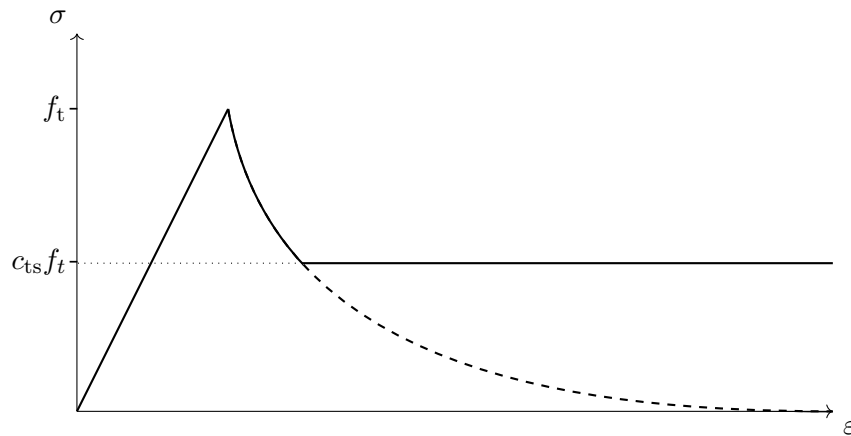


Figure 8.9: Tension stiffening

Tensional fracture energy G_F determines the material's resistance to crack propagation (Toygar et al, 2009) as it can, for example, modify the line failure. The fracture energy implies the area under the tensile stress – displacement curve (Fig. 8.10). Hence, if not tested experimentally, as in this case, an empirical calculation could be used based upon concrete's mechanical properties. The software developers (Červenka et al, 2012) recommend using Equation (8.1). Other approaches were considered through Equations (8.2–8.6), provided by Fédération Internationale du Béton (2013). There were no approaches found in literature to determine fracture energy for masonry materials.

$$G_f = 0.000025 f_t \quad (8.1)$$

$$G_f = G_{f0} \left(\frac{f_{cm}}{f_{cm0}} \right) \quad (8.2)$$

$$G_f = G_{f0} \ln \left(1 + \frac{f_{cm}}{f_{cm0}} \right) \quad (8.3)$$

$$G_f = G_{f0} \ln \left(1 - 0.77 \frac{f_{cm}}{f_{cm0}} \right) \quad (8.4)$$

$$G_f = 73 f_{cm}^{0.18} \quad (8.5)$$

$$G_f = G_{f0} \left(\frac{f_{cm}}{f_{cm0}} \right)^{0.18} \quad (8.6)$$

Where $G_{f0} = 0.03$ MPa is fracture energy based on maximum aggregate size of 16 mm and $f_{cm0} = 10$ MPa Fédération Internationale du Béton (2013).

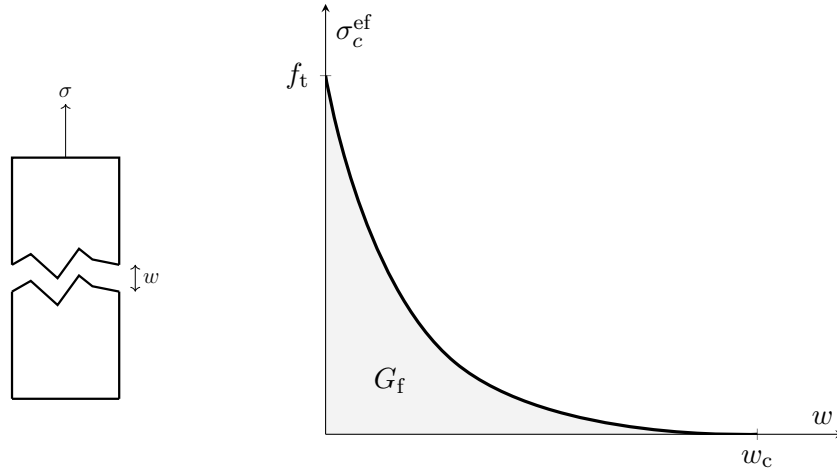


Figure 8.10: Fracture energy

The reduction of compressive strength after cracking ($r_{c,\text{lim}}$) in the direction parallel to the cracks is formulated within the *compression field theory* (Vecchio and Collins, 1986). In the computational software, different functions were used for the *reduction*, in order to allow for user's adjustment of this effect. The function (Fig. 8.11) is derived from several experimental data (Červenka et al, 2012). For the zero normal strain, $\varepsilon_v = 0$ there is no strength reduction, and for the large strains, the strength is asymptotically approaching the minimum value $f_c^{\text{ef}} = r_{c,\text{lim}} f_c$ (Fig. 8.11). In Kollegger and Mehlhorn (1988) the value has been determined as $k_{\text{red}} = 0.4$; however Červenka et al (2012); Dyngeland (1989) authors states reduction as $r_{c,\text{lim}} \geq 0.8$.

The computational software allows fixed ($FCTM = 1$), rotated ($FCTM = 0$), and anything in between $FCTM \in \langle 0, 1 \rangle$. In the fixed crack model, in Cervenka (1985) the principal stress directions provide the crack direction at the moment of the crack initiation. During further loading, these directions are fixed and represent the material axis of the orthotropy. The principal stress and strain directions coincide in the uncracked concrete, assuming isotropy in the concrete component. After cracking, orthotropy is introduced. The weak material axis m_1 is normal to the crack direction, the strong axis m_2 is parallel with the cracks (Fig. 8.12b). In a general case, the principal strain axes ε_1 and ε_2 are rotated and need not coincide with the axes of the orthotropy m_1 and m_2 . This produces shear stress on the crack face as shown in Figure 8.12b (Červenka et al, 2012).

In the rotated crack model (Vecchio and Collins, 1986) the direction of principal stress coincides with the direction of principal strain. Thus, no shear strain occurs on the crack plane, and only two normal stress components must be defined, as shown in Figure 8.12a. If the principal strain axes rotate during the loading, then the direction of the cracks would rotate as well.

Plastic flow β is defined in *Drucker-Prager Plasticity Model*. The return mapping algorithm

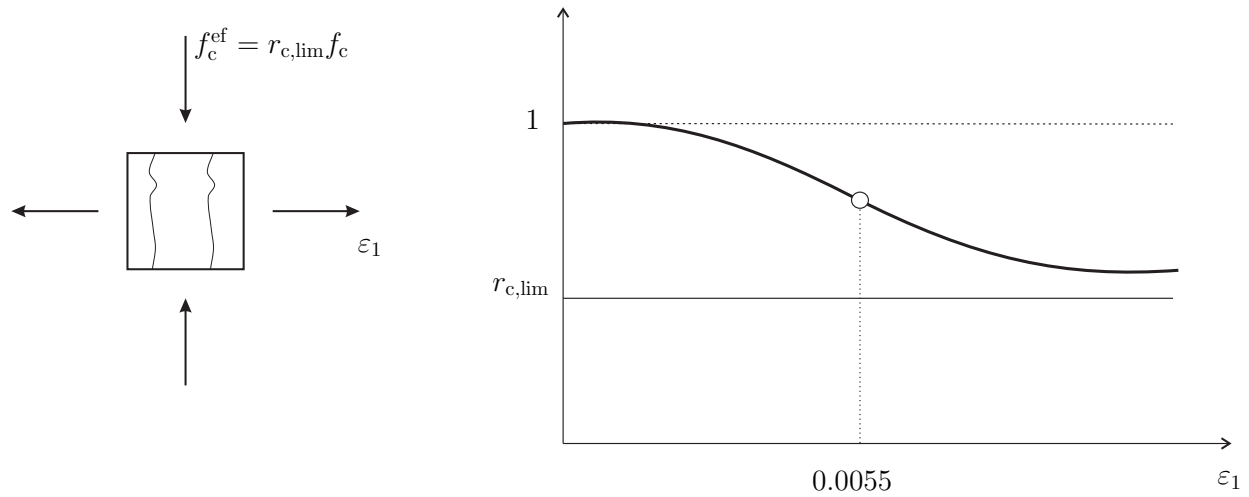


Figure 8.11: Compressive strength reduction within cracked concrete

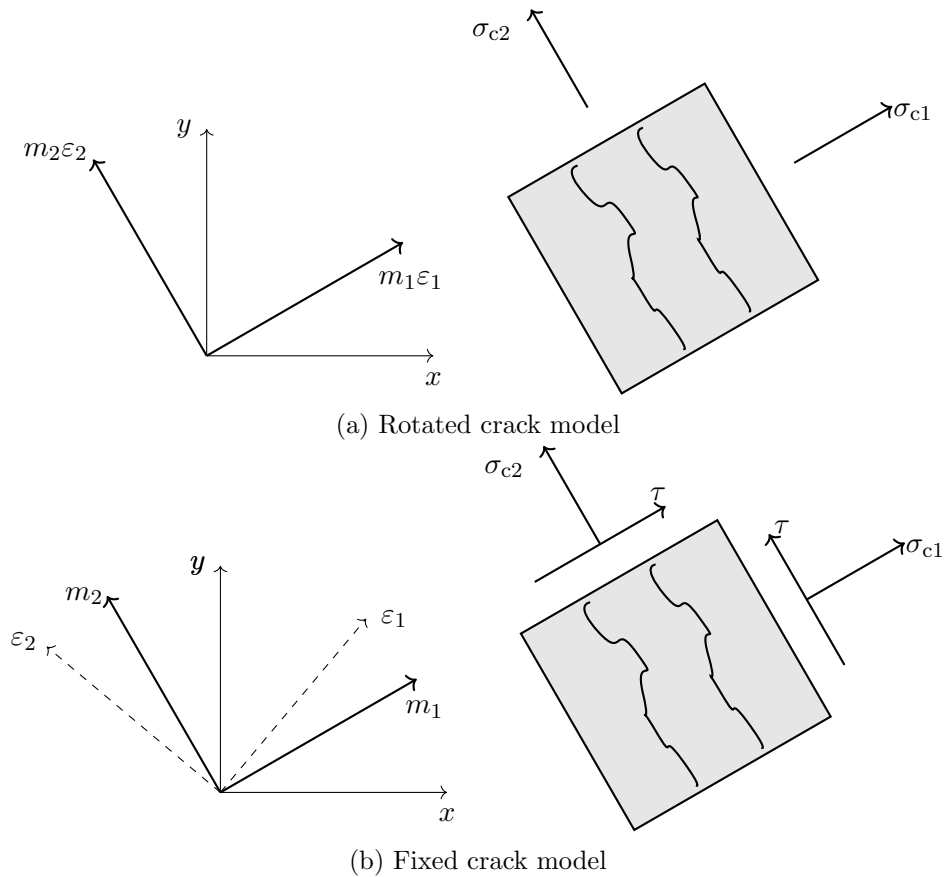


Figure 8.12: Crack model stress and strain state

for the plastic model is based on the predictor-corrector approach as shown in 8.13. During the corrector phase of the algorithm in Figure 8.13, the failure surface moves along the horizontal axis to simulate the hardening and softening of concrete. Therefore, with $\beta = 0$ the volume is preserved, $\beta < 0$ the volume is shrunken; and $\beta > 0$ the volume expands. Software developers Červenka et al

(2012) recommend negative values in case of crushing. Both positive ($\beta > 0$), negative ($\beta < 0$), and neutral ($\beta = 0$) were tested within this thesis.

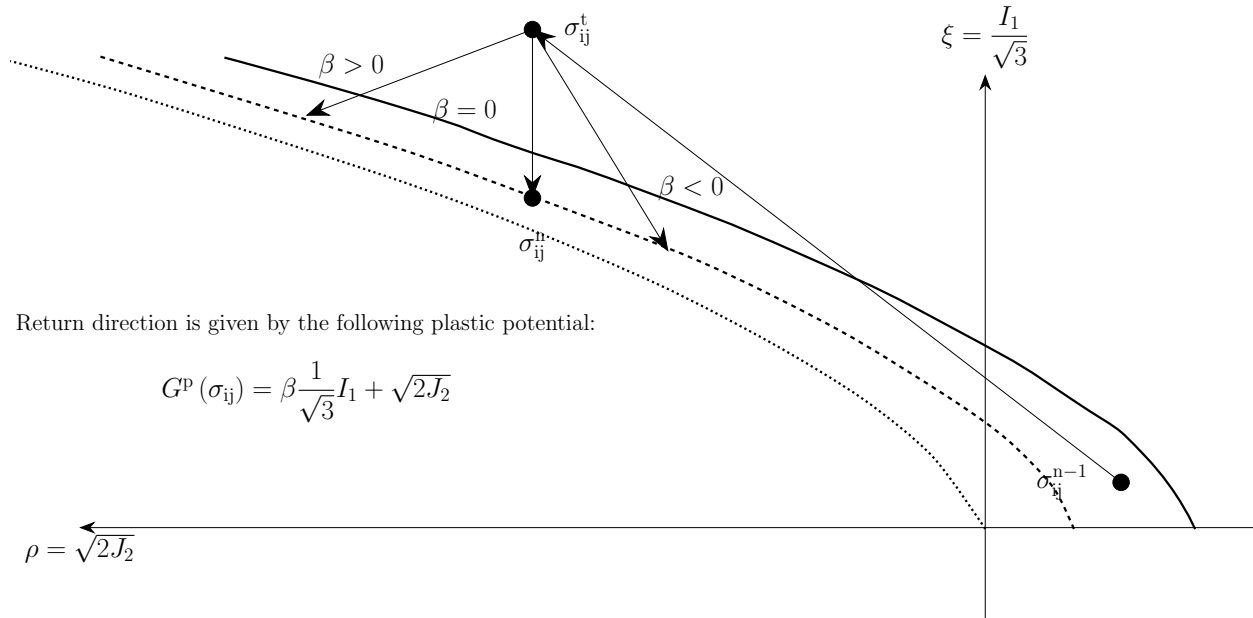


Figure 8.13: Plastic predictor-corrector algorithm for plastic flow β

The initial values used for the simulations of concrete and masonry properties are presented in Table 8.2. Those values were adopted from Penava et al (2016), and later on calibrated (Sec. 9).

Table 8.2: Initial non-linear cementitious 2 material properties for each constituent

Description	Symbol	Frame Concrete	Concrete Lintel	Clay Block	Unit
Elastic modulus	E	4.100 E+04	3.032 E+04	5.650 E+03	MPa
Poisson's ratio	μ_u	0.200	0.200	0.100	/
Tensile strength	f_t	4.000	2.317	1.800	MPa
Compressive strength	f_c	-5.800 E+01	-2.550 E+01	-1.750 E+01	MPa
Specific fracture energy	G_f	1.200 E-04	5.739 E-05	4.500 E-04	MN/m
Crack spacing	s_{max}	0.125	0.125	/	m
Tensile stiffening	c_{ts}	0.400	0.400	/	/
Critical compressive disp.	W_d	-1.010 E-03	-5.000 E-04	-5.000 E-04	/
Plastic strain at f_c	ε_{cp}	-1.417 E-03	-8.411 E-04	-1.358 E-03	/
Reduction of f_c due to cracks	$r_{c,lim}$	0.800	0.800	0.800	/
Crack shear stiffness factor	SF	2.000 E+01	2.000 E+01	2.000 E+01	/
Aggregate size		1.600 E-02	2.000 E-02	/	m
Direction of shear flow	β	0.000	0.000	0000	/

8.2.2 Interface gap (contact) model

The interface model is used to simulate contact between two solids, connection between masonry wall units and between the units and the surrounding frame. The implemented material model was adopted from geotechnical research, where it was used to simulate contact between different layers of soil. The interface material is based on *Mohr-Coulomb criterion with tension cut off*.

In short, the initial failure surface (Fig. 8.14) corresponds to *Mohr-Coulomb condition* with ellipsoid in tension regime. After stresses violate aforementioned condition (Eq. 8.7), this surface collapses to a residual surface which corresponds to dry friction $\sigma\phi$. The ellipsoid is formed by two tangents, whereas the vertical one is perpendicular to the normal σ axis at tensile strength f_t ; while the other intersects shear axis τ at cohesion c value with $-\phi$ inclination.

$$\begin{aligned}
 |\tau| &\leq c - \sigma\phi, & \sigma &\leq 0 \\
 \tau &= \tau_0 \sqrt{1 - \frac{(\sigma - \sigma_c)^2}{(f_t - \sigma_c)^2}}, & 0 < \sigma &\leq f_t \\
 \tau &= 0, & \sigma &< f_t \\
 \tau &= \sqrt{\tau_1^2 + \tau_2^2}
 \end{aligned} \tag{8.7}$$

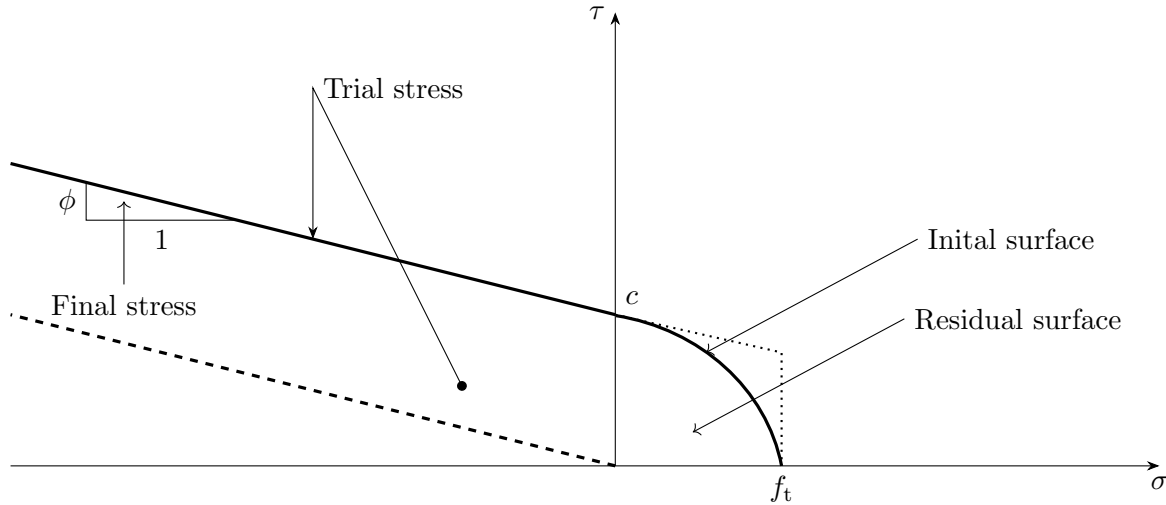


Figure 8.14: Failure surface for interface elements

Additionally, zero thickness interfaces contain both shear and normal stiffness, where K_{nn} and K_{tt} are the initial ones. Software developers suggest using Equation (8.8) (Červenka et al, 2012). Where E and G are the minimal moduli values surrounding the interface, and t is the width of the interface zone. There are also two counterparts to each stiffness referred as minimal K_{nn}^{\min} , K_{tt}^{\min} . Their purpose is plainly numerical, to avoid infinite global stiffness after interface fails and its stiffness reaches zero. The suggested values are recommended to be 1/1000 of their normal counterparts (Červenka et al, 2012).

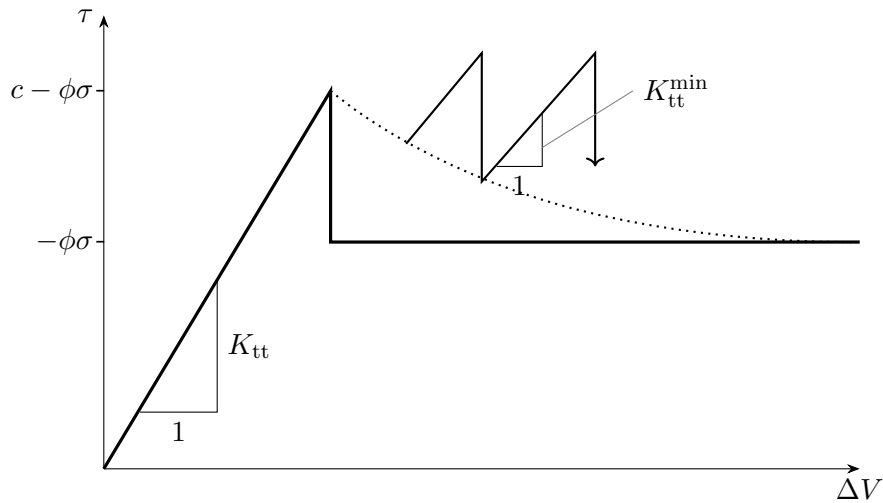
$$K_{nn} = \frac{E}{t}, \quad K_{tt} = \frac{G}{t} \tag{8.8}$$

$$K_N = \frac{E_U E_J}{t_j (E_U - E_J)} \tag{8.9}$$

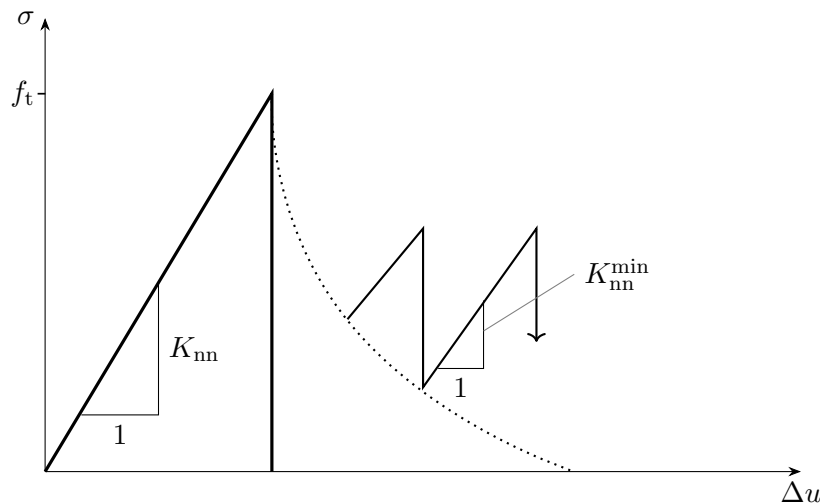
$$K_T = \frac{G_U G_J}{t_j (G_U - G_J)} \quad (8.10)$$

Where U and J are brick and mortar modulus with U being the one that has greater value.

Within the software, it is possible to define evolution laws for *tensile* as well as *shear softening* by arbitrary multi-linear laws. It is possible to simulate the degradation of tensile strength caused by the degradation of shear and vice versa. Such a behaviour under defined law can be seen in Figure 8.15, where there is no softening introduced, tension drops to zero (Fig. 8.15b solid line path) while shear drops and reverts to dry friction (Fig. 8.15a solid line path). Yet, when the laws are introduced it resorts to softer degradation (dotted lines in Fig. 8.15b & 8.15a).



(a) Shear behavior



(b) Tension behavior

Figure 8.15: Behavior of interface material model (dotted line – if softening is included)

The aforementioned tensional and shear law was implemented in order to simulate *mortar interlocking*. Mortar interlocking was previously described in Section 4.2. In short, the mortar that was layered on the block, it falls in its holes, and thus interlocking two blocks into one jointed action. It results in greater shear strength, and it bypasses sliding failure resulting in tensional

failure of blocks. The numerical simulation of its affects was developed by Penava (2012), and it was adopted in research herein. The points for the multi-line function were set following Equation (8.11) (Penava et al, 2016). It is visible in Equation (8.11) and Figure 8.16, both shear hardening and softening was modelled in order to simulate the effects correctly.

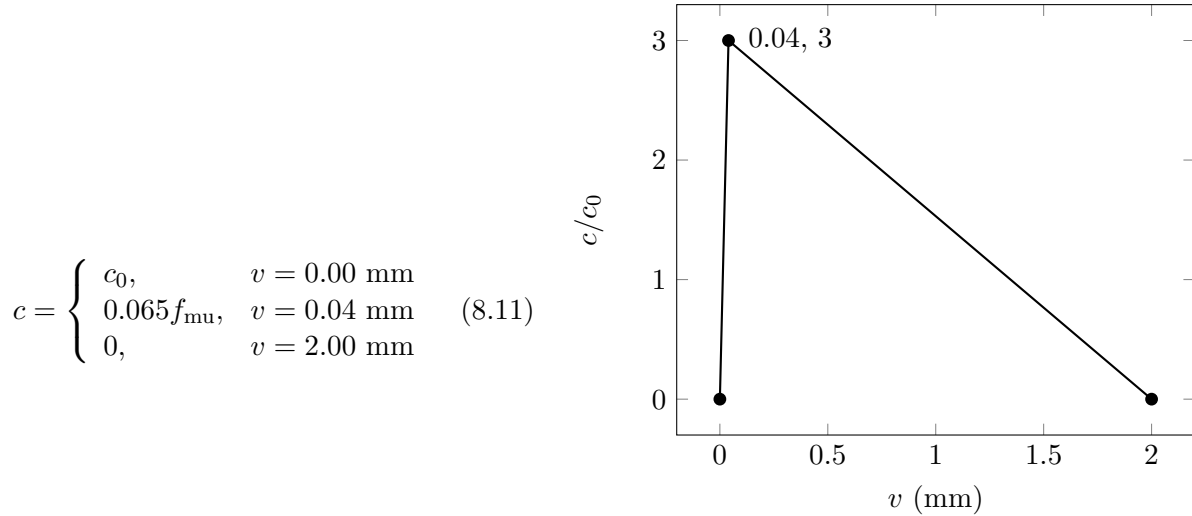


Figure 8.16: Cohesion hardening/softening function

The initial values used for the simulations of interface material are presented in Table 8.3. Those values were adopted from Penava et al (2016), and later on calibrated (Sec. 9).

Table 8.3: Initial interface material properties

Description	Symbol	Mortar bedjoint	Mortar headjoint	Unit
Normal stiffness (Eq. 8.8)	K_{nn}	5.65 E+05	8.50 E+04	MPa
Tangential stiffness (Eq. 8.8)	K_{tt}	2.57 E+05	3.86 E+04	MPa
Min. normal stiffness	K_{nn}^{\min}	5.65 E+02	8.50 E+01	MPa
Min. tangential stiffness	K_{tt}^{\min}	2.57 E+02	3.86 E+01	MPa
Tensile strength	f_t	0.20	0.20	MPa
Cohesion	c	0.35	0.35	MPa
Friction coefficient		0.24	0.24	/
Interlock function (Fig. 8.16)		Where applicable*	No	

* Only on bedjoint interfaces between masonry units

8.2.3 Friction spring model

Due to large vertical, *i.e.* gravity load of 365 kN that was introduced at the column ends, the friction could not be undermined even though the rolling supports were used. Friction coefficient for sliding steel roller bearing was estimated as $\mu_F = 0.03$ (Hirt and Lebet, 2013). Hence, friction force T_F for one column end was calculated following the Equation (8.12).

$$T_F = \mu_F \cdot 365 \text{ kN} \approx 10 \text{ kN} \quad (8.12)$$

Calculation of IP spring stiffness is shown in Equation (8.13). Likewise, the OoP spring was calculated using Equation (8.14). The surface springs were implemented in the computational models via non-linear functions (Fig. 8.17). The functions had values that had an incline to ensure computational stability.

$$K_{\text{IP},s} = \frac{2T_{\text{F}}}{A_{\text{beam}}} = 0.83 \text{ MPa} \quad (8.13)$$

$$K_{\text{OoP},s} = \frac{2T_{\text{F}}}{A_{\text{column}}} = 0.50 \text{ MPa} \quad (8.14)$$

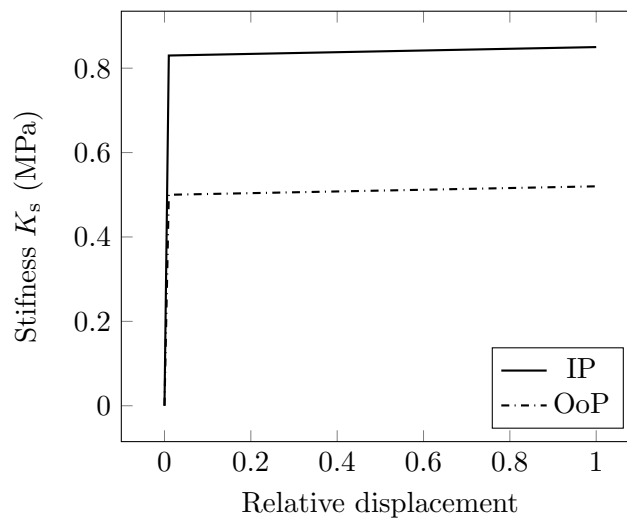


Figure 8.17: Multi-linear spring functions

8.2.4 Reinforcement model

Discrete reinforcement is implemented in the form of reinforcing bars modelled by truss elements. The reinforcing steel stress-strain behaviour was described with *bilinear law with hardening* and modified by the nonlinear model of *Menegotto and Pinto* (Fig. 8.18). The recommended *Menegotto and Pinto* values were used (optimal in Fig. 8.18), while only the yielding and tensile strength were inputted, based on the tests. The material properties used within the software are presented in Table 8.4. Note that there were no changes in the reinforcement material model during the calibration.

8.3 Elastic plates

Elastic plates were used in order to avoid singularities when introducing point forces on the frames. It employs *linear-elastic, isotropic* material model with elastic modulus of $E = 200000$ MPa.

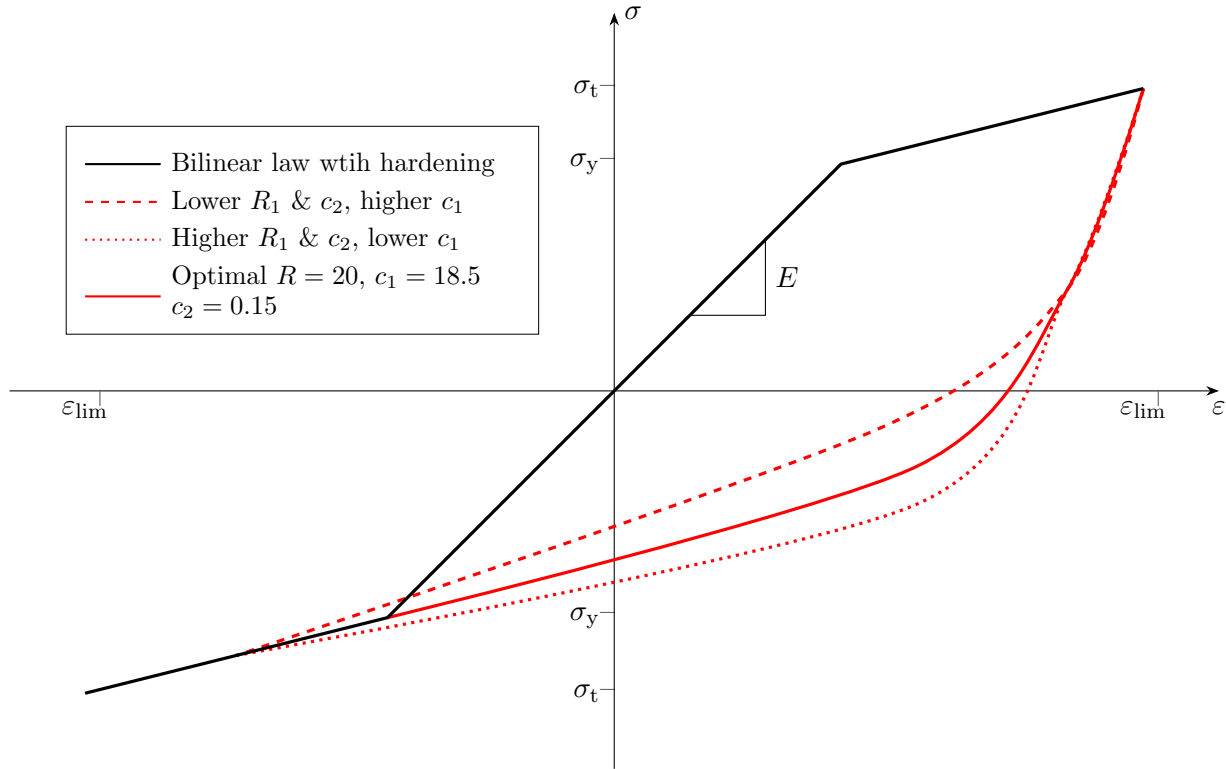


Figure 8.18: Reinforcement bilinear law with hardening

Table 8.4: Bilinear steel reinforcement material properties

Description	Symbol	Value	Unit
Elastic modulus	E	2.10 E+05	MPa
Yield strength	σ_y	5.50 E+02	MPa
Tensile strength	σ_{tn}	6.50 E+02	MPa
Limited ductility of steel	ε_{lim}	0.01	/
Bauschinger effect exponent	R	2.00 E+01	/
Menegotto-Pinto parameter	C_1	0.93	/
Menegotto-Pinto parameter	C_2	0.15	/

8.4 Solution of non-linear equations

8.4.1 Newton-Raphson method

The *Newton-Raphson method* finds a good approximation for the root of a non-linear function. It uses the principle that a straight line tangent can approximate a continuous and differentiable function.

The Newton-Raphson retains the load constant as it iterates displacements in the case of prescribed force. Vice-versa in the case of prescribed deformation. *Full Newton-Raphson* method uses the tangential stiffness from the previous iteration until equilibrium is met (Eq. 8.15). Therefore, it recalculates stiffness matrix at each iteration (Fig. 8.19a). Contrariwise, *Modified Newton-Raphson* does not recalculate stiffness matrix each iteration. Rather, it calculates only once at the first iter-

ation; that way, all the tangents are parallel to each other (Fig. 8.19b). Thus, effectively changing the derivation of $f'(x_n)$ to $f'(x_1)$ in Equation (8.15). This way, the computational time is reduced while exhibiting the worst convergence of the solution procedure.

$$x_{n+1} = x_n - \frac{f(x_n)}{f'(x_n)} \quad (8.15)$$

The Newton-Raphson method has its drawbacks; when iteration reaches functions limit point, it cannot accurately predict the solution. This is depicted in Figure 8.20c, where the tangent on the limit point (F_i, d_i) skips the functions indentation. This kind of behaviour is called *snap-through instability* and is also depicted in Figure 8.20a (Vasios, 2015). Similarly, the problem can occur another way around, called *Snap-Back instability* (Fig. 8.20b). To avoid such problems, it is suggested to combine prescribed force, and deformation controls (Sabir and Lock, 1972), a special technique of including artificial spring as presented by Wright and Gaylord (1968) by rejecting the equilibrium iterations in the close vicinity of limit point Bergan et al (1978).

The *modified Newton-Raphson* method was the used as the main solver due to its time saving properties.

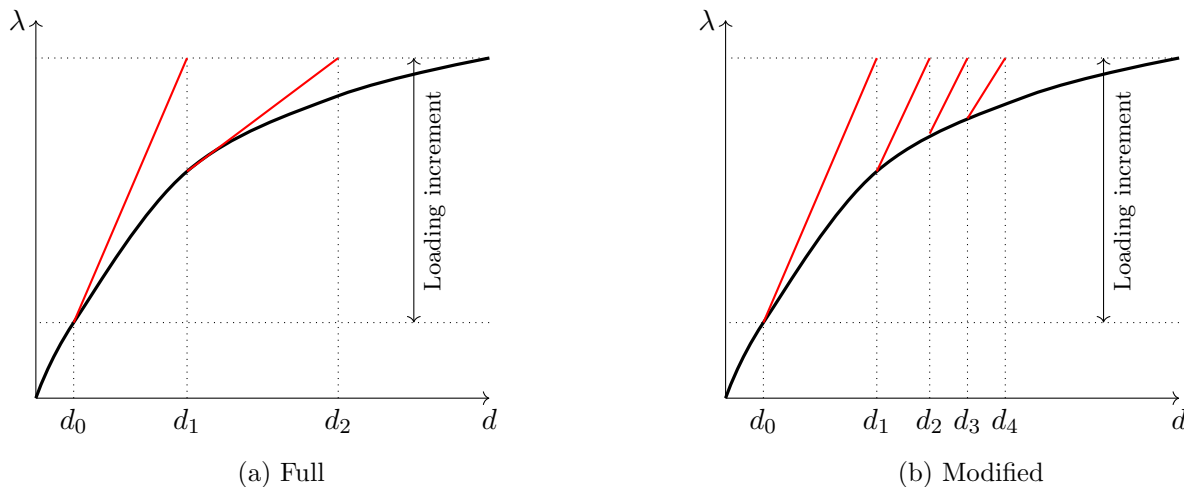


Figure 8.19: Newton-Raphson methods
Newton-Raphson methods (q - load, d - displacement)

8.4.2 Arc-length method

The *Arch-length* is another method used for non-linear computing equations that is available for selection within the software. It is very efficient for simple load and unloading problems, and it is generally better at coping with the limit points, unlike the Newton-Raphson method. Likewise, it postulates both displacement (d) and force-factor (λ). The iterative process begins by using defined *radius*, and the next converged point is then obtained as the point of intersection between the equilibrium path and that circle. The derivation, *i.e.* tangent is calculated from the point after which the intersection with the circle is found. Then, the ordinate is lowered from the intersection until it intersects the equilibrium function. The process loops until reaching the endpoint of the circle–equilibrium function intersection (Fig. 8.21).

The process had its drawbacks; also termed *snap-back* and *-trough* problems (Fig. 8.21b, 8.21c) mainly due to the nature of quadratic equation as it provides two solution (Vasios, 2015). In the

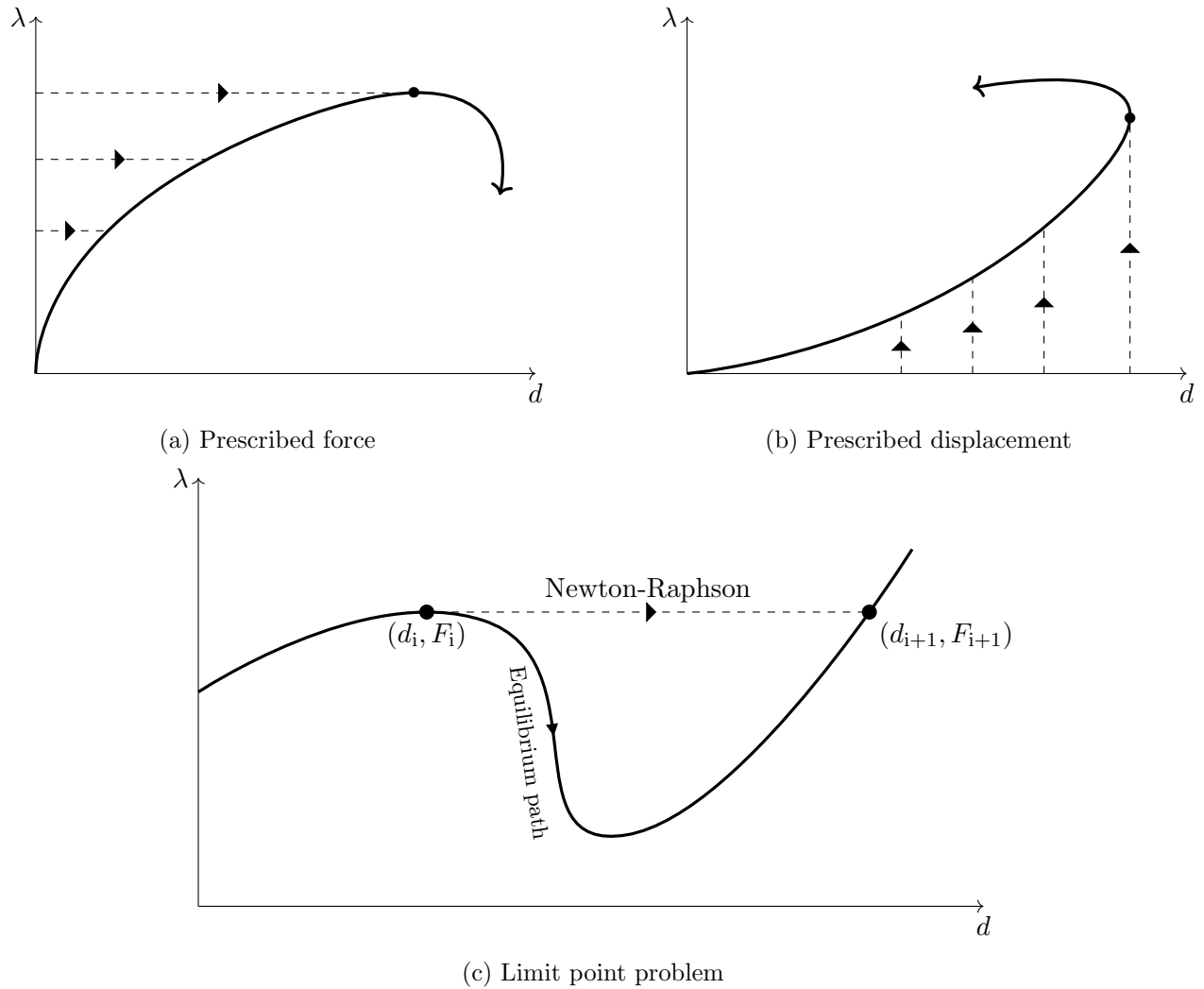
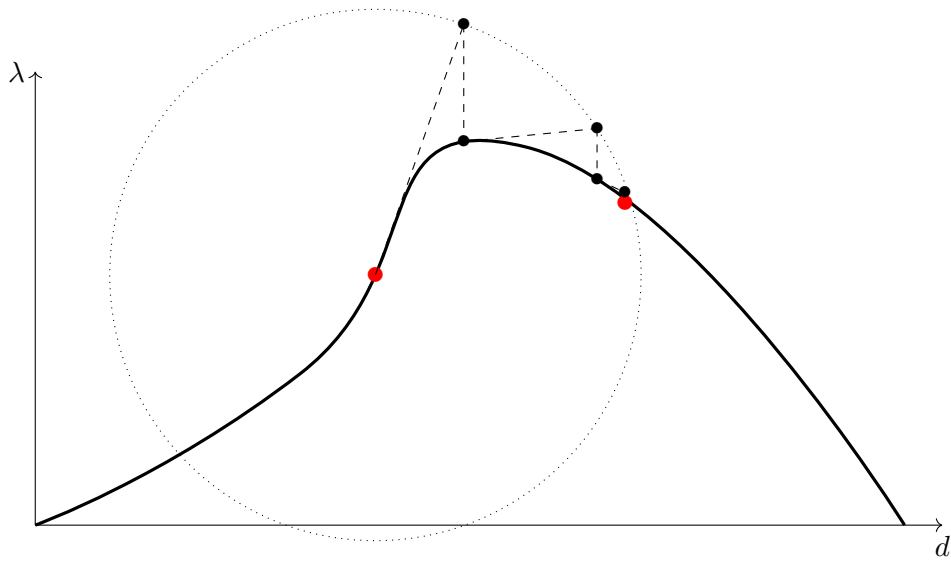


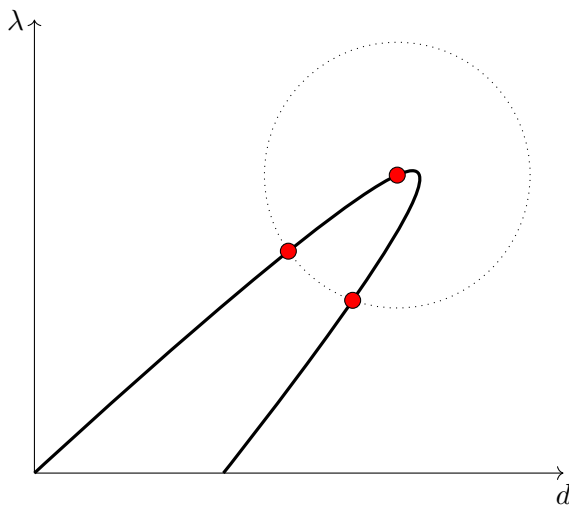
Figure 8.20: Example of unstable *Newton-Raphson* computing due to load controls (Vasios, 2015)

case of snap-back behaviour, the two solutions that correspond to the candidates for the next point are both located at the same region adjacent to the current point (Fig. 8.21c). Yet, in snap-through, the two solutions corresponding to the candidates for the next point are located bilaterally adjacent to the current point.

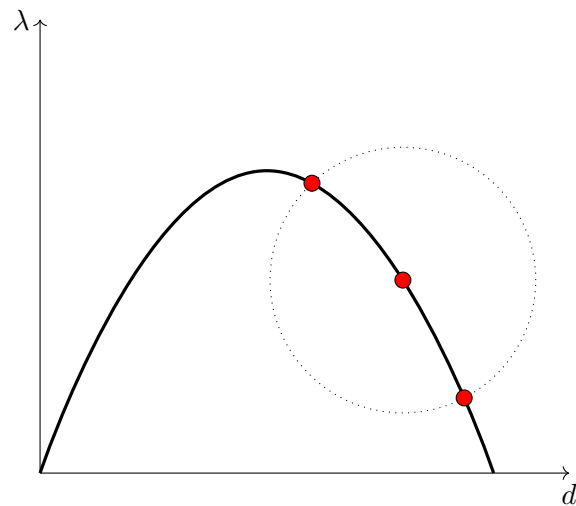
This method was avoided since it had a problematic performance with cyclic loads.



(a) Arc-length method example



(b) Snap-back problem



(c) Snap-Through problem

Figure 8.21: Arc-length method (Vasios, 2015)

Chapter 9

Micro-model development, calibration and sensitivity analysis

The calibration process followed the flowchart presented in Figure 9.1. The calibration starts with the BF model. When the results matched those from the experiments, or the computational stability was archived, the calibration preceded to the FI model. Next was the CD model, and so on. If there was a change in the properties of the concrete, the calibration reverted the first step, *i.e.* BF model. If there was a change in the parameters of the masonry but not on the concrete, the calibration process reverted the second step, *i.e.* FI model. When the IP finished, the OoP calibration started. Similarly, with an adopted change in the material model, the OoP calibration reverted to the IP start.

The parameters that were tested for the purpose of calibration and, by doing so, sensitivity analysis are shown in Table 9.1. They present the parameters varied in all three test simulations. In summation, there were 26 modifications to concrete, 33 to masonry, 26 to interface material model and 19 combinations of multiple parameters that adds up to 104 tested models. In the table, column *Old* referred to initial values, while the *New* the selected, *i.e.* adopted ones. The column *property* presents the varied parameter, while the *range/value* column exactly that; range and values of the varied parameters. The *reference* column presents the citations from where the variations were found, *i.e.* justified. Most values were preserved, hence, in this section the focus will be on those that were adopted rather than rejected (Tab. 9.1, Fig. 9.2 & 9.3).

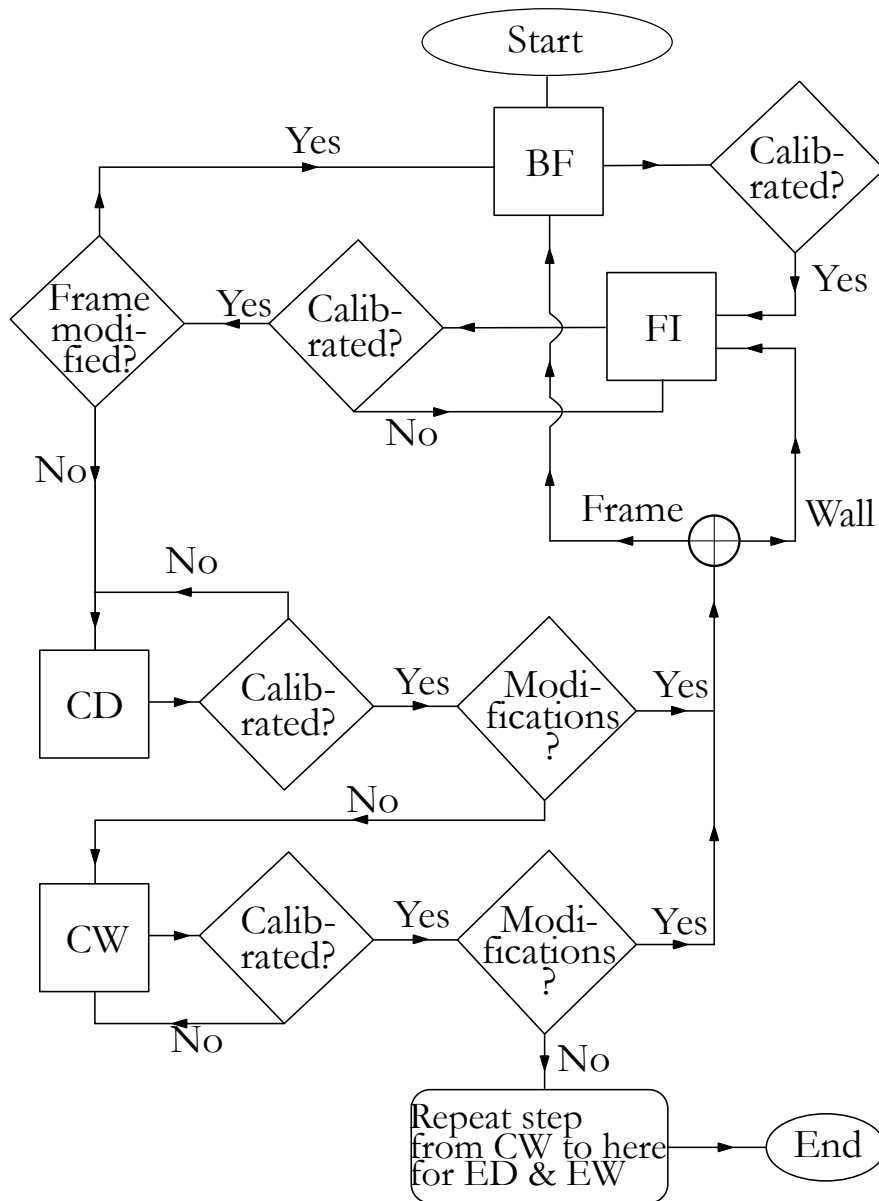


Figure 9.1: Calibration flowchart

Table 9.1: Tested parameters for both IP and OoP calibration

Model #	Property	Reference	Range / value	Value		Unit
				Old	New	
1	FCMC*		0.00, 1.00	1	1	/
2	w_d	(van Mier, 1986; Vonk, 1992)	-0.10, -0.20, ..., -0.50	-0.1	-0.1	mm
3	f_t (Eq. 9.1)	Phani et al (2013)	3.35	4	3.35	MPa
4	$r_{c,lim}$	Červenka et al (2012); Vecchio and Collins (1986)	0.7	0.8	0.8	/
5	β	Vos (1983)	-0.5, -0.4, ..., 0, 0.1, 0.2, 0.5, 1	0	-0.1	/
	(Eq. 8.1)	Červenka et al (2012)	0.084			
	(Eq. 8.2)		0.103			
	(Eq. 8.3)		0.125			
6	G_f	Fédération Internationale du Béton (2013)	0.156	0.084	0.084	N/mm
	(Eq. 8.4)		0.151			
	(Eq. 8.5)		152000			
	(Eq. 8.6)					
Concrete						
1	w_d	(van Mier, 1986; Vonk, 1992)	5.00, 0.50, 0.05, 0.005	0.5	0.5	mm
2	$f_{c,0} = f_c$		-58	-5.14	-5.14	MPa
3	FCMC*		0.00, 1.00	1	0	/
4	$r_{c,lim}$	Červenka et al (2012); Vecchio and Collins (1986)	0.8, 0.7, 0.6, 0.50, 0.49, ..., 0.4	0.8	0.4	/
5	ε_{cp}		-0.01	-1.36	-1.36	%
6	β	Vos (1983)	0, -0.05, -0.10, -0.20, -0.30	0	0	/
7	f_t	Anić et al (2019)	0.38	1.8	0.38	MPa
Clay masonry						
1	$\max\{c/c_0\}$ x		100, 10, 1, 0.10, 0.25, 0.50, 0.75	2	0.75	mm
2	$\max\{c/c_0\}$		1.0, 1.5, 2.0, 2.5, ..., 5.0	3	3	/
3	K_N (Eq. 8.9)	DIANA (2017)	140, 140, 0.140	565	565	N/mm ³
3	K_T (Eq. 8.10)		14, 1.4, 0.014	275	275	N/mm ³
4	$\max\{\sigma/f_t\}$		3.0, 2.5, 2.0, ..., 0.5	1	1	/
5	$\max\{\sigma/f_t\}$ x	Anić et al (2019)	0.01	0.1	0.01	mm
Interface						

* FCMC – fixed crack model coefficient

 $\max\{f(x)\}$ x – Maximal x values of a given function $f(x)$

9.1 In-Plane cyclic, quasi-static micro-model evaluation

The developed micro-model used the material model properties that were developed based on the 2D micro-model done in the Penava et al (2016). However, the inherited material model properties produced comparatively greater values.

Only the physical parameters that were not measured and those purely mathematical ones were varied. Therefore, the physical values were recalculated using different equations found in the literature. For example, Equation (9.1) for tensile strength of the concrete (Phani et al, 2013) and fracture energy Equations (8.1–8.6) in the case of concrete material model.

On the BF model, it was found that recalculation (Eq. 9.1) of the tensile strength (lowering it by 18 %) did, as expected, cause the lower response of the model. Therefore, the value was adopted.

$$f_t = 0.44\sqrt{f_c} \quad (9.1)$$

The variation of fracture energy, based on the Equations (8.1–8.6) provided by Fédération Internationale du Béton (2013) did not have significant impact on the overall response (Fig. 9.2b). Hence, the initial value was preserved.

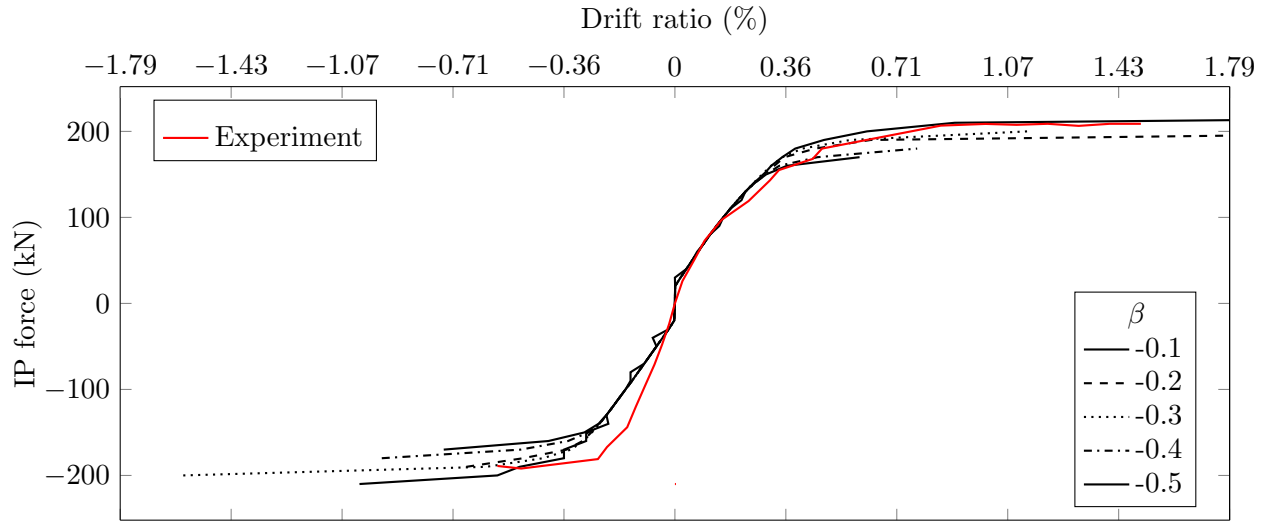
The interface stiffnesses were calculated initially using Equation (8.8) and recalculated using Equations (8.9) and (8.10). The impact was considerable; however, the output was not satisfactory. Therefore, the recalculated values were rejected.

Parameter $r_{c,\text{lim}}$ regulates the *reduction of compressive strength* of the concrete due to cracks. The parameter is in function of either the reinforcement or *crack bridging effect*. The recommended value for concrete with fine mesh was found by Kollegger and Mehlhorn (1988) to be $r_{c,\text{lim}} = 0.45$, while Dyngeland (1989) found (also recommended by Červenka et al (2012)) $r_{c,\text{lim}} \geq 0.8$. Values of $r_{c,\text{lim}} \in \{0.8, 0.7, \dots, 0.4\}$ were tested in case of masonry and $r_{c,\text{lim}} \in \{0.8, 0.7\}$ in case of concrete material model. The value for concrete was preserved as $r_{c,\text{lim}} = 0.8$, while a new one was adopted in case of masonry material model where $r_{c,\text{lim}} = 0.4$.

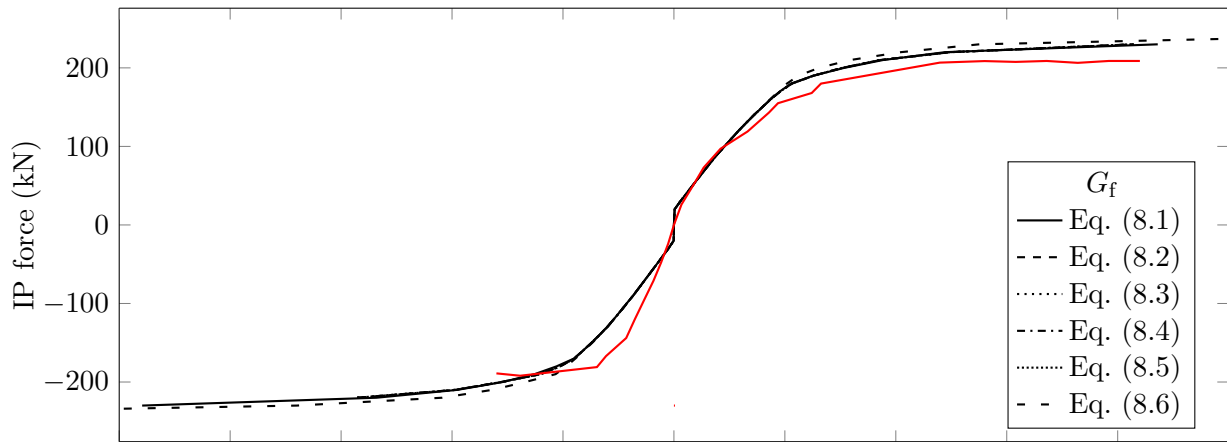
One purely mathematical parameter that was tested, was the direction of plastic flow (β). In short, if $\beta = 0$ the volume due to cracks is preserved; whereas, if $\beta < 0$ it will compact (recommended for crushing), and dilate if $\beta > 0$. It was observed that the direction of plastic flow has a significant impact on the concrete while nearly non on masonry material model (Fig. 9.2a vs. 9.3a). In the end, the masonry model preserved the value of $\beta = 0$, while concrete one was adopted for *crushing* $\beta = -0.1$.

The computational stability was compromised with the newly adopted parameters listed above. This was exaggerated in the case of models with openings. The problem was aided with the *fixed crack model coefficient (FCMC)*, that was varied $FCMC \in \{0, 1\}$ in both concrete and masonry material model. The concrete value was preserved, while in the case of masonry, the rotated crack model was adopted ($FCMC = 1$). The change produced more stable computations, with only a slight impact on the response (Fig. 9.3c).

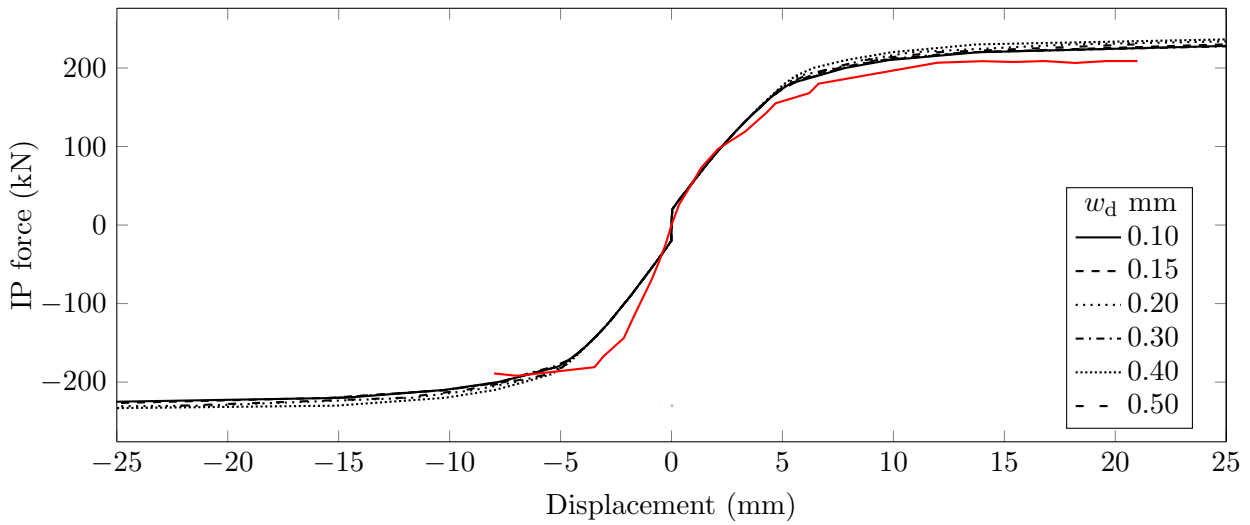
Furthermore, from the analysis of the results, it was shown that changes to the concrete do not mirror the same impact on overall behaviour if the same changes were done to the masonry material model. It was observed that in the IP analysis, the infill wall was more affected by the change in *interface* properties than with the masonry. This is best exemplified in the significantly lower model response caused by reducing the tensile strength of concrete by 18 %, while no significant difference was observed when masonry's tensional strength was reduced by 80 %. However, when the *cohesion* was varied, it produced great differences (9.3b).



(a) Direction of plastic flow β

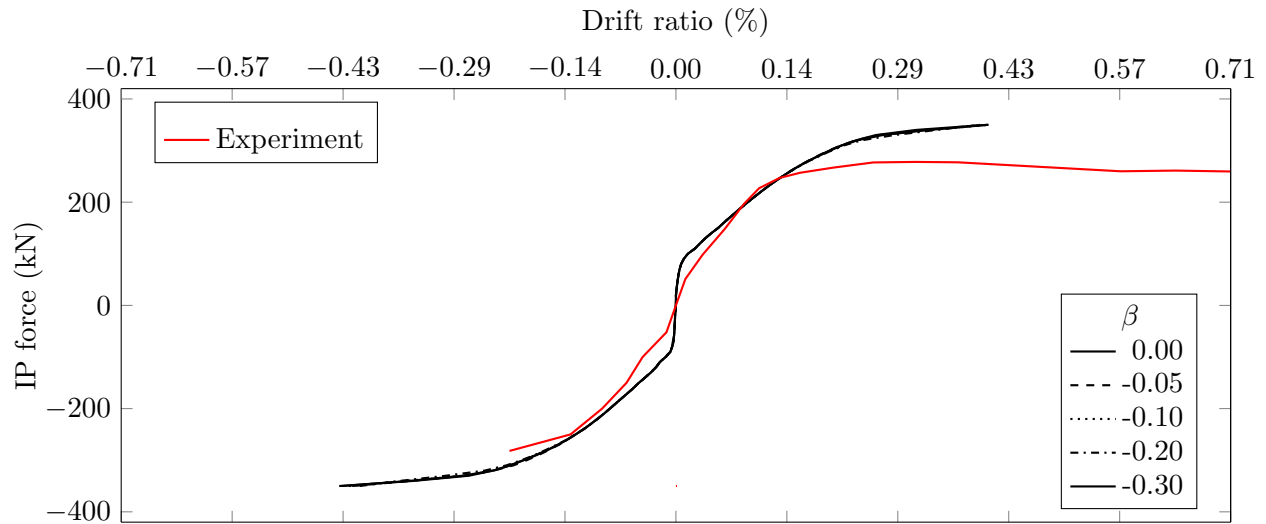
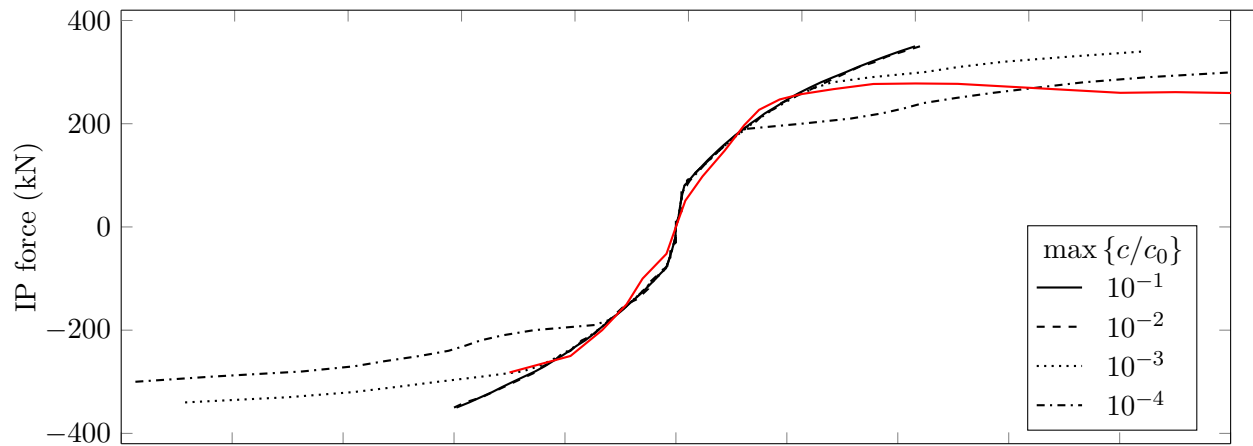
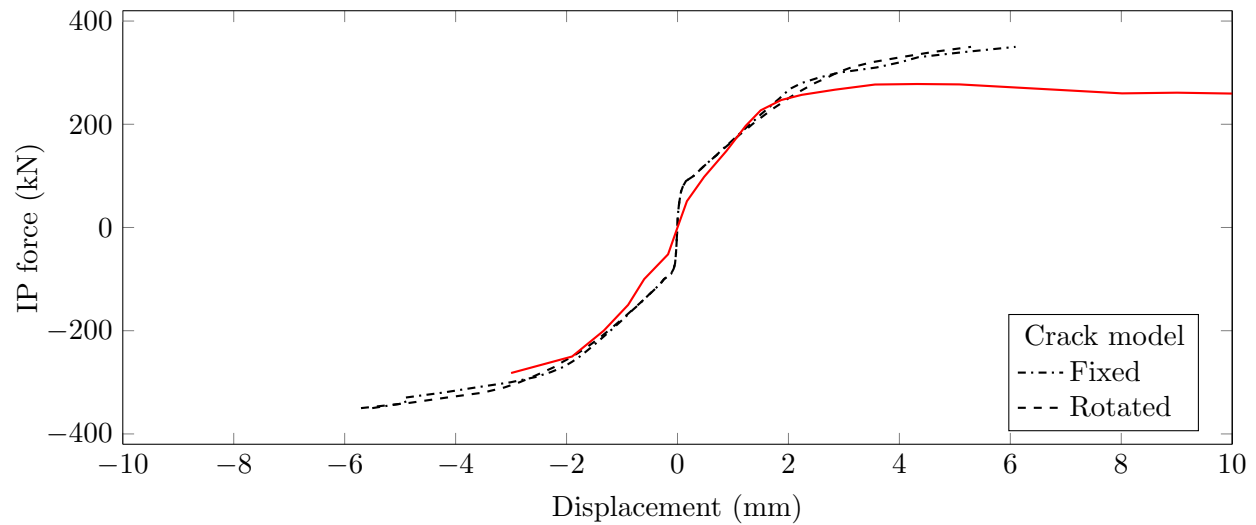


(b) Fracture energy G_f



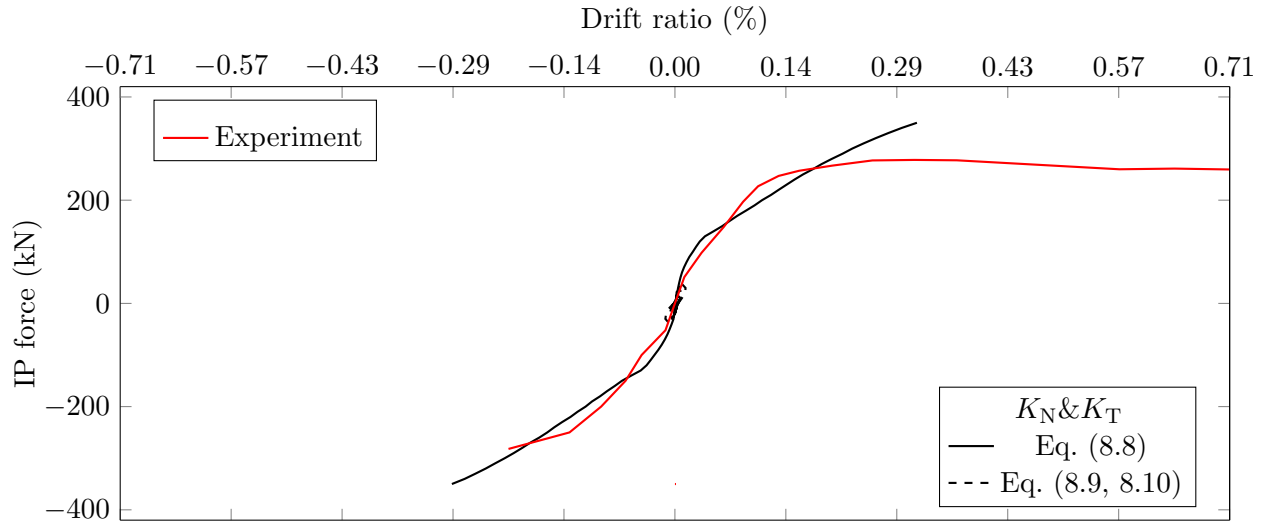
(c) Plastic deformation w_d

Figure 9.2: Parts of calibration results of BF model

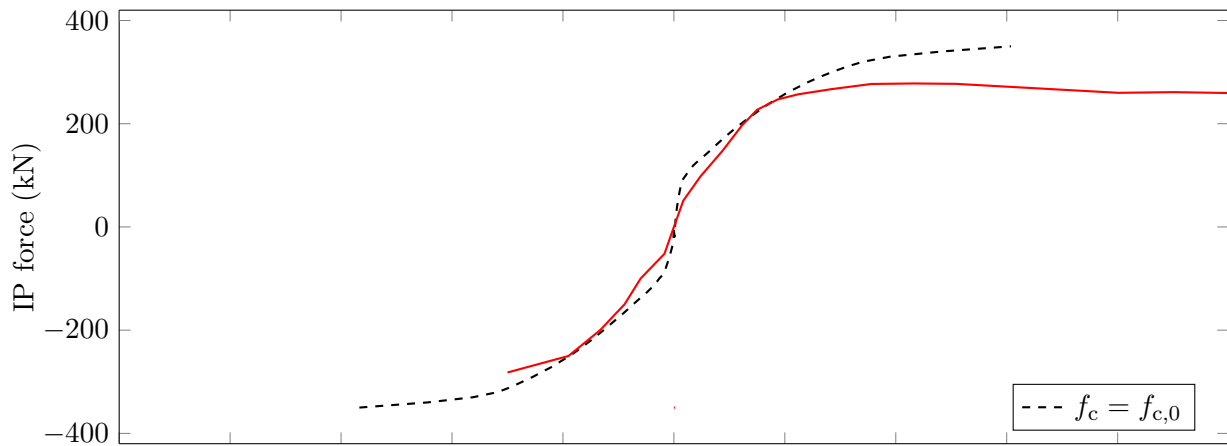
(a) Direction of plastic flow β in masonry material model(b) Cohesion c/c_0 peak value

(c) Crack model calibration in masonry material model

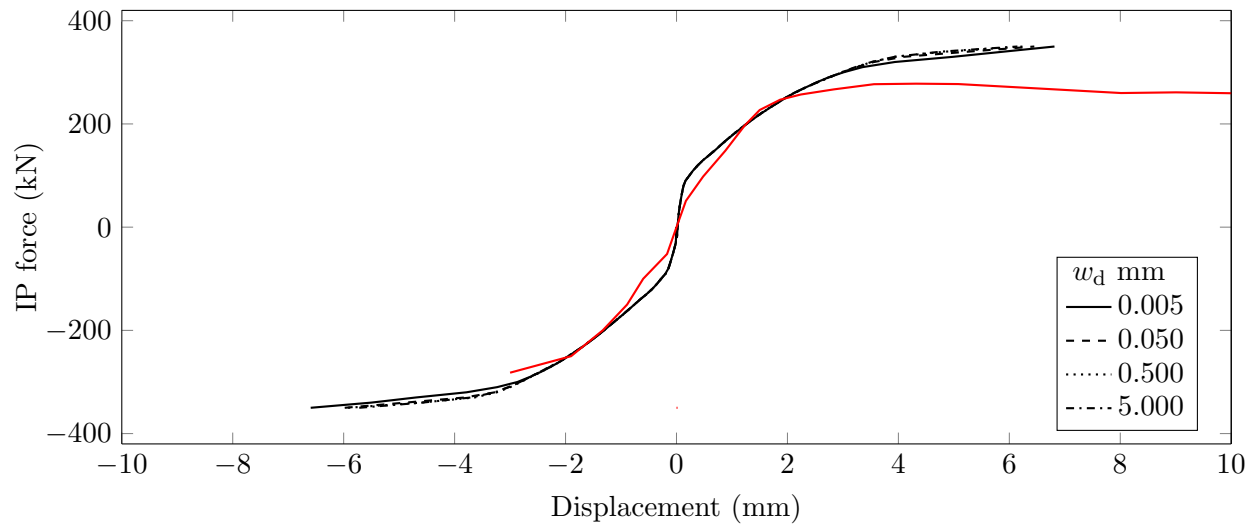
Figure 9.3: Parts of calibration results from FI model



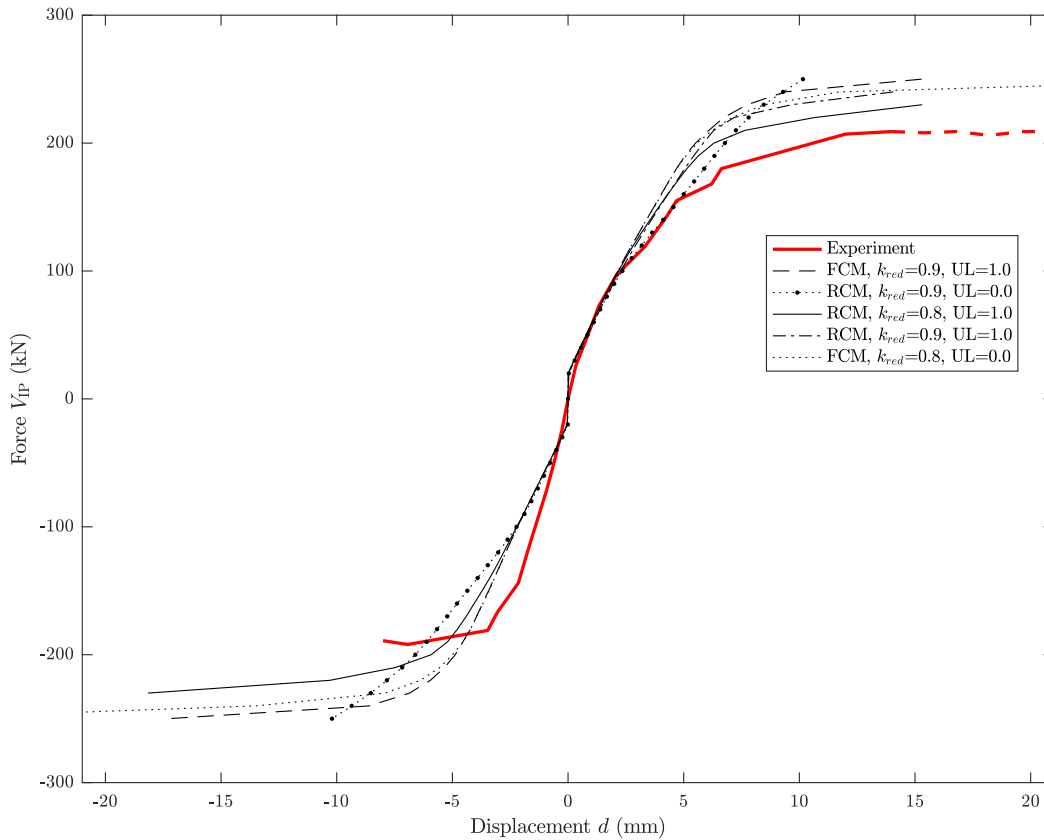
(d) Change in interface stiffness



(e) Fracture energy G_f modification in masonry material model



(f) Change of plastic displacement w_d in masonry material model
 Figure 9.3 (cont.): Parts of calibration results from FI model



(g) Miscellaneous properties

Figure 9.3 (cont.): Parts of calibration results from FI model

Summarily, the parameters that were adopted purely for IP calibrations were: 1) Crack model of infill unit (fixed \rightarrow rotated); 2) Concrete's direction of plastic flow (β 0.0 \rightarrow -0.1); 3) Masonry's reduction of compressive strength due to cracks ($r_{c,lim}$ 0.8 \rightarrow 0.4); 4) Concrete's tensile strength (f_t 4.00 \rightarrow 3.35 MPa). With the newly adopted parameters, the models were considered calibrated in the IP direction. The rest of adopted parameters in Table 9.1, are caused by the OoP calibration.

The calibrated graphs are plotted against the experimental ones in the Figure 9.4, numerically they are compared in Table 9.2, and the crack patterns, *i.e.* damage stated in Figure 9.5. Note that the references noted in this paragraph show micromodels fully calibrated, *i.e.* accounted for all test simulations, not only the IP ones. However, the changes from the OoP tests had only a minor effect on the IP simulations, as described in Section 9.2 and 6.

From Figure 9.4 it is visible that the calibrated models were in good relation with experimental ones in terms of initial stiffness, yielding point, load-bearing capacity and ductility. The IP shear forces were compared with the experimental ones on every drift ratio of $d_r = \pm 0.25\%$ using the *mean average percentage error (MAPE)* (Eq. 9.2). The forces were linearly interpolated for the given drift ratios. The table is divided into 3 rows, referring to the cyclic envelope, the *negative* (-), *positive* (+) part, and the *average* of two (Avg.). This separation was needed as the experimental positive, and negative envelopes do not align (Fig. 5.5).

The computational against experimental crack patterns, *i.e.* *damage states* showed good correlation between the calibrated computational and experimental models (Fig. 9.5). In detail, it is visible that they developed very similar patterns and failure mods, *i.e.* patterns that illustrate *compression struts* and *sequenced failures, bedjoint sliding*. Specifically, the computational models followed typical failure modes in line with the experimental ones: 1) BF model developed plastic hinges and ended with flexural failure (Fig. 9.5a); 2) FI model had a bedjoint sliding failure 9.5b; 3) CD had a diagonal tensional failure of masonry piers developed on the sides of the opening 9.5c; 4) CW had a diagonal tensional failure of masonry piers developed on the sides of the opening 9.5d; 5) ED had a diagonal tensional failure of masonry pier that developed on the side of the opening 9.5e; 6) EW bedjoint sliding failure of the masonry pier that developed on the side of the opening 9.5f.

$$MAPE = \frac{1}{n} \sum_{i=1}^n \frac{V_{i,\text{exp}} - V_{i,\text{comp}}}{V_{i,\text{exp}}} \quad (9.2)$$

When plotted positive *vs.* negative parts of the cyclic envelope (Fig. 9.6), it is observable that the micromodel captured the influence of *load position*. Namely, this is best observed when the load is closer to the opening in the case of ED and EW models. In those models, the a more significant difference starts at around 0.10 % up to 0.60 % in ED and 0.40 % d_r in EW model, at which the influence of infill wall and therefore the load position diminishes. In the case of others, the difference was negligible, yet a small amount can be attributed to loss of stiffness due to previous contra-load and *Bauschinger's effect*.

Table 9.2: IP mean average percentage error of calibrated micromodel vs. experimental

MAPE (Eq. 9.2) IP calibrated micromodel vs. experimental values compared for every $\pm 0.25\%$

Part	d_r , values in %					
	BF	FI	CD	CW	ED	EW
+	-0.37	-5.86	-14.88	-12.6	-5.93	7.93
-	-21.77	9.03	-15.39	-10.3	-4.1	-2.66
Avg.	11.07	7.45	11.23	11.62	5.01	5.3

The minimal principle stresses were extracted for 0.05, 0.20, 0.25 d_r (%) with the exception of FI model with the highest d_r of 1.10% and are presented in Figure 9.7. Note that for models with eccentric openings, the images were divided based on positive (+) and negative (-) parts; based on the direction of load.

In all models, it was observed that the principal stress increases in value and area at the infill wall's corners. That results in their crushing. Similarly, stress concentration was observed at the corners of openings.

The FI model (Fig. 9.7a) shows initial development of diagonal compression strut. Afterwards, the stress concentrates at bedjoints, at about $1/3$ height.

The CD model (Fig. 9.7b) presented the forming of two infill wall columns that each developed congressional struts. Higher stresses were observed in line with lintel at a higher drift ratio, causing the infill wall to uncouple into 2 columns and beam above the lintel. Similar progression was observed with CW model (Fig. 9.7c)

The ED (Fig. 9.7d,e) model showed similar diagonal strut behaviour as the CD model at the initial steps of loading. However, stress concentrated highly in line with the lintel at higher drift ratios.

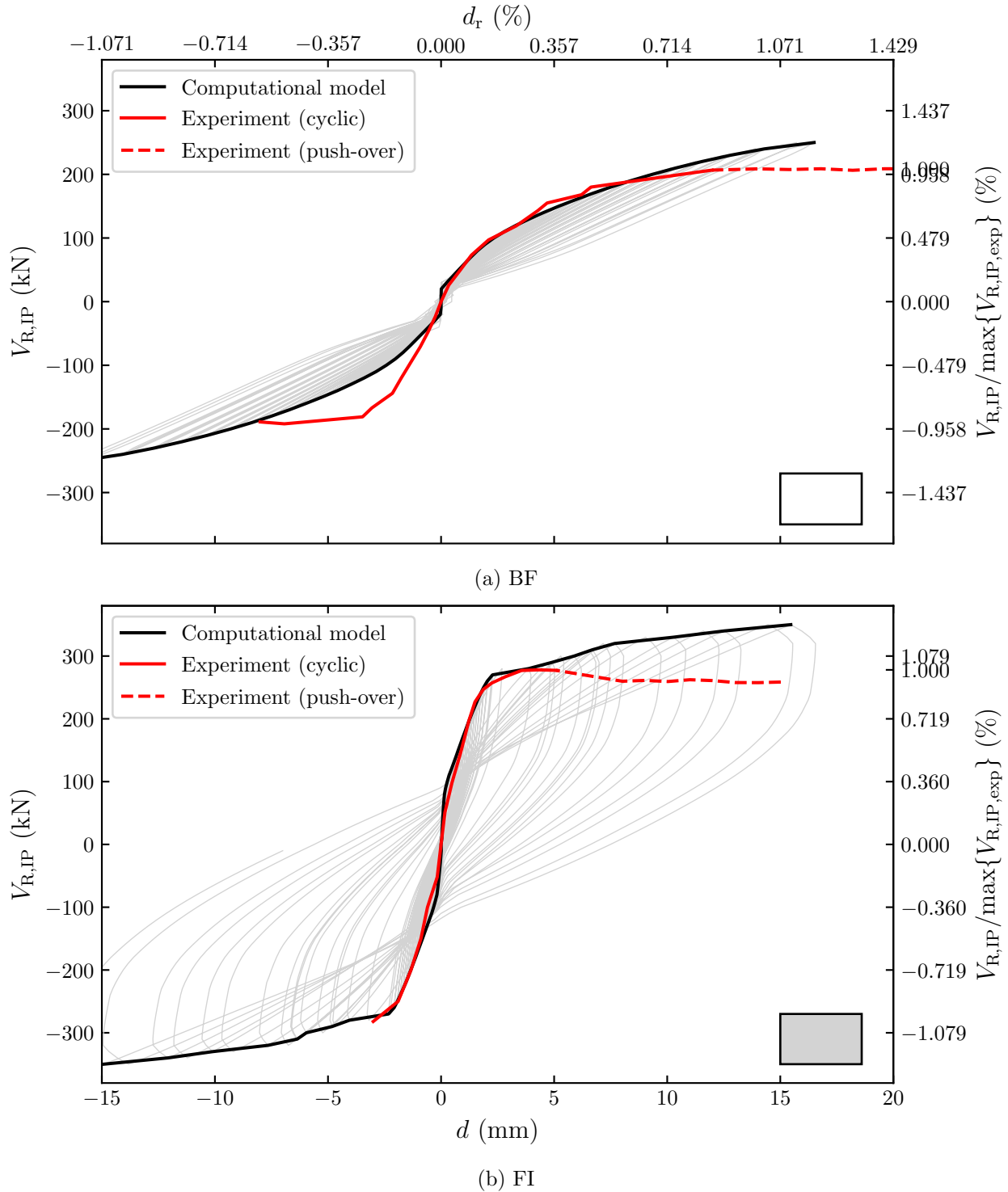
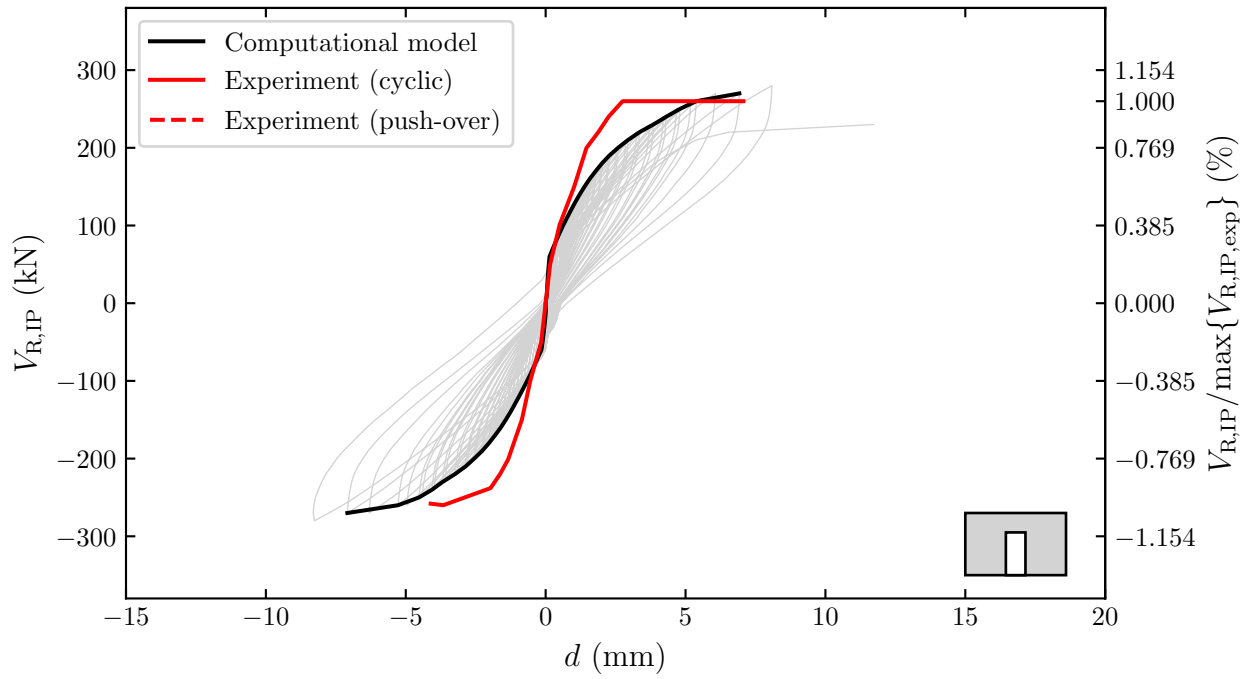


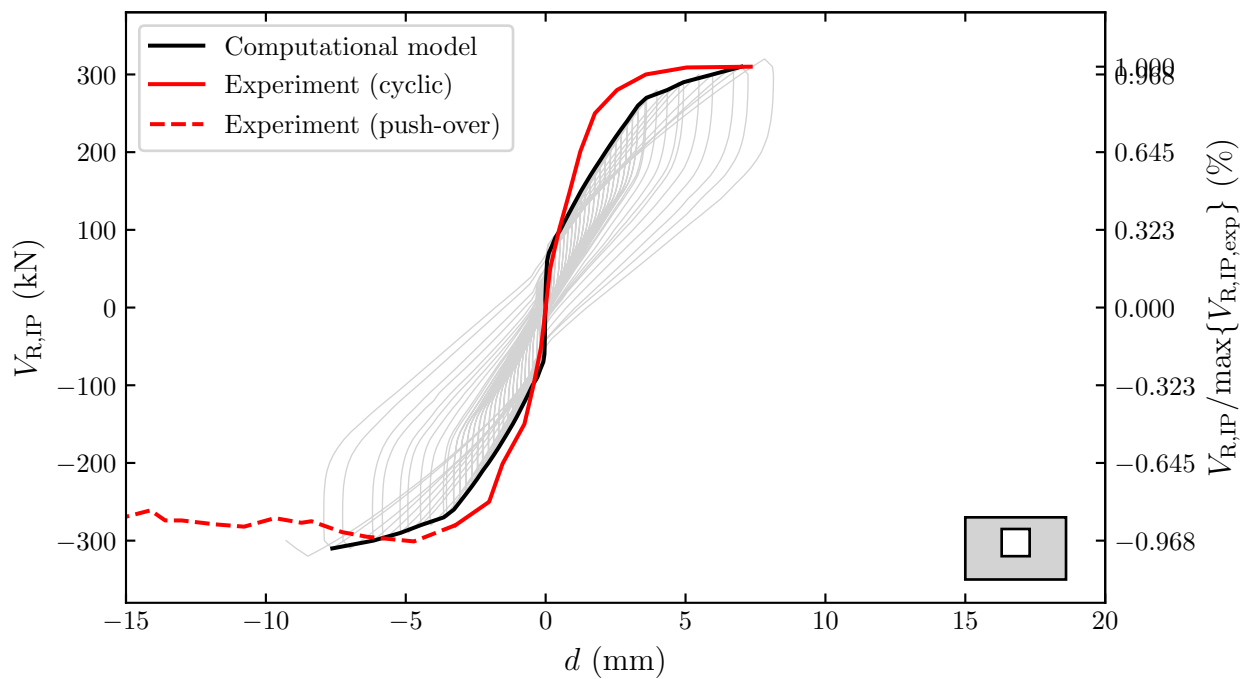
Figure 9.4: Calibrated IP cyclic-quasi static micro-model results

On the other hand, the EW model had at higher drift ratios stress concentration in line atop and bottom of the opening; effectively, separating the infill wall into 2 beams and 2 columns.

All the points above were also observed in the IP experimental campaign, see Table 5.1.

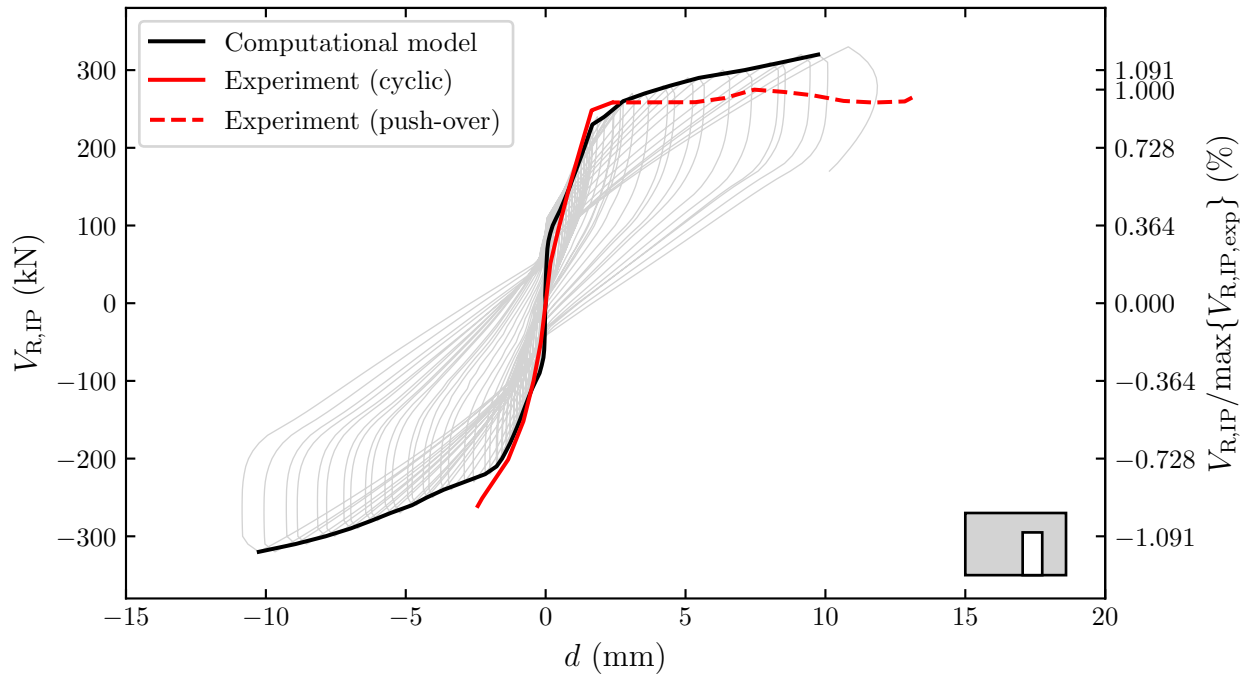


(c) CD

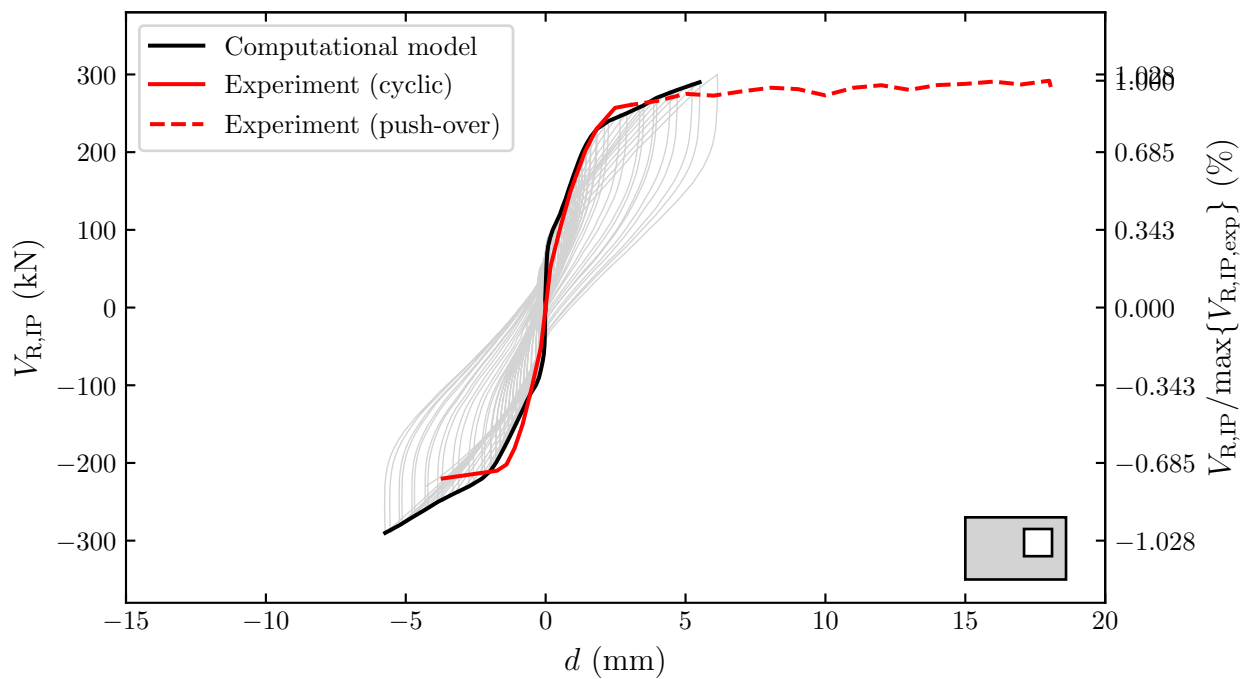


(d) CW

Figure 9.4 (cont.): Calibrated IP cyclic-quasi static micro-model results



(e) ED



(f) EW

Figure 9.4 (cont.): Calibrated IP cyclic-quasi static micro-model results

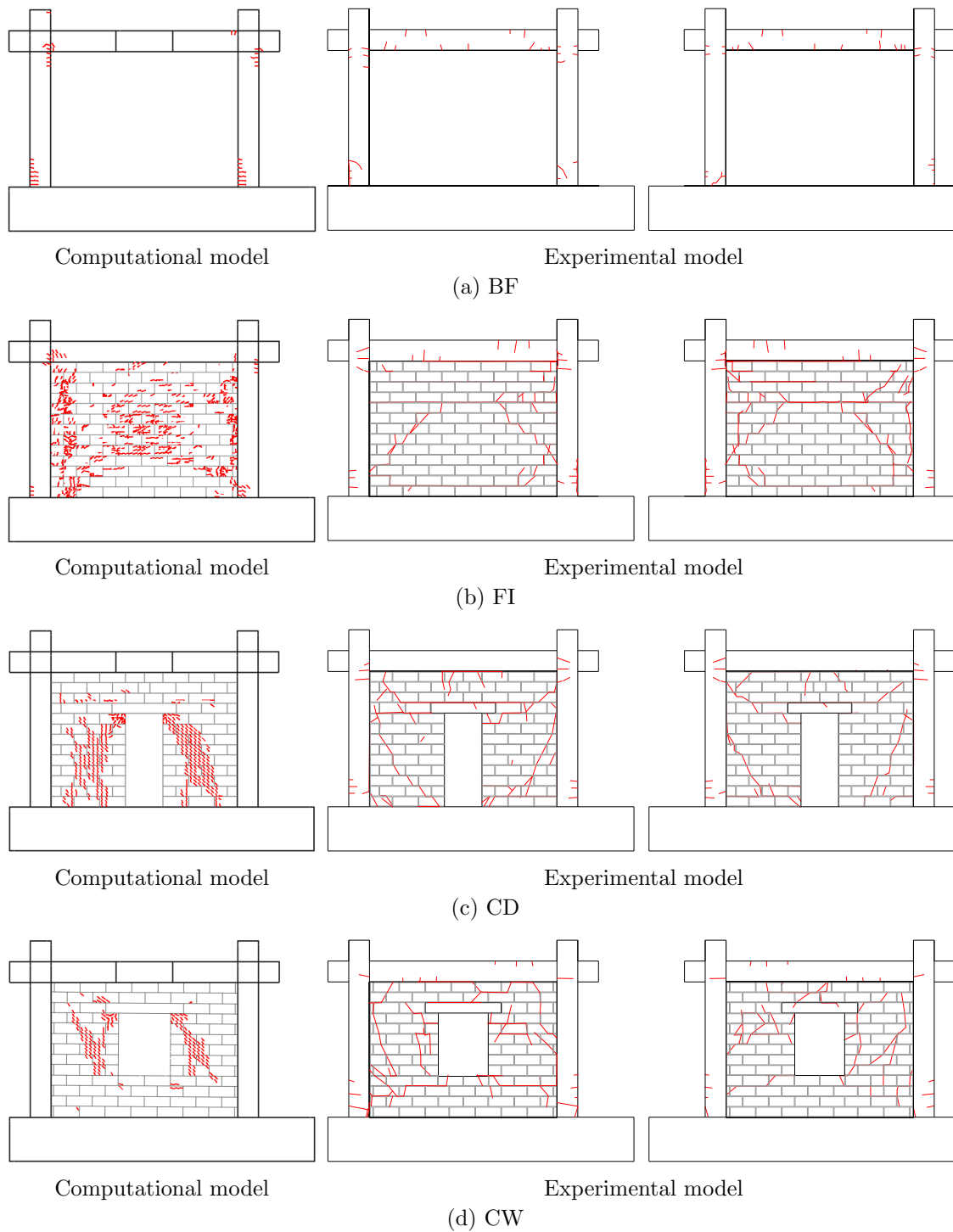
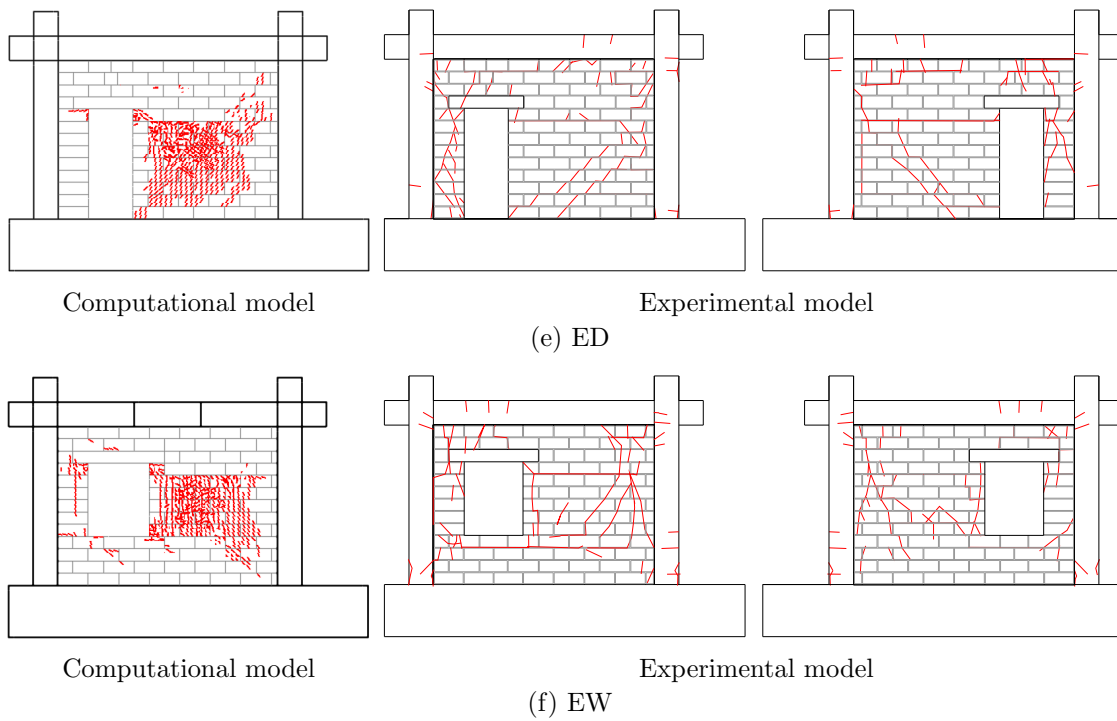


Figure 9.5: Damage state of computational vs. experimental IP model



Min. crack width	0.1	mm	Crack width multiplier	1.0	Deformation multiplier	0.0
------------------	-----	----	------------------------	-----	------------------------	-----

Figure 9.5 (cont.): Damage state of computational vs. experimental IP model

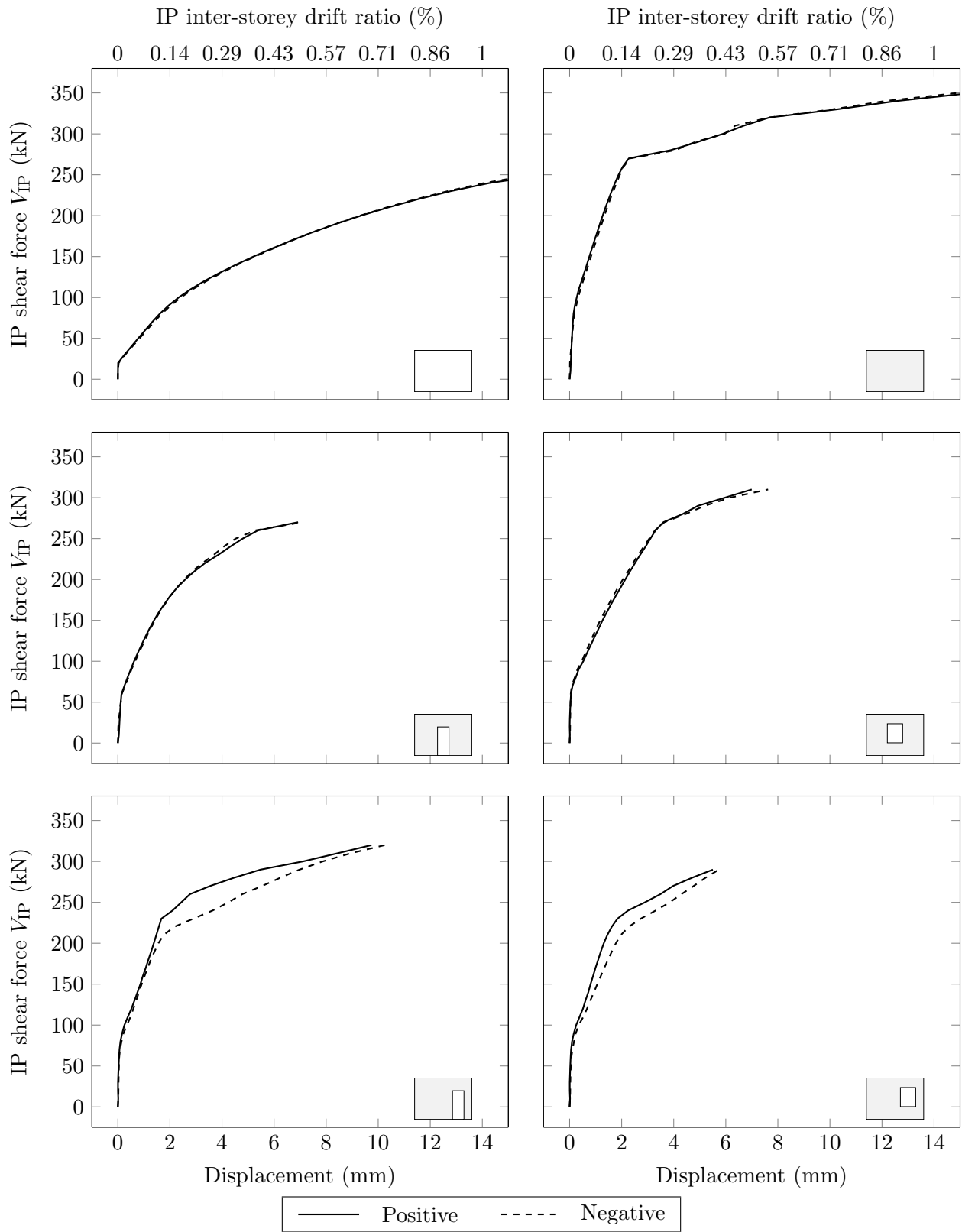


Figure 9.6: IP computational positive *vs.* negative cyclic envelopes

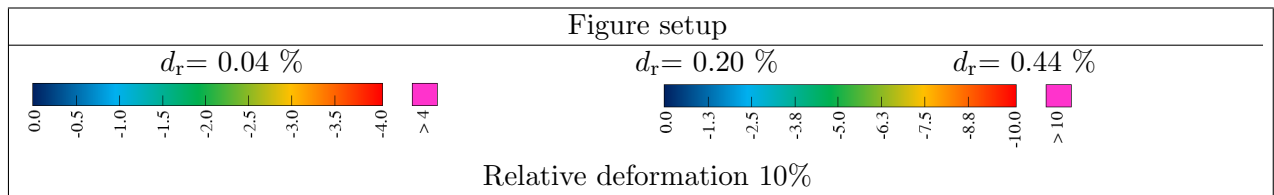
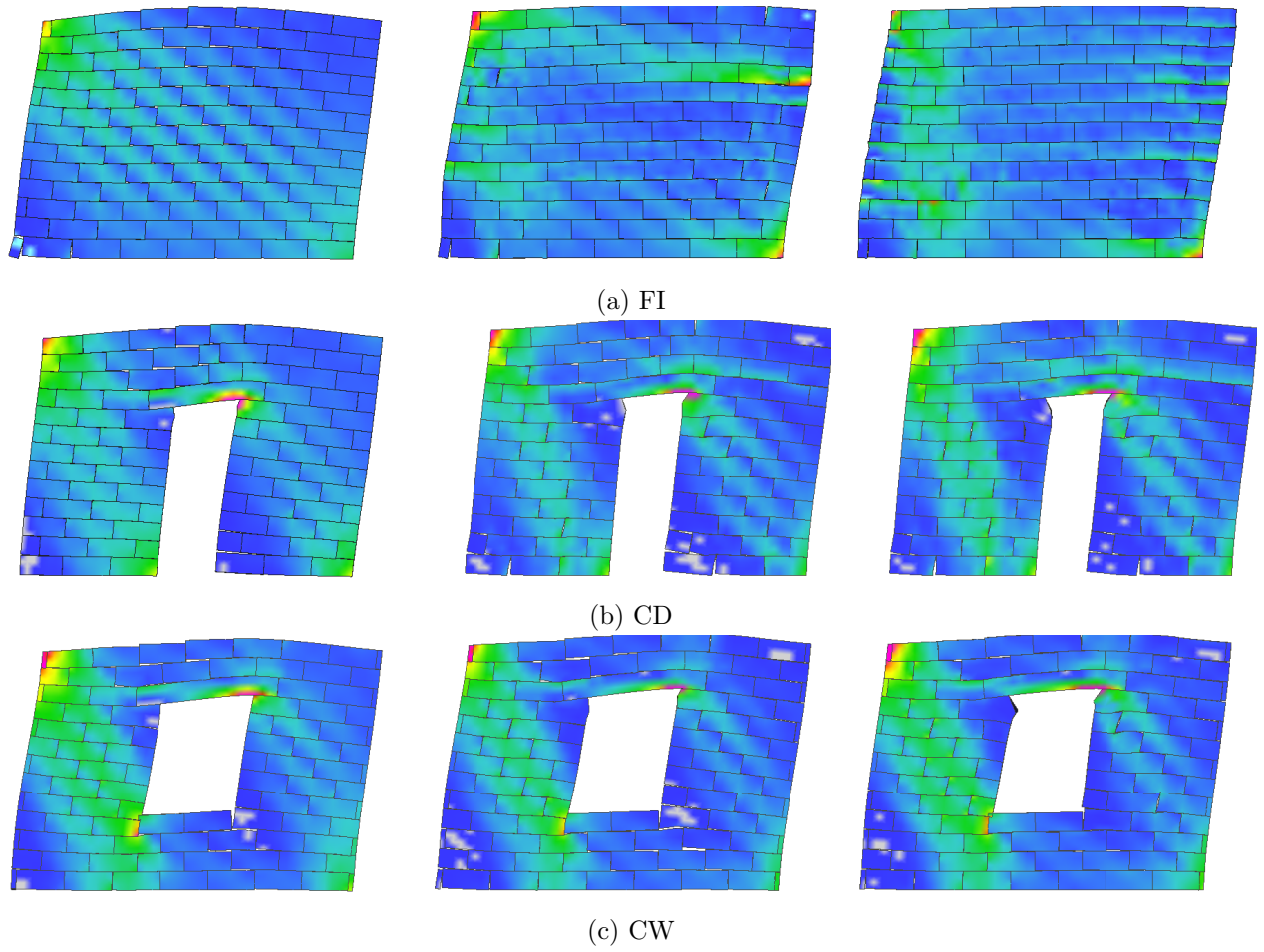


Figure 9.7: IP infill wall principal stress σ_{\min} (MPa)

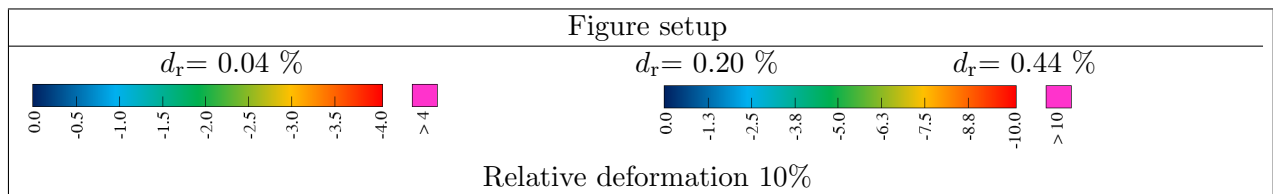
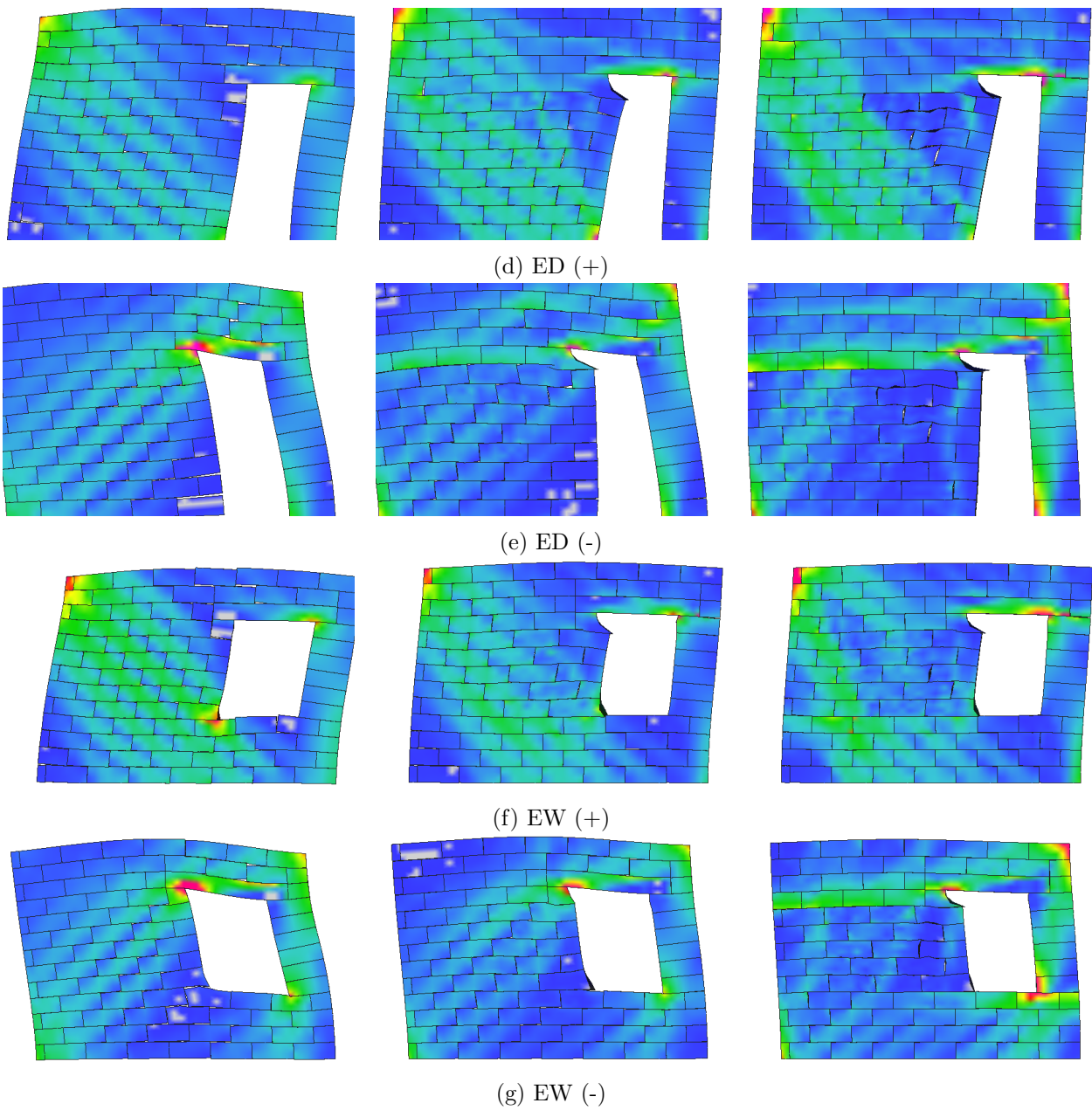


Figure 9.7 (cont.): IP infill wall principal stress σ_{\min} (MPa)

9.2 Out-of-Plane bending tests of masonry walls

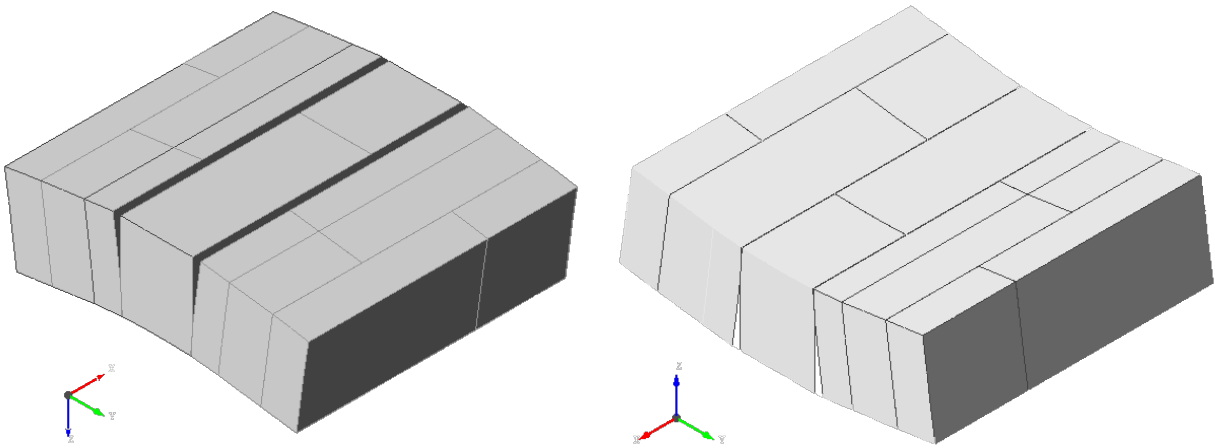
The developed masonry wall models that simulated bending introduced via line load parallel (\parallel) and perpendicular (\perp) to the bedjoints were initially computed with the IP calibrated material models properties. As expected, the load-bearing capacity was much greater than their physical counterparts. Instinctively, it was because the failure was governed by the OoP, *i.e.* tensile strength perpendicular to the voids, while in the model, the one that is *parallel* was used. Hence, it was changed from direction parallel to perpendicular to voids f_t 1.80 \rightarrow 0.38 MPa. Since the fracture energy G_f is also dependent on the tensile strength (Eq. 8.1), it was recalculated to the new value. However, those changes resulted in a modest computational instability that was aided by extending the reach of tensile softening from 0.010 mm to 0.001 mm, and by reverting the fracture energy to the previous value (when f_t was \parallel with the voids).

With all the aforementioned adjustments, the walls were calibrated and in good relation with the experiments. The failure modes were in line with experimental ones (Fig. 9.8 & 9.9 vs. 4.12), *i.e.* when the load is parallel to bedjoints was a de-bonding in the bedjoints (Fig. 9.8a vs. 4.12a) due to breaching mortar–masonry bond strength (Fig. 9.9a). Likewise, when the load was perpendicular to the bedjoints, there was separation in headjoints and cracking (Fig. 4.12b vs. 9.8b) due reaching OoP tensile strength of the blocks (Fig. 9.9b). The exact values are presented in Table 9.3. Note that stress in the case of load parallel to the bedjoints could not be read as the interface elements had zero thickness. The values have satisfactory correlations.

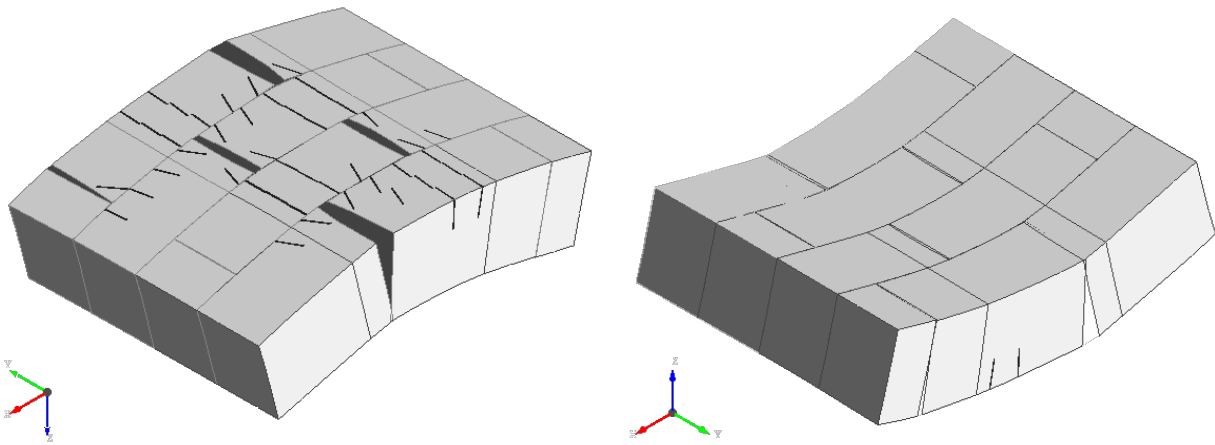
Table 9.3: Values and differences between computational and experimental outcomes of the wall OoP bending test

Load to bedjoint	Experiments		Computational model		Difference	
	Force (kN)	Stress (MPa)	Force (kN)	Stress (MPa)	Force (%)	Stress (%)
\parallel	4.07	0.21	4.50	/	9.55	/
\perp	6.69	0.38	6.20	0.37	7.32	2.63

Due to changes in the material models values, there was a concern that it could affect the previous IP numerical calibrated models. This was analysed on the FI model and it was found that the effects were minimal on its behaviour (Fig. 9.10), damage grades and stress distributions (Fig. 9.11). The same was done for the rest of the specimens. Hence, it can be deduced that the interface elements and their material models and properties mostly govern the IP behaviour.



(a) Load parallel with bedjoints



(b) Load perpendicular to bedjoints

Figure setup			
Deformation	×300	Min. crack width	0.001 mm
Crack width multiplier	×1	Shift cracks outwards	×0

Figure 9.8: Computational model of OoP bending test deformation and crack patterns

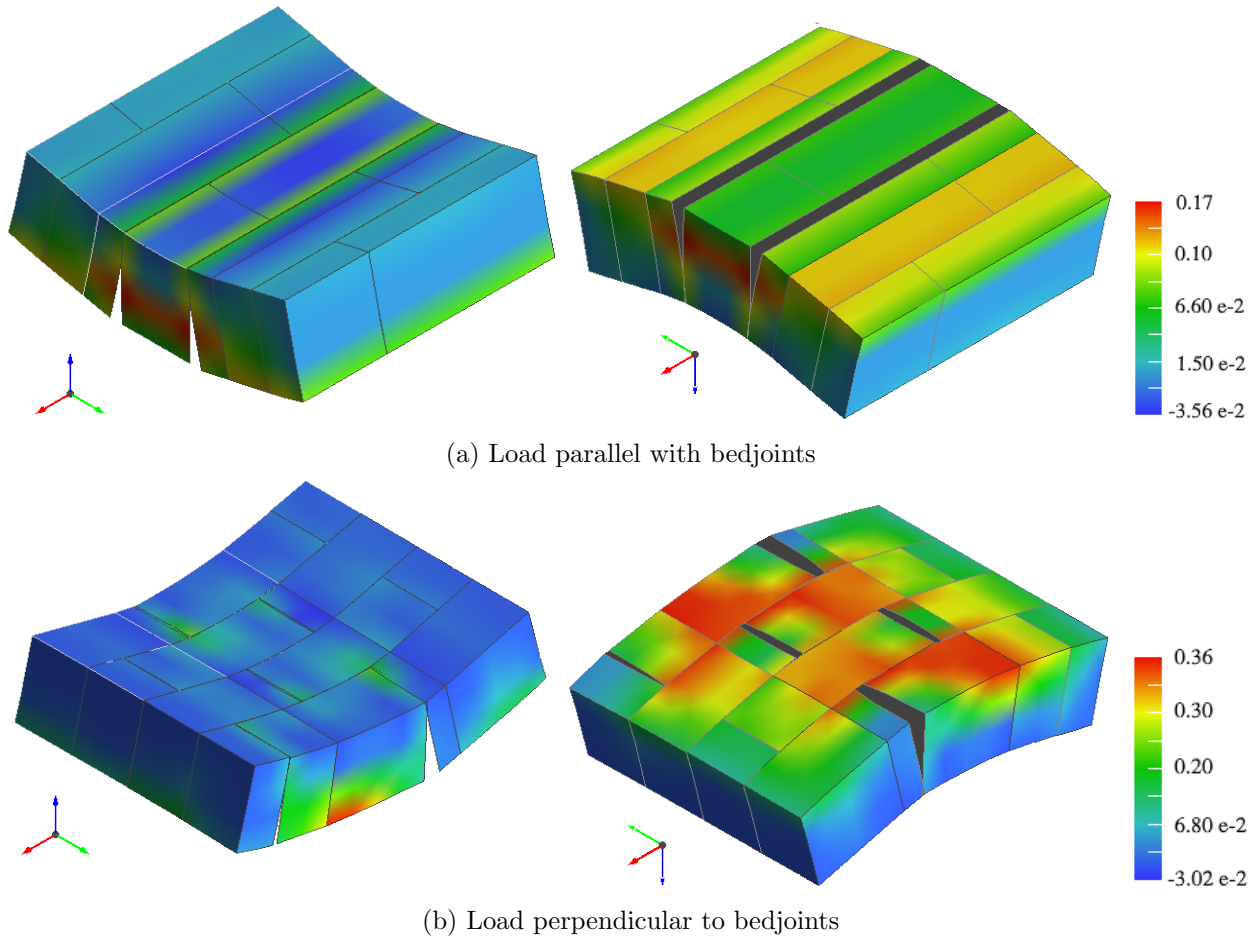


Figure 9.9: Computational model of OoP bending tests maximal principal stress (Figure setup: deformations $\times 300$, colorbar in MPa)

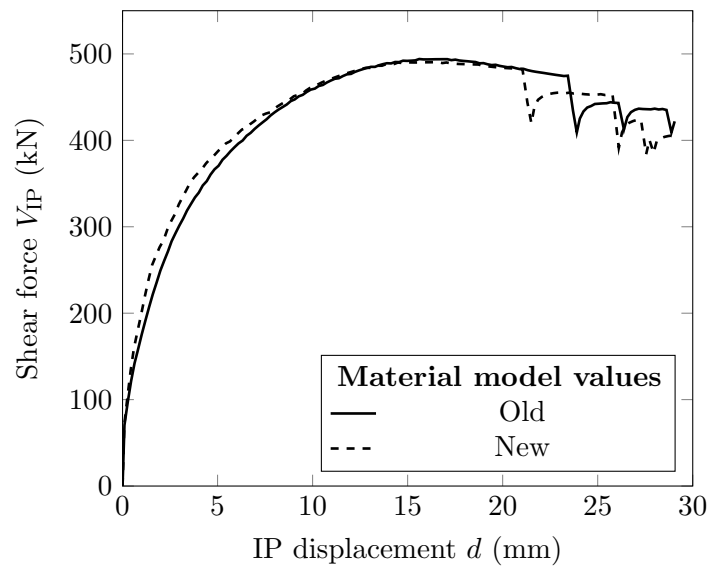
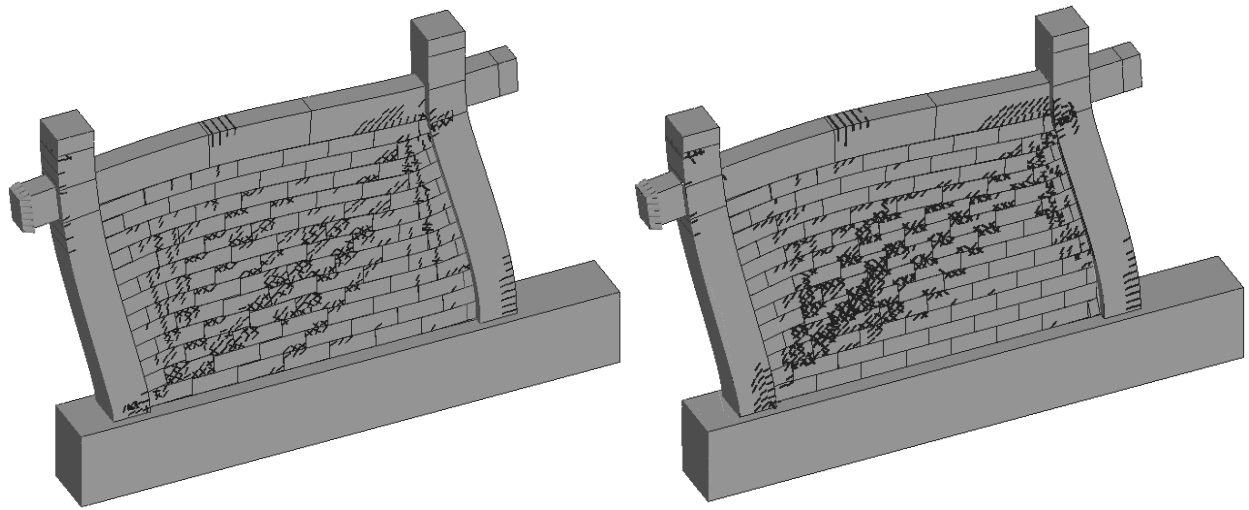
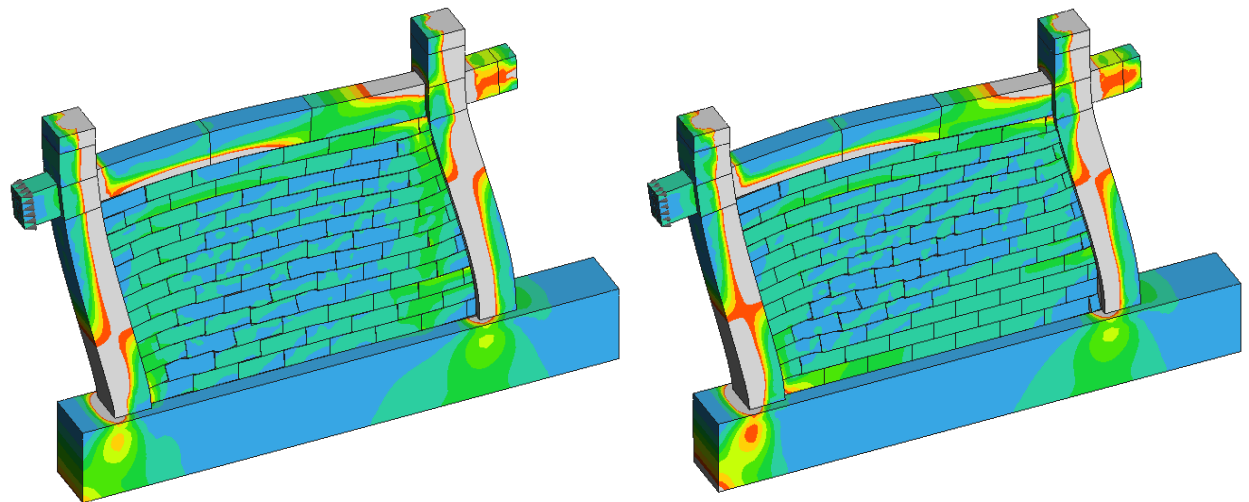


Figure 9.10: Behaviour of FI push-over model with newly obtained values



(a) Crack patterns



(b) Minimal principal stress

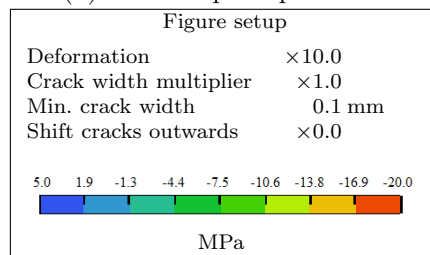


Figure 9.11: Comparison of modified material model properties (*old* left, *new* right) values on FI, IP push-over model

9.3 Out-of-plane drift driven test on frames with and without masonry infill walls and openings

This section describes the validity of OoP drift driven computational test simulation, based on the experimental studies as described in Section 6. Both the experiment and the micromodel showed great computational stability, enduring to drift ratios $d_r \geq 10\%$. However, such high drift ratios are unrealistic and not part of a standard engineering practice.

Since the RC frames were previously used and damaged, the calibration of the same computational models cannot rely on its absolute values as was in previous (IP, OoP bend) calibrations. Thus, an approach of evaluating the micromodel based on relative aspects was adopted. As expected, the computational models had a greater response than averages to a difference of approx. 40 % (Fig. 9.13b).

The computational models showed a key aspect of the real, physical specimens. Mainly, both did not have greater interaction with the masonry infill wall. Both did not record any significant energy damping, resulting in more or less linear hysteresis loops (Fig. 6.8 & 9.13). The deformation maps from ARAMIS and computational models showed that infill walls and frames moved synchronously (Fig. 6.16 vs. 9.15). The synchronous behaviour was also observed in dynamical OoP tests (Tu et al, 2010; Fowler, 1994) and those of drift driven tests by Henderson et al (1993); Flanagan and Bennett (1999b).

Likewise, the damage states, and crack propagations were matched (Fig. 9.14). The tension side shows debonding and opening of the bedjoints, while the frame follows with horizontal crack lines. Furthermore, on the compression side, there are visible signs of *crushing* damage. The high damage state of the infill wall outlines the same conclusion of *unidirectional* frame–infill wall interaction. That is, the frame transmits forces, displacements onto the infill wall, causing damage. Contrariwise, the infill wall has little effect on the frame’s behaviour. Similar findings were found in dynamical (Tu et al, 2010; Fowler, 1994) and other drift driven Henderson et al (1993); Flanagan and Bennett (1999b) tests, where the frame failed, leaving the infill wall only slightly damaged.

The physical specimens (Fig. 6.10), due to previous damages, demonstrated a bit unrealistic results. To be clear, the FI specimen had the lowest performance, while BF the greatest. The opposite is accurate and, thus, more realistic performance in the case of computational simulations (Fig. 9.16). Where in between the two are the models with openings. If looked close enough, the micromodels with door (CD, ED) had lower performance than their window opening counterparts. However, the difference is so small that it is practically negligible. The same goes for the difference between the FI and models with openings. The difference between the FI and BF models is about 5 %.

Furthermore, the minimal and maximal principal stresses of infill walls were captured from the models and presented in Figure 9.12. All models showed that the lower two-thirds of the infill wall’s face had either compression or tension, while the upper half, especially near the beam, had none. Hence, no *arching-action* effects were captured. This is surely in question, as with the introduction of gravity load, the upper beam would press the infill wall, thus creating an area to form the arching-action mechanism, similar to that reported in Tu et al (2010) dynamical tests.

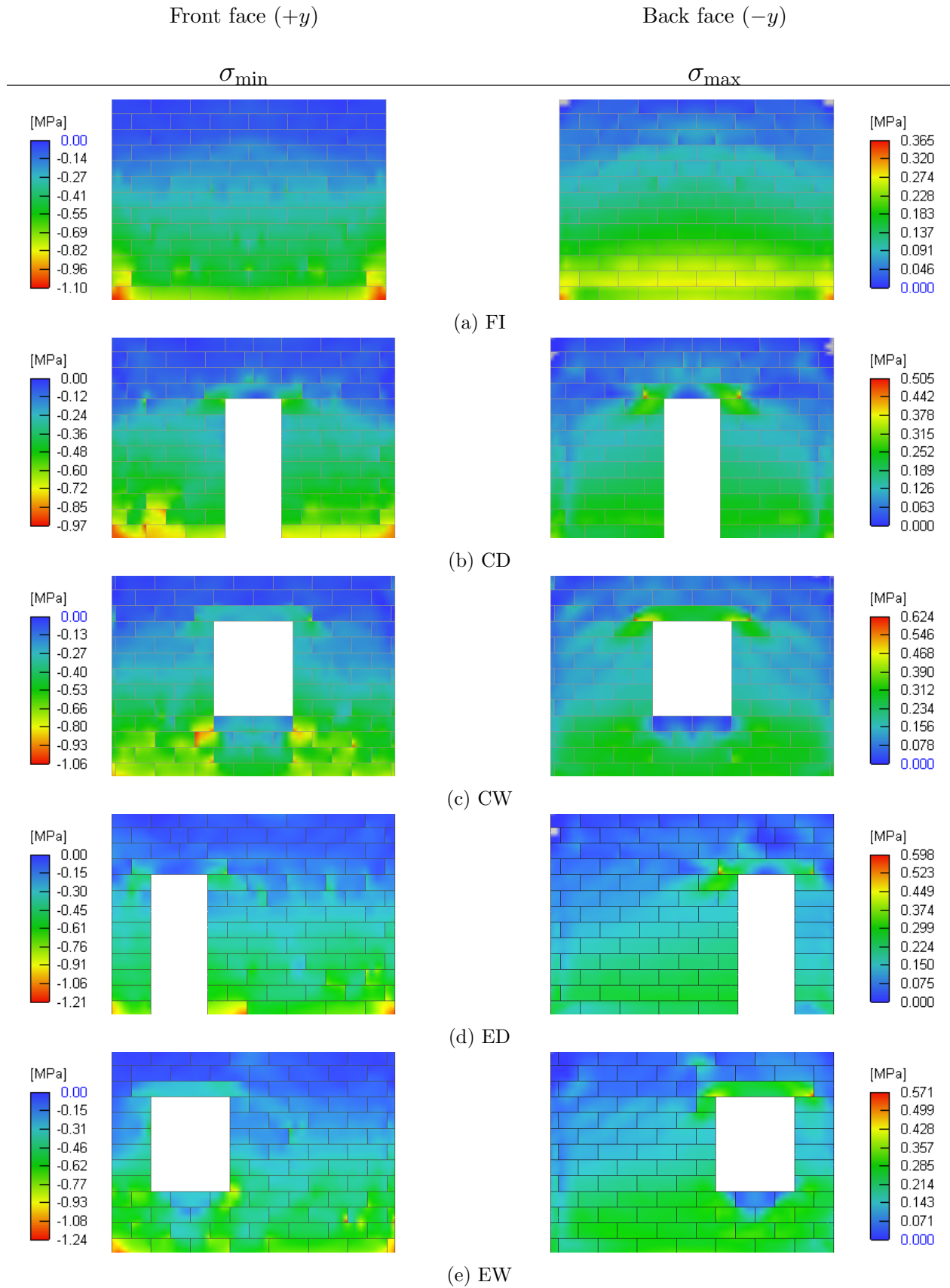
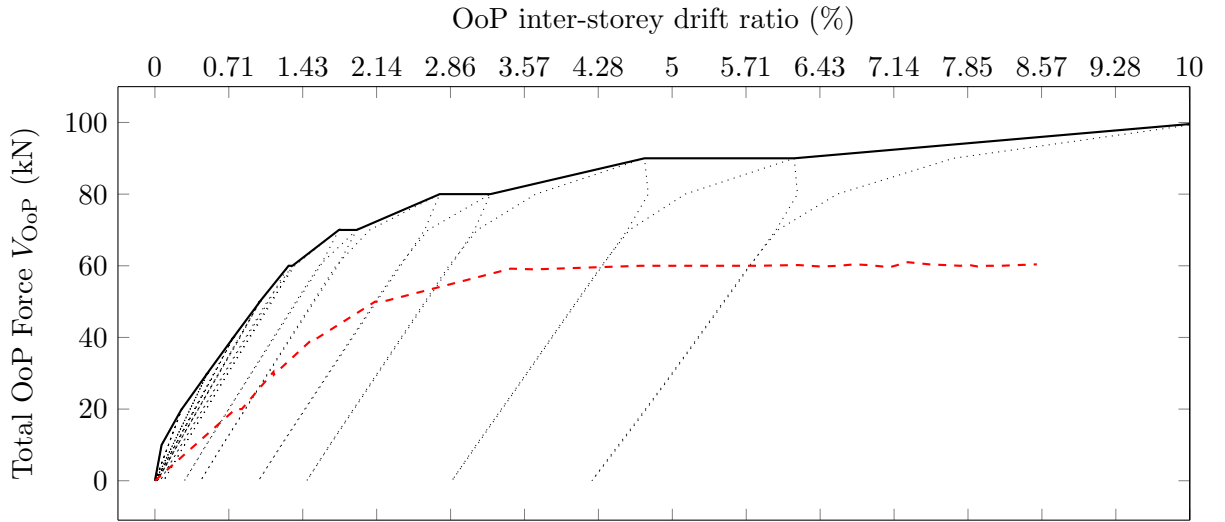
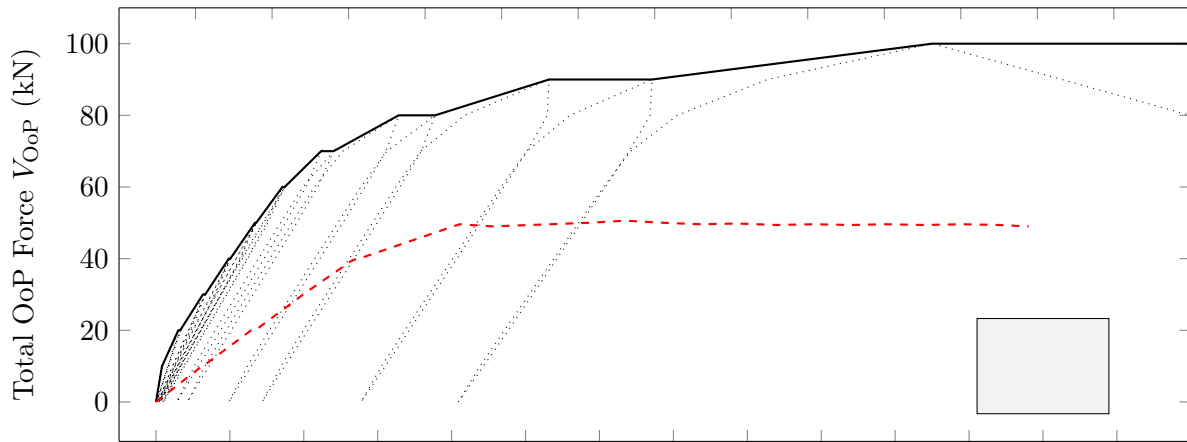


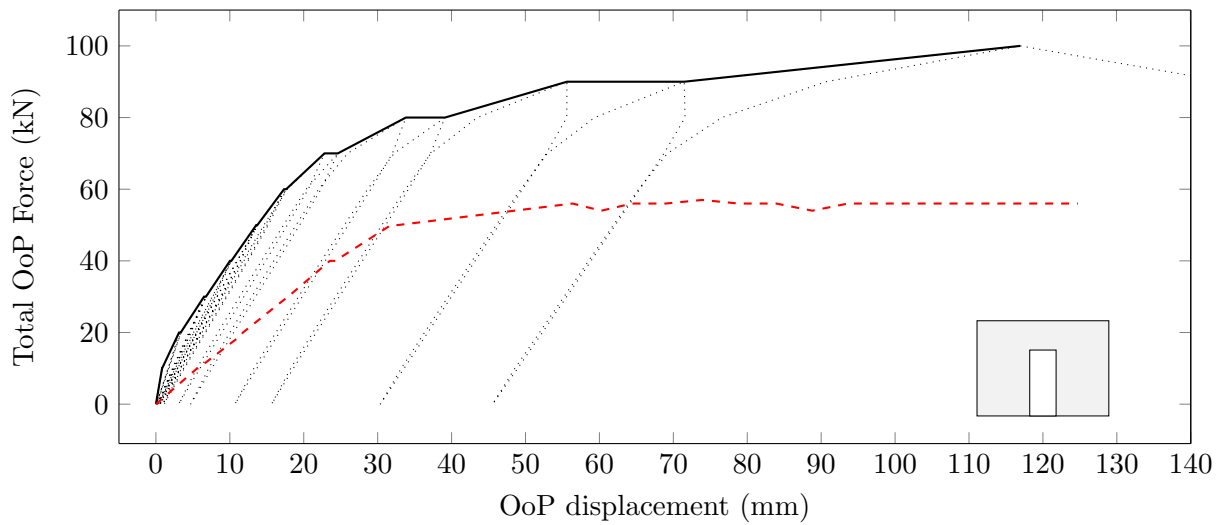
Figure 9.12: OoP principal stresses of masonry infill walls @ 1.25 % d_r of cyclic, quasi-static load protocol



(a) BF



(b) FI



(c) CD

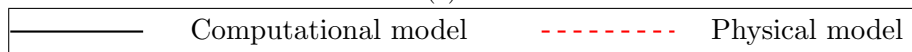
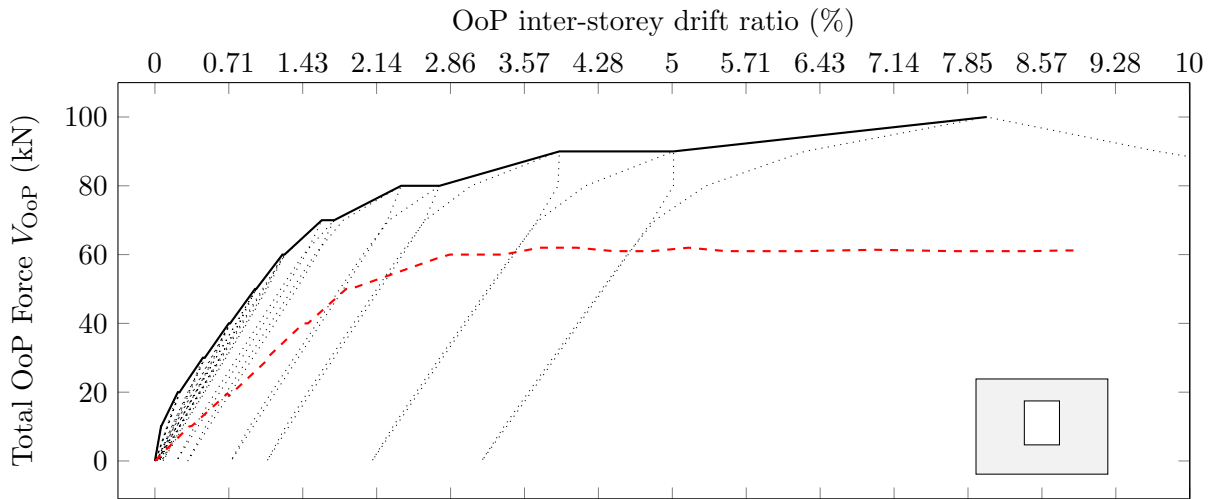
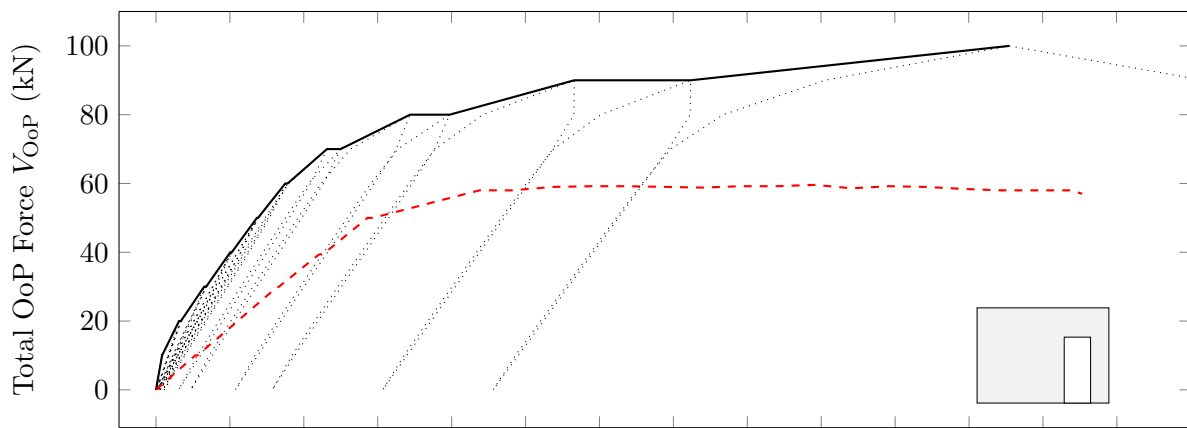


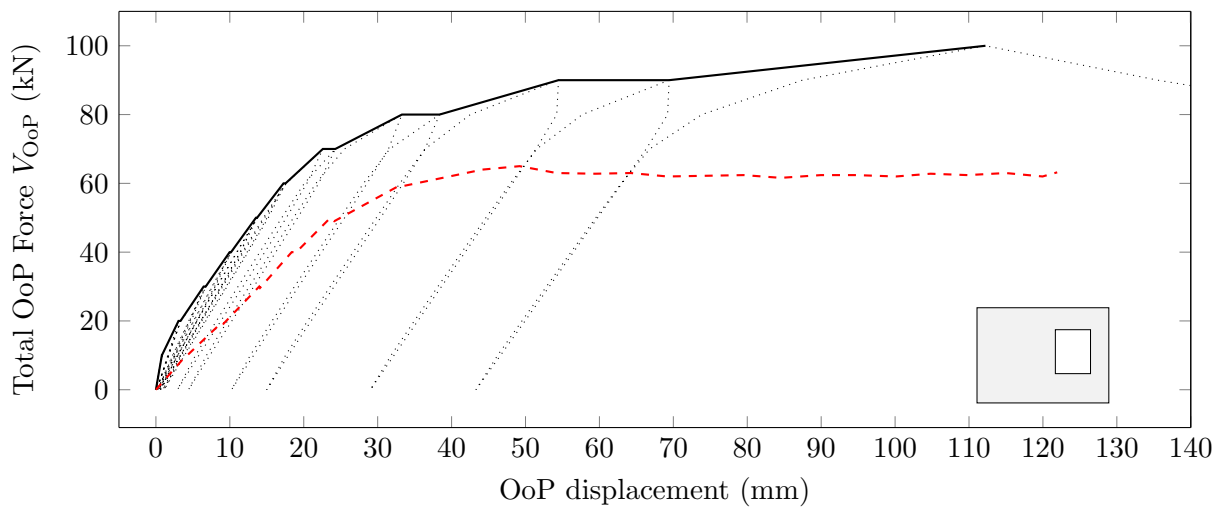
Figure 9.13: OoP drift driven test computational model simulation results



(d) CW



(e) ED



(f) EW

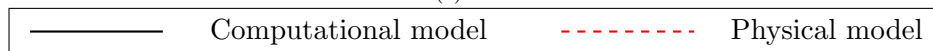


Figure 9.13 (cont.): OoP drift driven test computational model simulation results

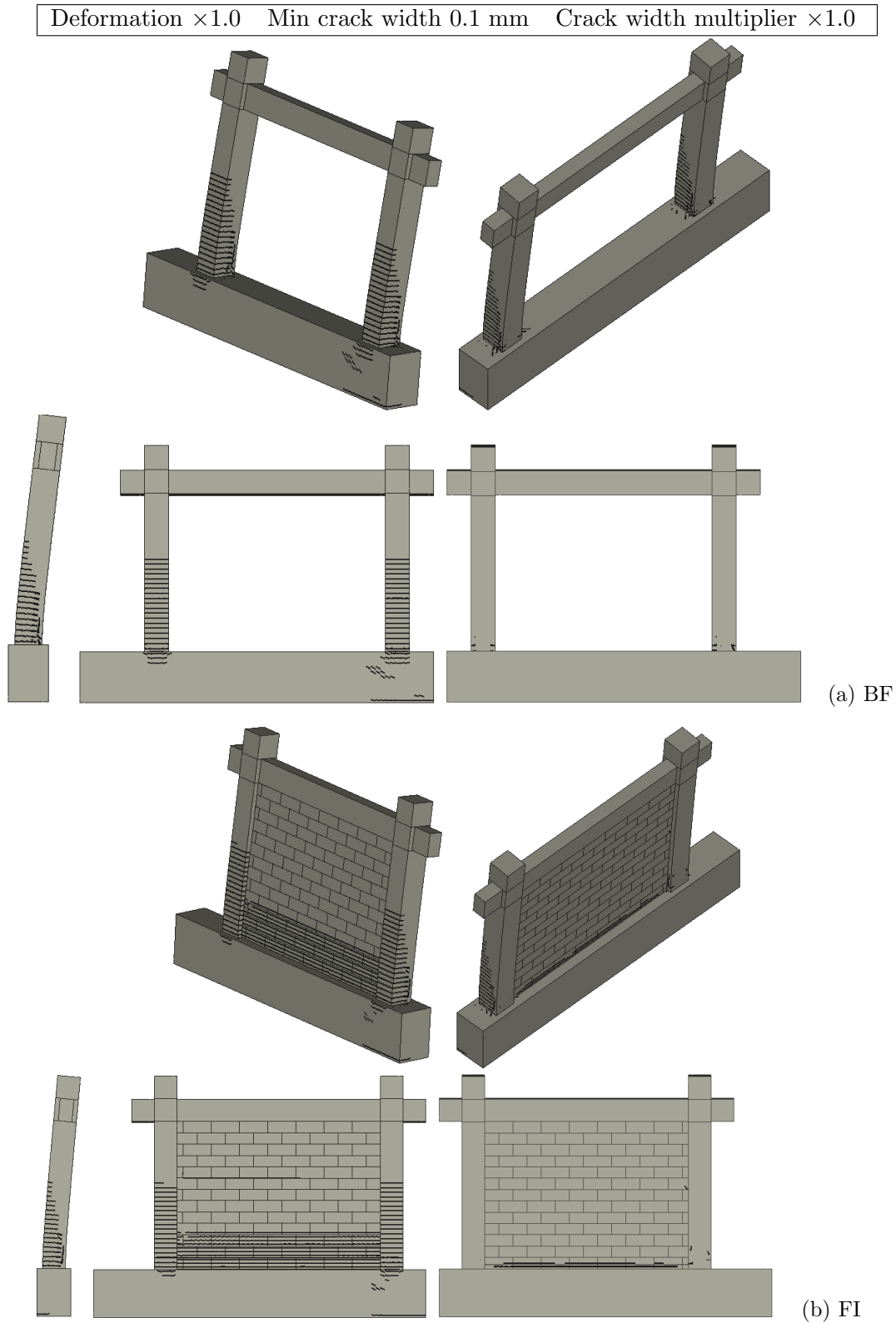


Figure 9.14: Computational frames micromodel OoP damage states
 OoP damage states of frames with infill walls computational models (@ approx. % d_T)

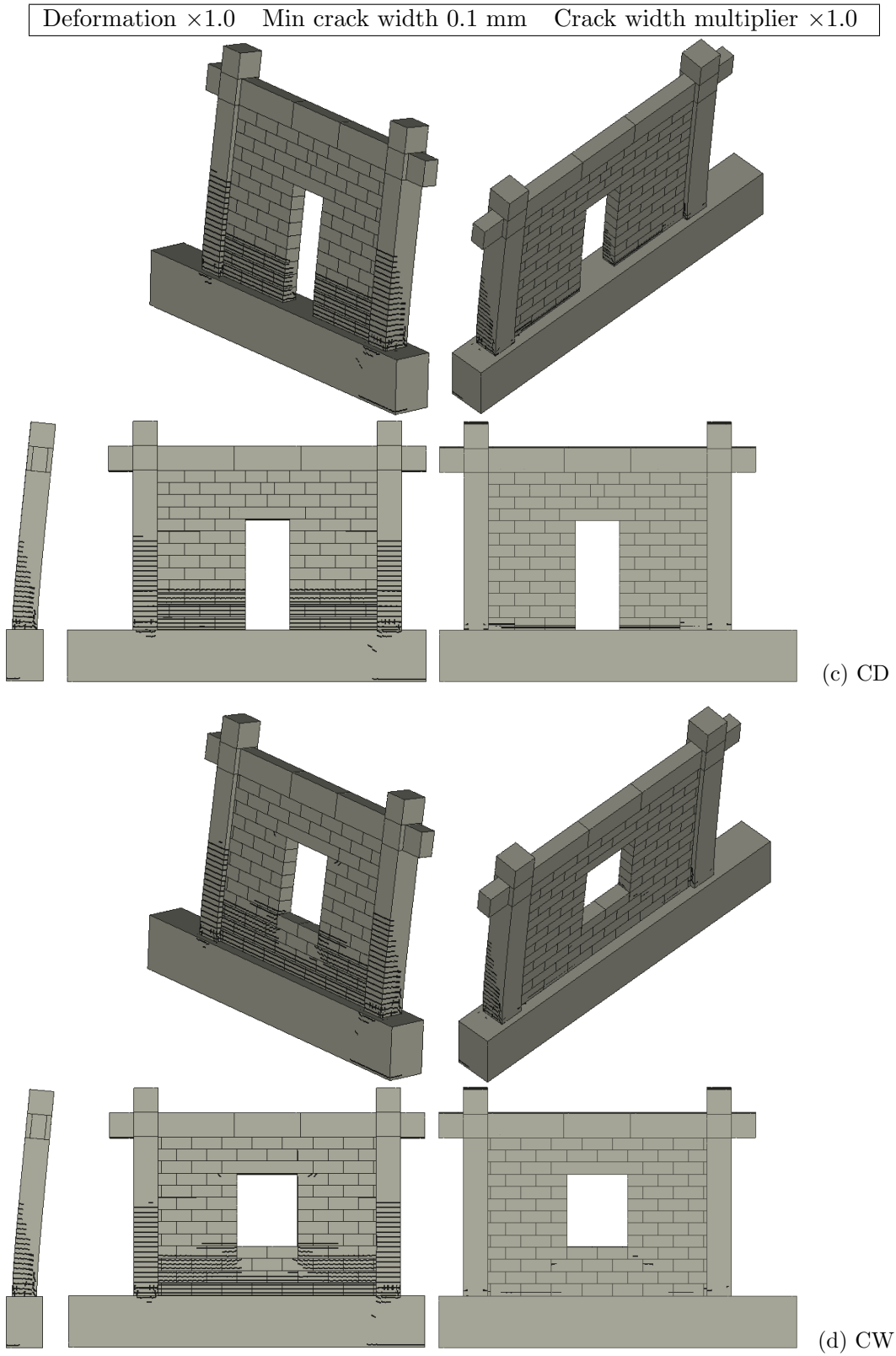


Figure 9.14 (cont.): OoP damage states of frames with infill walls computational models (@ approx. $\% d_r$)

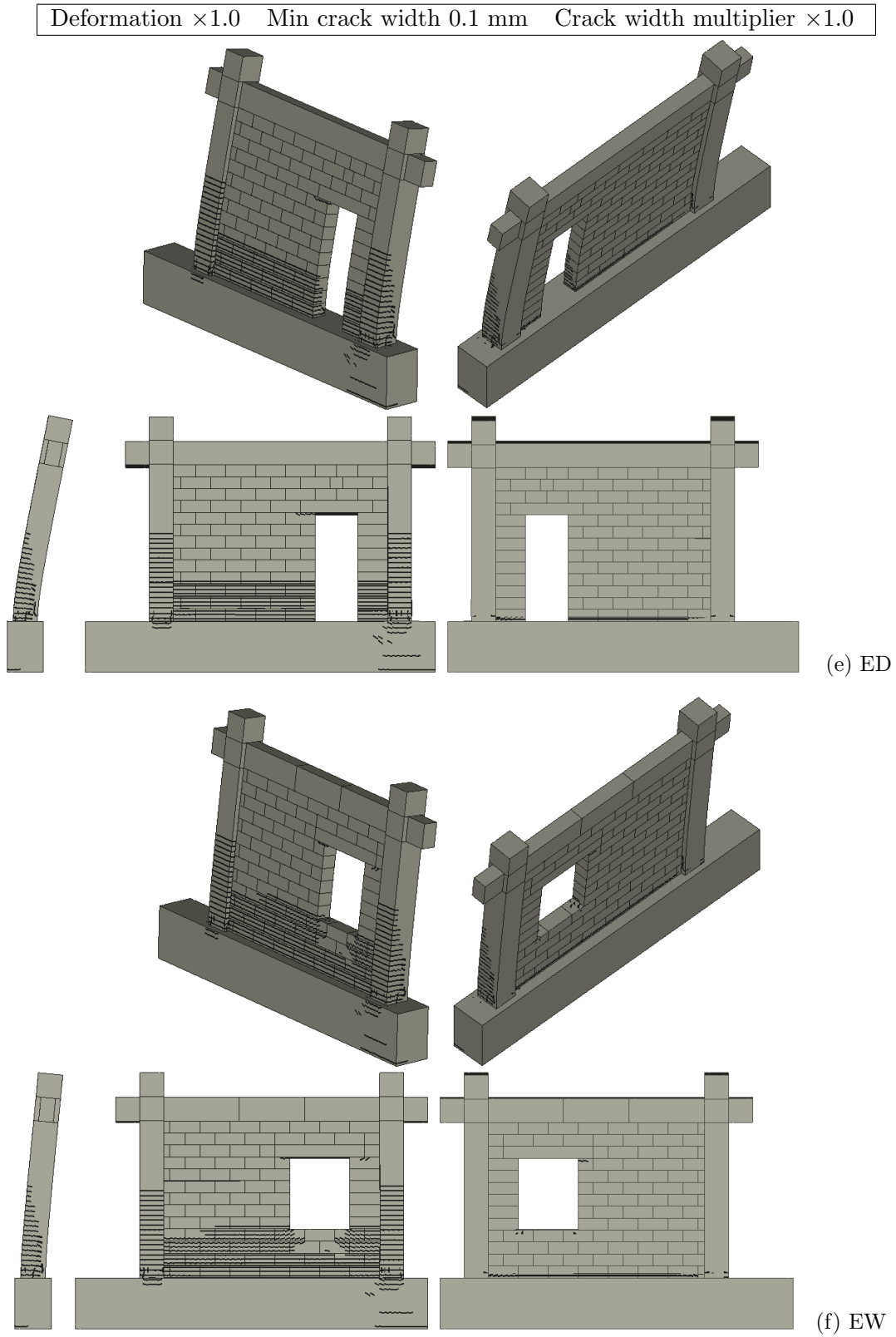


Figure 9.14 (cont.): OoP damage states of frames with infill walls computational models (@ approx. $\% d_r$)

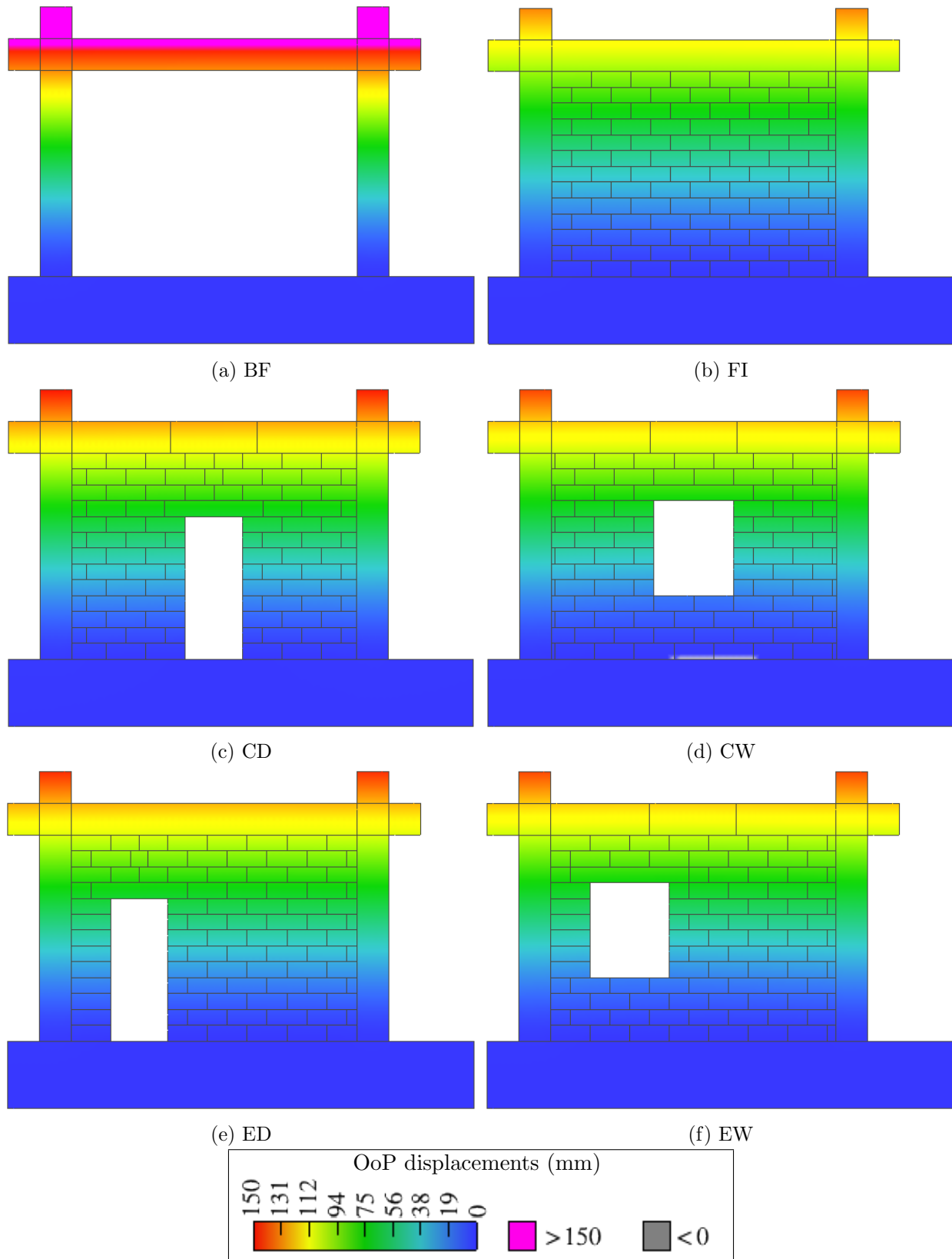


Figure 9.15: OoP displacement maps of frames with infill walls computational models

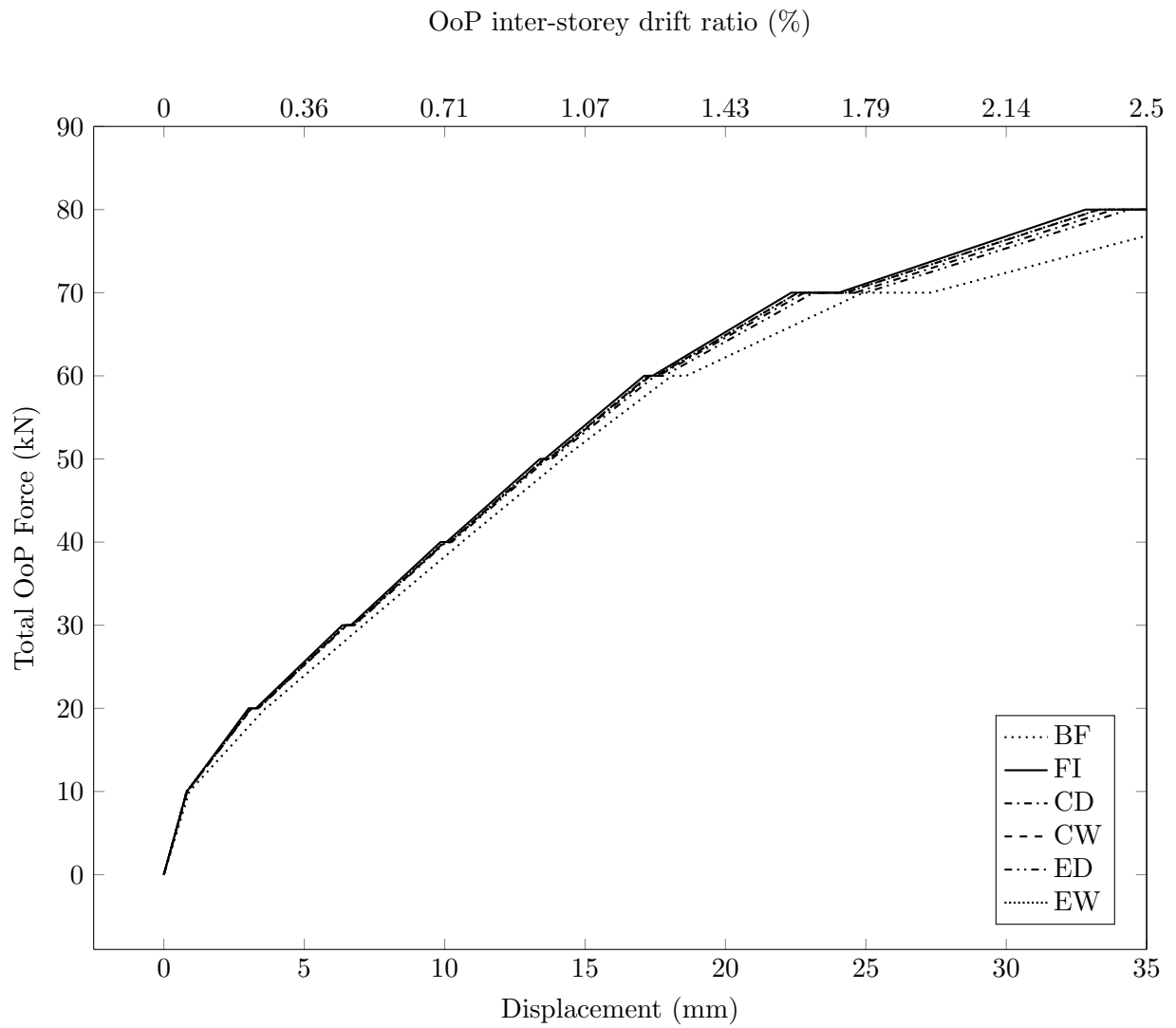


Figure 9.16: OoP drift-driven simulation (all models plotted)

Chapter 10

Simultaneous IP and OoP load on models with and without infill wall and various openings

10.1 Load protocol transition

By calibrating both frames and infill walls in IP and OoP direction, they were eligible for further, combined simulations. However, note that those simulations were not done with cyclic, quasi-static load protocols. A rather, monotonic; *i.e. pushover method* was used. The reason is the computational time, where it takes about 6 days of computing (without step result saving) for the FI model under IP cyclic, quasi-static load.

Furthermore, no IP experimental studies could be found where pushover and cyclic load protocols were compared. There is only a mention in Tomaževič (1999) that pushover had about 30% stronger response than the cyclic counterpart. This coheres to the fact that cyclic loadings produce a history of damages, especially true with multiple repeated loads. Furtado et al (2016a) tested masonry infill walls with OoP cyclic, quasi-static single directional and monotonic inertial load. However, one had axial load while the other did not. The cyclic one had about 18 % lower load-bearing capacity than its monotonic counterpart that additionally had the axial load.

The 30% reduction was found to be true in the case of the BF model herein, but not with FI or others. Therefore, to evaluate it further FI micro-model was loaded monotonically and with 1, 2, and 3 repeating cyclic. The results are presented in Figure 10.1. From the Figure, it is visible that by increasing the number of cycles, the greater the reduction of load-bearing capabilities; whereas, the 1 cycle matches the response of the pushover model. Note that the pushover positive curve was mirrored to get the negative one.

From the evidence gathered, the micro-models are considered capable of simulating pushover loading and its effects.

10.2 Opening size and load protocol selection

The options that were considered for the case of combined IP and OoP simulations for the further studies included:

1. First load in IP direction (with varying drifts), unload and load in OoP direction until failure;
2. First load in OoP direction (with varying drifts), unload and load in IP direction until failure;

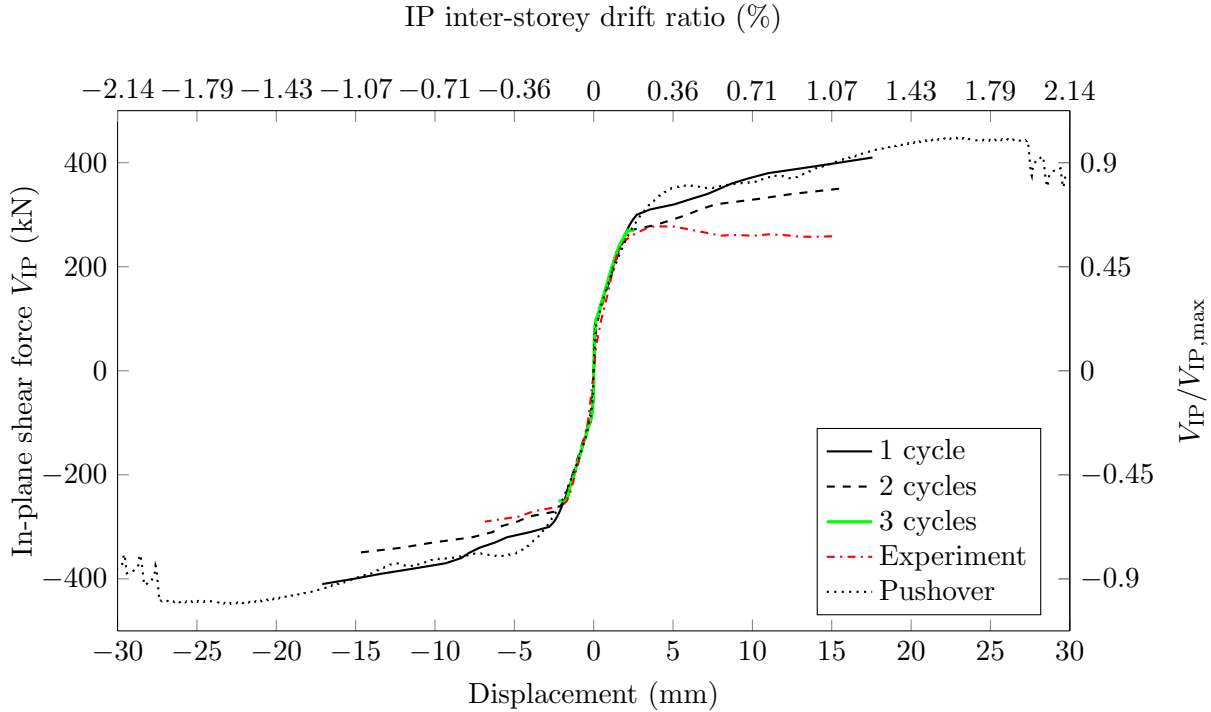


Figure 10.1: Effects of IP load protocols on FI model

3. First load in IP direction (with varying drifts), hold the previous load and load it additionally in the OoP direction until failure;
4. First load in OoP direction (with varying drifts), hold the previous load and load it additionally in the IP direction until failure;
5. Simultaneous IP and OoP loading with varying angle of IP+OoP resultant force.

The latter, *i.e.* the simultaneous IP and OoP loading was chosen based on the following points: a) nearly all combined studies were done with previous IP loading, followed by OoP inertial loading of the infill wall; b) only two authors tested previous OoP inertial force damage (Flanagan and Bennett, 1999a; Henderson et al, 1993); c) Only two authors tested simultaneous IP and inertial force OoP damage (Flanagan and Bennett, 1999a; Misir et al, 2016). Hence, with drift driven OoP tests, there were no combined studies, and the least investigated was the simultaneous action. Furthermore, the two studies mentioned above with simultaneous loads did not check for the differences within the angle that encloses the IP and OoP resultant force; instead, it was straight forward evenly loaded. Therefore, this thesis aims to cover the aforementioned unexplored parts of the research field.

The angles that were selected for further simulations are presented in Equation (10.1), where 0° is pure IP and 90° pure OoP load. The angles correspond to $+15^\circ$ up to 75° , which is refined to every $+5^\circ$, to cover an abrupt drop in load-bearing capacity.

$$\alpha = \arctan\left(\frac{d_{p,OoP}}{d_{p,IP}}\right), \alpha \in \{0, 15, 30, 45, 60, 75, 80, 85, 90\} \text{ (}^\circ\text{)} \quad (10.1)$$

Note that $\text{atan}(V_{R,OoP}/V_{R,IP}) \neq \alpha$ as the load was introduced by the prescribed deformation and then read through monitor point as a *reaction* to the deformation.

In addition to combined loadings, the effects of openings are yet to be resolved. There were no systematic studies of opening in the OoP field, while those studied had contrasting results, and all were done with an inertial load. Until the paper that is a part of this thesis researchers (Anić et al, 2021a) there were no studies with openings and OoP drift driven tests. Therefore, this thesis aimed to check the effects of varying opening size and position in addition to the simultaneous load. To choose the proper opening sizes, the standard and architecturally recommended ones from Neufert et al (1980) were plotted against opening to wall ratio A_o/A_i (Fig. 10.2). Two additional window and door openings were within the interval of $A_o/A_i \in [0.10, 0.30]$ and were recommended by Neufert et al (1980). The interval is chosen based on criteria of EN1996-1-1 (BSI, 2004b) that states $A_o/A_i \geq 0.10$ in order for opening to be accounted for, Similarly, EN1998-1-1 (BSI, 2005) states that openings with an area larger than $A_o > 1.5 \text{ m}^2$, which translates to $A_o/A_i > 0.10$ should implement confining elements around the openings. On the other hand, Tomažević (1999) states the BSI (2005) limit is too strict, and proposes a more relaxed area limit of 2.5 m^2 that translates to $A_o/A_i \leq 0.17$. The latter limit of $A_o/A_i \leq 0.30$ was chosen based on the Penava et al (2018), where openings above the limit have little to no influence on the IP behaviour of frames with infill walls.

The details of geometry are visible in Table 10.1 and Figure 10.3.

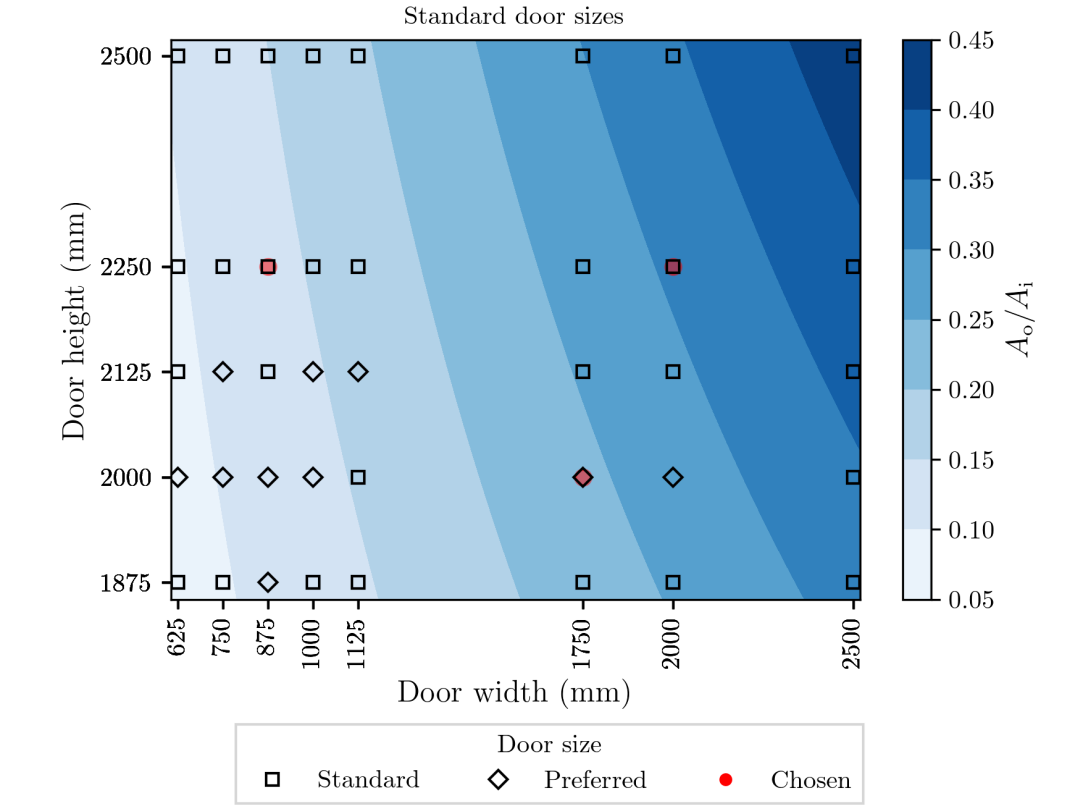
Table 10.1: Implemented geometrical characteristics of additional openings, (sizes are in 1.0:2.5 scale, units in mm)

Type	#	Opening size		A_o/A_i (%)	Distance from opening to infill edge				
		Width	Height		Below	Above	Cen. L/R	Ecc. L	Ecc. R
Window	1	480	600	12.31	400	300	470	570	250
	2	840	600	21.54	400	300	230	695	125
	3	840	840	30.15	400	60	230	695	125
Door	1	350	900	13.46	0	400	475	700	250
	2	700	800	23.93	0	500	300	475	125
	3	800	900	30.77	0	400	250	375	125

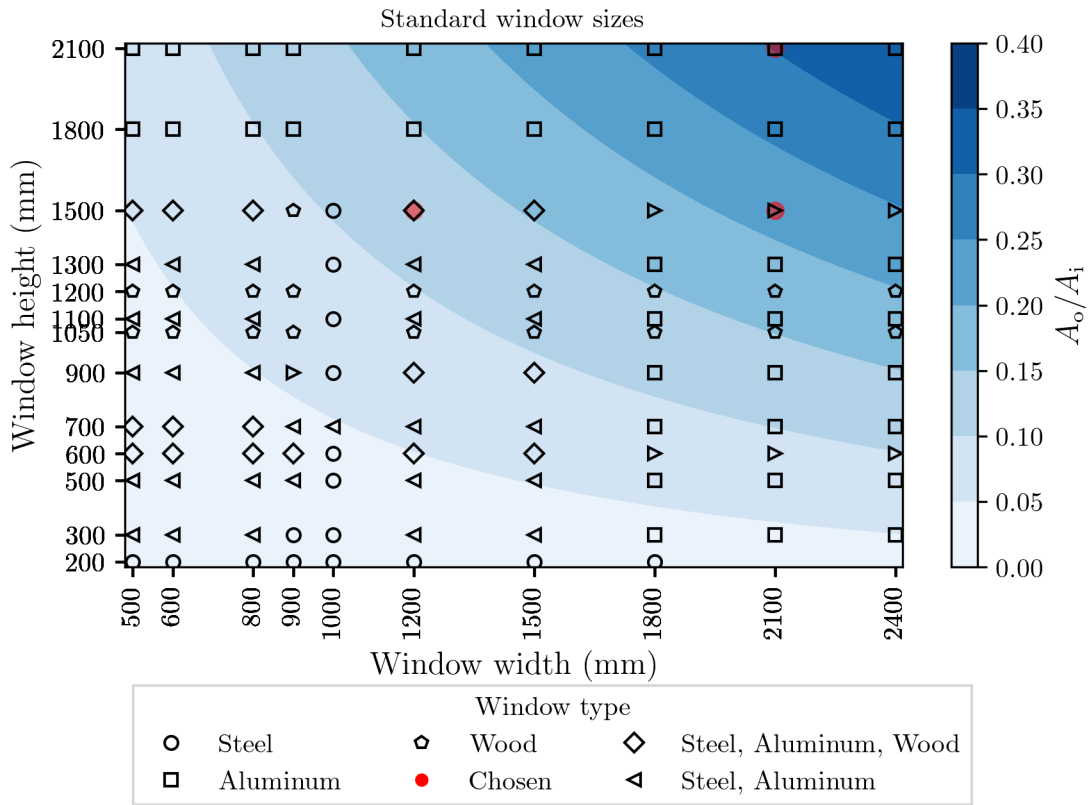
L/R - Left/Right

Cen. - centric; Ecc. eccentric opening

In regard to boundary conditions, they are as those outlined in the row number 5 of Table 8.1 (in combination with Fig. 8.3). In short, the following boundary conditions were used: a) prescribed deformation (p_d) was used for both IP and OoP loading. In the case of IP loading, all models had $d_{p,IP} = 0.5 \text{ mm/step}$; on the other hand, different OoP prescribed deformation values were used in order to achieve the angle of the resultant force α , *i.e.* $d_{p,OoP} = d_{p,IP} \tan(\alpha) \text{ mm/step}$. Additionally, in the case of eccentric openings, the IP loading was applied in left and right direction; b) Vertical, *i.e.* gravity load was applied 75 kN/step for 5 steps, adding to 365 kN as imposed on the prototype structure (Sec. 3); c) Both IP and OoP friction spring (Fig. 8.17) were applied in their respectful directions; d) Foundation supports were used in all steps, while on steps > 5 the column ones were also active.



(a) Doors



(b) Window

Figure 10.2: Map of recommended Neufert et al (1980) and chosen opening sizes (not corrected for 1.0:2.5 scale of specimens)

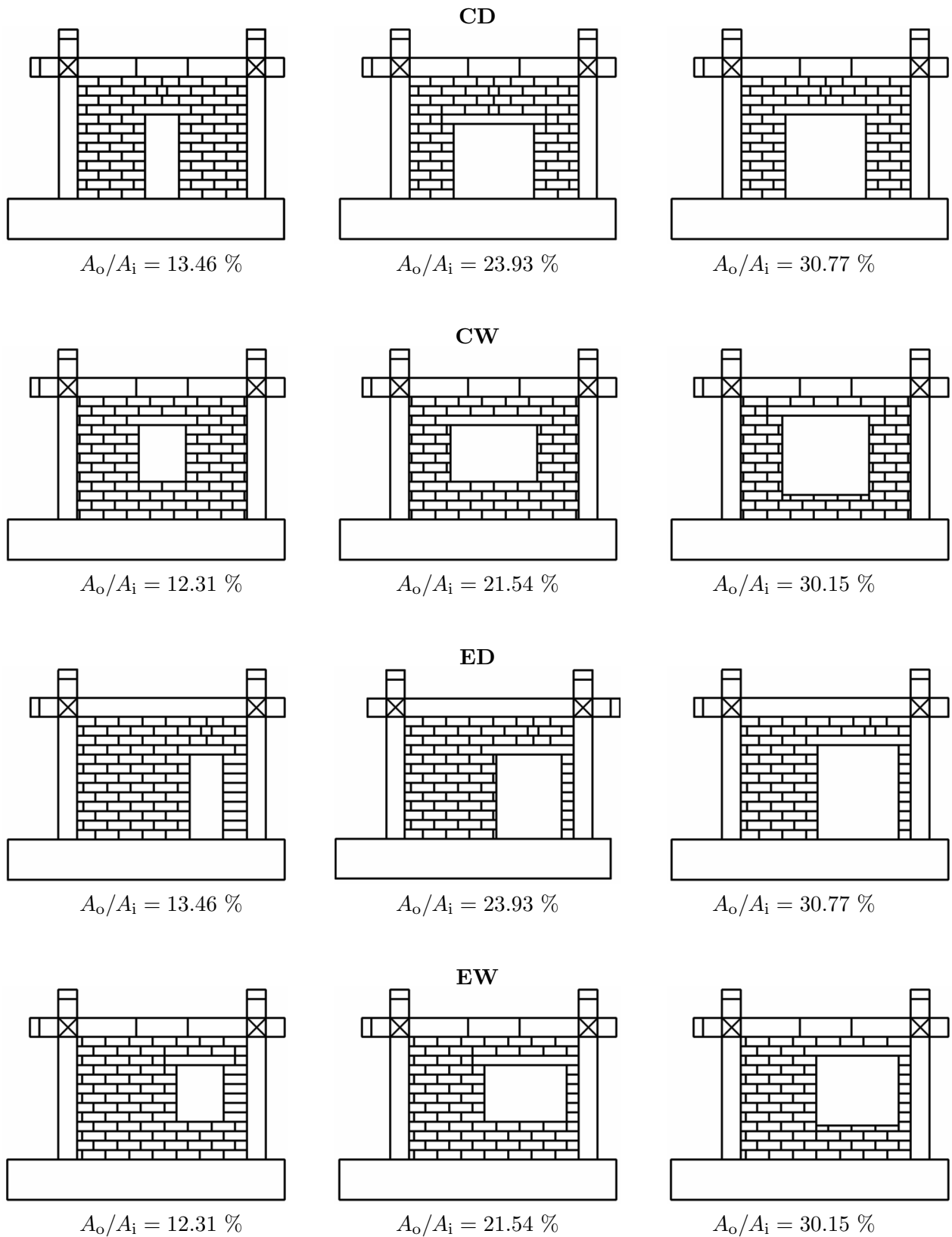


Figure 10.3: Developed micromodels for further simulations

10.3 Results

The results from simultaneous IP and OoP loading is presented in this section. The resultant load-bearing force V_R is calculated (Eq. 10.2) as a hypotenuse of IP ($V_{R,IP,\alpha}$) and OoP load-bearing capacity ($V_{R,OoP,\alpha}$) under angle α .

$$V_R = \sqrt{V_{i,IP,\alpha}^2 + V_{i,OoP,\alpha}^2} \quad (10.2)$$

for i in position of $\max\{V_{R,IP}, V_{R,OoP}\}$

10.3.1 General

The EW(0.2r) model for $\alpha < 45^\circ$ had experienced computational instabilities, for undetermined reasons. Whereas the rest, nearly 175 models, did not experience such problems.

Models were group based on the opening type, position and sorted by the angle α . The load-bearing capacity curves were then plotted for the IP and OoP part of the simultaneous load in Figures 10.4 and 10.5. As expected, from IP curves (Fig. 10.4), it was observed that in the case of the IP part with the increase of angle, the load-bearing capacity and drift ratio decrease. Contrariwise, in the OoP curves (Fig. 10.5), it is visible that with the increase of angle, the OoP load-bearing capacity is higher. When IP capacity curves were compared to the OoP ones (Fig. 10.4 *vs.* 10.5), it was observed that the IP curves vary by opening type and position, while the OoP ones do not. The OoP curves were more uniform.

The coupled IP and OoP curves were plotted against the coupled displacement (Fig. 10.6). The coupling was carried out by Equation (10.2). The graph resembles the IP ones, yet more elongated.

In Figure 10.7 the load-bearing capacity force is plotted against the resultant angle in a polar coordinate system. The horizontal axis shows the values normalized to the capacity of the BF model when loaded in the IP direction. The vertical axis shows the absolute values in kN. The BF-IP model was chosen as a dependent variable as most codes, scientific or technical discussions were based on IP models, while bare-frames represent the fundamental prototype.

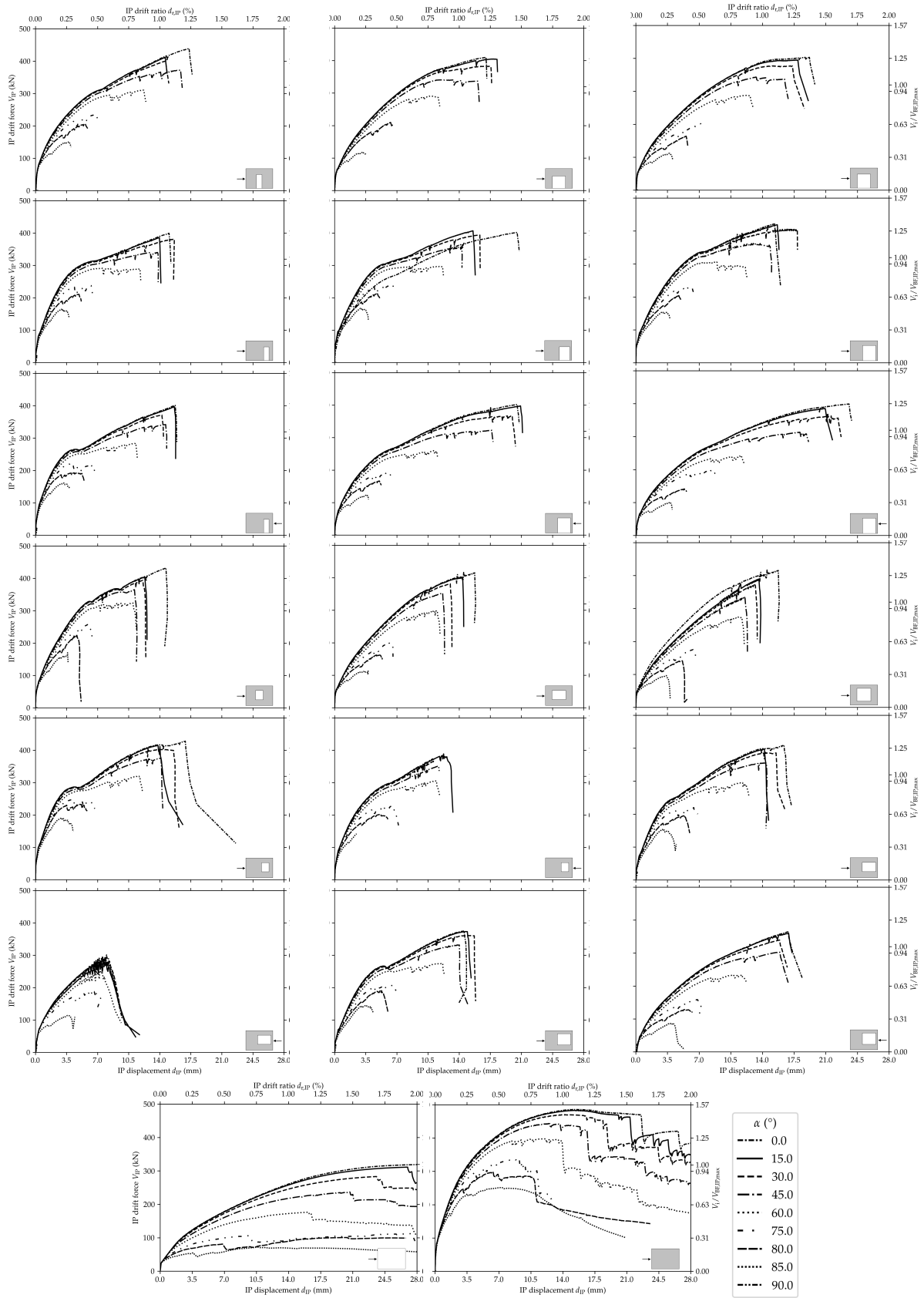


Figure 10.4: IP behavior from simultaneous IP and OoP simulations

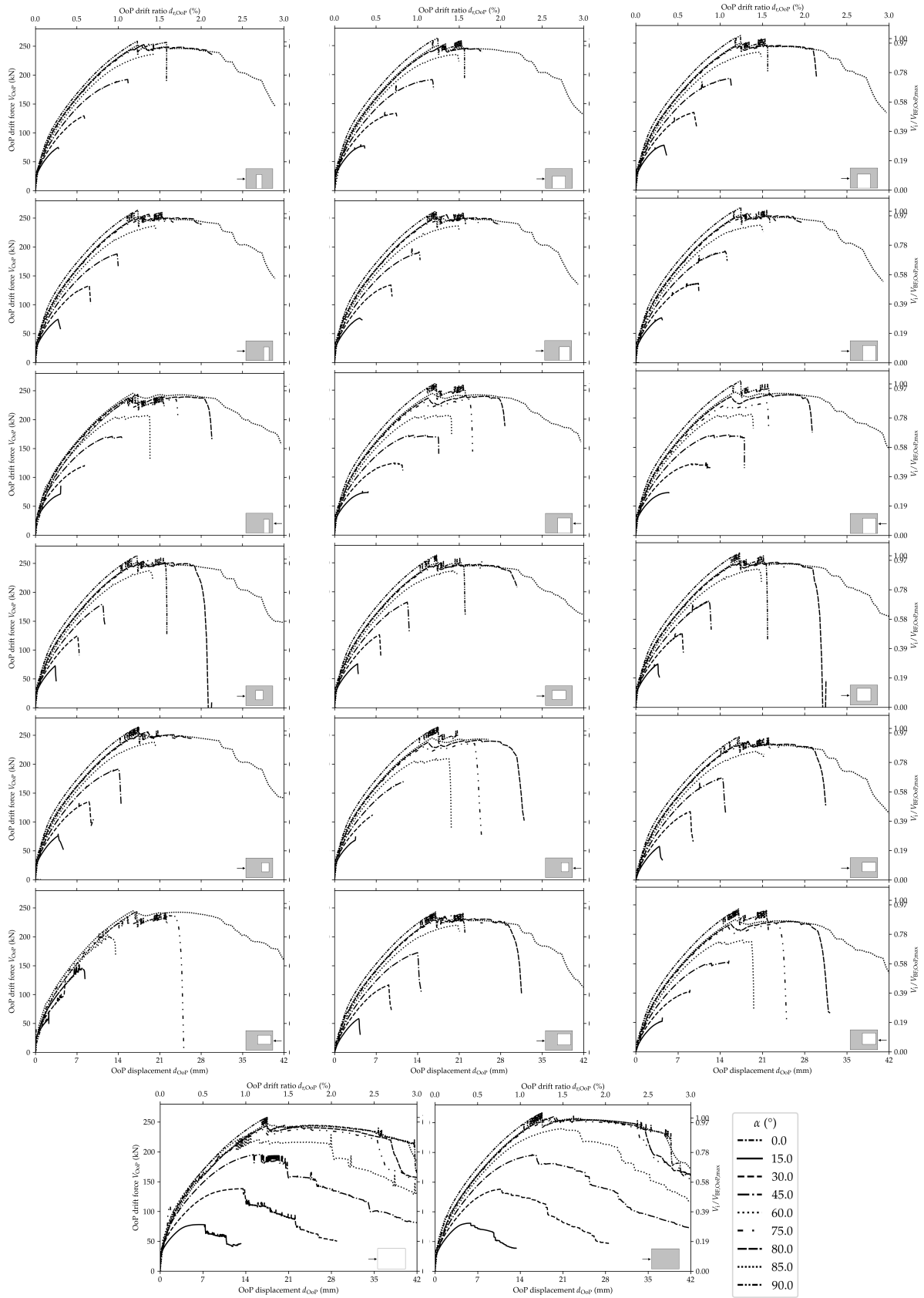


Figure 10.5: OoP behavior from simultaneous IP and OoP simulations

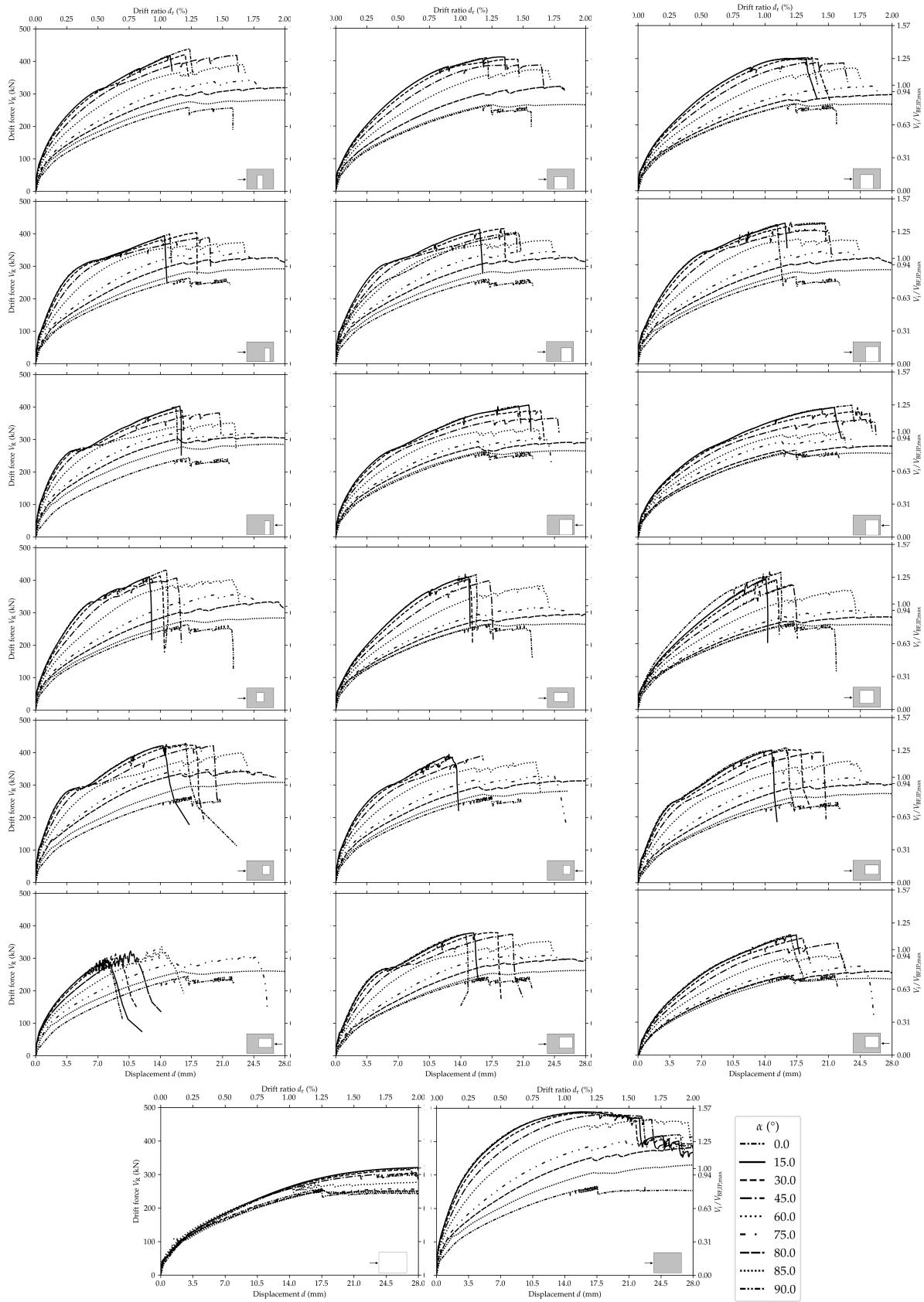


Figure 10.6: Coupled IP and OoP behavior from simultaneous IP and OoP simulations

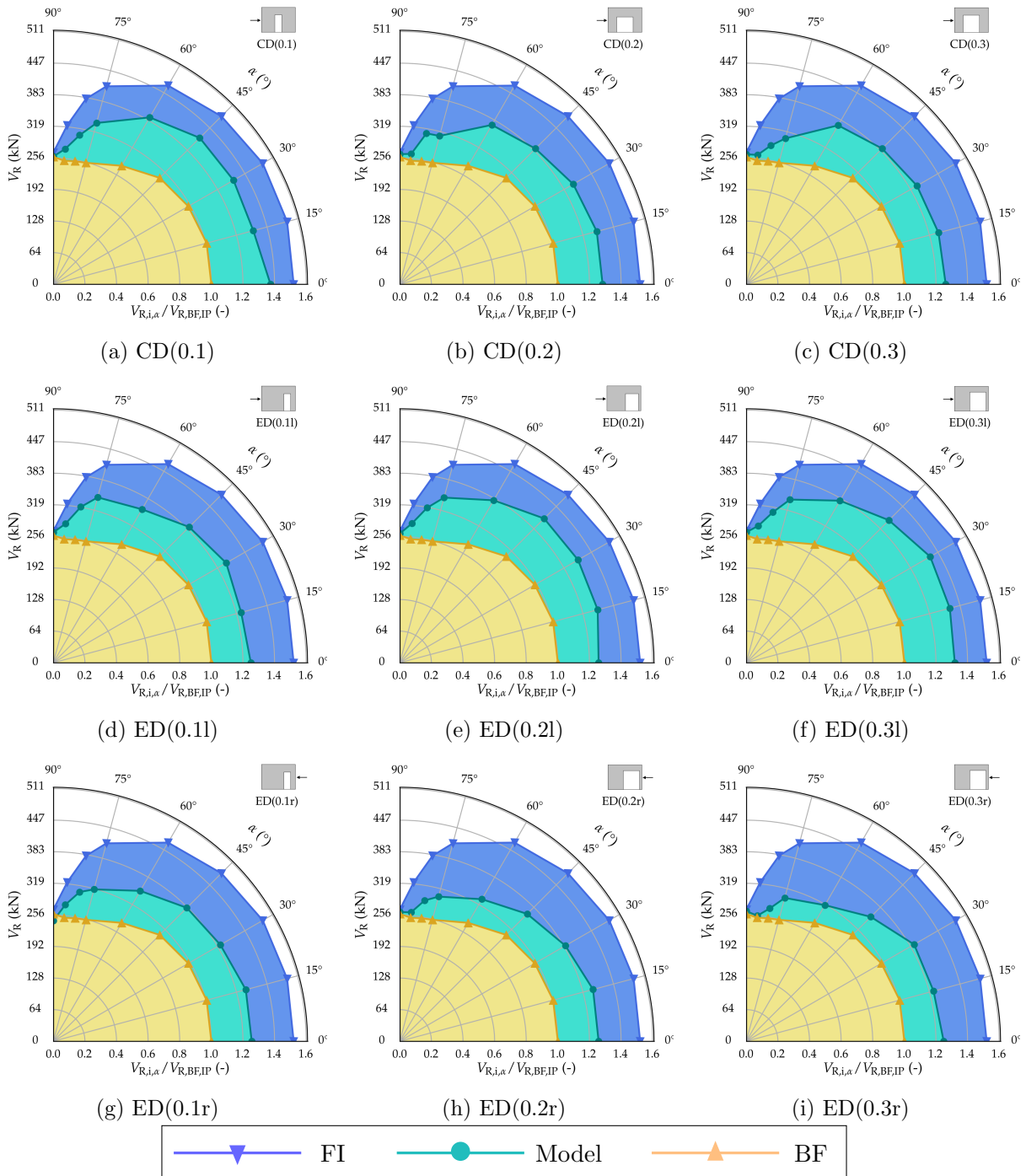


Figure 10.7: Resultant resistance force V_R vs. angle (α)

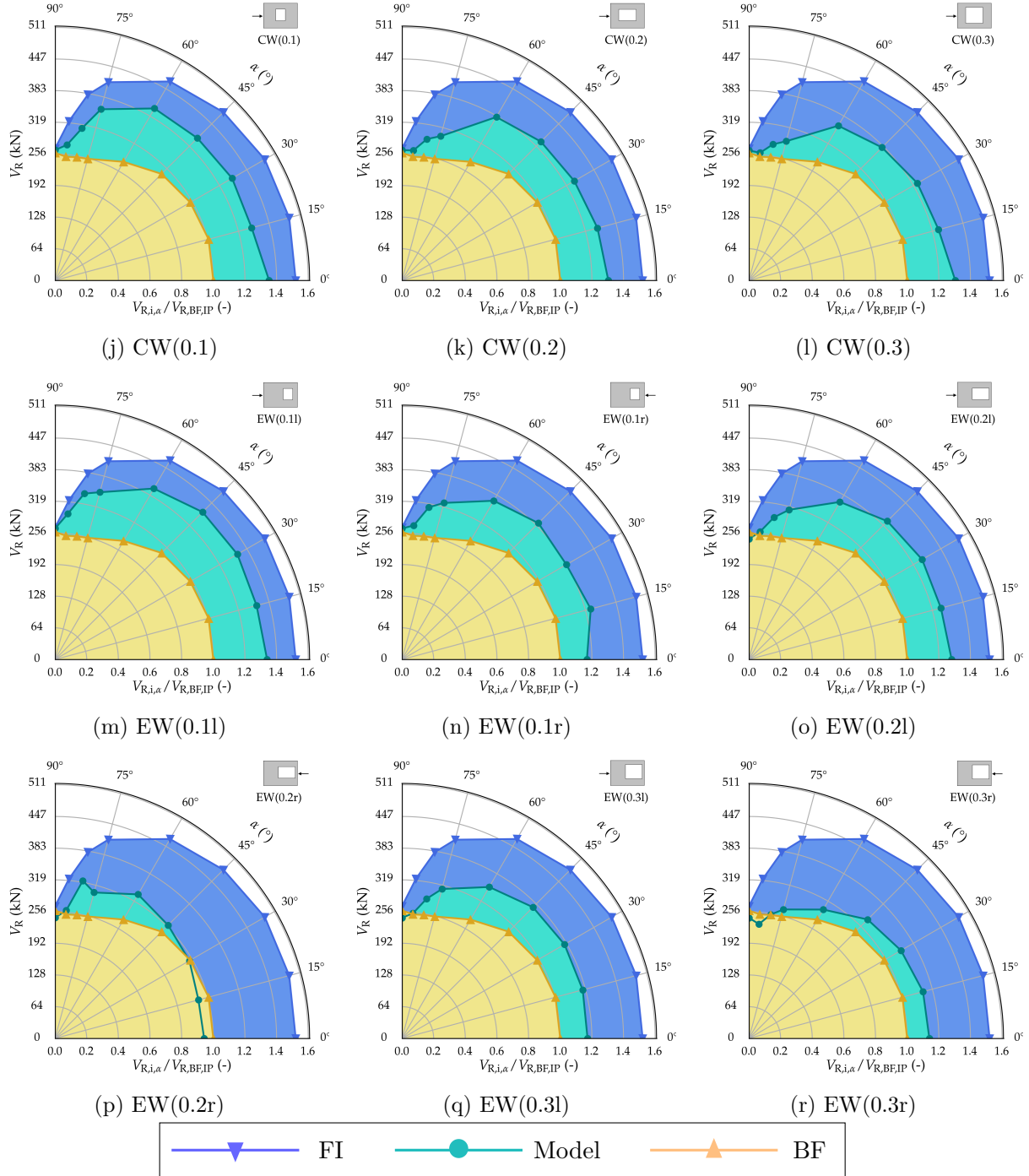


Figure 10.7 (cont.): Resultant resistance force V_R vs. angle (α)

It was observed that when the model reached either IP or OoP maximum load, it did not mean that it automatically reached the maxima in the other direction. In the same cases, mostly OoP load-bearing capacity was reached before the IP one, resulting in the IP graph plateauing, after which it gains strength again. This is also visible in Figure 10.6.

In Figure 10.8 all door and window openings are plotted better to comprehend the distribution between various sizes and positions. The minimum V_R limit of the graph is set as BF's OoP load-bearing capacity; the maximum, on the other hand, was set as FI's IP load-bearing capacity. The capacity lines are differentiated by opening location (C - centre, E - eccentric), IP load direction (L - left, R - right) and opening to infill wall area ratio (A_o/A_i).

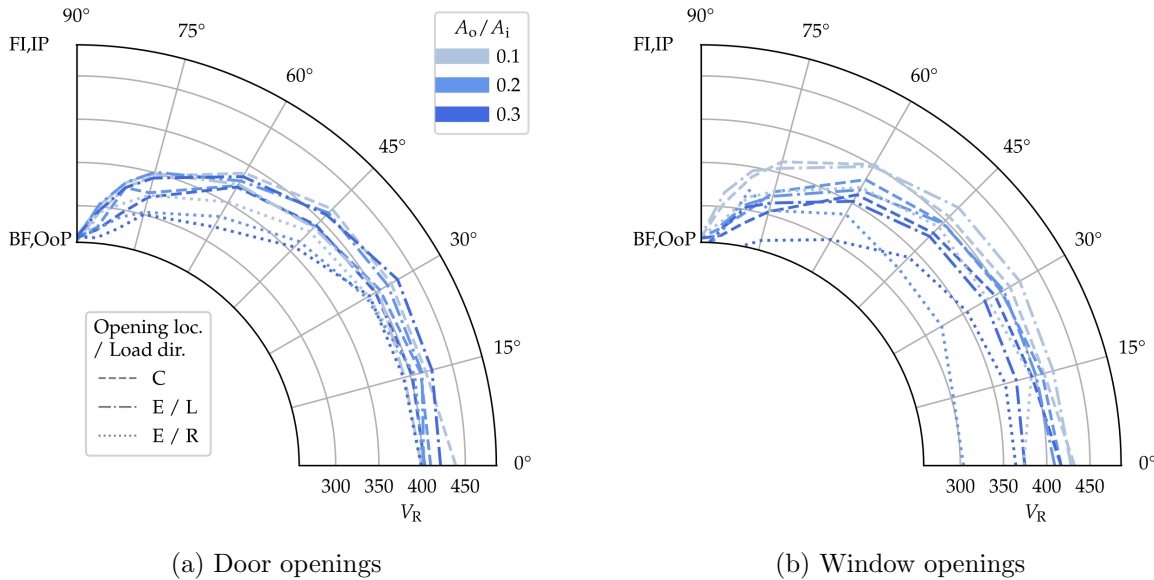


Figure 10.8: Sorted openings plotted against each other

It was observed that the load-bearing capacity begins at its maximum value with $\alpha = 0$ and then drops to that of the BF model at $\alpha = 90$. The significant drops start at about $\alpha = 45$, and from that point, the value decreases at a higher rate. The reason is undoubtedly in the changing from *frame* to *cantilever* dominant mechanical system, along with evidence of diminishing the influence of diagonal strut due to tensional stress imposed by OoP loading.

The displacements were plotted in a polar plot format within Figures 10.10 and 10.9. The figures show that all models have a drastic shift in behaviour after $\alpha \geq 45$; where the BF model has a sudden drop, and others rise. Yet, they rise when $45 \leq \alpha \leq 80$, after which they fall until they reach the displacement of the BF model. The FI model is always nearly opposite to the BF behaviour, where BF is maximal FI is minimal and vice versa. The other models were between the two, where the larger the opening, the closer the behaviour is to the BF model. In detail, the IP curves had a very mild drop when $\alpha \leq 45$, after which its rate of fall increases (Fig. 10.9b). Contrariwise, the OoP raise is nearly linear until ≈ 75 , which also drops.

Comparatively, the reason is due to the presence of the stiff infill wall, where it restricts deformations of more ductile frames in the IP dominated system $\alpha \leq 45$, while in the OoP $\alpha \geq 45$ braces enough to stabilize the models to achieve greater deformation capabilities.

10.3.2 Influence of gravity load on OoP tests

The question had arisen in Section 9.3 as to whether the infill wall would have more apparent *arching-action* when the gravity load was introduced. Without the gravity load, half of the front face braced in compression, yet, it did not extent to the other corner (Fig.9.12).

Observing the same models at the same drift ratios, it was observed that infill walls did manage

to develop the arching-action effect (Fig. 10.11). The lower half had similar stress distribution as models without gravity load (Fig.9.12). However, the main difference was in the upper corners that developed higher compressive stress. From the corners, the stress distributes to the entire length of the wall on the opposite edge, thus effectively rendering arching action, best visible in side views.

This *arching-action* is basically an OoP strut. Same kind of arching action was observed by Tu et al (2010) in her dynamical studies (Fig. 2.10c), and the effect was described in Section 2.3. However, due to the nature of such a short strut, its effects on the overall behaviour are, again, minimal. However, for the infill walls themselves, the additional bracing provides additional protection from *falling-* or *walking-out* effects.

10.3.3 Damage development and resistance mechanisms

Since there are 180 models, only figures for FI models were extracted. The other models followed similar patterns.

It was found that there was a shift in the mechanism that resists the resultant forces as α goes from 0 to 90°. This is illustrated on an infill wall sketch in Figure 10.12. At $\alpha = 0$, there is a compressional strut that stretches through the whole width of the wall. Due to OoP bending, one side is in compression while the other is in tension (Fig. 5 vs. 4). The tensional side unloads the compression strut on that side, rendering it less effective with the increase of α . This is observable by comparing the infill wall's front and back face principal stress (Fig. 5 vs. 4); wherewith the increase of α compression side gains, and tension loses minimal principal stress. Contrariwise, in the case of maximal principal stress, the tension side increases. This results in a progressively asymmetric minimal principal stress map due to stress accumulation at the corner where IP and OoP struts were pinned. The other corner had just the stress from the OoP strut, while the rest of the wall was unloaded. There are additional struts on the walls face on the compression side that stretch from the corners to the bottom at a certain angle. Those activate as the infill wall bends, the upper part of infill wall *braces* against the lower beam. For the sake of standardization, this effect will be called *bracing effect*. The compressive stresses from OoP struts and bracing effects are low since they do not have sufficient length OoP-wise. Therefore, the stresses add up on the compression side, yet not significantly. Nevertheless, due to cancelling of IP compressive strut on the other side, the system loses its beneficial effects from the infill wall. Furthermore, the tension and shear stresses combined in the bedjoints would propagate the bedjoint sliding failure.

As observable, the lower the α , lower is the stress in the frame, yet larger in the infill wall. Contrariwise, OoP load develops significant higher and more stress area coverage (Fig. 5). This results in a more damaged frame. Within $\alpha \in (0, 90)$, the resulting cracks were asymmetrical (best observable at higher drifts, Fig. 7, 8) by the same reason as described in the upper paragraph: due to stress accumulation at the corner where IP and OoP struts were pinned (Figs. ,6, 7, 8). Obviously, due to the low tensional strength of all material involved (except the reinforcement), most cracks occurred on the tensional side of the infill wall with additional bedjoints opening that occurs around $\alpha > 80$. If the tension side of both frame and infill walls are compared, most of the damage was accumulated at about $\alpha = 80$. While on the compression side it in pure IP direction $\alpha = 0$.

The failure of the system is best observable by the increasing drift ratio and α , where pictures of minimal principal stresses were grouped at about $V_{R,max}/2$, $V_{R,max}$, and after $V_{R,max}$ (Fig. 4, 5). The minimal stress developed until $V_{R,max}$, after which bedjoint sliding failure occurs. The tension side is then, mostly unloaded, while the compression side still acquires stress.

After the load-bearing capacity was reached mostly by IP fail modes as described in Table 5.1 and/or admixture of OoP bending. The IP fail modes are easily observable in the infill wall, as by

separating infill wall columns and bejoint failments. The OoP, especially in combination with IP load does heavy damage to the columns.

10.3.4 IP and OoP interaction curves

Interaction curves from computational models

The data from computational models was gathered and sorted based on opening location (C - centric, E - eccentric), resultant capacity angle (α), load direction (l - left, r - right), and opening to infill wall area ratio (A_o/A_i) in Figure 10.13. The topographic view of the 3D functions (right figs) is plotted on the left of the Figure.

From Figure 10.13 it is noticeable that there is, as reported in the previous subsection, relativity low decline of load-bearing capacity up to $\alpha = 45$; after which the rate of drop dramatically increases. Similarly, the drop caused by the change in A_o/A_i is relatively linear that changes in some models at $\alpha = 45$ mark. Furthermore, similar linear relation was observed by Mays et al (1998) in OoP inertial and Penava et al (2018) in IP studies. As expected, interaction curves showed greater capacity is in the domain of lowest α and A_o/A_i , while the opposite is also true, *i.e.* the other corner.

Finding the interaction curve equations

The purpose of this subsection is to find an equation that can be used to estimate frames with infill wall load-bearing capacity based on that of a bare frame. Namely, the intention is for designers to obtain the IP load-bearing capacity ($V_{R,BF,IP}$), either by calculation, simulation or experiment and then estimate the capacity of an infilled frame with or without opening based on its type (D, W), size ($\beta = A_o/A_i$), position or load direction (l, r) and the angle of resultant force (α). All the variables would be condensed into parameter k , forming the estimation equation for calculating the aforementioned load-bearing capacity $V_{R,i}$.

$$V_{R,i} = V_{R,BF,IP} k \quad (10.3)$$

Where k is dependable on $\alpha \in [0, 90]$ ($^\circ$), $\beta \in [0.1, 0.3]$, opening type $\in \{\text{door, window}\}$, and load direction $\in \{\text{left, right}\}$.

From the plotted curves in Figure 10.13 it is visible that there is a non-linear relationship between the models' response to changing the resultant angle (α). This is best illustrated in Figure 10.14t, where from 0 - 40 $^\circ$ there is a more or less linear part of the curve after which there is a drastic decrease in load-bearing capacity. The sudden drop in capacity can be attributed to shifting from *frame* to *fixed-fixed column* mechanical system, and the loss of bracing

Since there is a linear and non-linear part of the curve, the function cannot be described in simple terms (*e.g.* $f(x) = ce^x$ or $\sin(x)$, *etc.*). In order to maintain a more *elegant* form of the equation, higher order polynomial equations were discarded, even though there was good correlation with polynomial equations of 3rd order or higher. Ultimately, the following functions were considered: a) poly ratio (Eq. 10.4); b) Michaelis-Menten growth model (Eq. 10.5); c) Bleasdale-Nelder (Eq. 10.6); d) Farazdaghi and Harris (Eq. 10.7); e) Monomolecular (Eq. 10.8); f) Sigmoidal (10.9).

$$k = \frac{c_1 + c_2x}{1 + c_3x} \quad (10.4)$$

$$k = \frac{c_1x}{c_2 + x} \quad (10.5)$$

$$k = (c_1 + c_2x)^{\frac{1}{c_3}} \quad (10.6)$$

$$k = \frac{1}{c_1 + c_2 x_3^c} \quad (10.7)$$

$$k = c_1 - \frac{c_2}{c_3} (1 - e^{-c_3 x}) \quad (10.8)$$

$$k = c_4 + \frac{c_1 - c_4}{1 + \left(\frac{x}{c_3}\right)^{c_2}} \quad (10.9)$$

In short, the Equation (10.8) was chosen on basis that it was easier to simplify the final expression without interdependent A_o/A_i and α variables.

The method was to firstly find the function of k in relation to $\alpha \rightarrow k(\alpha)$ using Equation (10.8). Then correlate the coefficients (a, b, c) with $\beta \rightarrow c_i(\beta)$, $i \in \{1, 2, 3\}$. Unify 2D equations, *i.e.* $k(\alpha)$ with $c_i(\beta)$ into 3D surface equation $k(\alpha, \beta)$.

The optimization of constants (c_i) in $k(\alpha)$ for each model was made using the *SciPy curve_fit* (Jones et al, 2001) tool. The results of optimizations, *i.e.* the value of constants and R^2 are presented in Table 10.2, while the same is visually presented in Figure 10.14.

Table 10.2: Results of nonlinear regression for effect of α

#	Model	c_1	c_2	c_3	R^2
0	BF	1.016135	0.000989	-0.01865	0.966002
1	FI	1.526488	0.000026	-0.08576	0.993902
2	CD(0.1)	1.349319	0.000368	-0.04733	0.993508
3	CD(0.2)	1.293112	0.000487	-0.04159	0.984913
4	CD(0.3)	1.278616	0.000588	-0.03897	0.985500
5	CW(0.1)	1.312715	0.000088	-0.06562	0.988984
6	CW(0.2)	1.303435	0.000614	-0.03900	0.984724
7	CW(0.3)	1.293589	0.001378	-0.02630	0.981969
8	ED(0.1l)	1.246009	0.000078	-0.06500	0.993599
9	ED(0.2l)	1.291887	0.000127	-0.06011	0.986152
10	ED(0.3l)	1.340882	0.000410	-0.04511	0.995041
11	ED(0.1r)	1.259905	0.000524	-0.03997	0.985252
12	ED(0.2r)	1.281118	0.002013	-0.01867	0.993364
13	ED(0.3r)	1.270927	0.002467	-0.01509	0.977681
14	EW(0.1l)	1.336160	0.000129	-0.06064	0.992629
15	EW(0.2l)	1.281822	0.000417	-0.04484	0.996879
16	EW(0.3l)	1.189682	0.000191	-0.05321	0.994437
17	EW(0.1r)	1.216696	0.000147	-0.05620	0.970074
18	EW(0.2r)	0.950851	0.056817	24.41952	0.000074
19	EW(0.3r)	1.166641	0.001868	-0.01880	0.978165

When constants were sorted for same opening type, location and load position, then plotted against β it was observed that they follow more-or-less linear relationship (Fig. 10.15). Hence, line function with $\{a(\beta), b(\beta), c(\beta)\} = m + n\beta$ form were developed for every model, where m, n were the new constants. The β linear dependency is also observable in the Figure 10.13. Note that it was not observable in the invalid EW(0.2r) model, only the 0.1 and 0.2 β were.

The line functions were then fed to $k(\alpha)$ forming Equation $k(\alpha, \beta)$. For the sake of simplicity $c_2(\beta)/c_3(\beta)$ part of the function was then unified to unique constant, named b . After subtractions

and simplifications, the equation obtained a form of Equations 10.11 and 10.10, where k_o is for openings and k_i for FI models. The coefficients a and b can be found in Table 10.3.

$$k_o = a + b\beta \left(1 - e^{-0.05\alpha(\beta-1)}\right) \quad (10.10)$$

$$k_i = 1.53 + 0.0003 \left(1 - e^{-0.085\alpha}\right) \quad (10.11)$$

$$\forall \alpha \in [0, 90], \beta \in [0.1, 0.3]$$

Table 10.3: Coefficients for Equation 10.10

Type	Opening Position	Load direction	a	b
Door	Centric	/	1.29	0.071
Window	Centric	/	1.30	0.075
Door	Eccentric	Left	1.30	0.065
Door	Eccentric	Right	1.24	0.070
Window	Eccentric	Left	1.27	0.070
Window	Eccentric	Right	1.23	0.070

The differences between the computational and analytical models are presented in Table 10.4 and Figure 10.17. Where in Equation (10.12) $V_{R,CALC}$ was calculated using Equations (10.10, 10.11, 10.3) and Table 10.3. It is noticeable that some models as CW(0.1), EW(0.11) have a smaller error at lower angles α , when compared to higher ones. In those cases the optimal parameters were found so they produce the lowest mean error for all angles. Regardless of the aforementioned, with the exclusion of flawed EW(0.2r) model, the correlations were, overall satisfactory. In Figure 10.17 the whiskers are the \pm standard deviations of the error.

The function k_o was plotted as a surface against the points from the computational models in Figure 10.16. As visible, some points are below, intersecting or above the k_o surface. From the EW(r) model (Fig. 10.16f) the extrapolated part $\alpha \leq 45$ is visible, and is in line with the other functions.

$$\Delta V_R = 1 - \frac{V_{R,CALC}}{V_{R,FEM}} \quad (10.12)$$

Note that the equation is limited to the following points for which the extrapolation is uncertain:

- The equation was developed on the RC, medium ductility frame (DCM), designed by following EC8 provisions (BSI, 2005);
- The openings with ratios outside $A_o/A_i \in [0.1, 0.3]$ were not covered;
- The eccentric opening positions were not varied;
- The opening aspect ratio was not parameterized;
- The influence of various gravity loads was not observed;
- The equation was developed on models without orthogonal boundary conditions, *e.g.* influence of diagonal strut form orthogonal wall, *etc.* ;

Table 10.4: Analytical model prediction error

α	$\Delta V_R \alpha$ (Eq. 10.12) (%)									Mean	
	0°	15°	30°	45°	60°	75°	80°	85°	90°		
Model	FI	0.58	-0.27	-0.61	-0.14	1.87	2.28	1.96	-0.62	7.36	1.74
	CD(0.1)	-6.53	-2.61	-5.34	-5.99	-6.71	-6.50	-2.05	-4.67	1.45	4.65
	CD(0.2)	0.53	-1.14	-1.55	1.16	-2.22	-0.36	-2.02	1.26	-0.37	1.18
	CD(0.3)	2.18	1.39	-0.07	0.68	-1.65	1.29	7.42	2.33	-0.20	1.91
	CW(0.1)	-4.05	0.00	-2.72	-2.29	-9.73	-12.34	-6.61	-10.13	-2.51	5.60
	CW(0.2)	-0.30	0.55	0.04	0.20	-4.19	-1.24	6.50	0.01	-2.38	1.71
	CW(0.3)	-0.30	3.54	2.26	4.39	1.31	6.12	10.47	3.25	-2.08	3.75
	ED(0.11)	3.85	4.47	0.00	2.84	-0.72	-4.10	-0.45	-2.38	4.86	2.63
	ED(0.21)	3.23	-0.65	-3.08	-3.23	-1.91	-4.52	-0.57	-2.82	6.05	2.90
	ED(0.31)	-1.48	-3.52	-6.35	-2.41	-3.45	-2.43	1.37	-0.25	5.05	2.92
	ED(0.1r)	-1.25	-3.44	-1.81	-0.69	-0.40	-4.16	-0.75	-10.37	1.53	2.71
	ED(0.2r)	-1.46	-3.26	-1.07	3.63	5.13	2.36	4.40	-3.03	-5.19	3.28
	ED(0.3r)	-0.73	0.03	-2.12	5.92	9.06	3.22	8.73	0.70	-6.27	4.09
	EW(0.11)	-5.52	-5.03	-8.30	-8.31	-10.93	-11.10	-10.01	-15.02	-2.57	8.53
	EW(0.21)	-0.87	0.07	-2.86	-1.68	-2.25	-0.67	2.54	-1.39	5.21	1.95
	EW(0.31)	7.66	5.93	3.49	3.78	2.01	1.85	3.59	0.37	5.37	3.78
	EW(0.1r)	5.00	-1.76	-0.75	-3.54	-6.95	-6.64	-4.33	-7.91	-7.91	4.98
	EW(0.2r)	22.70	22.21	15.42	14.22	3.35	0.66	-7.04	-2.76	0.27	9.85
	EW(0.3r)	7.29	6.21	6.53	9.60	13.13	12.38	14.92	8.31	0.44	8.76
Mean	2.93	2.44	2.72	3.36	4.65	4.64	4.93	4.16	3.71	3.73	

Note that flawed EW(0.21) model was excluded from calculating Mean

- The influence of inertial forces was not considered, hence it is better suited for ground floors;
- Models were developed based on block places so that voids are parallel with columns which is not a traditional building technique in countries such as Portugal, Albania or Turkey;
- Neither the equations, nor the models could be verified against other specimens as this is the first research that included drift driven load against RC frames.

10.3.5 Example of determining load-bearing capacity

Here, an example of determine load-bearing capacity is described.

Problem Determine the load-bearing capacity of a frame with infill wall and centric door opening under the angle of loading $\alpha = 45$. The IP load-bearing capacity of the frame was calculated as $V_{R,IP,BF} = 400$ kN, the ratio of opening and infill wall are is $A_o/A_i = \beta = 0.24$.

Using equations one can obtain more refined answer when compared to the interaction curves. Firstly, one should obtain coefficients from Table 9.3: $a = 1.29$ and $b = 0.071$. Then use Equation the 10.10 with the data from the problem and the aforementioned table.

$$\begin{aligned} k_o &= a + b\beta \left(1 - e^{-0.05\alpha(\beta-1)}\right) \\ &= 1.29 + 0.071 \cdot 0.24 \left(1 - e^{-0.05 \cdot 45(0.24-1)}\right) \\ &\approx 1.213 \end{aligned}$$

Finally, multiply the BF's IP capacity with k_o , thus obtaining the requested capacity:

$$\begin{aligned} V_{R,CD,\alpha=45} &= k_o V_{R,BF,IP} \\ &= 1.213 \cdot 400 \\ &\approx 485.20 \text{ kN} \end{aligned}$$

Interaction curves The process is described in Figure 10.18. The first one should find the appropriate interaction curve. In this case, the CD one. Then find the A_o/A_i and draw a horizontal line, in this case, red. Then find the angle and draw the vertical line, in this case, green-coloured. The intersection of the red and green lines is the requested coefficient. A more conservative approach would read it as 1.2, more detailed would estimate as 1.23.

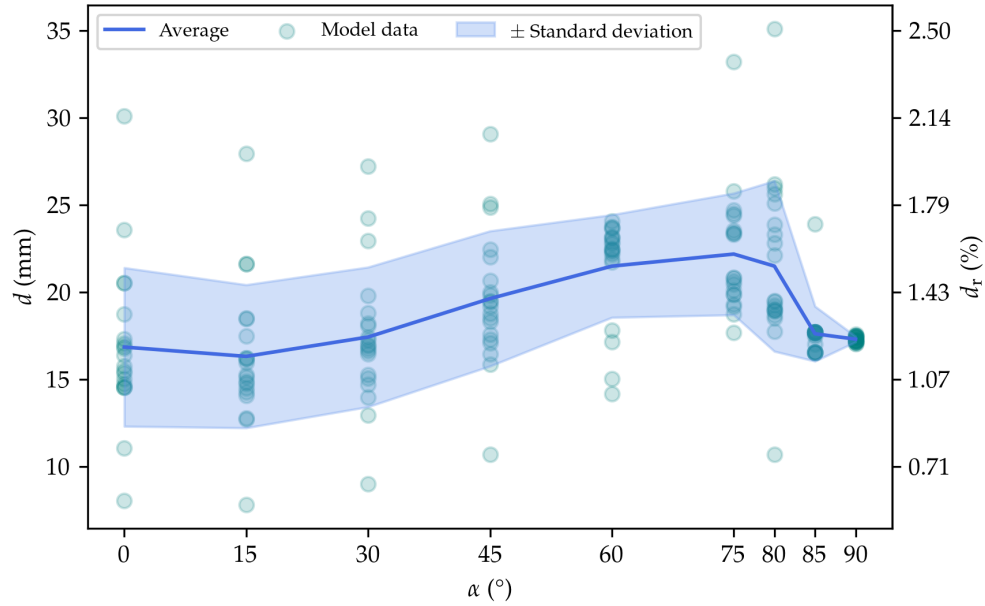
Finally, multiple the BF's IP capacity with the coefficient:

$$\begin{aligned} V_{R,CD,\alpha=45} &= k_o V_{R,BF,IP} \\ &= 1.23 \cdot 400 \\ &\approx 492 \text{ kN} \end{aligned}$$

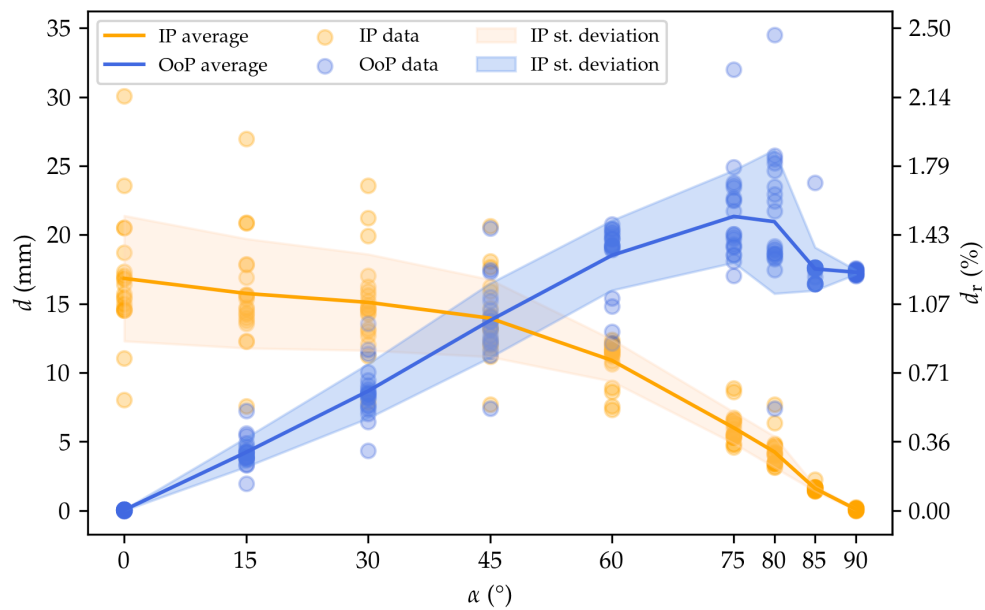
Conservative approach:

$$\begin{aligned} &= 1.2 \cdot 400 \\ &\approx 480 \text{ kN} \end{aligned}$$

Both methods yield approximately the same results.

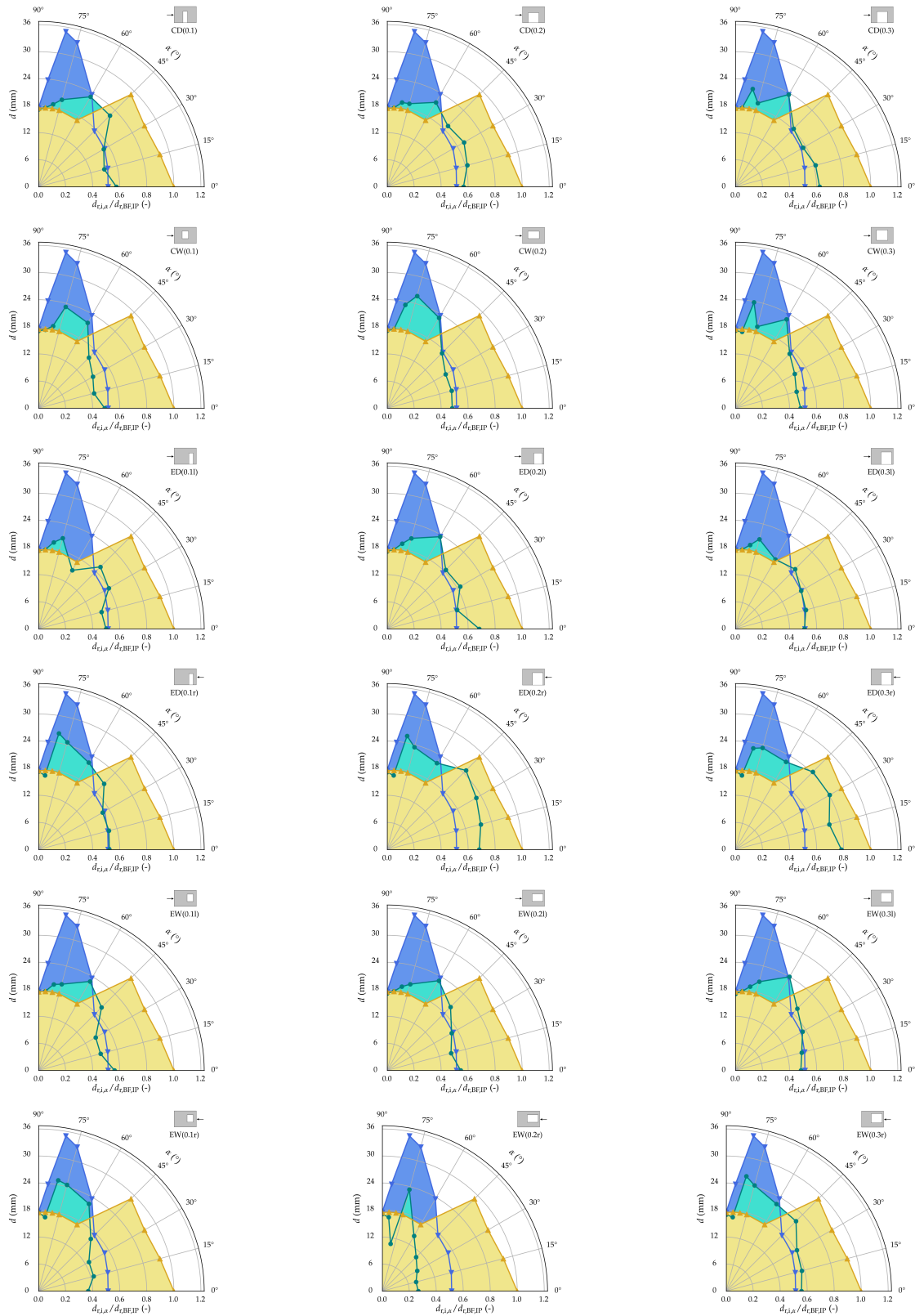


(a) Coupled IP and OoP displacement



(b) IP and OoP displacement

Figure 10.9: IP and OoP displacement @ $V_{R,max}$ vs. α

Figure 10.10: Coupled IP and OoP displacements @ $V_{R,max}$ in relation with angle α

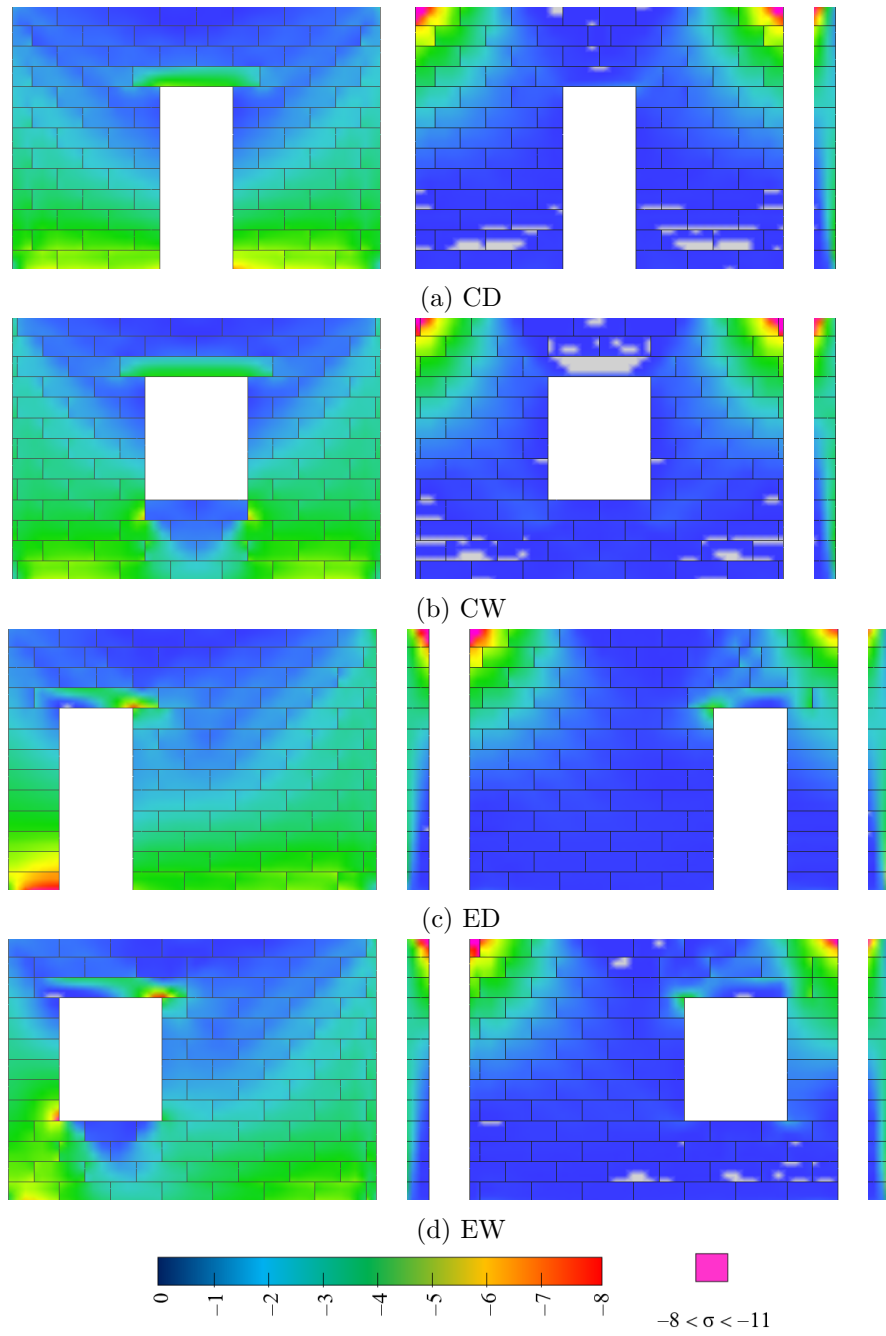


Figure 10.11: OoP minimal principal stresses @ 1.25 % d_r with gravity load

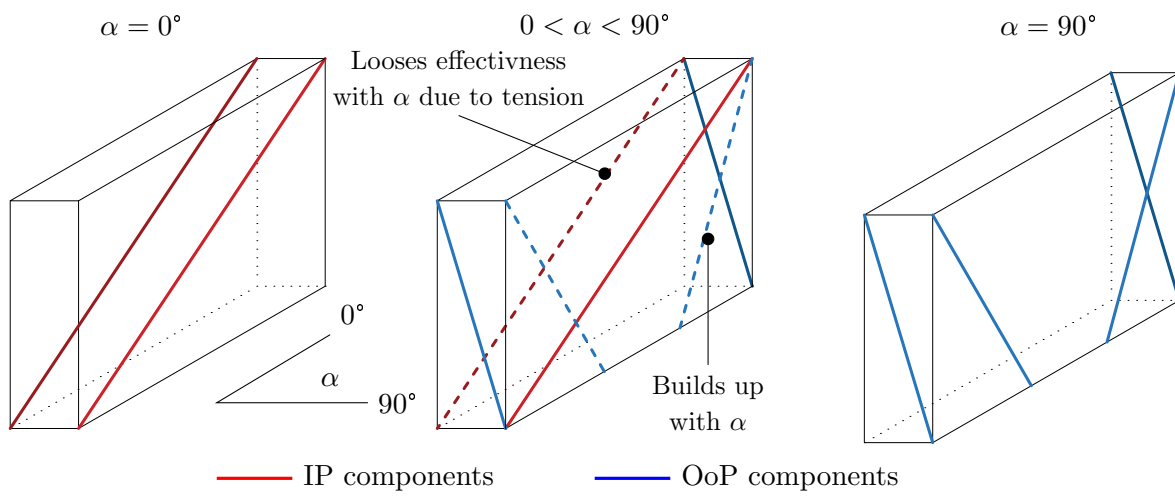
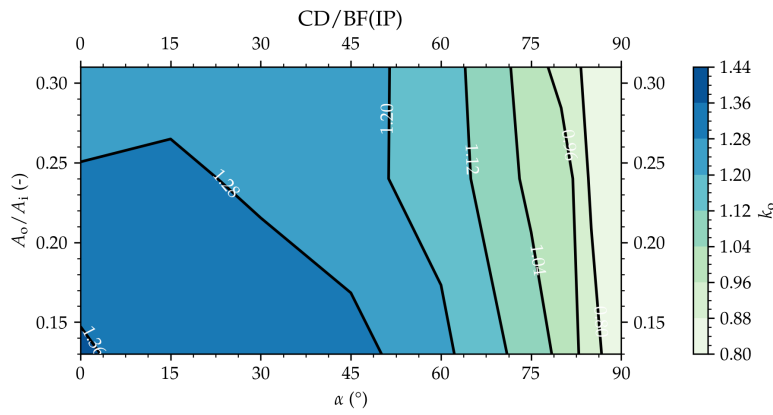
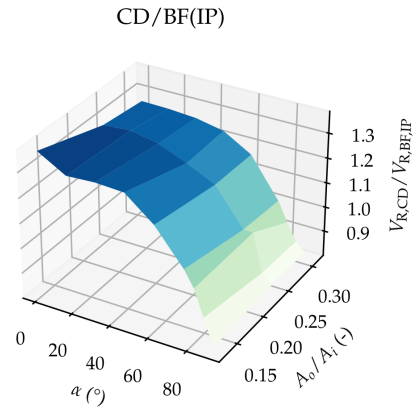


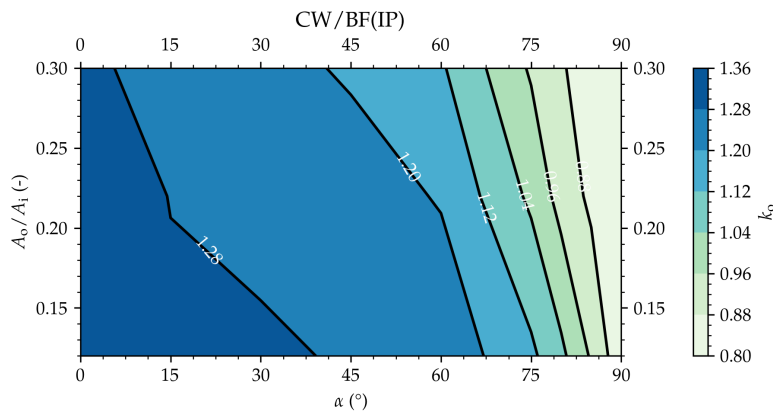
Figure 10.12: Resistance mechanism development



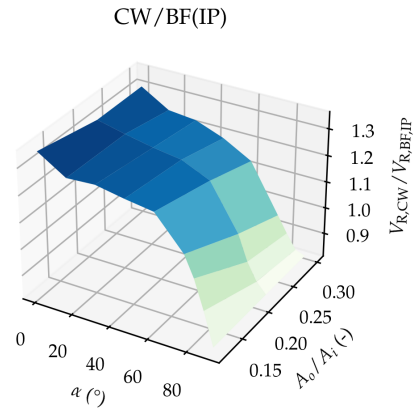
(a) CD models topographic view



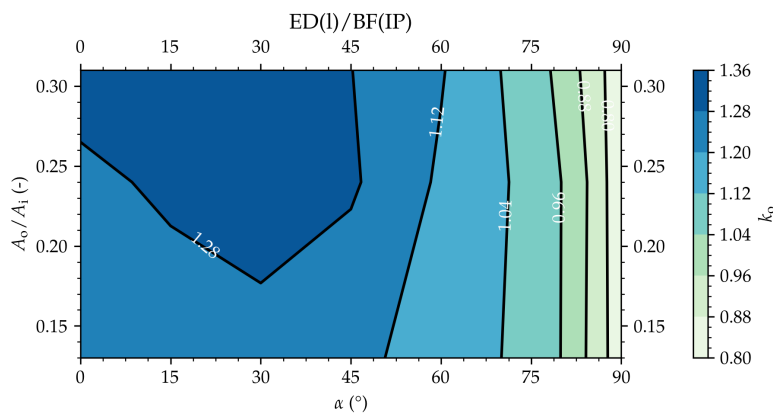
(b) CD models 3D view



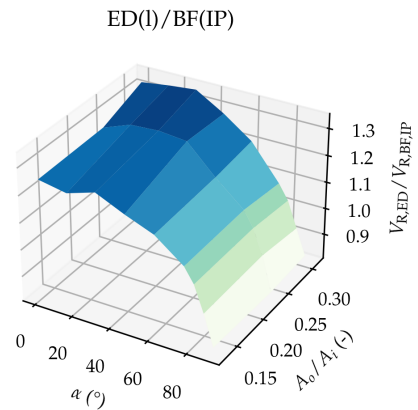
(c) CW models topographic view



(d) CW models 3D view

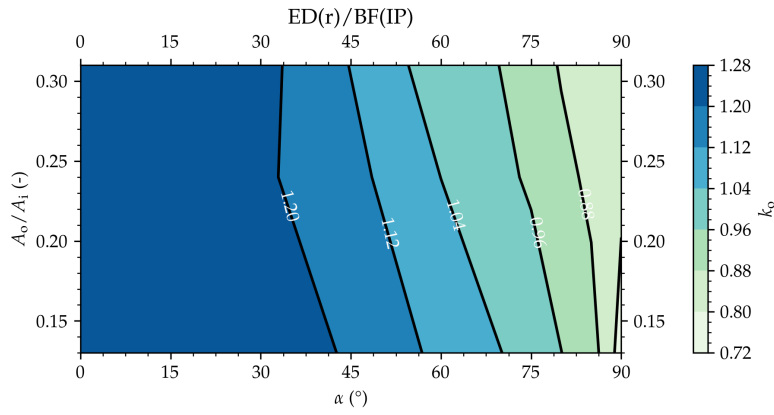


(e) ED(l) models topographic view

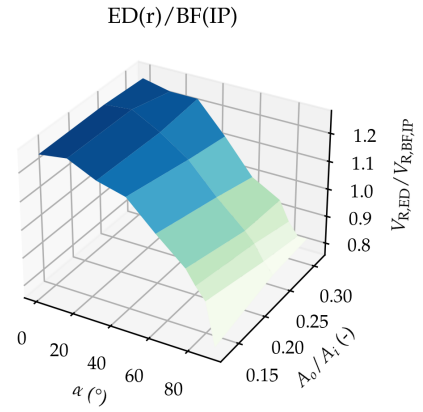


(f) ED(l) models 3D view

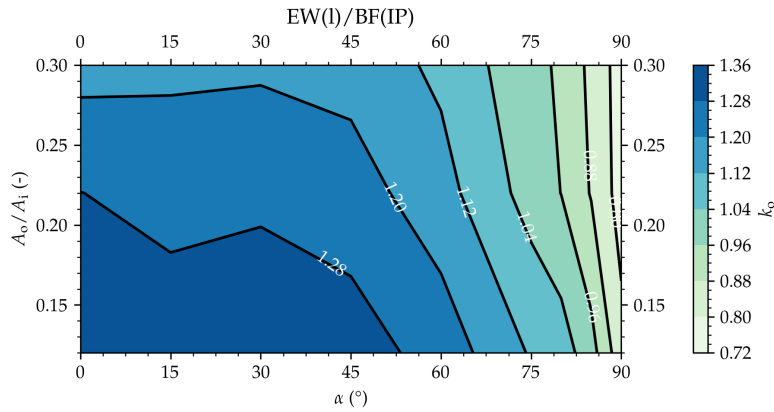
Figure 10.13: Capacity interaction function



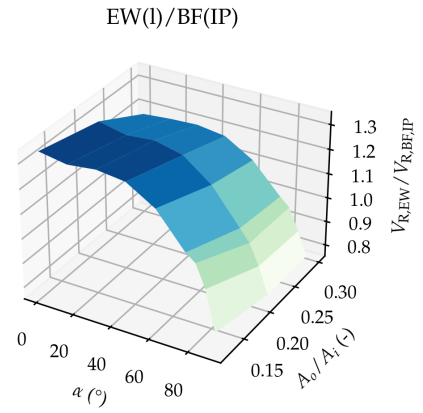
(g) ED(r) models topographic view



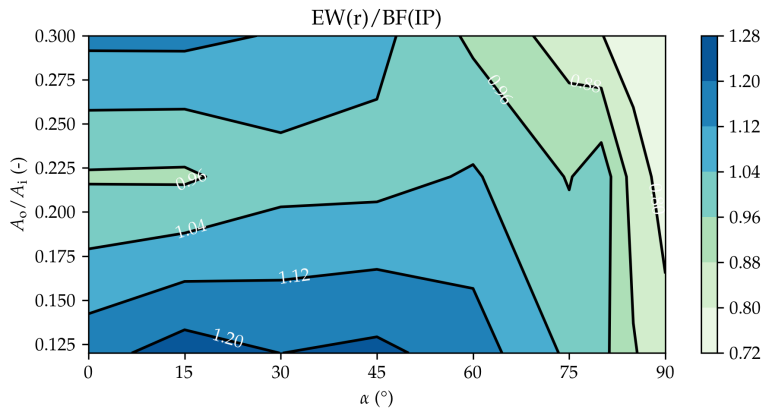
(h) ED(r) models 3D view



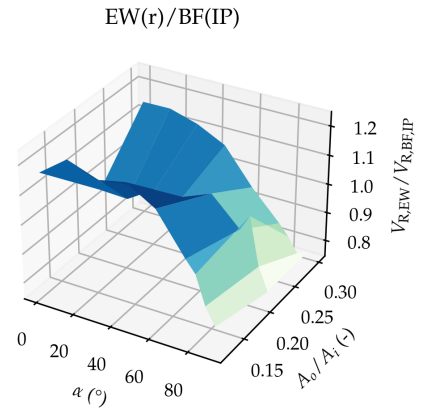
(i) EW(l) models topographic view



(j) EW(l) models 3D view



(k) EW(r) models topographic view



(l) EW(r) models 3D view

Abbreviations in figures captions	
l	left load direction
r	right load direction

Figure 10.13 (cont.): Capacity interaction function

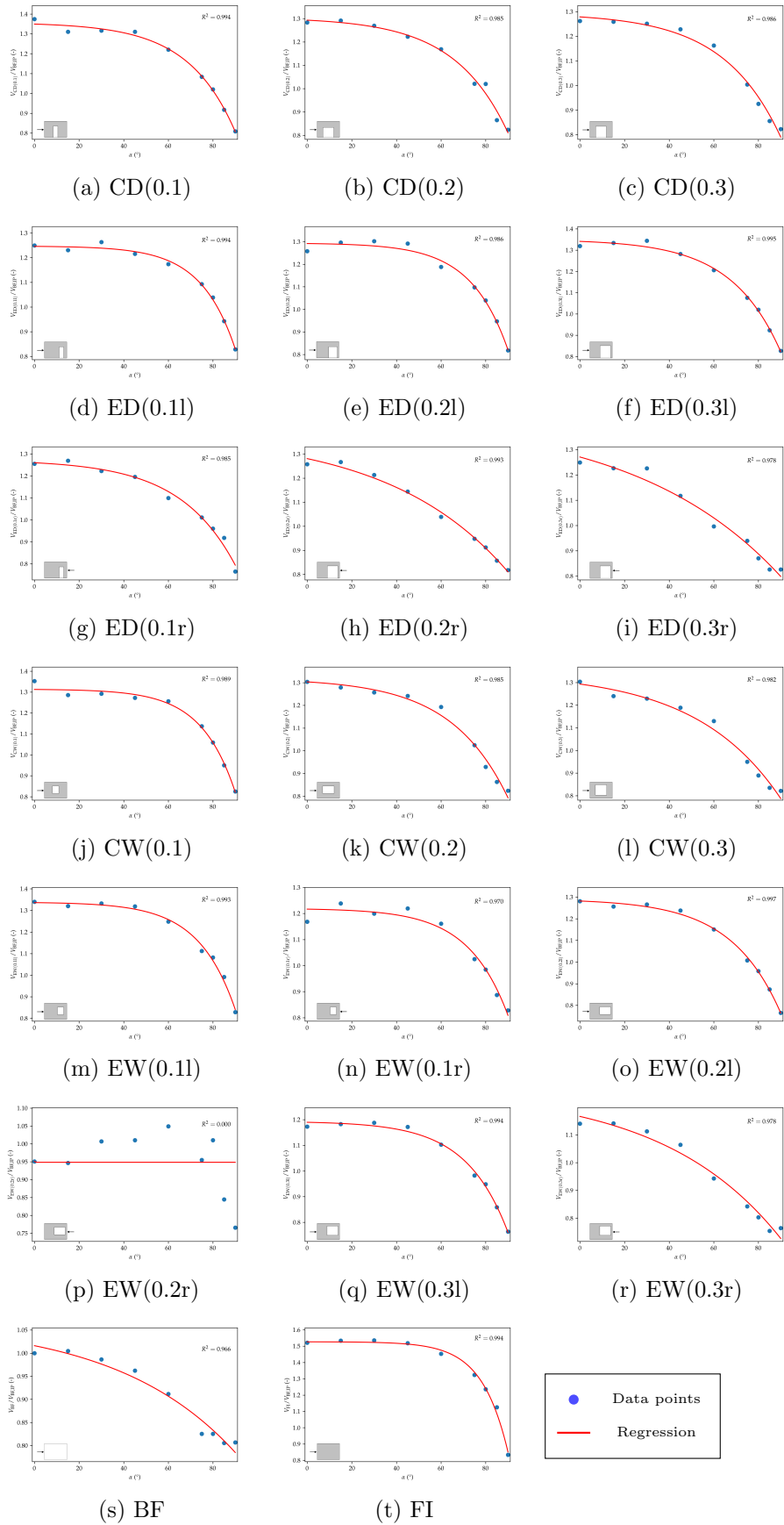


Figure 10.14: Regression results for depending variable α

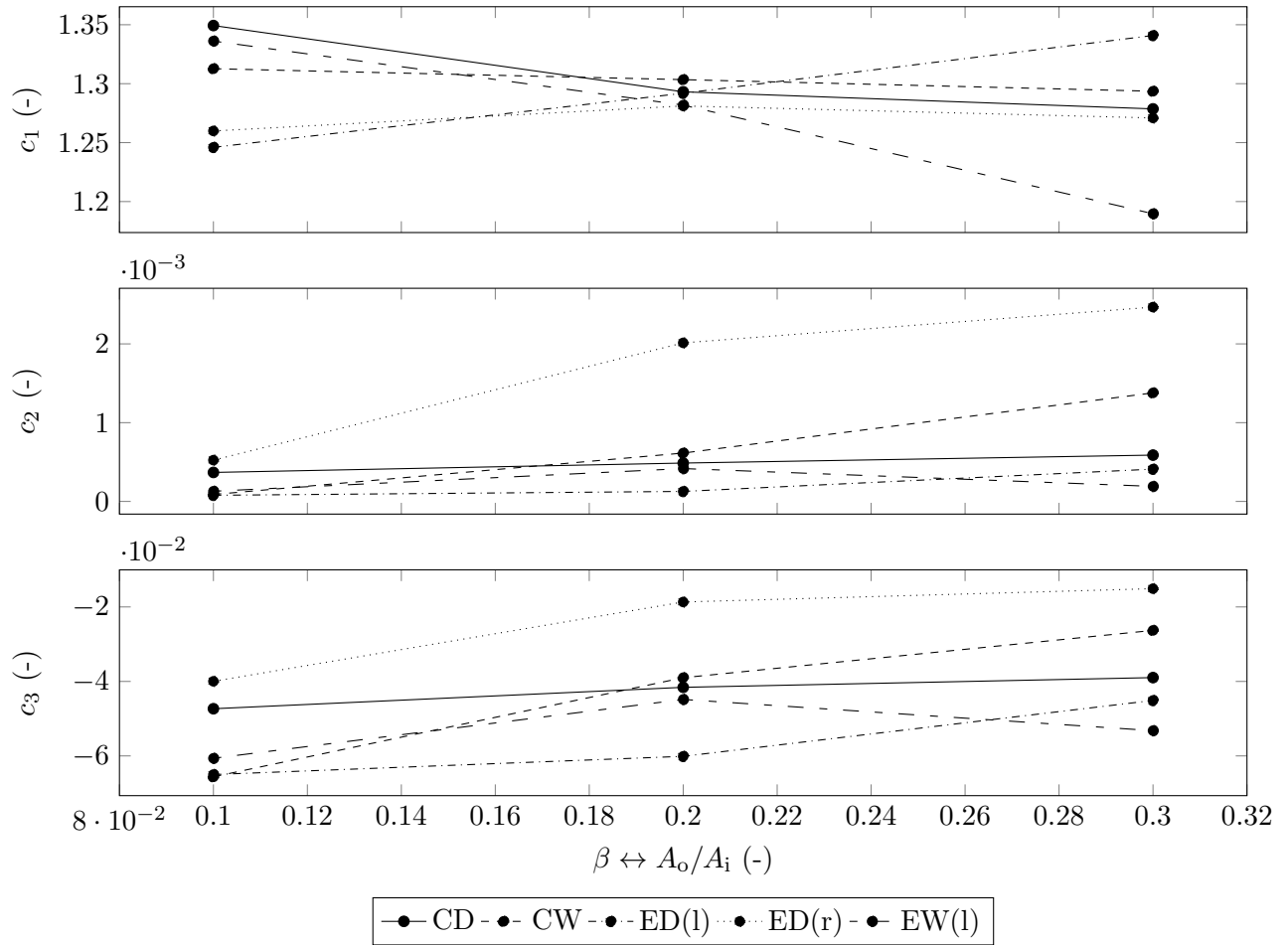
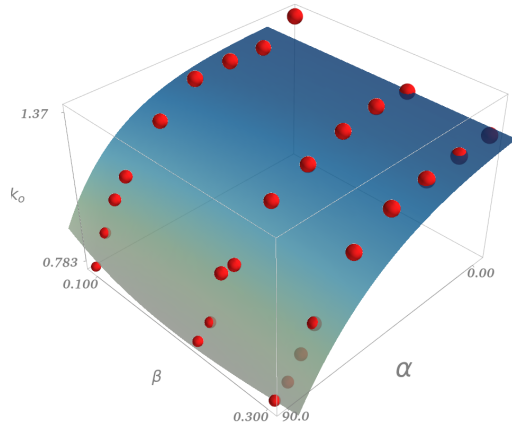
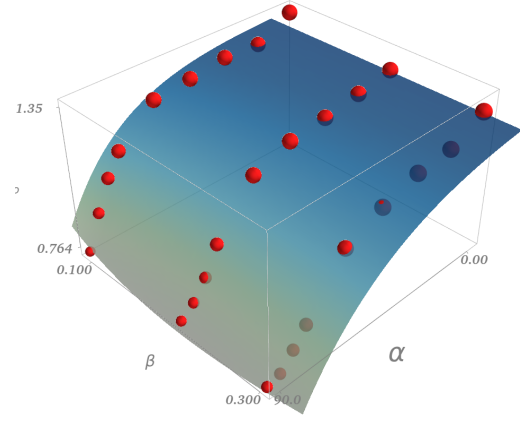


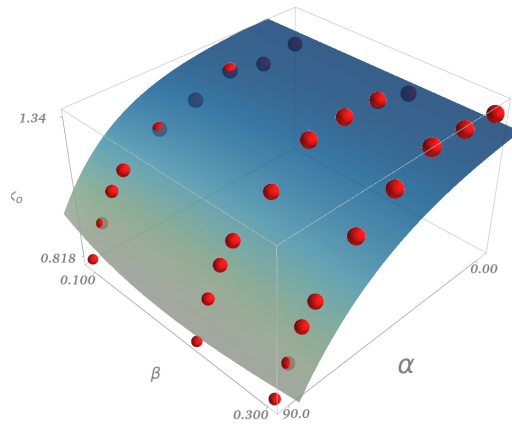
Figure 10.15: Constants obtained from optimizing $k(\alpha)$ functions



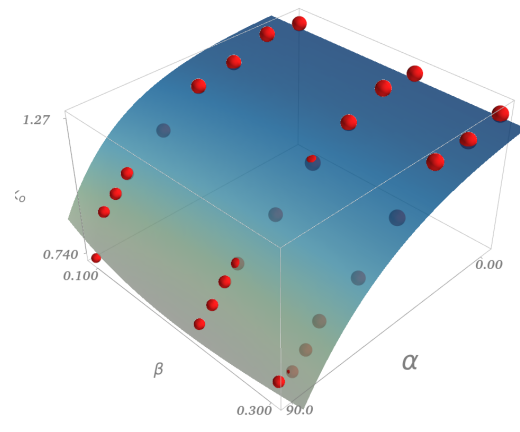
(a) CD



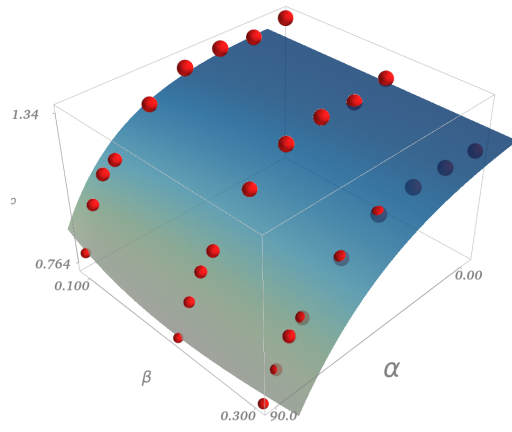
(b) CW



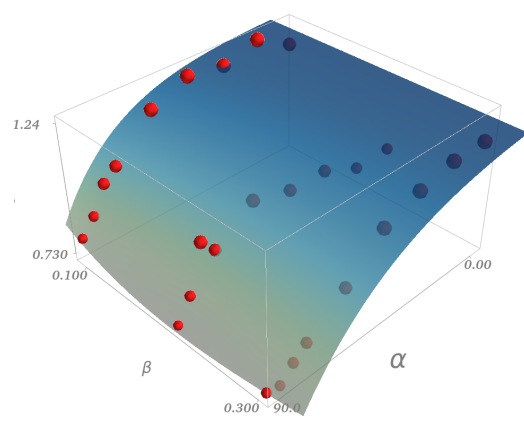
(c) ED(l)



(d) ED(r)



(e) EW(l)



(f) EW(r)

Figure 10.16: k_0 function (surface) vs. data from computational models

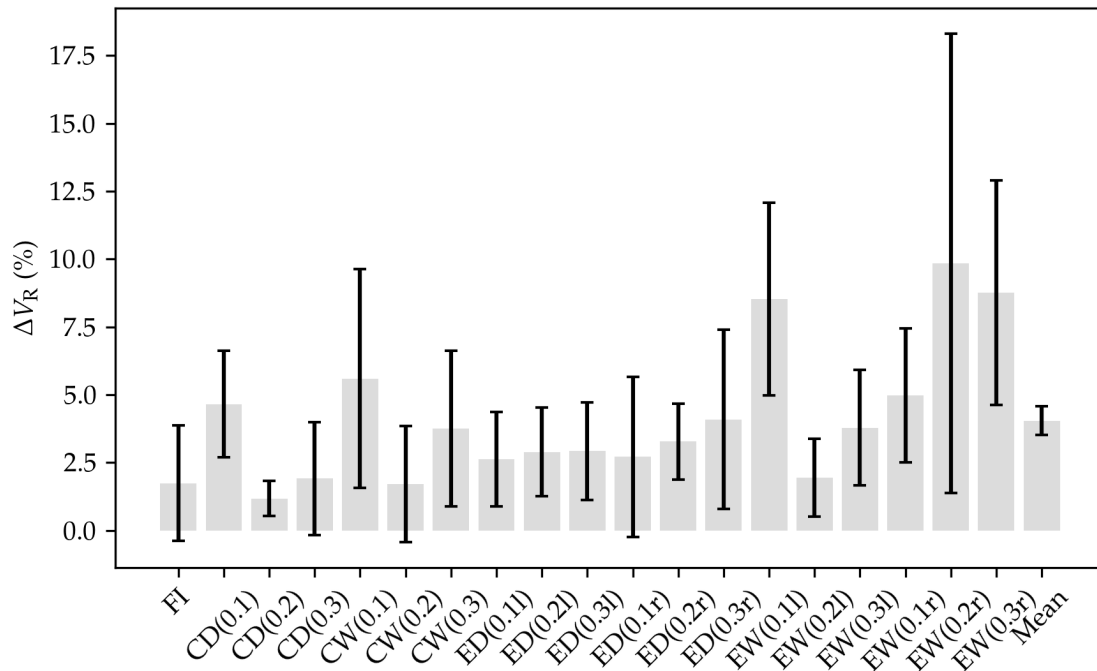


Figure 10.17: Differences between the computational and analytical model, where caps are \pm standard deviation of the error

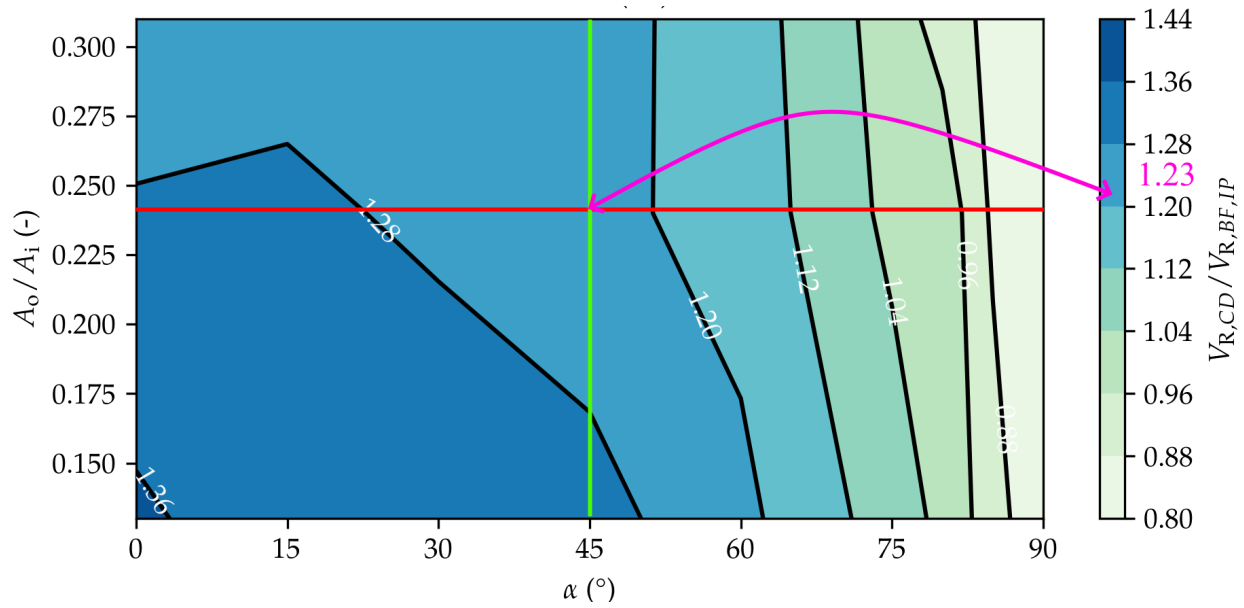


Figure 10.18: Determination of coefficient for the example

Chapter 11

Conclusions and summary of the computational studies

11.1 Micro-model development

To simulate experimental tests and expand the research to combined loadings, a non-linear finite element (FE) software *Atena Engineering 3D* (Cervenka Consulting s.r.o., 2015) was used to create 3D micromodels. The software provides means of non-linear analysis for concrete and RC structures, including concrete cracking, crushing and reinforcement yielding (Červenka et al, 2012).

The micromodels consisted of *solid* 3D elements that simulate concrete and masonry, 2D elements that simulate *interface* elements and 1D *truss* elements that simulate reinforcement (Fig. 8.2, 8.1).

Six FE computational models were made separately for IP and OoP cyclic, quasi-static simulations. The six models included a bare frame, infilled frame, infilled frames with centric and eccentric door and window openings (Tab. 3.4). The geometry and boundary conditions mirrored those of their experimental counterparts (Fig. 8.3).

Likewise, computational models were assembled to simulate pure OoP bending of masonry wall both with line load parallel and perpendicular to bedjoints (Fig. 8.4).

11.2 Micromodel calibration and sensitivity analysis

The 3D micromodel's material model properties were adopted from its 2D counterpart (Penava et al, 2016). Yet, the 3D model had a greater response when compared to the latter one and to the physical specimens. Hence, calibration and, with it, sensitivity analysis was undertaken. Firstly, the IP tests of a frame with masonry infill walls series were calibrated, then OoP bending of masonry walls and finally, the OoP test of frames with infill walls. The calibration protocol (Fig. 9.1) was initially carried out on the bare frame model, after which it was transferred on the fully infilled one. If there was a change in *concrete* material properties, the calibration reverts to bare frame model, while if it was on the *masonry*, to the fully infilled one. Also, if there was a change while calibrating in the OoP direction, the calibration process is then reverted again to *start* of the IP phase.

The initial, *i.e.* inherited properties from Penava et al (2016) produced a stronger response overall. This could be attributed to the confinement effect of the 3D rebar model. Hence, a calibration of certain parameters was needed. Note that only the purely computational, *i.e.* mathematical or calculated mechanical values were varied. So, those measured, *i.e.* obtained by the experiments were not varied. Some parameters had no effects, some modified model's behavior while few modified the computational stability (Fig. 9.2 & 9.3). In the end, only a few parameters were changed in

regards to the initial ones (Tab. 9.1). Those were: 1) Crack model of masonry infill units (from *fixed* to *rotated*); 2) Blocks tensile strength (from parallel to perpendicular to voids f_t 1.80 \rightarrow 0.38 MPa); 3) Concrete's direction of plastic flow, adjusted for crushing ($\beta = 0.0 \rightarrow -0.1$); 4) Block's reduction of compression strength due to cracks ($r_{c,lim} = 0.8 \rightarrow 0.4$); 5) Frame concrete's tensile strength ($f_t = 4.00 \rightarrow 3.35$ MPa); 6) Interface tension softening function (end value of softening displacement 0.10 \rightarrow 0.01). Most of the calibration and change in the parameters was done with ip-plane cyclic, quasi-quasi static test simulations (points from 1-4), and yielded good correlation with the physical specimens (Fig. 9.4 & 9.5, Tab. 9.2). After the models were calibrated in the IP direction, the calibration was shifted to the OoP bending test of masonry walls. This calibration was short as only two parameters were changed. The first was the tensile strength of the block from parallel to perpendicular to its voids, which prompted recalculation of fracture energy based on Equation (8.1). The newly found changes caused unstable computations. This was aided by shortening the tensional softening arm of the bedjoint model and reverting the fracture energy to its original value. The changes caused by the OoP masonry wall simulations had minimal effects on IP ones. Finally, the simulations provided satisfying correlation with the experiments in terms of load-bearing capacity (Fig. 9.8, 9.9, Tab. 9.3). Also, the micromodels were able to capture the influence of load-position (Fig. 9.6) and failure modes. The OoP drift driven test simulations were evaluated rather than calibrated, as calibration was nearly impossible in absolute terms based on a history of the frame's damages. Hence, the evaluation was set based on relative values and principles between the physical and computational models (Figs. 9.13c; 9.14 *vs.* 6.13; 9.15).

Overall, the calibrated models had a good correlation when compared with their physical counterparts in terms of performance, behaviour, initial stiffness, ductility, yielding points, damage states, load positions, *etc.* The calibration process scoped: a) RC frames with and without masonry infill walls and openings, positioned eccentrically and eccentrically; b) Cyclic, quasi-static IP and OoP inter-storey loads; c) OoP loads on masonry infill wall; c) Gravity loads on frames with infill walls.

The result analysis observed that the IP model was more sensitive to changes in concrete and interface material properties than masonry. This is best illustrated in the fact that IP behaviour was affected more by lowering concrete's tensile strength by 18 %, than the 80 % drop in masonry's. Similar was the case of plastic flow (Fig. 9.2a *vs.* 9.3a). On the other hand, changes of *cohesion* in interface material model had greater change (Fig. 9.3b)

11.3 Simultaneous IP and OoP load on models with and without infill wall and various openings

In order to fill the gap in the field of study, *i.e.* to answer the question as to how opening size, location and load combination influence overall structural response, further computational studies were deployed.

Based on the research of Penava et al (2018), it was found that the infill wall with openings had no effects when their ratios were $A_o/A_i > 0.30$. Likewise, EN1996-1 provision (BSI, 2004b) states that with the ratio of $A_o/A_i < 0.10$ openings can be omitted. Hence, the $0.1 \leq A_o/A_i \leq 0.30$ The openings' dimensions were selected based on architectural recommendations (Fig. 10.2) and to satisfy the end limits and their mean. Therefore, the ratios of $A_o/A_i \in \{0.1, 0.2, 0.3\}$ were used. For that purpose, 12 models were developed (Fig. 10.3) with various window and door openings sizes and positions (Tab. 10.1).

On those models, an IP and OoP pushover load protocol was used. The load was implemented through prescribed deformation with angles of $\alpha \in 0, 15, 30, 45, 60, 75, 80, 85, 90$ ($^\circ$) that encloses IP

and OoP load. Note that the gravity load was also included. Models had good computational stability, except for eccentric window model with $A_o/A_i = 0.2$ and right load direction for $\alpha < 45$. The reason behind the computational instability was unknown.

By analysing the resultant load-bearing capacity (Eq. 10.2, Fig. 10.7) the following key outcomes were observed: a) The greatest load-bearing capacity across all models was observed with pure IP load $\alpha = 0$. It progressively dropped by increasing α ; b) Significantly higher capacity drop rate was observed when $\alpha > 45$ (Fig. 10.14), this was explained by shifting from *frame* to *sliding, fixed-fixed column* mechanical system, while also, the IP diagonal strut loses its effectiveness due to tension from rising OoP load; c) All models dropped to the bare frame's OoP load-bearing capacity when $\alpha = 90$; d) Load-bearing capacities of models with openings were enclosed between fully infilled and bare frame; e) The opening size affected the load-bearing capacity. The relation was linear.

The critical displacements at $V_{R,max}$, for models with openings were positioned between the FI and BF model. Namely, models with infill walls increase the value of critical displacements along with α , while the BF model had a drop after $\alpha \geq 45$. The models with infill walls had lower displacement when $\alpha \leq 45$ and greater after when compared with BF model. This was contributed to the stiff infill wall that limited the displacements in IP dominated and provided more stability when OoP dominated.

A new mechanism of resisting shear forces with simultaneous IP and OoP load was found (Fig. 10.12). Pure IP load is resisted by its diagonal strut, which is effective across infill walls length. A similar strut was found for pure OoP load, where it connects opposite corners along the width of the wall. This was also observed in dynamical research by Tu et al (2010) (Fig. 2.10c). In addition to the OoP strut, a bracing mechanism occurs on the compressive face of the infill wall. In between the pure IP and OoP loads, all the aforementioned mechanisms are active, and they interact. For instance, compressive stress at infill wall corners and compression side add up, while the tension face of the infill wall due to OoP bending unloads the IP compressive strut. Such mechanism results in asymmetric damages and stress distributions (Fig. 5–8). Also, the nature of tension and shear stress within the bedjoints can speed up the bedjoint–sliding failure.

By obtaining load-bearing capacities for each model, and sorting them by opening type, size, position, and IP load direction, the $A_o/A_i - \alpha$ interdependence was found. They were displayed as capacity - interaction curves (Fig. 10.13). Those curves and surfaces displayed the same characteristics described in the previous paragraph. Based on those curves, functions for estimating load-bearing capacity under angle α was found for frames with infill walls and openings in Equation (10.10) (with the use of Tab. 10.3) and without openings in Equation (10.11). The method of estimating load-bearing capacity in relation to α and A_o/A_i is to firstly obtain the load-bearing capacity of bare-frame loaded in IP direction; either by calculation, computational simulation or experiment, then multiplying it in accordance with the equations mentioned above based on given α and A_o/A_i . The estimations had good matching with the models (Figs. 10.17, 10.16, and Tab. 10.4). The process of determining the aforementioned load-bearing capacity is presented in Section 10.3.5.

Part IV

Concluding remarks

Chapter 12

Summary and conclusions

12.1 Summary

During an earthquake event, multi-storey buildings are generally loaded by inter-storey drift and inertial forces. The seismic event excites the structure in an arbitrary direction. When observing the structure's plane, the load can be divided onto the IP and OoP forces. The IP forces are by their nature inter-storey drift ones, while the OoP forces are both inter-storey drift and inertial.

By examination of literature, it was determined that most of experiments in the OoP field were conducted with inertial, less with dynamical and only two using inter-storey drift methods. From the data gathered, it was observed that the static and quasi-static inter-storey drift force methods have more similarities with dynamical test than the inertial methods. This is most certainly due to the fact that the dynamical tests were done on single storey buildings. Hence, magnifying the inter-storey drift effect more so than inertial. Alongside limited OoP inter-storey drift studies, none of which were done with RC frames, the field had few and conflicting studies with openings. The research laid in this thesis answers just that; influence of infill walls with and without openings on RC frames subjected to drift driven OoP and IP loads.

The research was built upon an existing IP cyclic, quasi-static study (Penava, 2012). The addition included experimental OoP cyclic, quasi-static load on frames with and without infill walls and openings, along with OoP bending test of masonry walls. Same materials, frames and tools were used for all three experiments. Overall, 12 frames with and without masonry infill walls and door or window opening positioned centrally or eccentrically were tested in IP and OoP direction (6 each). The OoP bending tests of masonry walls included 20 specimens, 10 for each load position (parallel or perpendicular to bedjoints).

After the experiments were conducted, computational models were developed and calibrated against them. The calibration yielded the factors that govern the simulated behavior of the models. Afterwards, the research was extrapolated to combine both IP and OoP loads in a simultaneous action. The combination was described by angle of the resultant force α . The simulations tests 20 configurations from bare frame, infill wall with or without openings with opening area ratios ranging approximately 0.1, 0.2 and 0.3 in relation to infill's area, positioned centrally or eccentrically, loaded from left or right under 9 angle positions (from IP to OoP). That adds up to 180 models, from which interaction curves were derived, as well as equations for estimating load-bearing capacity based on that of an IP's bare frame.

12.2 Conclusions

As showed here and in multiple other works, the IP loads show that infill wall contributes substantially to the overall behaviour, even if the infill wall contains openings up to the area ratio of $A_i/A_o \leq 0.30$. Yet, if the OoP drift forces were introduced to the frame, infill walls practically have no influence on to the overall behavior of the frames with infill walls. This is in line with other dynamical and drift-driven studies. Contrariwise, if the OoP inertial forces were introduced the outcome is polar opposite to the drift-driven loads. Namely, in those cases, the infill wall is damaged whereas the frame only provides boundary conditions.

Based on the experimental data, computational 3D models were developed and calibrated. The micromodels showed great sensitivity to certain parameters. It goes without saying that bare frame models were governed by the properties of the concrete material. The behaviour of frames including infill walls with and without openings during the IP simulations were mostly governed by the interface (gap) material model properties. Whereas, the OoP masonry wall bend tests were governed by both masonry and interface material model. More precisely their tensional properties.

With the OoP inter-storey drift forces, it was found that the frame and infill wall interaction is one sided. That is, the infill wall does not influence the frame, while the frame does influence the infill wall. The damage to the infill walls were attained by deflection transmission from the frame. The damage to the infill wall were a result of bedjoint opening, *i.e.* reaching its bond strength, while on the other side, crushing by compression. The infill walls resistance mechanism was found. Namely, a diagonal strut form connecting opposite corners along the width of the infill wall. This was also observed in dynamical tests. In addition, it was found that there is additional bracing from compressive stress on the face of the wall. Those stresses stabilize the infill wall; yet, due to their short length not enough to influence the behavior of the frame.

From strict IP to OoP loads, the damages, and stresses on the frame increase incrementally in their size and area. This is due to the effectiveness of infill wall to strip the frame from stress, by changing the bending moment from one axis to another.

When both IP and OoP inter-storey drift forces were simultaneously introduced via tangent of prescribed deformations α , the load-bearing capacity dropped exponentially as α reached OoP load (90°). This was most certainly due to shift from *frame* dominated to *sliding, fixed-fixed column* dominated mechanical system. Additionally, the effectiveness of IP diagonal strut diminishes due to tensional stress on one face of the wall. On the other side, the compressive stresses added up, yet not enough to make up for the loss of unloading the other side.

Based on the data gathered, opening to infill wall area ratio and the angle of resultant force interaction curves were derived. Also, equations were developed for estimating load-bearing capacity of frames with the infill walls and openings. Both interaction curves and equations outputs are a coefficient that is then multiplied by the IP, load-bearing capacity of a bare frame to estimate the capacity of frame including infill wall with and without openings. The equation estimation provided good correlation with the data

Chapter 13

Recommendations and future work

13.1 Recommendations

Based on the research laid here, the following recommendations were defined:

- (a) **Frame with infill wall design** seems to be a more complex matter than initially perceived. On one hand, infill wall and frame interact together rendering its IP overall behaviour and failure modes. This holds true even with openings if they satisfy $A_o/A_i < 0.3$. Yet when it comes to the OoP loads, it is not so clear. For example, with inertial loads, the infill wall is engaged while the frame is intact and only provides boundary conditions. The inter-storey drift loads, shows the exact opposite, *i.e.* small damages to the infill wall and huge on the frame. The current European anti-seismic design codes (BSI, 2005) laid suitable rules and approaches for designing RC frames. Those rules, disregard the influence of infill wall, which is consistent with the worked laid here and in the literature within the pure OoP – inter-storey drift or dynamical load tests. Furthermore, if an engineer wants to estimate load-capacity of a frame subjected to inter-storey drift forces in systems with infill wall and openings based on the load angle, follow the Equations (10.11, 10.10) provided in this thesis as described in (b) point here or Section 10.3.5. Yet, if one is interested in determining the inertial load-bearing capacity of infill walls, one should use Equation (2.13), that showed the best fitting with data overall. As for inclusion of openings with inertial loads, the research is scarce and there is only Equation (2.20) from Mays et al (1998) that was developed on the FEM analysis of RC walls, and did not show good alignment with the experiments. Furthermore, if one is interested in calculating combined IP and inertial OoP load capacity, non of the equations showed good correlation beyond their experimental data. That being said, the recommended one would be that of Angel et al (1994) (Eq. 2.5) based on the sheer number of their experimental data.
- (b) **Determining load-bearing capacity** of RC frames with infill walls, with and without openings based on the angle of loading, opening type, position and size. There are two approaches, either by using interaction curves in Figure 10.13 or calculating by hand using Equations (10.11, 10.10) and Table 9.3. Either way, firstly the load-bearing capacity of IP loaded bare RC frame should be determined (*e.g.* calculation, FEM model, experiment). Then by using the appropriate interaction curve or equation it should be multiplied by its output value. Both methods are illuminated on a working example in Section 10.3.5.
- (c) **Structural detailing** should be in line with those stated in EN 1998-1 provisions, *e.g.* - providing more shear reinforcement in critical regions for local ductility; -strong column, weak beam principal; structural regularities; *etc.* In addition, infill wall's boundary conditions

should be taken with special care. Namely, most often the gap between infill wall and upper beam is hard to fill; therefore it is often partially filled or even unfilled. Nevertheless, an effort should be committed as so the gap is fully filled. Workers often come up with alternative solutions, *e.g.* filling it with polyurethane foams or some other, more workable glues or likewise materials. There is no research that observed different kinds of gap fillings; yet, if the glue has equal or greater mechanical characteristics than that of the mortar, it can be considered as a valid alternative. Also between themselves, the masonry units should be covered by mortar on all sides, in order to obtain the beneficial *interlocking effect*. Furthermore, as observed from the field studies after the Albanian earthquake, all the masonry units should be bounded with mortar by all sides in regard with adequate thickness. Also, it was found that RC elevator shafts served as a shear core and had better performance than those with masonry shafts.

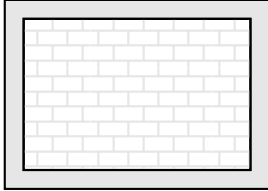
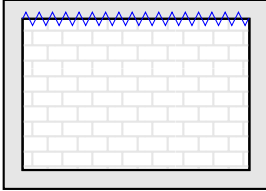
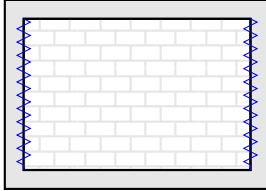
- (d) **Structural retrofitting** of frames with infill walls should be taken with caution. Within the laboratory conditions, by using static and quasi-static loads, the infill wall's falling/walking out of the frame was hardly observed. That is in opposition with the real-earthquake scenarios and some dynamical tests. Since, the dynamical tests were subjected to laboratory conditions, such scenes were presumed as a result of (or lack of) infill wall's boundary conditions. As research showed here, that is also in line with the EN1998-1 regulations of omitting the influence of the infill wall, the eventual loss of it should not jeopardize the frames resistance due to its redundancy. Yet, the prevention of infill walls falling out should be considered in order to minimize the possibility of damaging life, health, property, and changing the structures stiffness that may magnify the $P - \Delta$ effects. The structural preventions of OoP collapse were in a nutshell done by covering the infill wall with some kind of mesh and connecting it with the frame. By doing so, infill wall has a prolonged *bending* period that bypasses or limits the arching-action until the very end. This kind of approach goes in hand with the IP retrofitting approaches that try to connect the frame and infill wall in a single unit. Yet, this is in direct contrast with approaches that try to separate the behaviour of infill wall from the frame. In line with the data available, pointing that any loss in infill wall's boundary conditions results in reduced resistance and limited, yet beneficial arching-action. Hence, such kind of approaches of retrofitting are not advices unless they are validated against OoP or combined IP and OoP loads.
- (e) **Terminology** within the OoP field of study is not unified and sometimes misleading. Usual terminology for crack patterns is *yield lines*. The term is wrong in the sense that the masonry cannot *yield*. This was probably a leftover transferred from plate theory where the forming yielding lines are analogous to those of the infill wall, yet they do yield. A more precise term should be *hinge lines*, as the infill wall rotates about those lines. Furthermore, the *one-way* arching action is used when there is a gap between the upper beam and the infill wall. Yet, infill wall does arch in both ways, with only single hinge missing in horizontal direction. The only, truly single directional, *i.e.* one-way arching action is when there are two parallel gaps. Therefore, from the literature a more appropriate terminology was gathered and displayed in Table 13.1.

13.2 Future work

Within this thesis, a few gaps in the literature were unveiled, and some questions and limits were raised that could refine the work described here. These are highlighted in the following points:

1. Literature review showed that most of the experiments were done with inertial, followed by

Table 13.1: Recommended terminology

		
Fully connected Two-way arching Rigid arching action	Partly connected	
	Semi-two-way arching Single-gap or gapped arching action	One-way arching Double-gap arching action

dynamic, and only two with inter-storey drift loads. The behaviour of frames with infill walls under inertial or drift loads are polar opposite. One damages the infill while preserving the frame and vice versa. The dynamical experiments showed more similarities with the drift load; however, those experiments are single-storey. Hence, inertial forces are not as magnified as those in higher storeys. Therefore, an experimental or/and computational study that includes both inertial and inter-storey drift forces should be initiated. Another question arises here if the static or quasi-static approaches should be used, as to how should one load the specimen as the inertial load changes direction multiple times while the frame bends once? The answer should be obtained from experimental studies, as those presented in Figure 2.26a. Also, an asymmetric inter-storey drift load should be examined. The asymmetry would be an addition of inter-storey drift with torsional forces;

2. The arching-action was an unknown effect in the OoP, drift-driven loads until the research presented here. It was discovered that a short-span diagonal strut forms with the addition of gravity load. That strut is the same as those observed in the dynamical tests (Fig. 2.10c). Due to its geometry, it can only increase the load-bearing capacity up to $\approx 5\%$. This could presumably be magnified by changing the boundary conditions, *i.e.* by adding gravity load to the upper beam and/or adding the part of the slab to the model that would act as a rotational spring. The gravity load on the beam would add load to the infill wall that would increase the pre-existing compressive stress from the arching action. The rotational spring from the slab would limit the rotation of the upper beam. Therefore, the beam and infill wall would rotate differently, resulting in the beam crushing the infill wall more than the other. Hence, it would render the arching-action more or less effective;
3. Along with the remark of the previous point of adding slabs boundary condition, the effects of orthogonal walls should also be considered. It is expected that it would not directly influence the arching-action effect; instead, the overall behaviour of the drift-driven OoP tests.
4. The openings do influence the behaviour of the frames with infill walls. Aside from a single variation of opening position, more insight into it and the effects of opening aspect ratios should be determined.
5. Following all the above points, they should be included as independent variables when calculating the coefficient k (Eqs. 10.11, 10.10). By doing so, the analytical model would be

complete and refined for more effects, not only the angle of load or the openings size and its two positions.

6. The gap between the upper beam and infill wall is hard to fill with regular mortar. Hence, it is often filled with alternative methods, such as polyurethane foam or more workable glues or similar materials. Their performance should be investigated. Furthermore, boundary conditions around the masonry units should be investigated, *e.g.* the difference between the fully bounded unit and those with head- or bedjoints unfilled.

Part V
Appendix

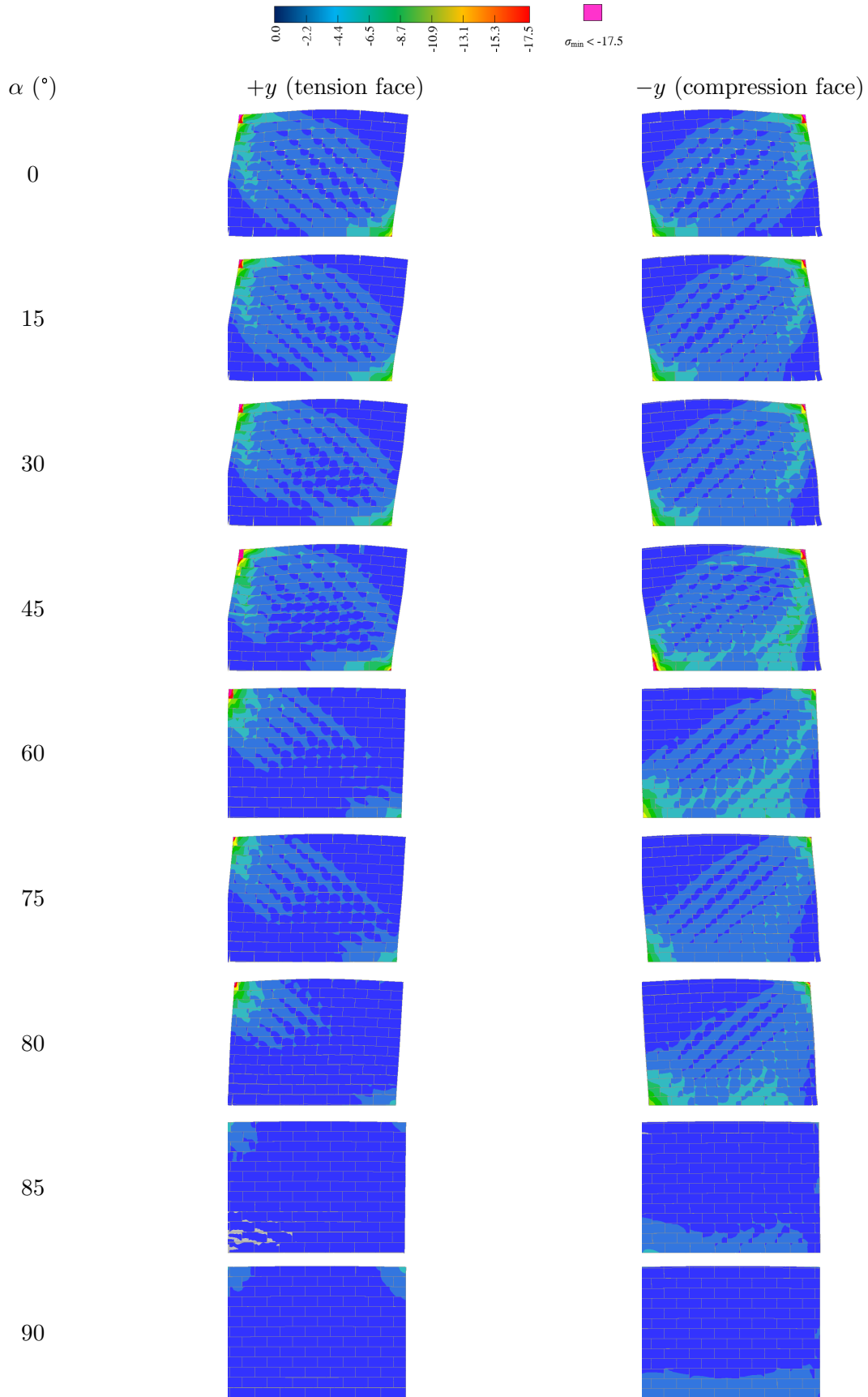


Figure 1: FI model's minimal principal stress @ $\approx V_{R,\max}/2$ on infill wall

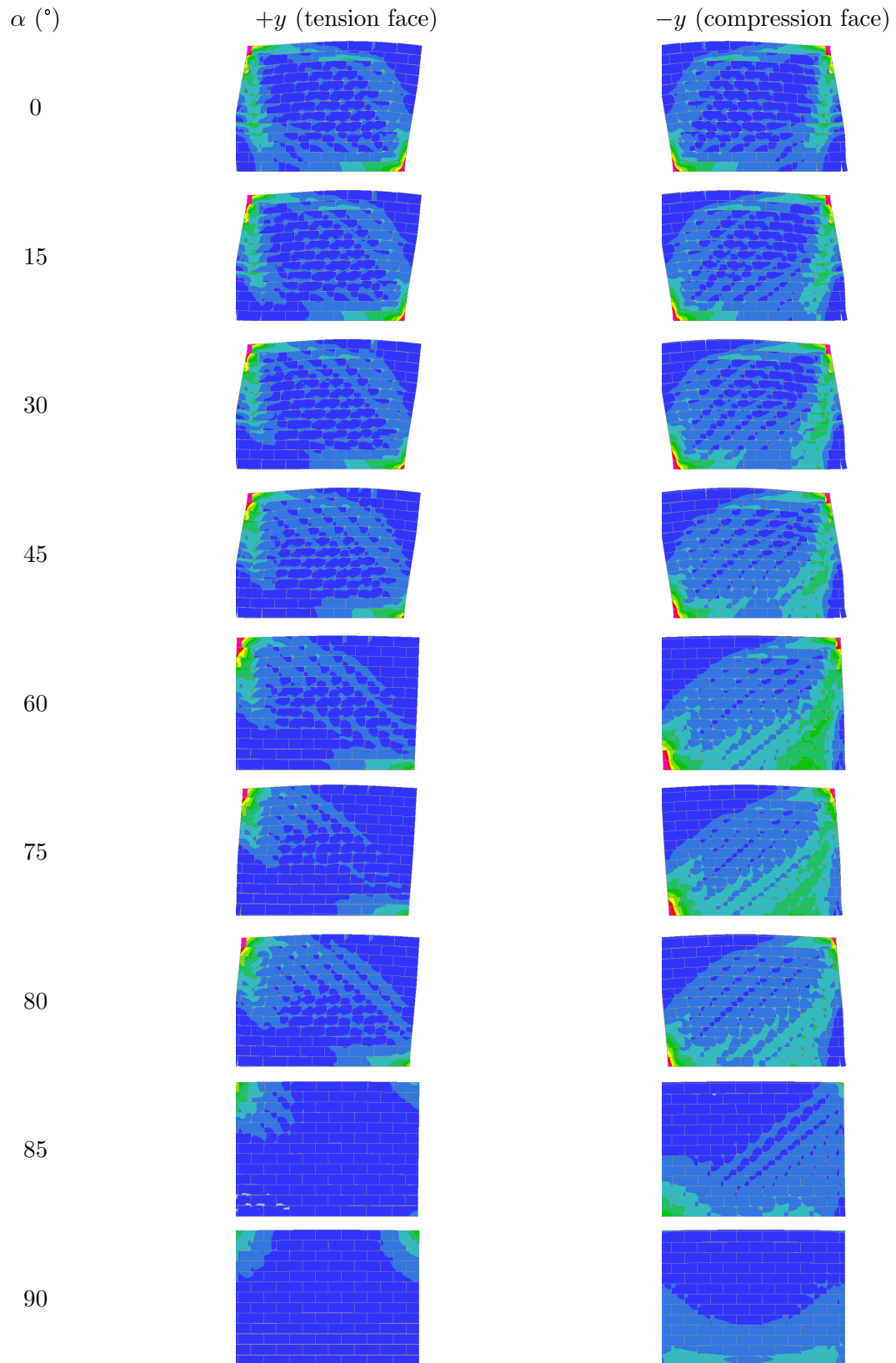


Figure 2: FI model minimal principal stress @ $\approx V_R$ on infill wall (legend same as in Fig. 1)

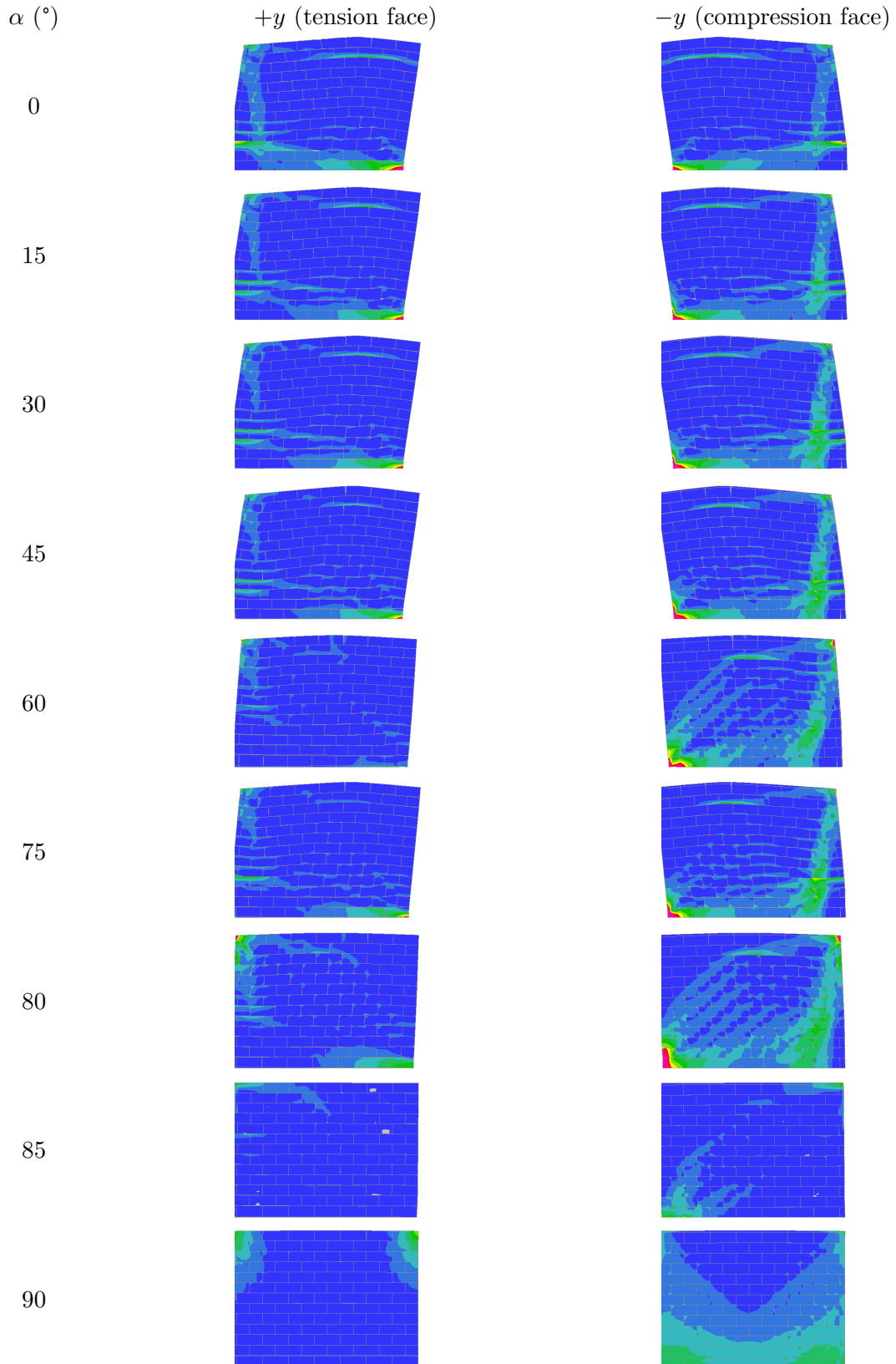


Figure 3: FI model minimal principal stress @ $> V_R/2$ on infill wall (legend same as in Fig. ??)

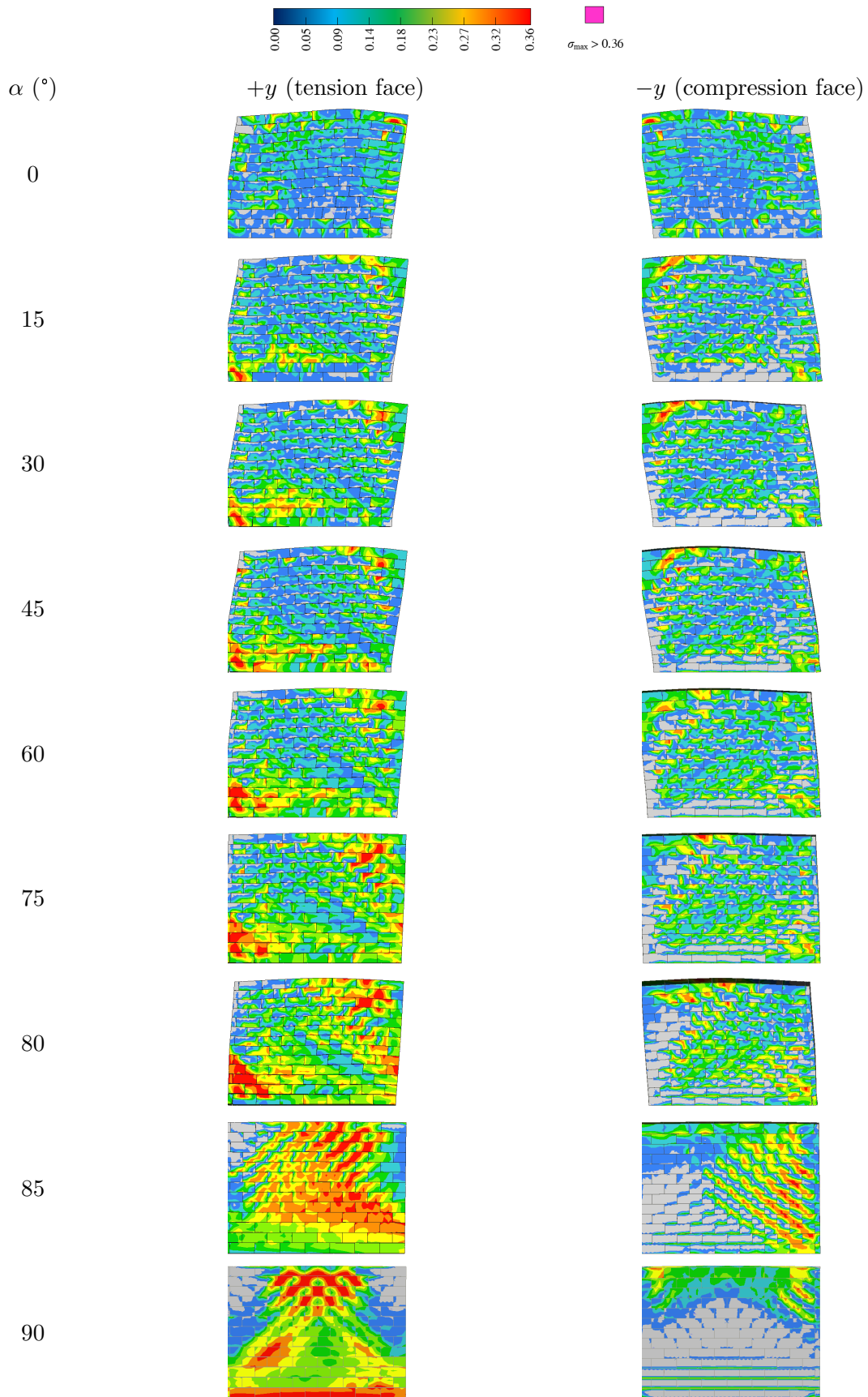


Figure 4: Maximal principal stress of FI model's infill wall

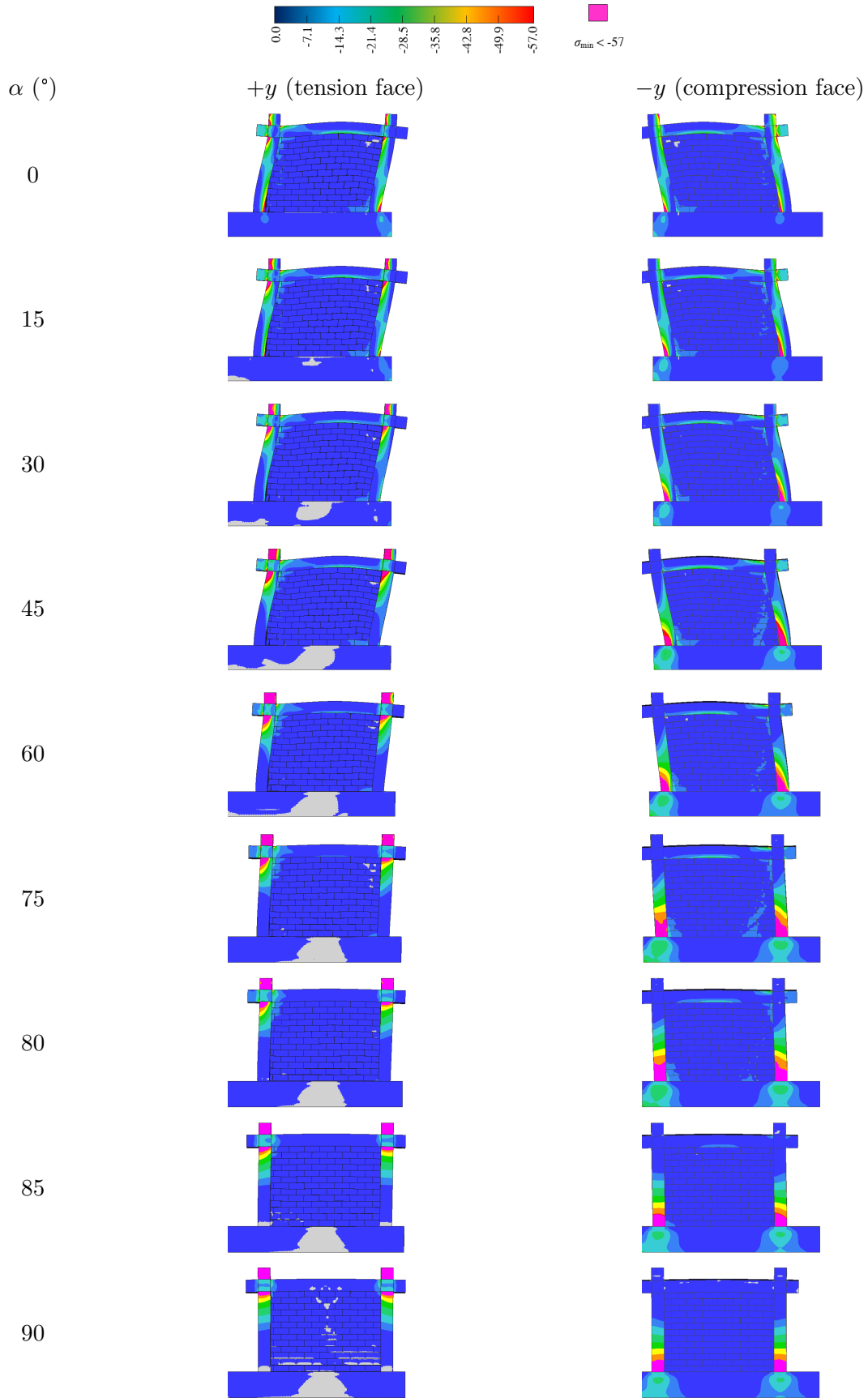


Figure 5: Minimal normal stress of FI model's frame

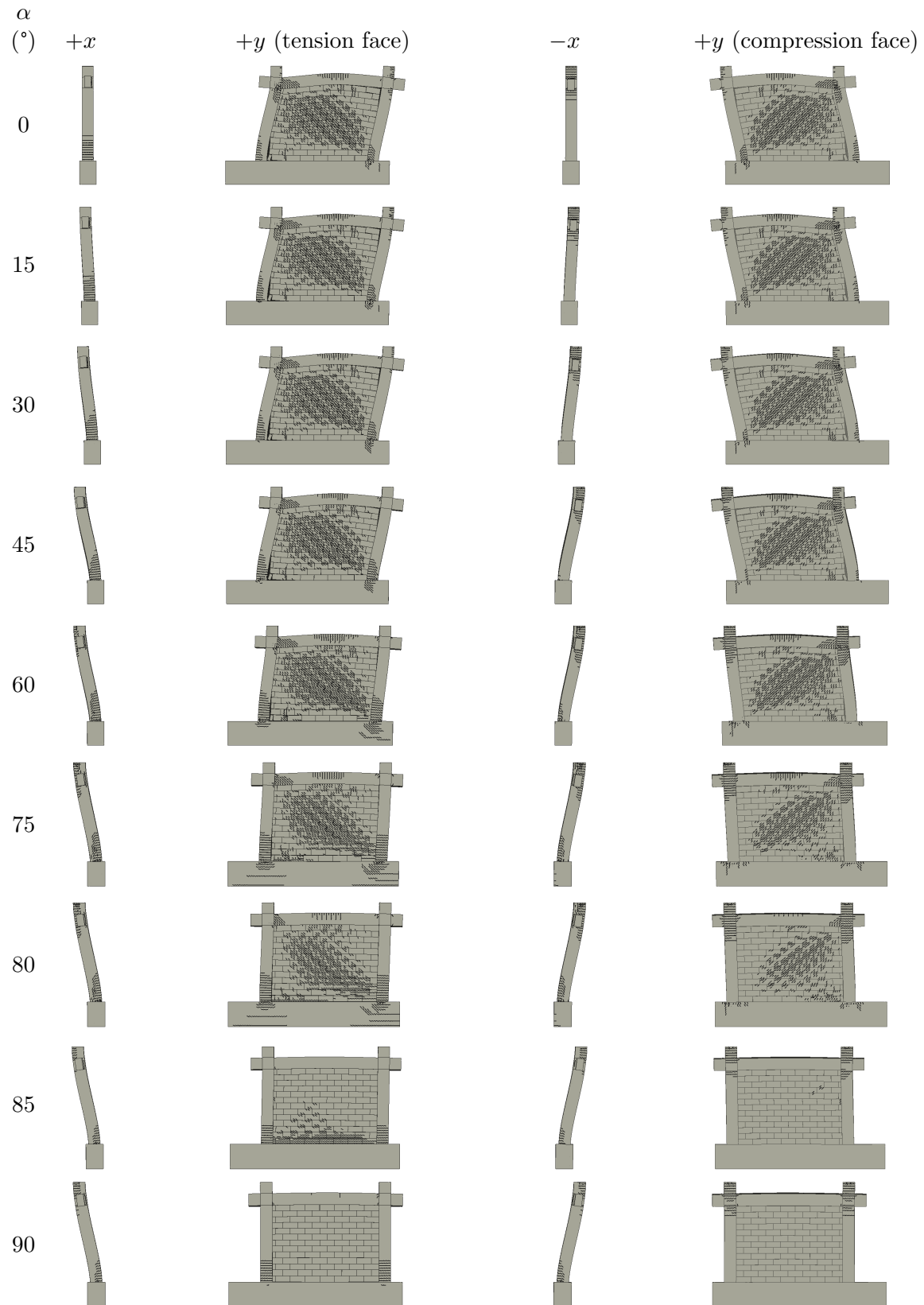


Figure 6: Crack patterns of infill wall @ $\approx V_{R,max}/2$

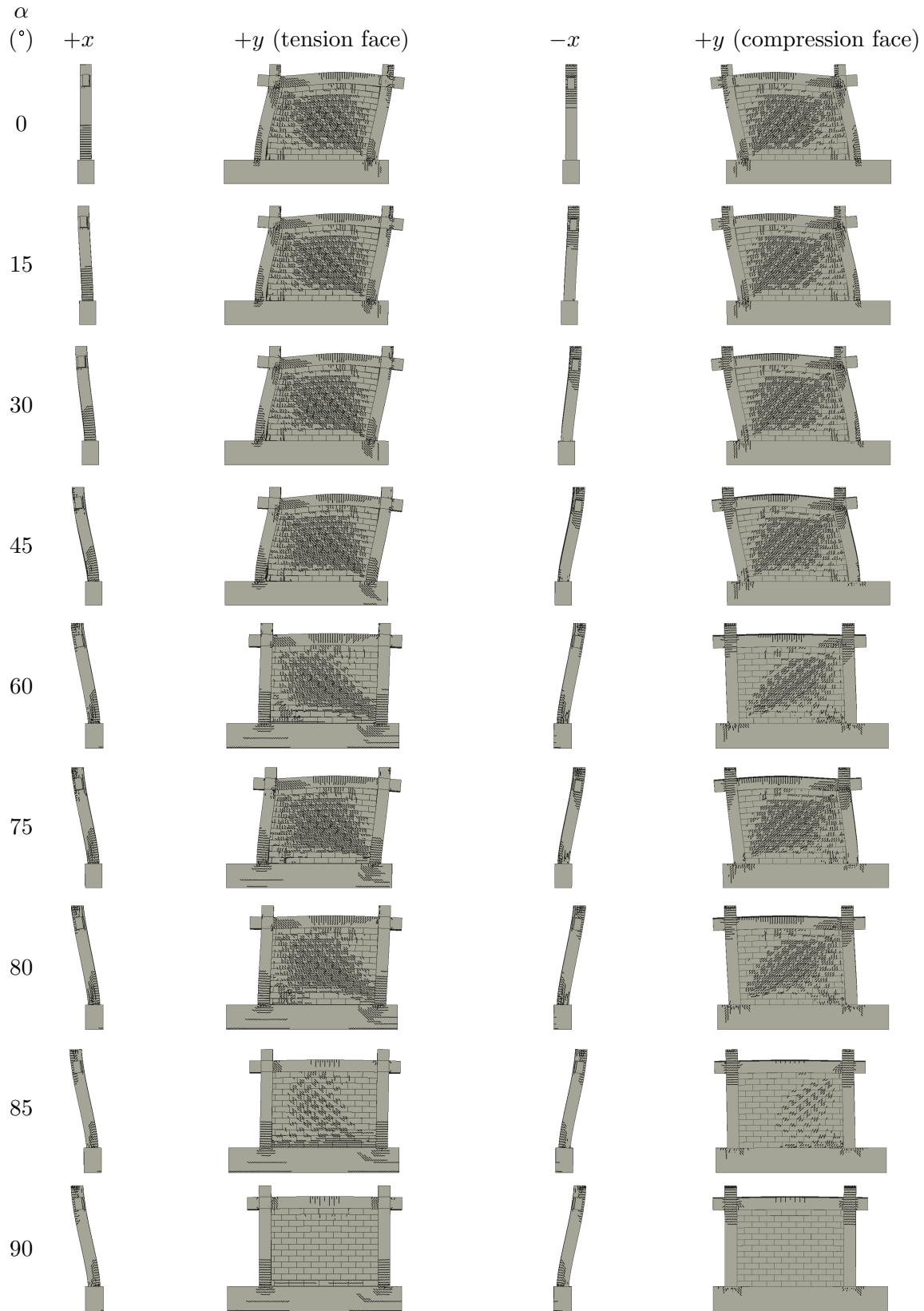


Figure 7: Crack patterns of infill wall @ $\approx V_{R,max}$

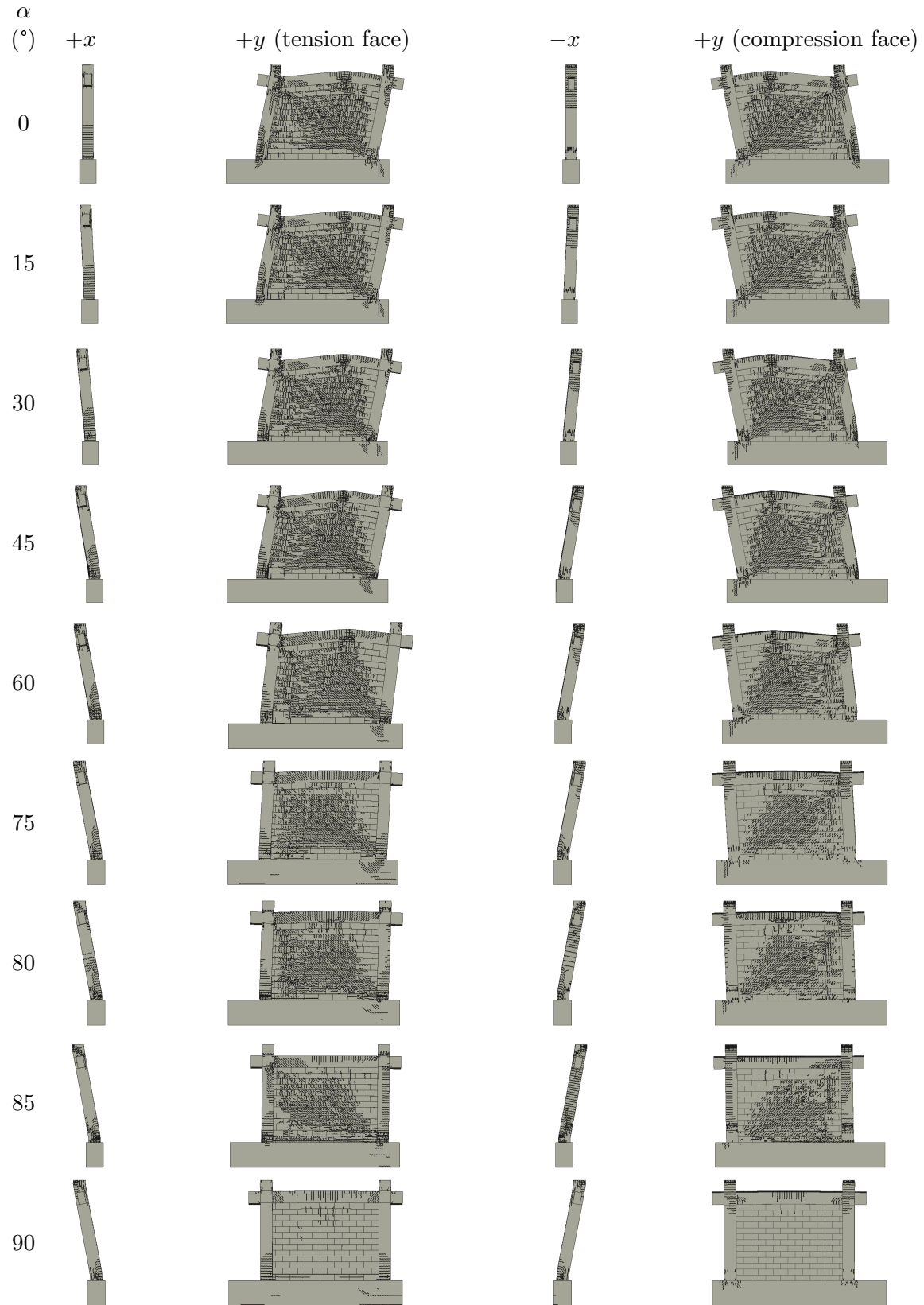


Figure 8: Crack patterns of infill wall @ $V_R > V_{R,max}$

Bibliography

- Abrams DP, Angel R, Uzarski J (1996) Out-of-plane strength of unreinforced masonry infill panels. *Earthquake Spectra* 12(4):825–844
- ACI (2011) Building code requirements for reinforced concrete. American Concrete Institute Structural Journal DOI 30CFR250.901(d)(1)
- Akhoundi F, Vasconcelos G, Lourenço PB, Palha CAO, Martins A (2015) Out-of-plane behavior of masonry infill walls. In: 7th International Conference on Seismology & Earthquake Engineering
- Akhoundi F, Vasconcelos G, Lourenço PB, Silva L (2016) Out-of-plane response of masonry infilled rc frames: Effect of workmanship and opening. In: 16th International Brick and Block Masonry Conference "Masonry in a world of challenges", Taylor & Francis, pp 1147–1154
- Akhoundi F, Vasconcelos G, Lourenço P (2020) Experimental out-of-plane behavior of brick masonry infilled frames. *International Journal of Architectural Heritage* 14(2):221–237
- Al Hanoun MH, Abrahamczyk L, Schwarz J (2019) Macromodeling of in-and out-of-plane behavior of unreinforced masonry infill walls. *Bulletin of earthquake engineering* 17(1):519–535
- Anderson C, Bright N (1976) Behavior of non-loadbearing block walls under windloading. *Concrete* 10(9):27–30
- Angel R, Abrams DP, Shapiro D, Uzarski J, Webster M (1994) Behavior of reinforced concrete frames with masonry infills. Tech. rep., University of Illinois Engineering Experiment Station. College of Engineering. University of Illinois at Urbana-Champaign.
- Anić F, Penava D, Abrahamczyk L, Sarhosis V (2019a) Computational evaluation of experimental methodologies of out-of-plane behavior of framed-walls with openings. *Earthquakes and Structures* 16(3):265
- Anić F, Penava D, Abrahamczyk L, Sarhosis V (2019b) A review of experimental and analytical studies on the out-of-plane behaviour of masonry infilled frames. *Bulletin of Earthquake Engineering* pp 1–56, DOI 10.1007/s10518-019-00771-5
- Anić F, Penava D, Guljaš I, Sarhosis V, Abrahamczyk L (2021a) Out-of-plane cyclic response of masonry infilled rc frames: An experimental study. *Engineering Structures* 238:112,258, DOI <https://doi.org/10.1016/j.engstruct.2021.112258>, URL <https://www.sciencedirect.com/science/article/pii/S0141029621004089>
- Anić F, Penava D, Sarhosis V, Abrahamczyk L (2021b) Development and calibration of a 3d micromodel for evaluation of masonry infilled rc frame structural vulnerability to earthquakes. *Geosciences* 11(11), DOI 10.3390/geosciences11110468, URL <https://www.mdpi.com/2076-3263/11/11/468>

- Anić F, Penava D, Varevac D, Sarhosis V (2019) Influence of clay block masonry properties on the out-of-plane behaviour of infilled rc frames. *Tehnički vjesnik* 26(3):831–836
- Arêde A, Furtado A, Melo J, Rodrigues H, Varum H, Pinto N (2017) Challenges and main features on quasi-static cyclic out-of-plane tests of full-scale infill masonry walls. In: Conference: 7th International Conference on Advances in Experimental Structural Engineering
- Asteris P, Cavaleri L, Di Trapani F, Tsaris A (2017) Numerical modelling of out-of-plane response of infilled frames: State of the art and future challenges for the equivalent strut macromodels. *Engineering Structures* 132:110–122, DOI 10.1016/j.engstruct.2016.10.012
- ATC (1998) Fema 306: Evaluation of earthquake damaged concrete and masonry wall buildings. Basic Procedures Manual
- Bashandy TW (1995) Behavior of reinforced concrete infilled frames under dynamic loading: Part 1. Master's thesis, The University of Texas at Austin, mS thesis
- Benedetti D, Benzoni G (1984) A numerical model for seismic analysis of masonry buildings: Experimental correlations. *Earthquake engineering & structural dynamics* 12(6):817–831
- Bergan P, Horrignoe G, Bråkeland B, Søreide T (1978) Solution techniques for non-linear finite element problems. *International Journal for Numerical Methods in Engineering* 12(11):1677–1696
- Booth E, Key D (2006) *Earthquake Design Practice for Buildings*. Thomas Telford, London, URL <http://ebooks.cambridge.org/ref/id/CB09781107415324A009>
- BSI (2002) En:1052-3: 2002, methods of test for masonry, part 3: Determination of initial shear strength. British standard institution
- BSI (2004a) Eurocode 2: Design of Concrete Structures: Part 1-1: General Rules and Rules for Buildings. British Standards Institution
- BSI (2004b) Eurocode 6: Design of masonry structures—Part 1–1: Common rules for reinforced and unreinforced masonry structures. ENV 1996-1-1: 2004: E, CEN Brussels
- BSI (2005) Eurocode 8: Design of structures for earthquake resistance-part 1: general rules, seismic actions and rules for buildings. British Standards Institution
- BSI (2015) En:772-1: 2011, methods of test for masonry units. part 1: Determination of compressive strength. British standard institution
- CAEE (1984) Colombian standards for seismic resistant design and construction nsr-84. Tech. rep., Colombian Association for Earthquake Engineering, Bogota, Colombia
- Canadian Standards Association and Standards Council of Canada (1978) *Masonry design and construction for buildings*. 1977, The Association
- CEN (2002) En 1052-2: 2002 method of test masonry. part 2 – determination of flexural strength
- CEN (2004) Methods of test for masonry - part 1: Determination of compressive strength (en 1052-1:2004).
- Cervenka V (1985) Constitutive model for cracked reinforced concrete. In: *Journal Proceedings*, vol 82, pp 877–882

- Cervenka Consulting sro (2015) ATENA for Non-Linear Finite Element Analysis of Reinforced Concrete Structures
- CNIC (1988) Venezuelan seismic code, 1988. regulations for earthquake resistant buildings. Comision De Normas Industriales, Covenin
- contributors W (2021) 2019 albania earthquake. URL https://en.wikipedia.org/wiki/2019_Albania_earthquake
- Dawe J, Seah C (1989) Out-of-plane resistance of concrete masonry infilled panels. Canadian Journal of Civil Engineering 16(6):854–864
- De Risi MT, Di Domenico M, Ricci P, Verderame GM, Manfredi G (2019) Experimental investigation on the influence of the aspect ratio on the in-plane/out-of-plane interaction for masonry infills in rc frames. Engineering Structures 189:523–540
- Di Trapani F, Shing P, Cavaleri L (2018) Macroelement model for in-plane and out-of-plane responses of masonry infills in frame structures. Journal of Structural Engineering 144(2):04017,198
- DIANA F (2017) Diana user's manual, release 10.1. DIANA FEA BV
- Domenico MD, Ricci P, Verderame GM (2018) Experimental assessment of the influence of boundary conditions on the out-of-plane response of unreinforced masonry infill walls. Journal of Earthquake Engineering 0(0):1–39, DOI 10.1080/13632469.2018.1453411, URL <https://doi.org/10.1080/13632469.2018.1453411>
- Drysdale R, Essawy A (1988) Out-of-plane bending of concrete block walls. Journal of Structural Engineering-asce - J STRUCT ENG-ASCE 114
- Drysdale R, Hamid A (2005) Masonry structures: behaviour and design. Mississauga. Canadian Masonry Design Centre
- Dyngeland T (1989) Behavior of reinforced concrete panels phd thesis. Trondheim University, Trondheim, Norway
- EAK GGJ Technical Chamber of Greece (2000) Greece code for seismic resistant structures. Greece code for Seismic Resistant Structures 2184
- ECUATORIANO CDP, INEN C (1898) Instituto ecuatoriano de normalización. NTE INEN 1996
- Červenka V, Jendele L, Cervenka J (2012) ATENA Program Documentation Part 1 Theory. Červenka Consulting Ltd., Prague
- Fardis M, Panagiotakos T (1997) Seismic design and response of bare and masonry-infilled reinforced concrete buildings part ii: infilled structures. Journal of Earthquake Engineering 1(03):475–503
- Fédération Internationale du Béton (2013) Code-type models for structural behaviour of concrete. Fédération Internationale du Béton: Bulletin, Lausanne, Switzerland
- FEMA 273 (1997) Guidelines for the seismic rehabilitation of buildings. Tech. rep., Federal Emergency Management Agency Washington, DC
- FEMA 356 (2000) Commentary for the seismic rehabilitation of buildings. FEMA-356, Federal Emergency Management Agency, Washington, DC

- Flanagan R (1994) Behavior of structural clay tile infilled frames. Tech. rep., Center for natural phenomena engineering
- Flanagan RD, Bennett RM (1999a) Arching of masonry infilled frames: Comparison of analytical methods. *Practice Periodical on Structural Design and Construction* 4(3):105–110
- Flanagan RD, Bennett RM (1999b) Bidirectional behavior of structural clay tile infilled frames. *Journal of Structural Engineering* 125(3):236–244, DOI 10.1061/(ASCE)0733-9445(1999)125:3(236)
- Fowler JJ (1994) Analysis of dynamic testing performed on structural clay tile infilled frames. PhD thesis, Oak Ridge National Lab.(ORNL), Oak Ridge, TN (United States)
- Freddi F, Novelli V, Gentile R, Velicu E, Andreev S, Andonov A, Greco F, Zhuleku E (2021) Observations from the 26th november 2019 albania earthquake: the earthquake engineering field investigation team (eefit) mission. *Bulletin of Earthquake Engineering* 19(5):2013–2044
- Furtado A, Rodrigues H, Arêde A, Varum H (2015) Experimental Characterization of the In-plane and Out-of-Plane Behaviour of Infill Masonry Walls. *Procedia Engineering* 114:862–869, DOI 10.1016/j.proeng.2015.08.041, URL <http://linkinghub.elsevier.com/retrieve/pii/S187770581501680X>
- Furtado A, Rodrigues H, Arêde A, Varum H (2016a) Experimental evaluation of out-of-plane capacity of masonry infill walls. *Engineering Structures* 111:48–63, DOI <https://doi.org/10.1016/j.engstruct.2015.12.013>, URL <https://www.sciencedirect.com/science/article/pii/S0141029615007774>
- Furtado A, Rodrigues H, Arêde A, Varum H (2016b) Simplified macro-model for infill masonry walls considering the out-of-plane behaviour. *Earthquake Engineering & Structural Dynamics* 45(4):507–524
- Furtado A, Rodrigues H, Arêde A, Varum H (2016c) Simplified macro-model for infill masonry walls considering the out-of-plane behaviour. *Earthquake Engineering & Structural Dynamics* 45(4):507–524
- Furtado A, Rodrigues H, Arêde A, Varum H (2018) Effect of the panel width support and columns axial load on the infill masonry walls out-of-plane behavior. *Journal of Earthquake Engineering* 0(0):1–29, DOI 10.1080/13632469.2018.1453400, URL <https://doi.org/10.1080/13632469.2018.1453400>
- Gabrielsen B, Wilton C, Kaplan K (1975) Response of arching walls and debris from interior walls caused by blast loading. Tech. rep., URS RESEARCH CO SAN MATEO CA
- Griffith MC, Vaculik J, Lam NTK, Wilson J, Lumantarna E (2007) Cyclic testing of unreinforced masonry wall in two way bending. *Earthquake Engineering & Structural Dynamics* 36(6):801–821, DOI 10.1002/eqe.654, URL <https://onlinelibrary.wiley.com/doi/abs/10.1002/eqe.654>
- Hak S, Morandi P, Magenes G (2014) Out-of-plane experimental response of strong masonry infills. In: 2nd European Conference on Earthquake Engineering and Seismology
- Hallquist Å (1970) Lateral loads on masonry walls. Norwegian building research institute Reprint from els Symposium on bearing walls, Warsaw 1969

- Harris HG, Sabnis G (1999) Structural modeling and experimental techniques. CRC press
- Haseltine BA (1976) Design of laterally loaded wall panels. Proceedings of the British Ceramic Society pp 115–126
- Hashemi SA, Mosalam KM (2007) Seismic evaluation of reinforced concrete buildings including effects of masonry infill walls. Tech. rep., Pacific earthquake engineering research center
- Henderson R, Jones W, Burdette E, Porter M (1993) The effect of prior out-of-plane damage on the in-plane behavior of unreinforced masonry infilled frames. In: The Fourth DOE Natural Phenomena Hazards Mitigation Conference
- Hendry AW (1973) Lateral strength of unreinforced brickwork. Structural Engineer 51(2):43–50
- Hirt M, Lebet JP (2013) Steel bridges: conceptual and structural design of steel and steel-concrete composite bridges. CRC Press
- Hobbs B, Ting M, Gilbert M (1994) An analytical approach for walls subjected to static and dynamic out-of-plane point loads. In: Proceedings of the tenth international brick/block masonry conference. University of Calgary, Alberta, pp 329–358
- Holmes M (1961) Steel frames with brickwork and concrete infilling. In: Proceedings of Institution of Civil Engineers, DOI 10.1680/iicep.1961.11305
- Hrynyk TD, Myers JJ (2008) Out-of-plane behavior of urm arching walls with modern blast retrofits: Experimental results and analytical model. Journal of structural engineering 134(10):1589–1597
- IGEO (2021) Strong motion records: Durres earthquake
- Jäger W, Vassilev T, Hoffmann J, Schöps P (2008) Unreinforced masonry basement walls—a comparison of theoretical design approaches and numerical simulations. In: Proceedings of the 14th International Brick & Block Masonry Conference. The University of Newcastle, Sydney/Australia, p 68
- Jones E, Oliphant T, Peterson P, et al (2001) SciPy: Open source scientific tools for Python. URL <http://www.scipy.org/>
- Kadysiewski S, Mosalam K (2009) Modeling of unreinforced masonry infill walls considering in-plane and out-of-plane interaction peer 2008/102. University of California, Berkeley
- Kakaletsis DJ, Karayannis CG (2009) Experimental investigation of infilled reinforced concrete frames with openings. ACI Structural Journal 106(2)
- Klingner R, Rubiano N, Bashandy T, Sweeney S (1996) Evaluation and analytical verification of shaking table data from infilled frames, part 2: Out-of-plane behavior. In: Proceedings of the 7th North American Masonry Conference, Colorado: Elsevier Science Ltd, pp 521–532
- Kollegger J, Mehlhorn G (1988) Experimentelle und analytische untersuchungen zur aufstellung eines materialmodells fuer gerissene stahbetonscheiben. Nr 6 Forschungsbericht, Massivbau, Gesamthochschule Kassel
- Komaraneni S, Rai DC, Singhal V (2011) Seismic behavior of framed masonry panels with prior damage when subjected to out-of-plane loading. Earthquake Spectra 27(4):1077–1103

- Kuang JS, Yuen YP (2010) Effect of out-of-plane loading on in-plane behaviour of unreinforced infilled rc frames. ICCCB, Nottingham
- Kupfer H, Hilsdorf HK, Rusch H (1969) Behavior of concrete under biaxial stresses. In: Journal proceedings, vol 66, pp 656–666
- Lam N, Griffith M, Wilson J, Doherty K (2003) Time–history analysis of urm walls in out-of-plane flexure. *Engineering Structures* 25(6):743 – 754, DOI [https://doi.org/10.1016/S0141-0296\(02\)00218-3](https://doi.org/10.1016/S0141-0296(02)00218-3), URL <http://www.sciencedirect.com/science/article/pii/S0141029602002183>
- Liu M, Cheng Y, Liu X (2011) Shaking table test on out-of-plane stability of infill masonry wall. *Transactions of Tianjin University* 17(2):125
- Masonry Standards Joint Committee and others (1999) Building code requirements for masonry structures. American Concrete Institute, Detroit, MI, ISBN 1929081022
- Mays GC, Hetherington JG, Rose TA (1998) Resistance-deflection functions for concrete wall panels with openings. *Journal of Structural Engineering* 124(5):579–587, DOI 10.1061/(ASCE)0733-9445(1998)124:5(579), URL <https://ascelibrary.org/doi/abs/10.1061/%28ASCE%290733-9445%281998%29124%3A5%28579%29>
- McDowell E, McKee K, Sevin E (1956a) Arching action theory of masonry walls. *Journal of the Structural Division* 82(2):1–8
- McDowell E, McKee K, Sevin E (1956b) Discussion of arching action theory of masonry walls. *Journal of the Structural Division* 82:27–40
- MHPP (1995) Nepal national building code for seismic design of buildings in nepal (nbc-105). Ministry of Housing and Physical Planning, Department of Buildings
- van Mier JG (1986) Multiaxial strain-softening of concrete. *Materials and structures* 19(3):190–200
- Misir IS, Ozcelik O, Girgin SC, Yucel U (2016) The behavior of infill walls in rc frames under combined bidirectional loading. *Journal of Earthquake Engineering* 20(4):559–586, DOI 10.1080/13632469.2015.1104748
- Moghaddam H, Goudarzi N (2010) Transverse resistance of masonry infills. *ACI Structural Journal* 107(4):461
- Monk CB (1958) Resistance of Structural Clay Masonry to Dynamic Forces: A Design Manual for Blast Resistance. 7, Structural Clay Products Research Foundation
- Morandi P, Hak S, Magenes G (2013) Simplified out-of-plane resistance verification for slender clay masonry infills in rc frames. In: ANIDIS 2013-XV Convegno di Ingegneria Sismica
- Mosoarca M, Petrus C, Stoian V, Anastasiadis A (2016) Behaviour of masonry infills subjected to out of plane seismic actions. part 2: Experimental testing. In: 16th International Brick and Block Masonry Conference
- NCH (1996) Earthquake-resistant design of buildings nch 433. National Institute of Normalization
- Neufert E, Jones V, Thackara J, Miles R (1980) Architects' data. Granada St Albans, Herts
- NSCP (1992) National structural code of philippines, vol. 1, fourth edition (nscp). The Board of Civil Engineering of the Professional Regulation Commission

- NTC LG (2008) Norme tecniche per le costruzioni. Italian technical norms for constructions
- NTS (1997) National technical standard e-030 “earthquake resistant design”. Ministry of Transportation, Communications and Housing
- NZS-3101 (1995) Code of practice for the design of concrete structures, part 1 (nzs-3101). Tech. rep., Standards Association of New Zealand, Wellington, New Zealand
- Pasca M, Liberatore L, Masiani R (2017) Reliability of analytical models for the prediction of out-of-plane capacity of masonry infills. *Structural Engineering and Mechanics* 64(6):765–781
- Penava D (2012) Utjecaj otvora na seizmički odgovor armirano-betonskih okvira sa zidanim ispunom. PhD thesis, Josip Juraj Strossmayer University of Osijek. Faculty of Civil Engineering.
- Penava D, Sigmund V (2017) Out-of-plane behaviour of framed-masonry walls with opening as a result of shaking table tests. In: 16th World Conference on Earthquake Engineering
- Penava D, Sigmund V, Kožar I (2016) Validation of a simplified micromodel for analysis of infilled rc frames exposed to cyclic lateral loads. *Bulletin of earthquake engineering* 14(10):2779–2804
- Penava D, Sarhosis V, Kožar I, Guljaš I (2018) Contribution of rc columns and masonry wall to the shear resistance of masonry infilled rc frames containing different in size window and door openings. *Engineering Structures* 172:105–130, DOI <https://doi.org/10.1016/j.engstruct.2018.06.007>, URL <https://www.sciencedirect.com/science/article/pii/S0141029617329681>
- Pereira MFP, Pereira M, Ferreira J, Lourenço PB (2011) Behavior of masonry infill panels in rc frames subjected to in plane and out of plane loads. In: 7th International Conference on Analytical Models and New Concepts in Concrete and Masonry Structures
- Petrus C, Stoian V, Marius M, Anastasiadis A (2015) Reinforced concrete frames with masonry infills. out of plane experimental investigation. *Acta Technica Napocensis*
- Phani S, Sekhar T, Rao S (2013) Sravana. evaluation of relationship between mechanical properties of high strength self compacting concrete. *Am J Eng Res* 2:67–71
- da Porto F, Guidi G, Dalla Benetta M, Verlato N (2013) Combined in-plane/out-of-plane experimental behaviour of reinforced and strengthened infill masonry walls. In: Proceedings of 12th Canadian Masonry Symposium
- Preti M, Bettini N, Plizzari G (2012) Infill walls with sliding joints to limit infill-frame seismic interaction: Large-scale experimental test. *Journal of Earthquake Engineering* 16(1):125–141, DOI 10.1080/13632469.2011.579815
- Preti M, Migliorati L, Giuriani E (2015) Experimental testing of engineered masonry infill walls for post-earthquake structural damage control. *Bulletin of Earthquake Engineering* 13(7):2029–2049, DOI 10.1007/s10518-014-9701-2, URL <http://link.springer.com/10.1007/s10518-014-9701-2>
- Rabinovitch O, Madah H (2011) Finite element modeling and shake-table testing of unidirectional infill masonry walls under out-of-plane dynamic loads. *Engineering Structures* 33(9):2683 – 2696, DOI <https://doi.org/10.1016/j.engstruct.2011.05.019>
- Radimpex Software doo (2012) Tower. <https://www.radimpex.rs/en>

- Reindl L, Butenweg C, Kubalski T (2011) Numerical simulation of unreinforced masonry walls subject to dynamic out-of plane loading. In: Proceedings of the 3rd international conference on computational methods in structural dynamics and earthquake engineering, pp 25–28
- Ricci P, Di Domenico M, Verderame GM (2018) Experimental assessment of the in-plane/out-of-plane interaction in unreinforced masonry infill walls. *Engineering Structures* 173:960–978
- Rupakhety R, Ólafsson S (2018) Earthquake Engineering and Structural Dynamics in Memory of Ragnar Sigbjörnsson, Geotechnical, Geological and Earthquake Engineering, vol 44. Springer International Publishing, Cham, DOI 10.1007/978-3-319-62099-2, URL <https://link.springer.com/content/pdf/10.1007/978-3-319-62099-2.pdf><http://link.springer.com/10.1007/978-3-319-62099-2>
- Sabir A, Lock A (1972) The applications of finite elements to large deflection geometrically nonlinear behaviour of cylindrical shells. In: Brebbia C, Tottenham H (eds) Variational methods in engineering: proceedings on an international conference held at the University of Southampton, 25th September, 1972, Southampton University Press, URL <https://eprints.soton.ac.uk/75511/>
- Savitzky A, Golay MJ (1964) Smoothing and differentiation of data by simplified least squares procedures. *Analytical chemistry* 36(8):1627–1639
- Sepasdar R (2017) Experimental investigation on the out-of-plane behaviour of concrete masonry infilled rc frames. Master's thesis, Dalhousie University
- Shapiro D, Uzarski J, Webster M, Angel R, Abrams DP (1994) Estimating out-of-plane strength of cracked masonry infills. Tech. rep., University of Illinois Engineering Experiment Station. College of Engineering. University of Illinois at Urbana-Champaign.
- SI (1995) Design provisions for earthquake resistance of structure (si-413). The Standards Institution of Israel
- Sigmund V, Penava D (2014) Influence of openings, with and without confinement, on cyclic response of infilled r-c frames — an experimental study. *Journal of Earthquake Engineering* 18(1):113–146, DOI 10.1080/13632469.2013.817362, URL <https://doi.org/10.1080/13632469.2013.817362>, <https://doi.org/10.1080/13632469.2013.817362>
- SNiP (1995) Building code on construction in seismic areas (snip-ii-7-81). The Ministry for Construction of Russia
- Sorić Z (2016) Zidane konstrukcije. Z. Sorić
- de Sousa H (2014) Typical masonry wall enclosures in portugal. *Enclosure Masonry Wall Systems Worldwide: Typical Masonry Wall Enclosures in Belgium, Brazil, China, France, Germany, Greece, India, Italy, Nordic Countries, Poland, Portugal, the Netherlands and USA* p 179
- Standard I (2002) Is 1893: Indian standard criteria for earthquake resistant design of structures: Part 1 general provisions and buildings. Tech. Rep. August, Indian Standard
- Surendran S, Kaushik HB (2012) Masonry infill rc frames with openings: review of in-plane lateral load behaviour and modeling approaches. *The open construction and building technology journal* 6(Suppl. 1-M9):126–154
- Tasnimi A, Mohebkah A (2011) Investigation on the behavior of brick-infilled steel frames with openings, experimental and analytical approaches. *Engineering Structures* 33(3):968–980

- Tomažević M (1999) Earthquake-Resistant Design of Masonry Buildings. Imperial College Press, London, DOI doi:10.1142/9781848160835_fmatter, URL <http://books.google.com.pk/books/about/Earthquake{ }resistant{ }Design{ }of{ }Masonry{ }B.html?id=u0hmaZWJ7wIC{&}pgis=1, arXiv:1011.1669v3>
- Tools for Engineer website (2019) Tools for engineer. <http://www.toolsforengineer.com/>, accessed: 13/02/2019
- Toygur ME, Toparli M, Sen F, Gungor MA (2009) Fracture energy determination and critical crack propagation between core and veneer ceramic interface by experiment and finite element method. *Materials & Design* 30(6):2278–2282
- Tu YH, Chuang TH, Liu PM, Yang YS (2010) Out-of-plane shaking table tests on unreinforced masonry panels in rc frames. *Engineering Structures* 32(12):3925 – 3935, DOI <https://doi.org/10.1016/j.engstruct.2010.08.030>, URL <http://www.sciencedirect.com/science/article/pii/S014102961000341X>
- Ugural AC, Fenster SK (2003) Advanced strength and applied elasticity. Pearson Education
- USGS (2021) M 6.4 - 15 km wsw of mamurras, albania. URL <https://earthquake.usgs.gov/earthquakes/eventpage/us70006d0m>
- Vaculik J (2012) Unreinforced masonry walls subjected to out-of-plane seismic actions. PhD thesis, The University of Adelaide; School of Civil, Environmental & Mining Engineering
- Varela-Rivera J, Polanco-May M, Fernandez-Baqueiro L, I Moreno E (2012) Confined masonry walls subjected to combined axial loads and out-of-plane uniform pressures. *Canadian Journal of Civil Engineering* 39:439–447
- Vasios N (2015) Nonlinear analysis of structures. URL <https://scholar.harvard.edu/files/vasios/files/ArcLength.pdf>
- VBS (2006) Vietnamese seismic design standard tcxdvn 375:2006. Tech. rep., Vietnamese Building Standard, Hanoi, Vietnam
- Vecchio FJ, Collins MP (1986) The modified compression-field theory for reinforced concrete elements subjected to shear. In: *Journal Proceedings*, vol 83, pp 219–231
- Verlato N, Guidi G, da Porto F, Modena C (2016) Innovative systems for masonry infill walls based on the use of deformable joints: combined in-plane/out-of-plane tests. In: *Proceedings of the 16th International Brick and Block Masonry Conference*
- Vonk RA (1992) Softening of concrete loaded in compression. PhD thesis, Technische Universiteit Eindhoven
- Vos E (1983) Influence of loading rate and radial pressure on bond in reinforced concrete. A numerical and experimental approach. PhD thesis, Delft University
- Wang C (2017) Experimental investigation on the out-of-plane behaviour of concrete masonry infilled frames. Master's thesis, Dalhousie University
- Wilton C, Gabrielsen BL (1973) Shock tunnel tests of preloaded and arched wall panels. Tech. rep., URS RESEARCH CO SAN MATEO CALIF

- Wright EW, Gaylord EH (1968) Analysis of unbraced multistory steel rigid frames. *Journal of the Structural Division* 94(5):1143–1164
- Zovkić J (2013) Behaviour of reinforced-concrete frames infilled with masonry under lateral forces. PhD thesis, Josip Juraj Strossmayer University of Osijek

